$\mathcal{CP}$ Violation studies of $B \to DD$ channels using the LHCb detector

Katherine Anne George
of
Trinity College, University of Cambridge

A thesis submitted to the University of Cambridge
for the degree of Doctor of Philosophy

March 2004.

$\mathcal{CP}$ Violation studies of $B \to DD$ channels using the LHCb detector

Abstract

LHCb is one of five experiments which will start data-taking at the Large Hadron Collider (LHC) in 2007. LHCb is a dedicated B-physics and rare decay experiment, with the aim to throughly test the internal consistency of the Standard Model, and in particular, to over-constrain the parameters of the CKM matrix and the unitarity triangle. This thesis outlines the main goals of the LHCb experiment, followed by a review of the theoretical background upon which physics at the LHCb experiment is based. The detector design of the LHCb experiment is also described, with emphasis placed upon the Ring-Imaging Cherenkov (RICH) detectors.

The photon detector choice for the RICH is the pixel Hybrid Photon Detector (HPD). Studies of the performance of a 10 MHz full-scale prototype pixel HPD are presented and despite significant bump-bond degradation during manufacture, its behaviour is shown to be consistent with that of previous prototypes. A method for determining the pixel HPD detection efficiency to single photoelectrons is outlined. The prototype was determined to have an efficiency of $\epsilon_{\text{p.e.}} = 0.827 \pm 0.001\,(\text{stat}) \pm 0.037\,(\text{syst})$. This figure is compared to the minimum requirement of $\epsilon_{\text{p.e.}} \sim 85\,\%$ criteria set by LHCb for the choice of the RICH photodetector technology.

Analysis software for $B \to DD$ channels; $B_d^0 \to D^+(\pi^+\pi^+K^-)\ D^-(\pi^-\pi^-K^+)$, $B_s^0 \to D_s^+(\pi^+K^+K^-)\ D_s^-(\pi^-K^+K^-)$ and $B_c^+ \to D_s^+(\pi^+K^+K^-)\ \overline{D}^0(\pi^-K^+)$ have been implemented and simulation studies carried out. Studies of these channels were motivated by two proposed theoretical methods to determine the sensitivity to the CKM angle γ. One proposed method is that γ can be extracted from a measurement of the time dependent $B_d^0 \to D^+D^-$ rate provided that the overall normalisation is fixed using the $\mathcal{CP}$-averaged $B_s^0 \to D_s^+D_s^-$ rate and assuming that the CKM angle β is known. It has also been proposed that γ can also be extracted from amplitude relations in the measurement of $B_c^+ \to D_s^+\overline{D}^0$ decays.

For each of these channels the optimised cuts and the resulting annual event yields are presented. The trigger and flavour tagging performance have also been investigated. It is shown that the $B_d^0 \to D^+D^-$ and $B_s^0 \to D_s^+D_s^-$ channels can be detected, reconstructed, selected and triggered with efficiencies of $0.107 \pm 0.09\%$ and $0.091 \pm 0.08\%$ respectively. This results in annual triggered event yields of 2.6 ± 0.2 k/year and 2.8 ± 0.3 k/year. Assuming that inclusive $b\overline{b}$ events are the dominant source of combinatorial background then an upper limit to the background-to-signal ratio (B/S) of < 1.7 and < 2.4 respectively has been set using $\sim \mathcal{O}(10^7)$ inclusive $b\overline{b}$ events. This corresponds to ~ 4 minutes of LHCb data-taking. Studies of the $B_c^+ \to D_s^+\overline{D}^0$ channel show that it is unlikely that this channel could be used to study γ and the B_c mass and lifetime at LHCb. Some of the work presented here has previously been published in [1–4].

Declaration

This dissertation is the result of my own work, except where explicit reference is made to the work of others, and has not been submitted for another qualification to this or any other university. It does not exceed the 60,000 word limit prescribed by the Degree Committee for Physics & Chemistry.

Katherine Anne George

Acknowledgements

It is thanks to the collaborative effort of many people from LHCb at Cambridge, the UK and elsewhere that I have been able to complete the work presented in this thesis. While at CERN, the work presented in Chapter 5 was carried out under the guidance of Thierry Gys. There are many people within the LHCb RICH group whose work contributed to the development of the HPDs. In particular Ken Wyllie, Maria Girone, David Websdale (and again) Thierry Gys were always willing to discuss work and answer my many questions. The analyses presented in Chapters 6-8 were carried out under the eyes of the LHCb Physics and DaVinci groups from which Gloria Corti was particularly helpful.

This PhD was financially supported by the Particle Physics and Astronomy Research Council (PPARC) under studentship number PPA/S/S/2000/03000. Through PPARC I was able to live and work in Geneva for nine months, and attend the 2002 SLAC Summer School in sunny California.

I am grateful to Professor Janet Carter for offering me a place within the Cambridge HEP Group. From the group I would particularly like to thank Jan White and Anna-Rosa Gejlsbjerg for their friendship, John Hill and Steve Wotton for keeping the computing hassle to a minimum and Pat & David Ward for being very approachable fonts of knowledge. Matthew Ford made it fun to share an office and along with Chris Ainsley was never slow to find the more surreal items on the BBC News website. Karl Harrison is thanked for being unflappable, calm and optimistic when I was none of these. Along with Karl Harrison, I am very grateful to Val Gibson for suggestions to, and proofreading of this thesis. Thanks to everyone who made me smile - especially Chris Lester, Clive Barham and Maurice Goodrick. While at CERN (and now at Liverpool) David Hutchcroft has always been a good person to know. The Liverpool BaBar Group and Christos Touramanis are thanked for their patience while waiting for me to write up.

Finally I am especially indebted to another (ex-Cambridge) Liverpool BaBarian, Adrian Bevan for reasons too numerous to list.

My family have always encouraged me through each stage of my education. This support has been essential in getting me this far. To Mam, Dad and Grandparents, a very big thank you.

Mam and Dad's wedding photo. October 1972.

Hang on to your hopes, my friend
That's an easy thing to say, but if your hopes should pass away
Simply pretend
That you can build them again
Look around, the grass is high
The fields are ripe, it's the springtime of my life
(Taken from *Hazy Shade of Winter.* Simon and Garfunkel. February 1968.)

Contents

List of Figures

List of Tables

Chapter 1

Introduction

The invariance of a physical property under the operation of a transformation is referred to as a symmetry. According to Noether's Theorem (1911), every symmetry of nature yields a conservation law, and conversely, every conservation law yields an underlying symmetry. For example, if a system is invariant under translations in space then momentum is conserved, and if a system is invariant under rotation then angular momentum is conserved. These translation and rotation operators, along with Lorentz boosts, are a set of independent continuous transformations which preserve the Minkowski interval $t^2 - \underline{x}^2$. The three independent discrete transformations which also preserve $t^2 - \underline{x}^2$ are charge conjugation $\mathcal{C}$, parity transformation $\mathcal{P}$ and time reversal $\mathcal{T}$.

$\mathcal{C}$ is the transformation of a particle into its antiparticle without changing its momentum $\underline{p}$ or spin $\underline{s}$. The parity transformation $\mathcal{P}$ acts to reverse the signs of the three spatial elements of the four vector, for example $(\mathrm{t}, \underline{x}) \rightarrow (\mathrm{t}, -\underline{x})$ and $(\mathrm{E}, \underline{p}) \rightarrow (\mathrm{E}, -\underline{p})$ but leaves the spin of the particle unchanged. $\mathcal{P}$ can be visualised as the mirror-image plus a π rotation normal to the plane of the mirror. The time reversal operator $\mathcal{T}$ acts to reverse the sign of the time component of the four vector $(\mathrm{t}, \underline{x}) \rightarrow (\text{-t}, \underline{x})$.

The $\mathcal{CPT}$ theorem states that the combined operation of $\mathcal{C}$, $\mathcal{P}$ and $\mathcal{T}$ ($\mathcal{CPT}$), is an exact symmetry in any Quantum Field Theory; i.e. that the laws of physics are invariant under the combined operation $\mathcal{CPT}$, with the consequence that the mass, lifetime and

magnetic moment of a particle and its antiparticle are the same [5].

In the early 1950s a paradox known as the τ-θ puzzle arose, where two spin-0 mesons (at that time called the τ^+ and the θ^+, but now known as the K^+), with the same mass and lifetime, were identical, apart from the fact that the θ^+ decayed into two pions and the τ^+ decayed to three pions. In other words, the τ^+ and the θ^+ decayed to states of opposite parity. Prior to 1956 it was always assumed that all physical processes were parity conserving, in other words, that the mirror image of any physical process, is also a possible physical process. Yang and Lee (1956) proposed an experimental test of this assumption having found out that there existed evidence for parity invariance in both strong and electromagnetic interactions, but none existed for the weak interaction [6]. This test was carried out in 1957 by Wu *et.al* who found that weak interactions did not conserve parity in the radioactive decay of cobalt-60 [7]. Despite this parity violation, it was thought that it was always violated together with $\mathcal{C}$, so as to respect the combined operation $\mathcal{CP}$.

In 1963, Cabibbo proposed the idea of "quark mixing", suggesting that in a two-generation Standard Model with 4 quarks, $\mathcal{CP}$ violation could not be accommodated since the rotation matrix transforming one set of quark states into another is restricted to real numbers [8]. However, in the following year, Christenson *et.al* observed the $\mathcal{CP}$-violating $K_L \to \pi^+\pi^-$ decay [9].

Interest in $\mathcal{CP}$ violation widened beyond particle physics when in 1967, Sakharov listed the violation of $\mathcal{C}$ and $\mathcal{CP}$ as one of the three necessary requirements for an initially matter-antimatter symmetric universe to evolve into a matter-dominated one, the other two conditions being that of baryon number violation, and a departure from thermal equilibrium [10]. The Standard Model is able to meet all of these requirements: baryon number violation through transitions to different vacuum states above the electroweak energy scale; and being out of thermal equilibrium at the electroweak energy scale through the first order phase transition [11].

Kobayashi and Maskawa (1973) proposed that Cabibbo's quark mixing could be

generalised to cover three generations of quark pairs [12]. In a theory containing six quarks, and therefore three generations, the rotation matrix known as the CKM matrix, can have a physical phase which allows $\mathcal{CP}$ violation to occur, thereby fulfilling the remaining Sakharov condition. Only three of the six quarks (u, d and s) had been observed experimentally by 1973, the remaining three (c, b and t) not being observed until 1974 [13], 1977 [14, 15] and 1994 respectively [16, 17]. However, there remains the complication that the level of $\mathcal{CP}$ violation predicted in the Standard Model is too small to explain the observed matter-antimatter asymmetry in the universe [18]. This fact alone provides a strong motivation to search for new physics in $\mathcal{CP}$ violation.

The NA31 experiment at CERN first published evidence for direct[a] $\mathcal{CP}$ violation in 1987 using the kaon decay modes $\mathrm{K}_L/\mathrm{K}_S$ to $\pi^+\pi^-$ and $\pi^0\pi^0$ [19], which was later confirmed in 2000 by the NA48 experiment (CERN) [20]. Also from 1990-1999, the CPLEAR experiment at CERN searched for $\mathcal{CP}$, $\mathcal{T}$ and $\mathcal{CPT}$ symmetries through a direct comparison of K^0 and $\overline{\mathrm{K}^0}$ time evolutions [21]. Among its many achievements, the experiment was able to demonstrate that $\mathcal{CP}$ violation in mixing is related to $\mathcal{T}$ violation and to measure the $\mathrm{K_L}$-$\mathrm{K_S}$ mass difference [22].

In 1999 the so-called "B-factory" $\mathrm{e^+e^-}$ experiments BaBar (SLAC) [23] and Belle (KEK) [24] started data-taking. These experiments are located at the PEP-II and KEK-B colliders respectively, which run at the $\Upsilon(4S)$ resonance, allowing the study of $\mathrm{B}^\pm$ and B^0_d decays. Their main results so far have been the first evidence of $\mathcal{CP}$ violation in the B meson system and the measurement of the unitarity angle β [25, 26]. This is discussed further in Section 2.8.2. Both of these experiments have exceeded their design luminosity and are expected to continue data-taking until at least 2007.

The two major Fermilab experiments CDF and D0 at the Tevatron $p\overline{p}$ collider collected more than 100 pb^{-1} of data between 1992 and 1996 at $\sqrt{s} = 1.8$ TeV. It was from data taken during this period, known as Run-I, where the $\mathrm{B_c}$ meson was first observed using the CDF detector [27]. Upgrades in both the CDF and D0 detectors mean that

[a]The different types of $\mathcal{CP}$ violation are described later in Section 2.2.2.

they should both be capable of similar performances in the B-physics sector during Run-II (2001-2009). The Tevatron is currently the only competitor to the B-factories and will remain the only experimental environment in which the B_s^0, $B_c^{\pm}$ and Λ_b states can be studied until the start of the Large Hadron Collider (LHC) in 2007 [28].

In 2007, the B-physics experiment, LHCb, based at the LHC will come into operation. The LHCb experiment has been designed to exploit as wide a range of B-physics topics as possible since the LHC will be a source of a full spectrum of B hadrons, $B^{\pm}$, B_d^0, B_s^0, $B_c^{\pm}$, Λ_b and others. The aims of the LHCb experiment are three-fold; firstly, to improve upon the precision of the measurements already made at BaBar and Belle; secondly, to investigate further the existence of $\mathcal{CP}$ violation in the B meson system; and finally to search for new physics in the B-meson sector, outside of that described by the Standard Model. LHCb will be able to disentangle the Standard Model and New Physics contributions to $\mathcal{CP}$ violation. Also at the LHC are the general purpose detectors ATLAS and CMS which have been optimised for high-p_T physics for example Higgs and Supersymmetry searches, but will also have specific features for B-hadron reconstruction accommodated into their design. They will be running a B-physics program during the first three years of the LHC which is a period of low-luminosity running when the LHC will not have reached the design luminosity of 10^{34} $\mathrm{cm}^{-2}\mathrm{s}^{-1}$. During this period triggering and reconstruction of low-p_T events, as required for B-physics, will be easier [29,30].

In addition, the B-physics experiment, BTeV, at Fermilab, is expected to start data-taking in 2009 and is designed to have a similar physics program to that of LHCb [31,32]. BaBar and Belle have provisional plans for detector upgrades to run at higher luminosities of $\sim 10^{35} - 10^{36}\mathrm{cm}^{-2}\mathrm{s}^{-1}$ (so-called "Super B-Factories") which will allow them to produce complementary results to that of LHCb in the B_d^0 and $B^{\pm}$ decay channels [33,34].

Future prospects of the measurements of $\mathcal{CP}$ violating parameters will be discussed at the end of the next chapter, before which the theoretical formalism of $\mathcal{CP}$ violation in the B meson sector will be introduced. Chapter 3 describes two methods of measuring the CKM angle γ using the $B_{d(s)}^0 \to D_{(s)}^+ D_{(s)}^-$ and $B_c^+ \to D_s^+ \overline{D}^0$ channels, which motivates the

analyses presented in Chapters 6-8. Chapter 4 describes the LHCb detector, in particular the Ring Imaging Cherenkov (RICH) sub-detector, for which the chosen technology is the Hybrid Photon Detector (HPD). Chapter 5 presents an analysis to determine the efficiency of a prototype HPD to single photoelectrons. Chapter 9 is the concluding chapter and summarises the main results from this thesis.

Chapter 2

Overview of $\mathcal{CP}$ Violation

2.1 Introduction

This chapter starts by introducing the phenomenology of mixing and $\mathcal{CP}$ Violation for the neutral b-flavoured mesons, B^0_d and B^0_s. Once this framework has been established, the different mechanisms and conventions of $\mathcal{CP}$ Violation in the B meson sector are discussed. The CKM matrix, the unitarity triangles, and the different parameterisations of the CKM matrix are then presented. The chapter concludes with a review of the recent measurements of the unitarity triangle angle β, and a discussion of the future prospects of measuring other $\mathcal{CP}$ violating parameters with respect to the current and anticipated performances of the BaBar, Belle and LHCb experiments.

2.2 Phenomenology of mixing and $\mathcal{CP}$ Violation

2.2.1 Neutral B-meson mixing

In the neutral B^0_q-meson systems, (q = d, s), the two possible states of well-defined flavour, known as flavour eigenstates, are those corresponding to the particle B^0_q ($\overline{b}q$),

$|\mathrm{B}_\mathrm{q}^0\rangle$ and its antiparticle $\overline{\mathrm{B}_\mathrm{q}^0}$ ($\mathrm{b}\overline{\mathrm{q}}$), $|\overline{\mathrm{B}_\mathrm{q}^0}\rangle$. If only the strong and the electromagnetic interactions existed, then B_q^0 and $\overline{\mathrm{B}_\mathrm{q}^0}$ would be stable and form a particle-antiparticle pair with a common mass. However, due to the presence of the weak interaction, the B_q^0 and $\overline{\mathrm{B}_\mathrm{q}^0}$ decay. Since there is no conservation law respected by the weak interaction which prevents B_q^0 and $\overline{\mathrm{B}_\mathrm{q}^0}$ from having both real and virtual transitions to some common state, then B_q^0 and $\overline{\mathrm{B}_\mathrm{q}^0}$ oscillate between themselves, known as mixing, before decaying.

As a starting point, we consider the evolution of initial flavour eigenstates $|\mathrm{B}_\mathrm{q}^0\rangle$ and $|\overline{\mathrm{B}_\mathrm{q}^0}\rangle$ in the form

$$a(t)\ |\mathrm{B}_\mathrm{q}^0\rangle\ +\ b(t)\ |\overline{\mathrm{B}_\mathrm{q}^0}\rangle\ + c_1(t)|n_1\rangle\ + c_2(t)|n_2\rangle\ + c_3(t)|n_3\rangle\ +\ \ldots\ , \tag{2.1}$$

where n_1, n_2 etc. are states to which either B_q^0 or $\overline{\mathrm{B}_\mathrm{q}^0}$ may decay, and t is the time measured in the B_q^0-$\overline{\mathrm{B}_\mathrm{q}^0}$ rest frame. Several assumptions allow Equation 2.1 to be simplified. The assumptions are that; at $t = 0$, only *a(t)* and *b(t)* are non-zero; we are only interested in computing the values of *a(t)* and *b(t)* and not c_i*(t)*; and that the time t in which we are interested are much larger than the typical strong-interaction scale [35]. Under these assumptions, Equation 2.1 reduces to the time-dependent quantum superposition

$$a(t)\ |\mathrm{B}_\mathrm{q}^0\rangle\ +\ b(t)\ |\overline{\mathrm{B}_\mathrm{q}^0}\rangle \tag{2.2}$$

which satisfies the Schrödinger equation

$$i\frac{\partial}{\partial t}\begin{pmatrix} a(t) \\ \\ b(t) \end{pmatrix} = \mathbf{H}\begin{pmatrix} a(t) \\ \\ b(t) \end{pmatrix}. \tag{2.3}$$

$\mathbf{H}$ is the Hamiltonian matrix of the form

$$\mathbf{H} = (\mathbf{M}\ -\ \frac{i}{2}\mathbf{\Gamma}) = \begin{pmatrix} M_{11} - \frac{i}{2}\Gamma_{11} & M_{12} - \frac{i}{2}\Gamma_{12} \\ \\ M_{21} - \frac{i}{2}\Gamma_{21} & M_{22} - \frac{i}{2}\Gamma_{22} \end{pmatrix} \tag{2.4}$$

where $\mathbf{M}$ and $\mathbf{\Gamma}$ are both Hermitian matrices.

Since a consequence of the $\mathcal{CPT}$ theorem is that the mass, lifetime and magnetic moment of a particle and its antiparticle are the same [5], then

$$M_{11} \;=\; M_{22} \;\equiv\; M \tag{2.5}$$

and

$$\Gamma_{11} \;=\; \Gamma_{22} \;\equiv\; \Gamma, \tag{2.6}$$

where M and Γ are the mass and decay width of the $\mathrm{B^0_q}$ and $\overline{\mathrm{B^0_q}}$ flavour states respectively. The off-diagonal terms M_{21} and Γ_{21} are the dispersive and absorptive parts of the transition amplitude from the particle $\mathrm{B^0_q}$ to its antiparticle $\overline{\mathrm{B^0_q}}$:

$$M_{21} \;=\; M^*_{12} \tag{2.7}$$

and

$$\Gamma_{21} \;=\; \Gamma^*_{12}. \tag{2.8}$$

The two eigenstates of the Hamiltonian matrix in Equation 2.4 are given by linear combinations of the particle and antiparticle flavour eigenstates $|\mathrm{B^0_q}\rangle$ and $|\overline{\mathrm{B^0_q}}\rangle$. Denoting the eigenstates of the Hamiltonian by $|\mathrm{B}_1\rangle$ and $|\mathrm{B}_2\rangle$, then

$$|\mathrm{B}_1\rangle \;=\; p|\mathrm{B^0_q}\rangle \;+\; q|\overline{\mathrm{B^0_q}}\rangle \tag{2.9}$$

and

$$|\mathrm{B}_2\rangle \;=\; p|\mathrm{B^0_q}\rangle \;-\; q|\overline{\mathrm{B^0_q}}\rangle. \tag{2.10}$$

p and q are complex numbers that represent the amount of meson state mixing. They are fixed via the normalisation condition

$$|p|^2 \;+\; |q|^2 \;=\; 1. \tag{2.11}$$

The eigenvalues of $|\mathrm{B}_1\rangle$ and $|\mathrm{B}_2\rangle$, λ_1 and λ_2 are obtained from the eigenvalue equation

$$| \mathbf{H} - \lambda \mathbf{I} | = 0, \tag{2.12}$$

where $\mathbf{I}$ is the 2×2 unit matrix, such that

$$\lambda_1 = \left(\mathbf{M} - \frac{i}{2}\mathbf{\Gamma}\right) + \sqrt{\left(M_{12} - \frac{i}{2}\Gamma_{12}\right)\left(M^*_{12} - \frac{i}{2}\Gamma^*_{12}\right)} \tag{2.13}$$

and

$$\lambda_2 = \left(\mathbf{M} - \frac{i}{2}\mathbf{\Gamma}\right) - \sqrt{\left(M_{12} - \frac{i}{2}\Gamma_{12}\right)\left(M^*_{12} - \frac{i}{2}\Gamma^*_{12}\right)}. \tag{2.14}$$

The values of p and q are determined from

$$(\mathbf{H} - \lambda \mathbf{I}) \begin{pmatrix} p \\ \pm q \end{pmatrix} = 0, \tag{2.15}$$

such that the ratio of q/p is given by

$$\frac{q}{p} = \sqrt{\frac{M^*_{12} - \frac{i}{2}\Gamma^*_{12}}{M_{12} - \frac{i}{2}\Gamma_{12}}}. \tag{2.16}$$

The time-evolution of the eigenstates of the Hamiltonian, $|\mathrm{B}_1\rangle$ and $|\mathrm{B}_2\rangle$ are given by the phases

$$e^{-i\lambda_1 t} = e^{-im_1 t}\, e^{-\frac{i}{2}\Gamma_1 t} \quad \text{and} \quad e^{-i\lambda_2 t} = e^{-im_2 t}\, e^{-\frac{i}{2}\Gamma_2 t} \tag{2.17}$$

such that

$$|\mathrm{B}_1(t)\rangle = |\mathrm{B}_1(0)\rangle\, e^{-im_1 t} e^{-\frac{i}{2}\Gamma_1 t} \tag{2.18}$$

and

$$|\mathrm{B}_2(t)\rangle = |\mathrm{B}_2(0)\rangle\, e^{-im_2 t} e^{-\frac{i}{2}\Gamma_2 t}, \tag{2.19}$$

with

$$m_{1,2} = M \pm \Re\sqrt{H_{12}H_{21}} \tag{2.20}$$

and

$$\Gamma_{1,2} = \Gamma \mp 2\Im\sqrt{H_{12}H_{21}}. \tag{2.21}$$

Using Equations 2.18 and 2.19, the time evolution of the initially pure flavour eigenstates $|\mathrm{B}^0_\mathrm{q}\rangle$ and $|\overline{\mathrm{B}^0_\mathrm{q}}\rangle$ defined in Equations 2.9 and 2.10, are described by

$$|\mathrm{B}^0_\mathrm{q}(t)\rangle \;=\; g_+(t)|\mathrm{B}^0_\mathrm{q}\rangle \;+\; \frac{q}{p}g_-(t)|\overline{\mathrm{B}^0_\mathrm{q}}\rangle \tag{2.22}$$

and

$$|\overline{\mathrm{B}^0_\mathrm{q}}(t)\rangle \;=\; g_+(t)|\overline{\mathrm{B}^0_\mathrm{q}}\rangle \;+\; \frac{p}{q}g_-(t)|\mathrm{B}^0_\mathrm{q}\rangle \tag{2.23}$$

where

$$g_\pm(t) \;=\; \frac{1}{2}\,(e^{-i\lambda_1 t} \pm e^{-i\lambda_2 t}). \tag{2.24}$$

Therefore a state which at $t = 0$ was a pure $|\mathrm{B}^0_\mathrm{q}\rangle$ eigenstate is, at a later time, a mixture of $|\mathrm{B}^0_\mathrm{q}\rangle$ and $|\overline{\mathrm{B}^0_\mathrm{q}}\rangle$ and similarly a state which at $t = 0$ was a pure $|\overline{\mathrm{B}^0_\mathrm{q}}\rangle$ eigenstate is, at a later time, also a mixture of $|\mathrm{B}^0_\mathrm{q}\rangle$ and $|\overline{\mathrm{B}^0_\mathrm{q}}\rangle$.

The probabilities of finding the various states at time t, starting with either $|\mathrm{B}^0_\mathrm{q}\rangle$ and $|\overline{\mathrm{B}^0_\mathrm{q}}\rangle$ at $t = 0$, are then:

$$\begin{aligned}
P(\mathrm{B}^0_\mathrm{q} \to \mathrm{B}^0_\mathrm{q}; t) &= \left|\langle \mathrm{B}^0_\mathrm{q}|\mathrm{B}^0_\mathrm{q}(t)\rangle\right|^2 = |g_+(t)|^2, \\
P(\mathrm{B}^0_\mathrm{q} \to \overline{\mathrm{B}^0_\mathrm{q}}; t) &= \left|\langle \mathrm{B}^0_\mathrm{q}|\overline{\mathrm{B}^0_\mathrm{q}}(t)\rangle\right|^2 = \left|\frac{q}{p}\right|^2 |g_-(t)|^2, \\
P(\overline{\mathrm{B}^0_\mathrm{q}} \to \overline{\mathrm{B}^0_\mathrm{q}}; t) &= \left|\langle \overline{\mathrm{B}^0_\mathrm{q}}|\overline{\mathrm{B}^0_\mathrm{q}}(t)\rangle\right|^2 = |g_+(t)|^2, \\
\text{and}\quad P(\overline{\mathrm{B}^0_\mathrm{q}} \to \mathrm{B}^0_\mathrm{q}; t) &= \left|\langle \overline{\mathrm{B}^0_\mathrm{q}}|\mathrm{B}^0_\mathrm{q}(t)\rangle\right|^2 = \left|\frac{p}{q}\right|^2 |g_-(t)|^2.
\end{aligned} \tag{2.25}$$

The magnitude of the oscillations (mixing) between B^0_q and $\overline{\mathrm{B}^0_\mathrm{q}}$ is given by the size of the oscillation parameter x_q, defined as

$$x_q \;=\; \frac{|\Delta m_q|}{\overline{\Gamma_\mathrm{q}}} \tag{2.26}$$

where

$$\overline{\Gamma_{\rm q}} \;=\; \frac{1}{2}(\Gamma_{1,\rm q} \;+\Gamma_{2,\rm q}). \tag{2.27}$$

The mass difference Δm_q and the width difference $\Delta\Gamma_q$ are defined as:

$$\Delta m_q \equiv m_{2,\rm q} - m_{1,\rm q} \qquad \Delta\Gamma_q \equiv \Gamma_{1,\rm q} \;-\; \Gamma_{2,\rm q}. \tag{2.28}$$

Δm_q is positive by definition and $\Delta\Gamma_{\rm q}$ is expected to be positive in the Standard Model [36, 37]. These quantities are discussed further in Section 2.3.4.

2.2.2 Mechanisms of $\mathcal{CP}$ Violation

If we let $\Gamma_f(\rm t)$ denote the time-dependent decay rate of an initially tagged $\rm B^0_q$ into some final state f, and let $\overline{\Gamma}_f(\rm t)$ denote the time-dependent decay rate of an initially tagged $\overline{\rm B^0_q}$ into the same final state f, then

$$\Gamma_f(t) \equiv \Gamma(\mathrm{B}^0_{\rm q}(t) \to f) = |\mathrm{A}_f|^2 \left\{ \underbrace{|g_+(t)|^2}_{(a)} \;+\; \underbrace{\left(\frac{q}{p}\frac{\overline{\mathcal{A}}_f}{\mathrm{A}_f}\right)^2 |g_-(t)|^2}_{(b)} \;+\; \underbrace{2\Re\left[\frac{q}{p}\frac{\overline{\mathcal{A}}_f}{\mathrm{A}_f} g_+^*(t) g_-(t)\right]}_{(c)} \right\} \tag{2.29}$$

and

$$\overline{\Gamma}_f(t) \equiv \Gamma(\overline{\mathrm{B}^0_{\rm q}}(t) \to f) = |\mathrm{A}_f|^2 \left\{ \underbrace{\left|\frac{\overline{\mathcal{A}}_f}{\mathrm{A}_f}\right|^2 |g_+(t)|^2}_{(a)} \;+\; \underbrace{\left(\frac{p}{q}\right)^2 |g_-(t)|^2}_{(b)} \;+\; \underbrace{2\left(\frac{p}{q}\right)^2 \Re\left[\frac{q}{p}\frac{\overline{\mathcal{A}}_f^*}{\mathrm{A}_f} g_+^*(t) g_-(t)\right]}_{(c)} \right\}, \tag{2.30}$$

where $\mathrm{A}_f \;\equiv \langle f|H|\mathrm{B}^0_{\rm q}\rangle$ and $\overline{\mathcal{A}}_f \;\equiv \langle f|H|\overline{\mathrm{B}^0_{\rm q}}\rangle$ denote the instantaneous decay amplitudes. Using the fact that

$$\Re\left[\left(\frac{q}{p}\frac{\overline{\mathcal{A}}_f}{\mathrm{A}_f}\right)^{(*)} g_+^*(t) g_-(t)\right] = \Re\left[\frac{q}{p}\frac{\mathrm{A}_{\overline{f}}}{\mathrm{A}_f}\right] \Re\left[g_+^*(t) g_-(t)\right] \mp \Im\left[\frac{q}{p}\frac{\mathrm{A}_{\overline{f}}}{\mathrm{A}_f}\right] \Im\left[g_+^*(t) g_-(t)\right], \tag{2.31}$$

then the third terms in Equations 2.29 and 2.30 can be expanded. This particular notation is referred to later in Section 2.2.5.

For $\mathcal{CP}$ Violation to occur, it is required that there is a difference in the decay rate of the initially tagged $\mathrm{B}_{\mathrm{q}}^{0}$ and $\overline{\mathrm{B}_{\mathrm{q}}^{0}}$ into the same final state f, i.e. that

$$\Gamma(\mathrm{B}_{\mathrm{q}}^{0}(t) \rightarrow f) \neq \Gamma(\overline{\mathrm{B}_{\mathrm{q}}^{0}}(t) \rightarrow f). \tag{2.32}$$

The possible mechanisms by which $\mathcal{CP}$ Violation can occur can be categorised in two different ways. The first convention is the notion of *direct* and *indirect* $\mathcal{CP}$ Violation. From [38], any effect which can be completely assigned to $\mathcal{CP}$ Violation in the neutral meson mass matrix $\mathbf{M}$ and which is independent of the final state, is termed indirect $\mathcal{CP}$ Violation. Alternatively any effect which cannot be described in this way and which explicitly requires $\mathcal{CP}$ violating effects in the decay amplitude itself, thereby depending upon the final state, is called direct $\mathcal{CP}$ Violation.

The second convention, and the one which is used here, is to subdivide into three categories [38, 39], the mechanisms of which can be deduced from comparing the three terms labelled (a),(b) and (c) in each of Equations 2.29 and 2.30. The three categories are

- $\mathcal{CP}$ Violation in decay,
- $\mathcal{CP}$ Violation in mixing, and
- $\mathcal{CP}$ Violation in the interference between decay and mixing.

It is possible to relate the two conventions by noting that $\mathcal{CP}$ Violation in decay is direct $\mathcal{CP}$ Violation, $\mathcal{CP}$ Violation in mixing is indirect, and $\mathcal{CP}$ Violation in the interference between decay and mixing contains aspects of both direct and indirect $\mathcal{CP}$ Violation. Each of these three categories is now discussed in turn.

2.2.3 $\mathcal{CP}$ Violation in decay

$\mathcal{CP}$ Violation in decay results from the interference among the decay amplitudes A_f and $\overline{\mathcal{A}}_f$ that lead to the same final states f. The two types of phases which may appear in A_f and $\overline{\mathcal{A}}_f$ where

$$\mathrm{A}_f = \langle f\,|H|\,\mathrm{B}^0_\mathrm{q}\rangle \quad \text{and} \quad \overline{\mathcal{A}}_f = \langle f\,|H|\,\overline{\mathrm{B}^0_\mathrm{q}}\rangle \tag{2.33}$$

are the weak and the strong phases. The complex parameters from the Lagrangian which contribute to the amplitude A_f appear in a complex conjugate form in the $\mathcal{CP}$ conjugate amplitude $\overline{\mathcal{A}}_f$. This means that the weak phases of A_f and $\overline{\mathcal{A}}_f$ will appear with opposite signs. However the strong phase appears in both amplitudes with the same sign, and therefore does not violate $\mathcal{CP}$. The strong phase arises from absorptive parts of the decay amplitudes and correspond to on-shell intermediate states rescattering into the desired final state.

The contributions to the amplitude A can therefore be split into three parts: a real magnitude A_k, a weak phase term $e^{i\phi_k}$ and a strong phase term $e^{i\delta_k}$. Then, if several amplitudes contribute to $\mathrm{B}^0_\mathrm{q} \to f$, its amplitude A_f and its $\mathcal{CP}$-conjugate amplitude $\overline{\mathcal{A}}_f$ are given by

$$\mathrm{A}_f = \sum_k \mathrm{A}_k\, e^{i(\delta_k+\phi_k)} \quad \text{and} \quad \overline{\mathcal{A}}_f = \sum_k \mathrm{A}_k\, e^{i(\delta_k-\phi_k)}. \tag{2.34}$$

The phase-independent quantity is the ratio

$$\left|\frac{\overline{\mathcal{A}}_f}{\mathrm{A}_f}\right| = \left|\frac{\sum_k \mathrm{A}_k\, e^{i(\delta_k-\phi_k)}}{\sum_k \mathrm{A}_k\, e^{i(\delta_k+\phi_k)}}\right| \tag{2.35}$$

which upon comparing term (a) in each of Equations 2.29 and 2.30, then

$$\Gamma(\mathrm{B}^0_\mathrm{q}(t) \;\to\; f) \;\neq\; \Gamma(\overline{\mathrm{B}^0_\mathrm{q}}(t) \;\to\; f)$$

when $\left|\overline{\mathcal{A}}_f/\mathrm{A}_f\right| \neq 1$. This will occur if there are at least two different strong and weak phases present for the same transition $\mathrm{B} \to f$. Generally for a case when two such

phases exist the asymmetry is given by

$$|\overline{\mathcal{A}}_f|^2 \; - \; |\mathrm{A}_f|^2 \propto \; 2A_1A_2 \sin(\phi_1 - \phi_2) \sin(\delta_1 - \delta_2). \tag{2.36}$$

In order that interesting weak phases can be extracted from such decays, the amplitudes A_k and their strong phases δ_k need to be calculated, which is theoretically difficult. The current experimental evidence for $\mathcal{CP}$ Violation in decay is the measurement of $\Re(\epsilon^{'}_{\mathrm{K}}/\epsilon_K) = (14.7 \pm 2.2) \times 10^{-4}$ [40][a]. $\Re(\epsilon^{'}_{\mathrm{K}}/\epsilon_K)$ is measured via the double ratio of the decay widths of neutral kaons into two pions R, where

$$R = \frac{\Gamma(\mathrm{K_L} \to \pi^0\pi^0)/\Gamma(\mathrm{K_S} \to \pi^0\pi^0)}{\Gamma(\mathrm{K_L} \to \pi^+\pi^-)/\Gamma(\mathrm{K_S} \to \pi^+\pi^-)} \; \approx \; 1 - 6\Re\left(\frac{\epsilon^{'}_{\mathrm{K}}}{\epsilon_K}\right). \tag{2.39}$$

In the B-meson sector, direct $\mathcal{CP}$ Violation may be observed in charged B decays from a measurement of the charge asymmetry,

$$\mathcal{A}_{\pm} = \frac{\Gamma(\mathrm{B}^+ \to f) - \Gamma(\mathrm{B}^- \to \overline{f})}{\Gamma(\mathrm{B}^+ \to f) + \Gamma(\mathrm{B}^- \to \overline{f})} = \frac{1 \; - \; \left|\overline{\mathcal{A}}_f/\mathrm{A}_f\right|^2}{1 \; + \; \left|\overline{\mathcal{A}}_f/\mathrm{A}_f\right|^2}. \tag{2.40}$$

2.2.4 $\mathcal{CP}$ Violation in mixing

$\mathcal{CP}$ Violation in mixing arises when the probability that an initially pure $|\mathrm{B}^0_\mathrm{q}\rangle$ eigenstate decays as $|\overline{\mathrm{B}^0_\mathrm{q}}\rangle$ or an initially pure $|\overline{\mathrm{B}^0_\mathrm{q}}\rangle$ eigenstate decays as $|\mathrm{B}^0_\mathrm{q}\rangle$ after a time t, are not the same. This is the same as saying that the eigenstates of the Hamiltonian $|\mathrm{B}_1\rangle$ and $|\mathrm{B}_2\rangle$ defined in Equations 2.9 and 2.10 are different from the particle and antiparticle flavour eigenstates $|\mathrm{B}^0_\mathrm{q}\rangle$ and $|\overline{\mathrm{B}^0_\mathrm{q}}\rangle$. Inspection of Equations 2.9 and 2.10 shows that this

[a] In the kaon sector the parameters ϵ_K and $\epsilon^{'}_{\mathrm{K}}$ are defined as follows:

$$\epsilon_K = \frac{1}{3}\left(\eta^{00} + 2\eta^{\pm}\right) \quad \text{and} \quad \epsilon^{'}_{\mathrm{K}} = \frac{1}{3}\left(\eta^{\pm} - \eta^{00}\right) \tag{2.37}$$

where

$$\eta^{\pm} \equiv \frac{\mathrm{A}\left(\mathrm{K_L} \to \pi^+\pi^-\right)}{\mathrm{A}\left(\mathrm{K_S} \to \pi^+\pi^-\right)} \quad \text{and} \quad \eta^{00} \equiv \frac{\mathrm{A}\left(\mathrm{K_L} \to \pi^0\pi^0\right)}{\mathrm{A}\left(\mathrm{K_S} \to \pi^0\pi^0\right)} \tag{2.38}$$

occurs if the parameters p and q have different magnitudes.

Comparing the (b) terms in Equations 2.29 and 2.30 then if $|q/p| \neq 1$, $\Gamma(\mathrm{B}^0_\mathrm{q}(t) \rightarrow f) \neq \Gamma(\overline{\mathrm{B}^0_\mathrm{q}}(t) \rightarrow f)$ even if $\left|\overline{\mathcal{A}}_f/\mathrm{A}_f\right| = 1$, and therefore $\mathcal{CP}$ in mixing is violated. From Equation 2.16, this can occur only if $M_{12} \neq 0$, $\Gamma_{12} \neq 0$ and if the phase difference between M_{12} and Γ_{12} is different from 0 or π.

$\mathcal{CP}$ Violation in mixing has been observed in the semi-leptonic decays $\mathrm{K_L} \rightarrow \pi^-\ell^+\nu$ and $\mathrm{K_L} \rightarrow \pi^+\ell^-\nu$ [37]:

$$\delta_K = \frac{\Gamma(\mathrm{K_L} \rightarrow \pi^-\ell^+\nu) - \Gamma(\mathrm{K_L} \rightarrow \pi^+\ell^-\nu)}{\Gamma(\mathrm{K_L} \rightarrow \pi^-\ell^+\nu) + \Gamma(\mathrm{K_L} \rightarrow \pi^+\ell^-\nu)} = (3.27 \pm 0.12) \times 10^{-3}. \tag{2.41}$$

For the neutral B system, $\mathcal{CP}$ Violation in mixing can be studied by measuring the asymmetry in B meson semi-leptonic decays:

$$\mathcal{A}_{mix} = \frac{\Gamma(\overline{\mathrm{B}^0_\mathrm{q}}(t) \rightarrow l^+\nu X) - \Gamma(\mathrm{B}^0_\mathrm{q}(t) \rightarrow l^-\nu X)}{\Gamma(\overline{\mathrm{B}^0_\mathrm{q}}(t) \rightarrow l^+\nu X) + \Gamma(\mathrm{B}^0_\mathrm{q}(t) \rightarrow l^-\nu X)} = \frac{1 - |q/p|^4}{1 + |q/p|^4}. \tag{2.42}$$

2.2.5 $\mathcal{CP}$ Violation in the interference between decay and mixing

$\mathcal{CP}$ Violation in the interference of the mixing and decay amplitudes is also known as "$\mathcal{CP}$ Violation between decays with and without mixing" or "mixing induced $\mathcal{CP}$ Violation" and it occurs due to the $\mathcal{CP}$ violating interference between the mixing and decay amplitudes of neutral B mesons. For example, if we consider the direct decay (without mixing) $\mathrm{B}^0_\mathrm{q} \rightarrow f$, and the decay via mixing $\mathrm{B}^0_\mathrm{q} \rightarrow \overline{\mathrm{B}^0_\mathrm{q}} \rightarrow f$, then we get interference between the amplitudes of these two terms. It is seen that in the absence of both direct $\mathcal{CP}$ Violation and $\mathcal{CP}$ Violation in the mixing

$$\left|\frac{q}{p}\frac{\mathrm{A}_{\overline{f}}}{\mathrm{A}_f}\right| = 1, \tag{2.43}$$

then $\mathcal{CP}$ Violation can still occur if

$$\Im\left\{\frac{q}{p}\frac{\mathrm{A}_{\overline{f}}}{\mathrm{A}_f}\right\} \neq 0. \tag{2.44}$$

We can re-express the time-dependent decay rates $\Gamma_f(t)$ and $\overline{\Gamma}_f(t)$ from Equations 2.29 and 2.30 in terms of two time-dependent functions $I_\pm(t)$ as

$$\Gamma_f(t) = \frac{|\mathrm{A}_f|^2}{2} e^{-\overline{\Gamma}t} \left[I_+(t) + I_-(t)\right] \tag{2.45}$$

and

$$\overline{\Gamma}_f(t) = \frac{|\overline{\mathcal{A}}_f|^2}{2|\lambda_f|^2} e^{-\overline{\Gamma}t} \left[I_+(t) - I_-(t)\right], \tag{2.46}$$

where the time-dependent functions $I_+(t)$ and $I_-(t)$ are given by

$$I_+(t) = \left(1 + |\lambda_f|^2\right)\cosh\left(\frac{\Delta\Gamma t}{2}\right) - 2\Re\{\lambda_f\}\sinh\left(\frac{\Delta\Gamma t}{2}\right) \tag{2.47}$$

and

$$I_-(t) = \left(1 - |\lambda_f|^2\right)\cos\left(\Delta M t\right) + 2\Im\{\lambda_f\}\sin\left(\Delta M t\right). \tag{2.48}$$

The parameter λ_f is defined as

$$\lambda_f = \frac{q}{p}\frac{\overline{\mathcal{A}}_f}{\mathrm{A}_f}, \tag{2.49}$$

which is a phase-independent parameter. The time-dependent $\mathcal{CP}$ asymmetry $\mathcal{A}_{CP}(t)$ can be expressed in terms of λ_f as

$$\mathcal{A}_{CP}(t) = \frac{\Gamma_f - \overline{\Gamma}_f}{\Gamma_f + \overline{\Gamma}_f} = \frac{(1 - |\lambda_f|^2)\cos(\Delta M t) - 2\Im(\lambda_f)\sin\left(\Delta M t\right)}{(1 + |\lambda_f|^2)\cosh(\frac{\Delta\Gamma t}{2}) + 2\Re(\lambda_f)\sinh\left(\frac{\Delta\Gamma t}{2}\right)}. \tag{2.50}$$

Alternatively, $\mathcal{A}_{CP}(t)$ can be expressed in terms of a direct $\mathcal{CP}$ violating component, $\mathcal{A}_{CP}^{dir}$ and a component describing $\mathcal{CP}$ Violation in the interference, $\mathcal{A}_{CP}^{int}$ such that,

$$\mathcal{A}_{CP}(t) = \mathcal{A}_{CP}^{dir}\cos(\Delta M t) + \mathcal{A}_{CP}^{int}\sin(\Delta M t). \tag{2.51}$$

In the Standard Model $\Delta\Gamma$ is small for the B^0_d system but is expected to be quite large in the B^0_s system (see Section 2.3.4). In the case that $\Delta\Gamma$ is small then the components

$\mathcal{A}_{CP}^{dir}$ and $\mathcal{A}_{CP}^{int}$ reduce to

$$\mathcal{A}_{CP}^{dir} = \frac{1-|\lambda_f|^2}{1+|\lambda_f|^2} \quad \text{and} \quad \mathcal{A}_{CP}^{int} = \frac{-2\Im(\lambda_f)}{1+|\lambda_f|^2}. \tag{2.52}$$

In the specific case of decays to $\mathcal{CP}$ eigenstates, $\lambda_f = 1$, and the decay is dominated by a single $\mathcal{CP}$ violating phase. As a consequence, $\mathcal{A}_{CP}^{dir}$ becomes negligible and Equation 2.52 reduces to

$$\mathcal{A}_{CP}(t) = \mathcal{A}_{CP}^{int}\sin(\Delta M t) = -\Im(\lambda_f)\sin(\Delta M t). \tag{2.53}$$

In Equation 2.53, the phase difference between the mixing amplitude and the phase of the decay amplitude is $\Im(\lambda_f)$. Decay channels which can be described in this way have clean experimental signatures and low theoretical uncertainties. The form of Equation 2.53 is referred to again in Section 2.8.2 where the recent measurements of $\mathcal{CP}$ Violation in the interference between mixing and decay in the B meson system are discussed.

2.3 B decays in the Standard Model

2.3.1 The charged-current weak interaction Lagrangian, and the CKM matrix

The charged-current weak interaction Lagrangian $\mathcal{L}_W$ in the Standard Model (SM) can be written as

$$-\mathcal{L}_{\mathrm{W}} = \frac{g_{\mathrm{W}}}{\sqrt{2}}\left(\begin{array}{ccc} -\overline{\mathrm{u}_{\mathrm{L}}^{\mathrm{i}}} & \overline{\mathrm{c}_{\mathrm{L}}^{\mathrm{i}}} & \overline{\mathrm{t}_{\mathrm{L}}^{\mathrm{i}}} \end{array}\right)\gamma^{\mu}\left(\begin{array}{c} \overline{\mathrm{d}_{\mathrm{L}}^{\mathrm{i}}} \\ \overline{\mathrm{s}_{\mathrm{L}}^{\mathrm{i}}} \\ \overline{\mathrm{b}_{\mathrm{L}}^{\mathrm{i}}} \end{array}\right)\mathrm{W}_{\mu}^{+} + \text{Hermitian conjugate} \tag{2.54}$$

where the superscript i represents the interaction (i.e. physical) eigenstates. γ^{μ} are the Dirac matrices and W_{μ}^{+} is the operator representing W-boson exchange. $\mathcal{L}_{\mathrm{W}}$ describes

the transitions between different quark flavours. Equation 2.54 can be rewritten in terms of the mass eigenstates $(\overline{\mathrm{u}}_\mathrm{L}\,\overline{\mathrm{c}}_\mathrm{L}\,\overline{\mathrm{t}}_\mathrm{L})$ and $(\overline{\mathrm{d}}_\mathrm{L}\,\overline{\mathrm{s}}_\mathrm{L}\,\overline{\mathrm{b}}_\mathrm{L})$ as

$$-\mathcal{L}_\mathrm{W} = \frac{g_\mathrm{W}}{\sqrt{2}}(\ \ -\overline{\mathrm{u}}_\mathrm{L}\ \ \overline{\mathrm{c}}_\mathrm{L}\ \ \overline{\mathrm{t}}_\mathrm{L}\ )\ \gamma^\mu\ \underbrace{(\ \mathrm{V_{uL}}\ \ \mathrm{V_{dL}^\dagger}\ )}_{\mathrm{V_{CKM}}} \begin{pmatrix} \overline{\mathrm{d}}_\mathrm{L} \\ \overline{\mathrm{s}}_\mathrm{L} \\ \overline{\mathrm{b}}_\mathrm{L} \end{pmatrix} \mathrm{W}_\mu^+ \ + \text{hermitian conjugate} \tag{2.55}$$

$(\mathrm{V_{uL}V_{dL}^\dagger})$ is the mixing matrix for three quark generations i.e. the CKM matrix, $\mathrm{V_{CKM}}$. The CKM matrix has the following form:

$$\mathrm{V_{CKM}} = \begin{pmatrix} V_{ud} & V_{us} & V_{ub} \\ V_{cd} & V_{cs} & V_{cb} \\ V_{td} & V_{ts} & V_{tb} \end{pmatrix} \tag{2.56}$$

where $\mathrm{V_{ij}}$ represents the matrix element that couples the $\mathrm{i^{th}}$ up-type quark (u,c,t) to the $\mathrm{j^{th}}$ down-type quark (d,s,b). The diagonal elements of $\mathrm{V_{ij}}$ describe the strength of the weak charged current transitions between quarks of the same generation, whereas the off-diagonal elements describe transitions between quarks of different generations.

The SM does not predict the elements $\mathrm{V_{ij}}$ of $\mathrm{V_{CKM}}$ - these have to be measured experimentally, but does require that $\mathrm{V_{CKM}}$ be unitary; i.e. that:

$$(\mathrm{V_{CKM}V_{CKM}^\dagger}) = (\mathrm{V_{CKM}^\dagger V_{CKM}}) = \hat{1}. \tag{2.57}$$

2.3.2 Weak B meson decays

The weak decays of B-mesons can be divided into leptonic, semi-leptonic and non-leptonic transitions [41]. The leptonic modes $\mathrm{B}^- \to \ell\,\overline{\nu}$ $(\ell = e, \mu)$ have branching ratios at the 10^{-10} and 10^{-7} level respectively, and consequently are very hard to measure. The semi-leptonic decays caused by $b \to c\,\ell^-\overline{\nu_\ell}$ and $b \to u\,\ell^-\overline{\nu_\ell}$ transitions are discussed

in Section 2.8. With respect to testing the Standard Model description of $\mathcal{CP}$ Violation, the major role is played by the non-leptonic B decays. At the quark level they are mediated by the $b \to q_1 \overline{q}_2 \, d\,(s)$ transitions where $q_1, q_2 \in \{u, d, c, s\}$.

2.3.3 Tree and Penguin Diagrams

The two kinds of topologies which contribute to the non-leptonic B decays are the "tree" and "penguin" diagram topologies. Tree diagrams are quark level Feynman diagrams in which the W-boson creates or connects to a different quark line from the line that starts out as the b quark. An example of such a diagram is shown in Figure 2.1. Tree diagrams are categorised into spectator, exchange and annihilation diagrams. In the spectator diagram, the light quark in the initial meson is disconnected in the weak decay diagram; in the exchange diagram, the W is exchanged between the two quarks of the initial meson; and in the annihilation, the quark and the antiquark of the initial meson annihilate to form the W. Whenever one or more of the tree diagrams contribute to the same decay amplitude, they do so with the same CKM matrix element and hence the same weak phase.

A penguin diagram is a loop diagram where the W reconnects to the quark line from which it was emitted. A new particle is then emitted from the quark line in the loop. and makes either a new quark pair or is absorbed by the spectator quark. Penguin diagrams are classified according to the identity of the particle emitted from the loop - a gluonic (QCD) penguin if the particle is a gluon as in Figure 2.2, and an electroweak penguin if the particle is a photon or a Z boson as in Figure 2.3. Penguin diagrams with different intermediate particles have different strong phases and different weak phases.

Depending on the flavour content, $b \to q_1 \overline{q}_2 \, d(s)$ transitions are classified as follows [41]:

- $\mathrm{q}_1 \neq \mathrm{q}_2 \in \{u, c\}$: only tree diagrams contribute.
- $\mathrm{q}_1 = \mathrm{q}_2 \in \{u, c\}$: tree and penguin diagrams contribute.
- $\mathrm{q}_1 = \mathrm{q}_2 \in \{d, s\}$: only penguin diagrams contribute.

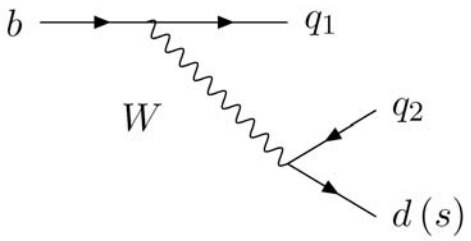

Figure 2.1: *Tree diagrams* (q_1,q_2 $\in \{u, c\}$).

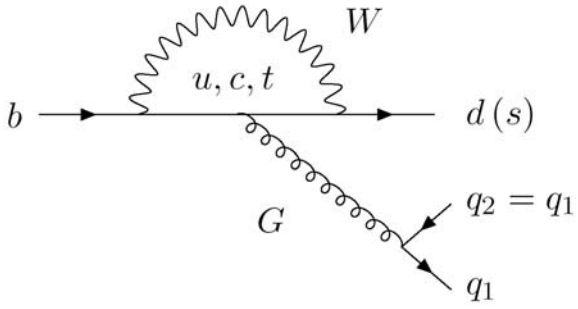

Figure 2.2: *QCD penguin diagrams* ($q_1 = q_2 \in \{u, d, c, s\}$).

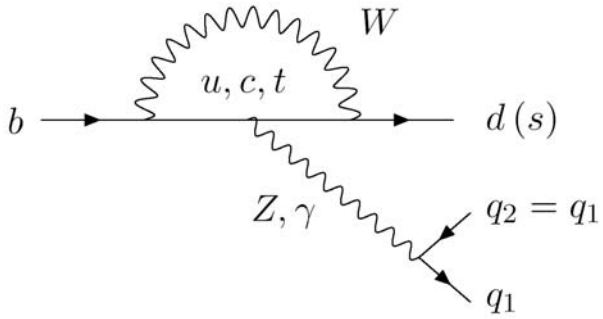

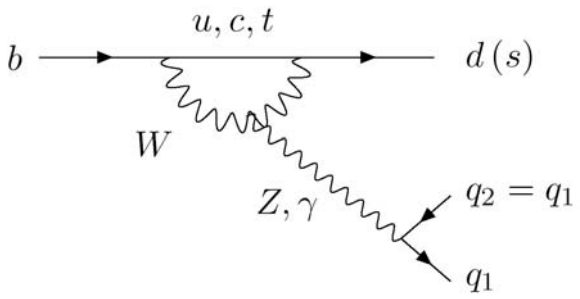

Figure 2.3: *EW penguin diagrams* ($q_1 = q_2 \in \{u, d, c, s\}$).

2.3.4 Box diagrams

The transitions $\mathrm{B^0_q} \to \overline{\mathrm{B^0_q}}$ and $\overline{\mathrm{B^0_q}} \to \mathrm{B^0_q}$ are described at the lowest order by box diagrams involving two W bosons and two up-type quarks as shown in Figure 2.4. The dispersive and the absorptive parts of the box diagrams are

$$M_{12} = -\frac{\mathrm{G_F^2\, m_W^2}\, \eta_B\, m_{\mathrm{B^0_q}}\, B_{\mathrm{B^0_q}}\, {f_{\mathrm{B^0_q}}}^2}{12\pi^2} S_0\left(\frac{\mathrm{m_t^2}}{\mathrm{m_W^2}}\right) (\mathrm{V_{tq}{}^* V_{tb}})^2 \tag{2.58}$$

and

$$\Gamma_{12} = \frac{\mathrm{G_F^2\, m_b^2}\, \eta_B^{'}\, m_{\mathrm{B^0_q}}\, B_{\mathrm{B^0_q}}\, {f_{\mathrm{B^0_q}}}^2}{8\pi} \times \left[(\mathrm{V_{tq}{}^* V_{tb}})^2 + \mathrm{V_{tq}{}^* V_{tb} V_{cq}{}^* V_{cb}}\, \mathcal{O}\left(\frac{\mathrm{m_c^2}}{\mathrm{m_b^2}}\right) + (\mathrm{V_{cq}{}^* V_{cb}})^2\, \mathcal{O}\left(\frac{\mathrm{m_c^4}}{\mathrm{m_b^4}}\right)\right]. \tag{2.59}$$

G_F is the Fermi constant, m_W the W boson mass and m_i the mass of quark i. $m_{B_q^0}$, $f_{B_q^0}$

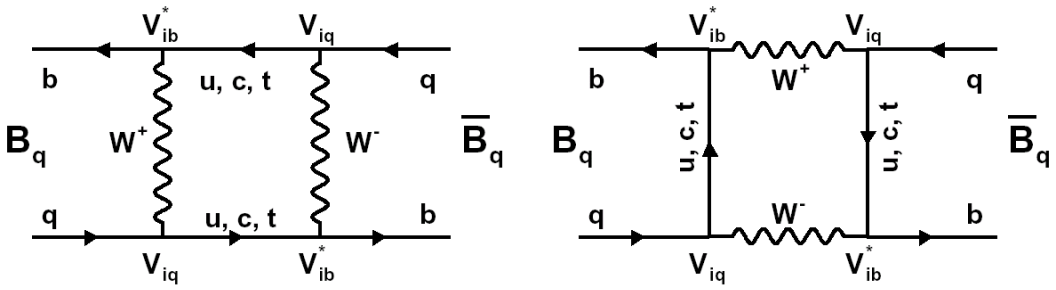

Figure 2.4: *Two dominant box diagrams which induce particle-antiparticle oscillation. The diagram is dominated by the t quark over the u and c quarks, since* $m_t \gg m_u$, m_c

and $B_{B_q^0}$ are the B_q^0 mass, weak decay constant and Bag parameter respectively. $f_{B_q^0}$ and $B_{B_q^0}$ are estimated using lattice QCD calculations. The current estimates are $f_{B_q^0} = 175 \pm 25$ MeV and $B_{B_q^0} = 1.4 \pm 0.1$ [37,39]. V_{ij} are elements of the CKM matrix. η_B and $\eta_B^{'}$ are QCD corrections which are of order unity.

The dominant contributions to M_{12} are from the box diagrams involving two top quarks since $m_t \gg m_u$, m_c. The phases of M_{12} and Γ_{12}, $\varphi_{M_{12}} = \arg(M_{12})$ and $\varphi_{\Gamma_{12}} = \arg(\Gamma_{12})$ satisfy

$$\varphi_{M_{12}} - \varphi_{\Gamma_{12}} = \pi + \mathcal{O}\left(\frac{m_c^2}{m_b^2}\right) \tag{2.60}$$

which implies that that we can redefine the mass difference Δm from Equation 2.28 in terms of a "heavy" state with mass $m_{H,q} = \max(m_{1,q}, m_{2,q})$ and a "light" state with mass $m_{L,q} = \min(m_{1,q}, m_{2,q})$ as

$$\Delta m_q \equiv m_{H,q} - m_{L,q}, \tag{2.61}$$

and width difference

$$\Delta\Gamma_q \equiv \Gamma_{L,q} - \Gamma_{H,q}. \tag{2.62}$$

The Standard Model predicts that $\Delta\Gamma_q/\Gamma_q$ is small for the $B_d^0 - \overline{B_d^0}$ system (below 1%) but larger for the $B_s^0 - \overline{B_s^0}$ system ($\sim$ 10 %) [36]. This width difference is caused by

the existence of final states to which both the B^0_q and $\overline{B^0_q}$ mesons can decay. Such decays involve $b \to c\bar{c}q$ quark level transitions, which are Cabibbo-suppressed if $q = d$ and Cabibbo-allowed if $q = s$.

Contrary to the neutral kaon sector where there is a large difference in lifetime but a negligible difference in mass between the two neutral K mesons, in the neutral B meson sector it is the mass difference that is large [37],

$$\Delta m_d \;=\; m_{B^0_{dH}} - m_{B^0_{dL}} \;=\; (0.502 \pm 0.006)\; ps^{-1}, \tag{2.63}$$

and

$$\Delta m_s \;=\; m_{B^0_{sH}} - m_{B^0_{sL}} \;>\; 14.4\; ps^{-1}. \tag{2.64}$$

Figure 2.5 shows a plot of the individual Δm_d measurements as quoted by the LEP (ALEPH, DELPHI, L3 and OPAL), CDF, BaBar, Belle, CLEO & ARGUS (combined) experiments [42]. This measurement is seen to be completely dominated by the measurements performed at the B factories.

The limits on Δm_s are calculated using the amplitude method for B^0_s oscillations as illustrated in Figure 2.6. The method consists of fitting the observed decay time distribution with the amplitude of the oscillations as a free parameter. The fitted amplitudes at given values of Δm_s, are then converted into the lower limit on the oscillation frequency. An amplitude consistent with 1 is expected at the true value of Δm_s. An amplitude consistent with 0 is expected far below the true value of Δm_s.

When combined with the measured B^0_d and B^0_s lifetimes of

$$\tau_d \;=\; (1.542 \pm 0.016) \times 10^{-12}s \quad \text{and} \quad \tau_s \;=\; (1.461 \pm 0.057) \times 10^{-12}s \tag{2.65}$$

then the values of Δm_d and Δm_s result in values of the mixing parameters (Equation 2.26) of [37]

$$x_d \;=\; 0.755 \pm 0.015 \tag{2.66}$$

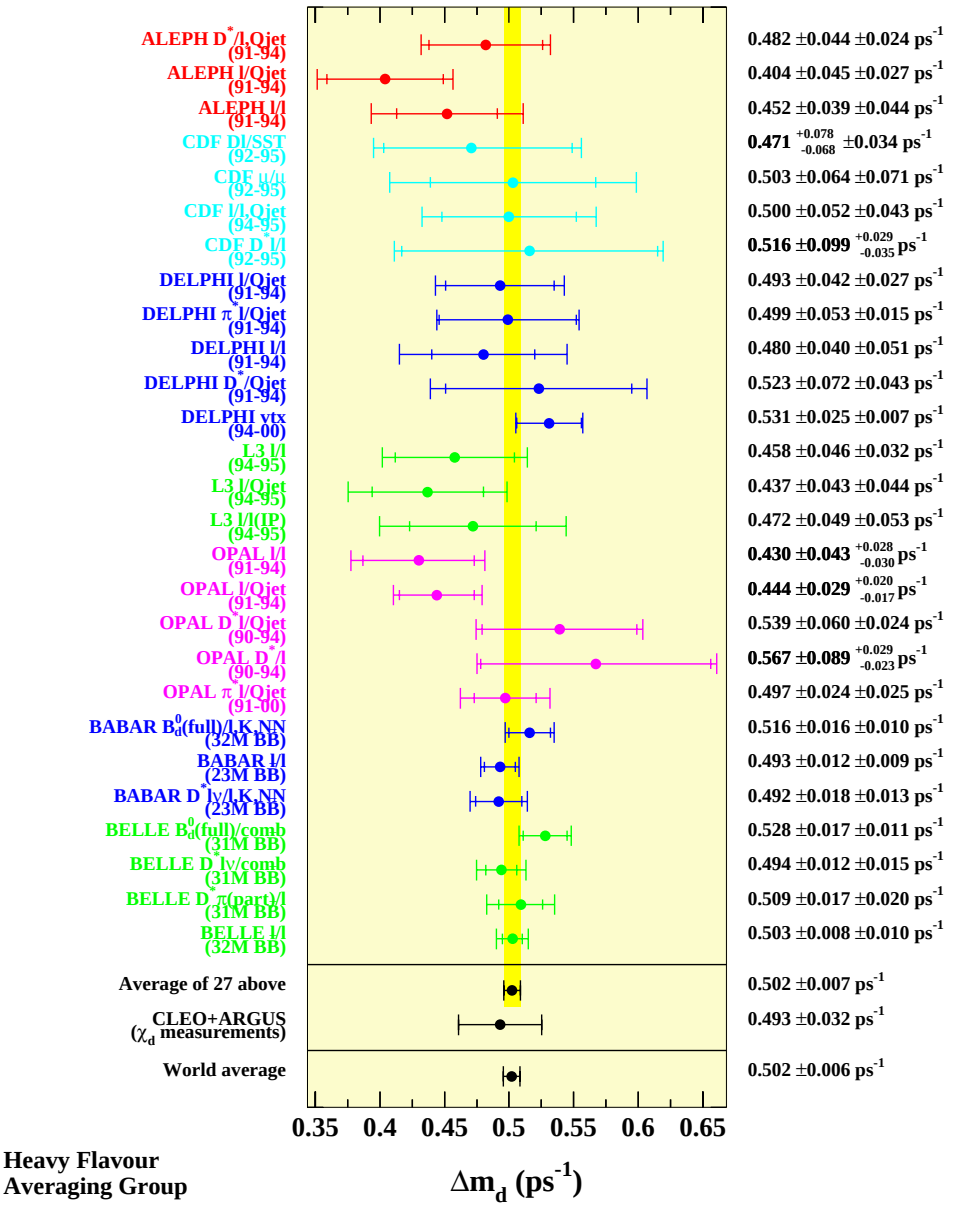

Figure 2.5: *Plot of Δm_d measurements and their averages.All individual measurements are listed as quoted by the experiments [42].*

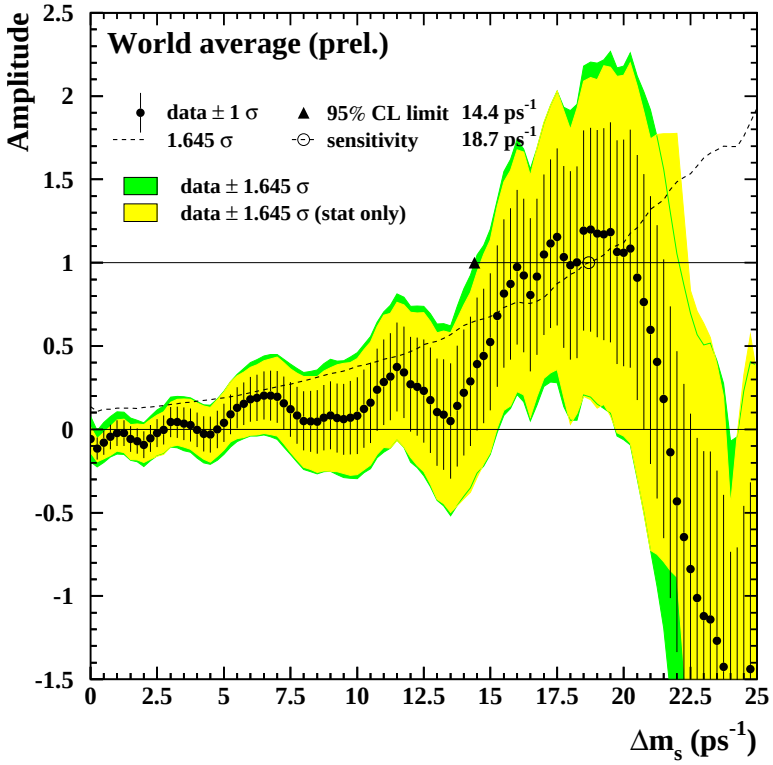

Figure 2.6: *Summary of Δm_s measurements using the amplitude method [42].*

and

$$x_s \geq 19.0,\ 95\%\ \text{CL}. \tag{2.67}$$

2.4 $\mathcal{CP}$ Violation in the Standard Model

The 3×3 $(n_g \times n_g)$[b] CKM matrix introduced in Equation 2.56 is parameterised by n_g^2 $(= 9)$ parameters V_{ij}. One of the fundamental properties of the CKM matrix is that of rephasing invariance [43], i.e. one has the freedom to rephase the quark fields

$$u_\alpha = e^{\psi_\alpha} u'_\alpha \quad \text{and} \quad d_\beta = e^{\psi_\beta} d'_\beta \tag{2.68}$$

[b] n_g = number of quark generations.

with n_g arbitrary phases ψ_α and n_g arbitrary phases ψ_β. Under these transformations, $\mathrm{V_{CKM}}$ transforms as

$$V'_{\alpha\beta} \;=\; e^{i(\psi_\beta - \psi_\alpha)}\, V_{\alpha\beta}. \tag{2.69}$$

Therefore one may arbitrarily change or eliminate the phases of $2n_g$ -1 matrix elements of $\mathrm{V_{CKM}}$. This gives the number of physical parameters of $\mathrm{V_{CKM}}$ as

$$N_{\text{param.}} = {n_g}^2 - (2n_g \,-1) \;=\; (n_g \,-1)^2 \tag{2.70}$$

which for n_g =3, gives $N_{\text{param.}}$ =4 physical parameters in $\mathrm{V_{CKM}}$. It should be emphasised that these four parameters are fundamental constants, and need to be determined by experiment.

Knowing that an unitary matrix is a complex form of an orthogonal matrix, and that a $n_g \times n_g$ orthogonal matrix can be parameterised by $n_g(n_g - 1)/2$ rotation angles known as Euler angles, then N_{angle} out of the $N_{\text{param.}}$ physical parameters should be identified with these Euler angles where

$$N_{\text{angle}} = \frac{1}{2} n_g \,(n_g \,-1), \tag{2.71}$$

which for $n_g = 3$, gives $N_{\text{angle}} = 3$ out of the 4 physical parameters in $\mathrm{V_{CKM}}$. The remaining $\frac{1}{2}(n_g - 1)(n_g - 2) = 1$ parameter of $\mathrm{V_{CKM}}$ is the complex phase, denoted by δ which generates $\mathcal{CP}$ Violation [12].

For the Lagrangian in Equation 2.54 to be $\mathcal{CP}$-violating then δ must satisfy $0<\delta<\pi$, none of the Euler (rotation) angles must be zero or $\pi/2$, and all of the up-type (u,c,t) and down-type (d,s,b) quarks must separately be different from one another.

2.5 Parameterisations of the CKM Matrix

The CKM matrix in Equation 2.56 is usually parameterised in some way - the purpose of which is to incorporate the constraints of 3×3 unitarity (Equation 2.57). Some of the parameterisations are in terms of the four fundamental physical parameters introduced in the previous section, i.e. the three Euler angles (which are angles of three successive rotations about different axes) and the one complex phase δ. Examples of these are the Kobayashi-Maskawa parameterisation [12] and the Chau-Keung parameterisation [44], both of which are outlined in Section 2.5.1.

Other parameterisations incorporate experimental information, such as the Wolfenstein parameterisation [45] described in Section 2.5.2. There also exists so-called Rephasing-Invariant parameterisations such as those suggested by Branco and Lavoura, Bjorken and Dunietz and Aleksan, Kayser and London [43] but these are not discussed here.

All of these parameterisations have one thing in common, which is that the CKM matrix elements V_{ud} and V_{us} are chosen as real and positive. The reason for this choice is due to the central role played by the quantity $\lambda_u \equiv V_{ud}V_{us}^*$ in the neutral kaon system.

2.5.1 Parameterisations using the Euler angles

2.5.1.1 The Kobayashi-Maskawa parameterisation

The first parameterisation of the CKM matrix was put forward by Kobayashi and Maskawa (1973) [12]. They wrote

$$V_{CKM} = \begin{pmatrix} 1 & 0 & 0 \\ 0 & c_2 & -s_2 \\ 0 & s_2 & c_2 \end{pmatrix} \begin{pmatrix} c_1 & -s_1 & 0 \\ s_1 & c_1 & 0 \\ 0 & 0 & e^{i\delta} \end{pmatrix} \begin{pmatrix} 1 & 0 & 0 \\ 0 & c_3 & s_3 \\ 0 & s_3 & -c_3 \end{pmatrix} \tag{2.72}$$

$$= \begin{pmatrix} c_1 & -s_1c_3 & -s_1s_3 \\ s_1s_2 & c_1c_2c_3 - s_2s_3e^{i\delta} & c_1c_2s_3 + s_2c_3e^{i\delta} \\ s_1s_2 & c_1s_2c_3 + c_2s_3e^{i\delta} & c_1s_2s_3 - c_2c_3e^{i\delta} \end{pmatrix}$$

where $c_{\rm i}$ and $s_{\rm i}$ are shorthand notation for cos $\theta_{\rm i}$ and sin $\theta_{\rm i}$, respectively. θ_1, θ_2 and θ_3 are the Euler angles. δ is the complex phase.

2.5.1.2 The Chau-Keung parameterisation

The parametrisation of the CKM matrix advocated by the Particle Data Group [37] is that by Chau and Keung (1984) [44]. They proposed

$$\mathrm{V_{CKM}} = \begin{pmatrix} c_{12} & s_{12} & 0 \\ -s_{12} & c_{12} & 0 \\ 0 & 0 & 1 \end{pmatrix} \begin{pmatrix} 1 & 0 & 0 \\ 0 & c_{23} & s_{23} \\ 0 & -s_{23} & c_{23} \end{pmatrix} \begin{pmatrix} c_{13} & 0 & s_{13}e^{-i\delta} \\ 0 & 1 & 0 \\ -s_{13}e^{i\delta} & 0 & c_{13} \end{pmatrix} \qquad (2.73)$$

$$= \begin{pmatrix} c_{12}c_{13} & s_{12}c_{13} & s_{13}e^{-i\delta} \\ -s_{12}c_{23} - c_{12}s_{23}s_{13}e^{i\delta} & c_{12}c_{23} - s_{12}s_{23}s_{13}e^{i\delta} & s_{23}c_{13} \\ s_{12}s_{23} - c_{12}c_{23}s_{13}e^{i\delta} & -s_{23}c_{12} - s_{12}c_{23}s_{13}e^{i\delta} & c_{23}c_{13} \end{pmatrix}$$

where $c_{\rm ij} = \cos\theta_{\rm ij}$ and $s_{\rm ij} = \sin\theta_{\rm ij}$. The generation labels (i,j = 1,2,3) and $c_{\rm ij}, s_{\rm ij}$ can all be chosen to be positive. θ_{12} is known as the Cabibbo mixing angle.

As c_{13} is known to deviate from unity only in the sixth decimal place, $\mathrm{V_{ud}}$=c_{12}, $\mathrm{V_{us}}$=s_{12} and $\mathrm{V_{tb}}$=c_{23} $\sim$1 to an excellent approximation, this leaves only four independent parameters, namely

$$s_{12} = |\mathrm{V_{us}}|, \quad s_{13} = |\mathrm{V_{ub}}|, \quad s_{23} = |\mathrm{V_{cb}}|, \quad \delta. \qquad (2.74)$$

2.5.2 The Wolfenstein Parameterisation

An alternative parameterisation of $\mathrm{V_{CKM}}$ is that due to Wolfenstein (1983) [45] after it was realised that the bottom quark decays predominantly to the charm quark, i.e. $|\mathrm{V_{cb}}| \gg |\mathrm{V_{ub}}|$. Wolfenstein introduced the real parameters λ, A, ρ and η [46,47] where

$$\lambda = s_{12}, \quad \mathrm{A} = \frac{s_{23}}{s_{12}^2}, \quad \rho = \frac{s_{13}\,\cos\delta}{s_{12}s_{23}}, \quad \eta = \frac{s_{13}\,\sin\delta}{s_{12}s_{23}} \tag{2.75}$$

such that to $\mathcal{O}(\lambda^3)$,

$$\mathrm{V_{CKM}} = \begin{pmatrix} 1-\lambda^2/2 & \lambda & A\lambda^3(\rho - i\eta) \\ -\lambda & 1-\lambda^2/2 & A\lambda^2 \\ A\lambda^3(1-\rho-i\eta) & -A\lambda^2 & 1 \end{pmatrix} + \mathcal{O}(\lambda^4). \tag{2.76}$$

In this parametrisation, each element of $\mathrm{V_{CKM}}$ is replaced by a power-series expansion in the parameter

$$\lambda = |\mathrm{V_{us}}| = s_{12} = \sin\theta_{12} = 0.2229 \pm 0.0022 \tag{2.77}$$

[48]. This emphasises the hierarchy in the size of the angles $s_{12} \gg s_{23} \gg s_{13}$.

2.6 The unitarity triangles

The unitarity relation in Equation 2.57 implies that any pair of columns, or any pair of rows of $\mathrm{V_{CKM}}$ are orthogonal. For three generations of quarks, this gives the six orthogonality relations

$$\mathrm{V_{ud}V_{us}^*} + \mathrm{V_{cd}V_{cs}^*} + \mathrm{V_{td}V_{ts}^*} = 0 \qquad (d,s), \tag{2.78}$$

$$\mathrm{V_{ud}V_{ub}^*} + \mathrm{V_{cd}V_{cb}^*} + \mathrm{V_{td}V_{tb}^*} = 0 \qquad (d,b), \tag{2.79}$$

$$\mathrm{V_{us}V_{ub}^*} + \mathrm{V_{cs}V_{cb}^*} + \mathrm{V_{ts}V_{tb}^*} = 0 \qquad (s,b), \tag{2.80}$$

$$V_{ud}V_{cd}^{*} + V_{us}V_{cs}^{*} + V_{ub}V_{cb}^{*} = 0 \qquad (u,c), \tag{2.81}$$

$$V_{ud}V_{td}^{*} + V_{us}V_{ts}^{*} + V_{ub}V_{tb}^{*} = 0 \qquad (u,t), \tag{2.82}$$

$$V_{cd}V_{td}^{*} + V_{cs}V_{ts}^{*} + V_{cb}V_{tb}^{*} = 0 \qquad (c,t). \tag{2.83}$$

There are also six relations governing the normalisation of the columns and rows of V_{CKM}. These are

$$|V_{ud}|^2 + |V_{cd}|^2 + |V_{td}|^2 = 1, \tag{2.84}$$

$$|V_{us}|^2 + |V_{cs}|^2 + |V_{ts}|^2 = 1, \tag{2.85}$$

$$|V_{ub}|^2 + |V_{cb}|^2 + |V_{tb}|^2 = 1, \tag{2.86}$$

$$|V_{ud}|^2 + |V_{us}|^2 + |V_{ub}|^2 = 1, \tag{2.87}$$

$$|V_{cd}|^2 + |V_{cs}|^2 + |V_{cb}|^2 = 1, \tag{2.88}$$

$$|V_{td}|^2 + |V_{ts}|^2 + |V_{tb}|^2 = 1. \tag{2.89}$$

Each of the six orthogonality equations requires the sum of three complex numbers to sum to zero and so can be depicted as a triangle (referred to as an unitarity triangle) in the complex plane as illustrated in Figure 2.7. Aleksan *et.al.* [49] show that if $\omega_{kl}^{ij} \equiv arg(V_{ki}V_{kj}^{*}/V_{li}V_{lj}^{*})$ with $k \neq l$ (k, l = u,c,t) and $i \neq j$ (i, j = d,s,b) is the phase of the side of an unitarity triangle involving the up-type quark k and the side of the unitarity triangle involving the up-type quark l in the ij column unitarity triangle, then at most, four of the ω_{kl}^{ij} can be independent, since four parameters, usually taken to be the three angles α, β and γ, and the one complex phase δ are fully sufficient to determine V_{CKM}.

Figure 2.7 shows that only two of the six triangles have three sides of comparable magnitude. These are the triangles that couple the (u,t) and (d,b) quarks. The other four triangles have one side that is suppressed relative to the others. In terms of the Wolfenstein parameter λ, the (u,t) and (d,b) triangles are identical up to $\mathcal{O}(\lambda^3)$.

The unitarity relations (Equations 2.78 - 2.83), and the normalisation equations

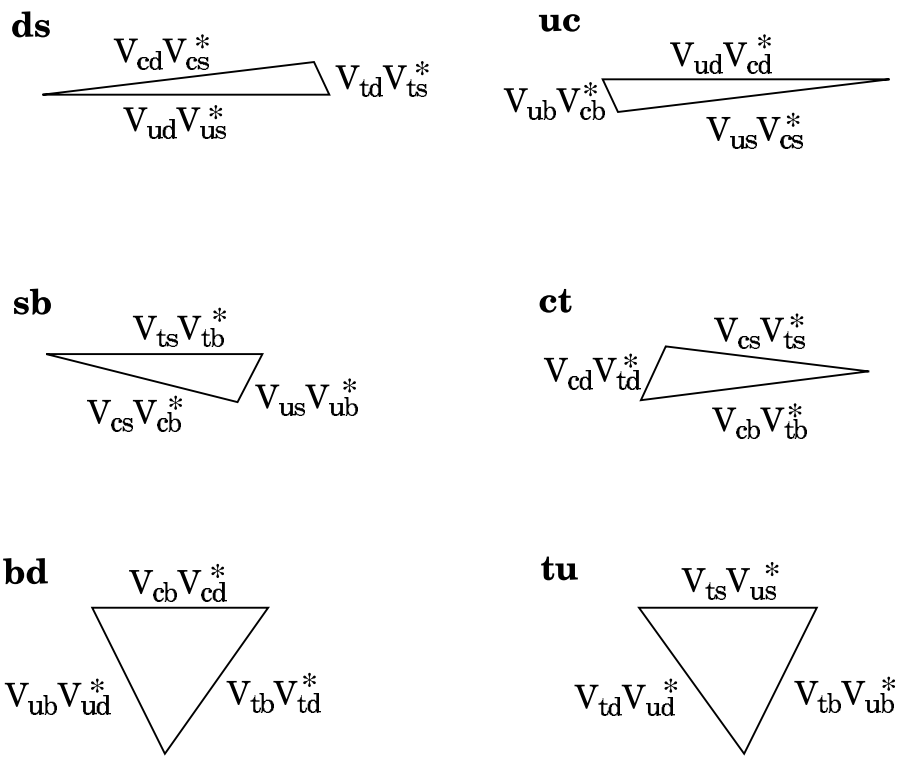

Figure 2.7: *The six unitarity triangles using current experimental measurements of the CKM matrix elements [37].*

(Equations 2.84 - 2.89), are only satisfied for the Wolfenstein parametrisation given in Equation 2.76 up to $O(\lambda^3)$. In the LHC era, the experimental accuracy will be such that higher-order terms within the Wolfenstein parametrisation will need to be taken into account therefore distinguishing between the (u,t) and (d,b) triangles described by Equations 2.79 and 2.82 [50]. A better approximation is that up to $O(\lambda^5)$ [46, 47, 51] which is written as

$$\mathrm{V_{CKM}} = \begin{pmatrix} 1-\frac{1}{2}\lambda^2-\frac{1}{8}\lambda^4 & \lambda & A\lambda^3(\rho-i\eta) \\ -\lambda\left[1+A^2\lambda^4\left(\rho+i\eta-\frac{1}{2}\right)\right] & 1-\frac{1}{2}\lambda^2-\frac{1}{8}\lambda^4\left(1+4A^2\right) & A\lambda^2 \\ A\lambda^3\left[\left(1-\rho-i\eta\right)\left(1-\frac{1}{2}\lambda^2\right)\right] & -A\lambda^2\left[1+\lambda^2\left(\rho+i\eta-\frac{1}{2}\right)\right] & 1-\frac{1}{2}A^2\lambda^4 \end{pmatrix} + \mathcal{O}(\lambda^6). \tag{2.90}$$

The dependence upon λ of the six unitarity triangles shown in Figure 2.7 is

$$
\begin{aligned}
&\mathrm{V_{ud}V_{us}^*} + \mathrm{V_{cd}V_{cs}^*} + \mathrm{V_{td}V_{ts}^*} = 0 \qquad (d,s), \\
&\mathcal{O}(\lambda) \qquad \mathcal{O}(\lambda) \qquad \mathcal{O}(\lambda^5) \\
&\mathrm{V_{ud}V_{ub}^*} + \mathrm{V_{cd}V_{cb}^*} + \mathrm{V_{td}V_{tb}^*} = 0 \qquad (d,b), \\
&\mathcal{O}(\lambda^3) \qquad \mathcal{O}(\lambda^3) \qquad \mathcal{O}(\lambda^3) \\
&\mathrm{V_{us}V_{ub}^*} + \mathrm{V_{cs}V_{cb}^*} + \mathrm{V_{ts}V_{tb}^*} = 0 \qquad (s,b), \\
&\mathcal{O}(\lambda^4) \qquad \mathcal{O}(\lambda^2) \qquad \mathcal{O}(\lambda^2) \\
&\mathrm{V_{ud}V_{cd}^*} + \mathrm{V_{us}V_{cs}^*} + \mathrm{V_{ub}V_{cb}^*} = 0 \qquad (u,c), \\
&\mathcal{O}(\lambda) \qquad \mathcal{O}(\lambda) \qquad \mathcal{O}(\lambda^5) \\
&\mathrm{V_{ud}V_{td}^*} + \mathrm{V_{us}V_{ts}^*} + \mathrm{V_{ub}V_{tb}^*} = 0 \qquad (u,t), \\
&\mathcal{O}(\lambda^3) \qquad \mathcal{O}(\lambda^3) \qquad \mathcal{O}(\lambda^3) \\
&\mathrm{V_{cd}V_{td}^*} + \mathrm{V_{cs}V_{ts}^*} + \mathrm{V_{cb}V_{tb}^*} = 0 \qquad (c,t), \\
&\mathcal{O}(\lambda^4) \qquad \mathcal{O}(\lambda^2) \qquad \mathcal{O}(\lambda^2).
\end{aligned}
\tag{2.91}
$$

The (d,b) triangle in Equation 2.79 is commonly referred to as *the* unitarity triangle for the B meson sector[c], and is the one that relates the two least well-determined entries of the CKM matrix, namely $\mathrm{V_{ub}}$ and $\mathrm{V_{td}}$. The angles within this triangle are denoted by α, β and γ, and are defined in terms of the elements of $\mathrm{V_{CKM}}$ as

$$
\alpha \equiv \arg\left(-\frac{\mathrm{V_{td}V_{tb}^*}}{\mathrm{V_{ud}V_{ub}^*}}\right), \quad \beta \equiv \arg\left(-\frac{\mathrm{V_{cd}V_{cb}^*}}{\mathrm{V_{td}V_{tb}^*}}\right), \quad \gamma \equiv \arg\left(-\frac{\mathrm{V_{ud}V_{ub}^*}}{\mathrm{V_{cd}V_{cb}^*}}\right). \tag{2.92}
$$

These then satisfy, by definition,

$$
\alpha + \beta + \gamma = \arg(-1) \; = \pi \bmod 2\pi. \tag{2.93}
$$

[c]Equation 2.78 is the corresponding unitarity triangle for the kaon sector, which from the (ds) triangle in Figure 2.7 is seen to be almost flat - therefore the kaon system exhibits small $\mathcal{CP}$ asymmetries in comparison to that of the B meson sector (d,b) triangle in Figure 2.7, in which large $\mathcal{CP}$ asymmetries are predicted [52].

Figure 2.8 shows the (d,b) and (u,t) triangles. The angles χ and $\gamma' = \gamma - \chi$ are defined in terms of the elements of V_{CKM} as

$$\chi \equiv \arg\left(-\frac{V_{ts}V_{tb}^*}{V_{cs}V_{cb}^*}\right), \quad \gamma' \equiv \arg\left(-\frac{V_{tb}V_{ub}^*}{V_{ts}V_{us}^*}\right). \tag{2.94}$$

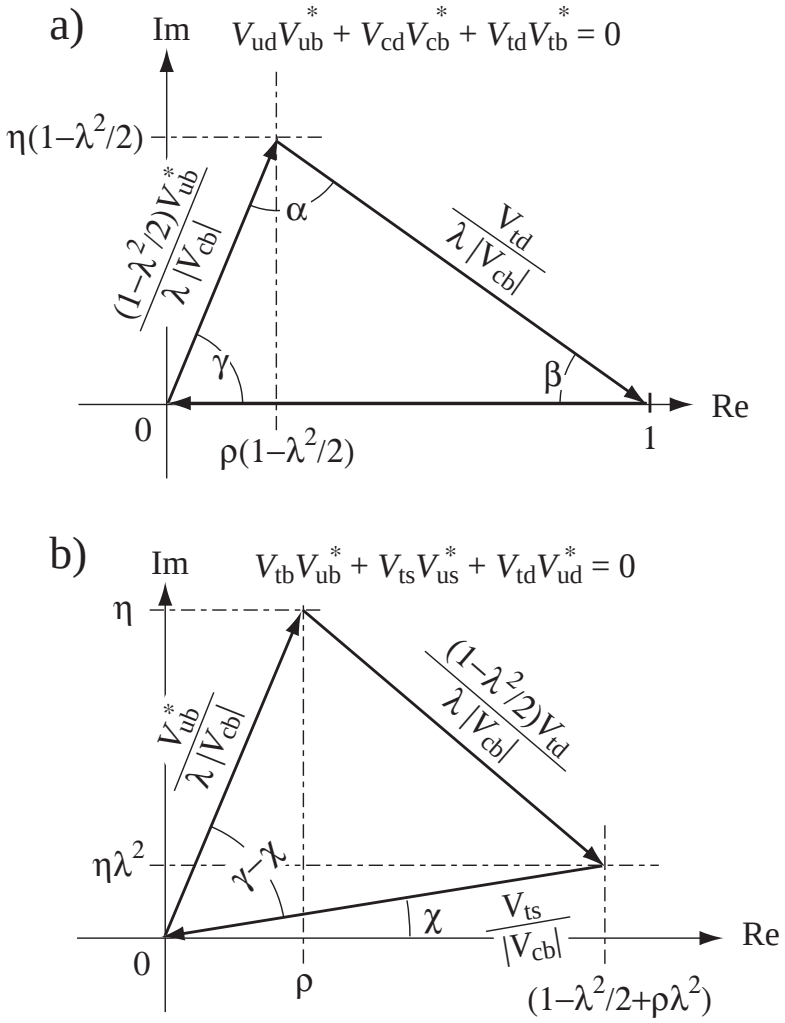

Figure 2.8: *Equations (2.79) and (2.82) shown as triangles in the complex plane.*

The angles β, χ and γ are commonly referred to as the B_d^0 mixing phase, the B_s^0 mixing phase and the weak decay phase respectively. Many models that go beyond the

Standard Model predict an additional contribution to $\mathrm{V_{CKM}}$ due to new physics so that $\beta(\text{measured}) \rightarrow \beta - \beta(\text{new})$ and $\alpha(\text{measured}) \rightarrow \alpha + \alpha(\text{new})$. Thus the requirement that the sum of the three angles α, β and γ must add up to π as in Equation 2.93 is not sensitive to new physics [53].

The Wolfenstein parameterisation to $\mathcal{O}(\lambda^5)$ in terms of the angles α, β and χ is

$$\mathrm{V_{CKM}} = \begin{pmatrix} 1 - \frac{1}{2}\lambda^2 - \frac{1}{8}\lambda^4 & \lambda & -|\mathrm{V_{ub}}|e^{-i\gamma} \\ -\lambda\left[1 + A^2\lambda^4\left(\rho + i\eta - \frac{1}{2}\right)\right] & 1 - \frac{1}{2}\lambda^2 - \frac{1}{8}\lambda^4(1 + 4A^2) & A\lambda^2 \\ -|\mathrm{V_{td}}|e^{-i\beta} & |\mathrm{V_{ts}}|e^{-i\chi} & 1 - \frac{1}{2}A^2\lambda^4 \end{pmatrix} + \mathcal{O}(\lambda^6). \tag{2.95}$$

The parameterisation in Equation 2.95 implies that

$$\arg \mathrm{V_{td}} = -\beta, \quad \arg \mathrm{V_{ub}} = -\gamma, \quad \arg \mathrm{V_{ts}} = -\chi + \pi. \tag{2.96}$$

The angles α, β, γ and χ are related to the Wolfenstein parameters ρ, η and λ via

$$\alpha = \tan^{-1}\left(\frac{\overline{\eta}}{\overline{\eta}^2 + \overline{\rho}\,(\overline{\rho} - 1)}\right), \quad \beta = \tan^{-1}\left(\frac{\overline{\eta}}{1 - \overline{\rho}}\right), \quad \gamma = \tan^{-1}\left(\frac{\overline{\eta}}{\overline{\rho}}\right), \quad \chi = \eta\lambda^2 \tag{2.97}$$

where

$$\overline{\rho} = \rho\left(1 - \frac{\lambda^2}{2}\right) \tag{2.98}$$

and

$$\overline{\eta} = \eta\left(1 - \frac{\lambda^2}{2}\right). \tag{2.99}$$

Using this notation, it is seen that Figure 2.8(a) as described by Equation 2.79 can be represented by a triangle in the complex $(\overline{\rho}, \overline{\eta})$ plane as shown in Figure 2.9(a), and that Figure 2.8(b) as described by Equation 2.82 can be represented by a triangle in the complex $(\overline{\rho}, \overline{\eta})$ plane as shown in Figure 2.9(b).

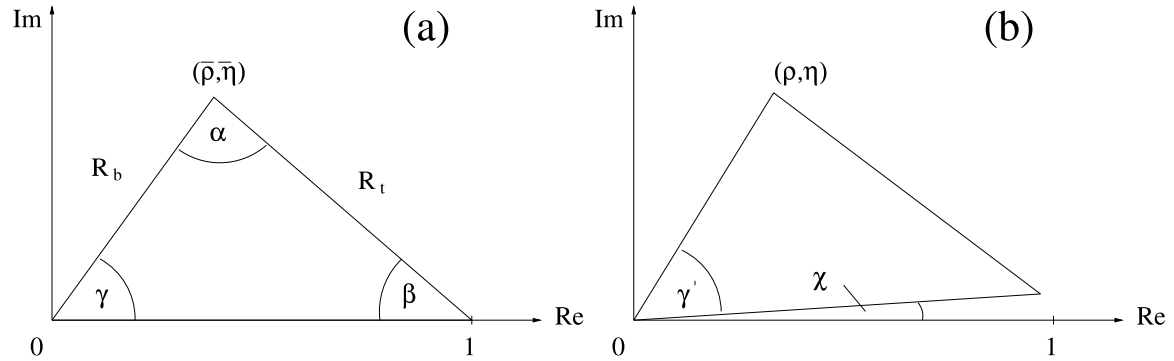

Figure 2.9: *The unitarity triangles in the* $\overline{\rho} - \overline{\eta}$ *plane. The sides of the triangle in (a) are denoted by* $\mathrm{R_b}$ *and* $\mathrm{R_t}$ *where* $\mathrm{R_b} = \sqrt{\overline{\rho}^2 + \overline{\eta}^2}$ *and* $\mathrm{R_t} = \sqrt{(1-\overline{\rho})^2 + \overline{\eta}^2}$ *[41]*

2.7 The Jarlskog parameter, J

It was shown by Jarlskog [54] that the determinant of the commutator of the up-type and down-type unitary mass matrices

$$M_i = \frac{v g_i}{\sqrt{2}} \tag{2.100}$$

where g represents the Yukawa couplings of the fermion field to the Higgs doublet and $i = u(d)$ for the up(down)-type quarks, is

$$det\,[M_u, M_d] = -2iF_u F_d J. \tag{2.101}$$

F_u and F_d are given by

$$F_{u(d)} = \frac{1}{{m_{t(b)}}^3}\big(m_{t(b)} - m_{c(s)}\big)\big(m_{t(b)} - m_{u(d)}\big)\big(m_{c(s)} - m_{u(d)}\big). \tag{2.102}$$

J is the Jarlskog parameter, and is a phase-independent measure of $\mathcal{CP}$ Violation. It is defined as

$$\Im\left[\mathrm{V_{ij}V_{kl}V_{il}^*V_{kj}^*}\right] = J\sum_{m,n=1}^{3}\epsilon_{ikm}\epsilon_{jln} \tag{2.103}$$

where $\mathrm{V_{ij}}$ are the elements of the CKM matrix and ϵ_{ikm} is the antisymmetric tensor.

The geometric interpretation of J is that all of the unitarity triangles in Figure 2.7 have the same area, $|J|/2$. In terms of the parameterisations discussed in the previous sections, J can be written as

- $J = c_{12}s_{12}{c_{13}}^2 s_{13}c_{23}s_{23}\sin\delta$ [Chau-Keung].
- $J = c_{12}s_{12}{c_{13}}^2 s_{13}c_{23}s_{23}\sin\delta$ [Kobayashi-Maskawa].
- $J \simeq A^2\eta\lambda^6$ [Wolfenstein].

Taking $i = u$, $j = d$, $k = t$ and $l = b$ in Equation 2.103 then [37, 55]

$$J \simeq \mathrm{A}^2\,\eta\,\lambda^6 \simeq 10^{-5}. \tag{2.104}$$

This means that $\mathcal{CP}$ Violation in the Standard Model is expected to be a small effect.

2.8 Current knowledge of the CKM parameters

Current knowledge of the CKM parameters in the B-meson system is limited to indirect measurements of the CKM matrix elements $\mathrm{V_{ij}}$ and to recent measurements of $\sin(2\beta)$. It is expected that the angles α and γ will remain unmeasured, or known only with a large statistical uncertainty, until the LHC comes into operation. In this section, the current knowledge of CKM parameters is discussed, along with recent direct measurements of β and the well-established decay modes for determining CKM parameters. This section concludes with a forecast of the knowledge of the CKM parameters in 2010 [56].

2.8.1 Measurements and current values of $\mathrm{V_{CKM}}$ elements

In principle, the values of the individual matrix elements can all be determined from the weak decays of the relevant quarks, or in some cases from deep-inelastic scattering. Assuming only three generations, then the 90% confidence limits on the magnitude of

the elements of the CKM matrix are: [37]

$$V_{CKM} = \begin{pmatrix} 0.9741 \text{ to } 0.9756 & 0.219 \text{ to } 0.226 & 0.0025 \text{ to } 0.0048 \\ 0.219 \text{ to } 0.226 & 0.9732 \text{ to } 0.9748 & 0.038 \text{ to } 0.044 \\ 0.004 \text{ to } 0.014 & 0.037 \text{ to } 0.044 & 0.9990 \text{ to } 0.9993 \end{pmatrix} \quad (2.105)$$

The range of matrix elements in Equation 2.105 corresponds to 90% confidence limits on the sines of the angles

$$s_{12} = 0.2229 \pm 0.0022, \quad s_{23} = 0.0412 \pm 0.0020, \quad s_{13} = 0.0036 \pm 0.0007. \quad (2.106)$$

The matrix elements $|V_{ud}|$, $|V_{us}|$ and $|V_{cb}|$ respectively are the most accurately measured, with $|V_{ts}|$ and $|V_{tb}|$ being the least constrained. Present knowledge of the matrix elements V_{ij}, (i = u,c,t), (j = d,s,b) come from the following sources:

- $|V_{ud}|$: Comparison of analyses performed on nuclear β decays that proceed via a vector current to muon decay.
- $|V_{us}|$: Analysis of K_{e3} [a] decays or hyperon decay data.
- $|V_{cd}|$: Neutrino and antineutrino production of charm off valence d quarks.
- $|V_{cs}|$: Neutrino production of charm, e.g charm- tagged W decays.
- $|V_{cb}|$: Measurements of $B \to \overline{D^*}\ l^+\ \nu_l$ decays based upon heavy quark effective theory (HQET) and also from $B \to \overline{D}\ l^+\ \nu_l$ decays.
- $|V_{ub}|$: Exclusive decays such as $B \to \pi\ l\ \nu_l$ and $B \to \rho\ l\ \nu_l$.
- $|V_{td}|$, $|V_{ts}|$ and $|V_{tb}|$:
  - Ratio of B mass differences implies that $\frac{|V_{td}|}{|V_{ts}|} < 0.24$.

[a] $K^+ \to \pi^0 e^+ \nu_e$ and $K_L^0 \to \pi^- e^+ \nu_e$

- Using the above result, $|V_{ts}| \approx |V_{cb}|$ implies that $|V_{td}| < 0.010$.
- Observation of $b \to s\gamma$ can be translated into $\frac{|V_{ts}|}{|V_{cb}|} = 1.1 \pm 0.43$
- Measured value of Δm_d from $B^0_d - \overline{B^0_d}$ mixing gives $|V^*_{tb}.V_{td}| = 0.0083 \pm 0.0016$

Measurements of $|V_{ud}|$, $|V_{us}|$, $|V_{ub}|$, $|V_{cd}|$, $|V_{cs}|$, $|V_{cb}|$ and $|V_{tb}|$ assume only first order weak interactions, i.e that they are described by the tree-level diagrams only, as illustrated in Figure 2.1. The remaining two elements $|V_{td}|$ and $|V_{ts}|$ are accessed through the so-called "loop" diagrams, such as the QCD or electroweak penguin diagrams shown in Figures 2.2 and 2.3 or the box diagrams shown in Figure 2.4.

2.8.2 Direct measurement of β

Direct measurements of the unitarity triangle angle β were first accomplished through studies of the $\mathcal{CP}$ asymmetries of $B^0_d \to J/\psi K_S$ decays. The decay $B^0_d \to J/\psi K_S$ is known as the "gold-plated" mode due to its clean experimental signature and its low theoretical uncertainty. The final state is a $\mathcal{CP}$ eigenstate, to which both B^0_d and $\overline{B^0_d}$ can decay. The interference between their direct and indirect decays via $B^0_d - \overline{B^0_d}$ mixing[d] leads to a time-dependent $\mathcal{CP}$ asymmetry given by

$$\mathcal{A}_{CP}(B^0_d \to J/\psi K_S) \equiv \frac{\Gamma(B^0_d \to J/\psi K_S) - \Gamma(\overline{B^0_d} \to J/\psi K_S)}{\Gamma(B^0_d \to J/\psi K_S) + \Gamma(\overline{B^0_d} \to J/\psi K_S)} = -\sin(2\beta)\sin(\Delta m_d t). \tag{2.107}$$

Here $\Gamma(B^0_d \to J/\psi K_S)$ represents the rate of particles that were produced as B^0_d decaying to $J/\psi K_S$ at proper time t. Δm_d is the oscillation frequency of the B^0_d, and β is as defined in Equation 2.92.

Upon comparison of Equation 2.107 with the generalised expression for the time-dependent asymmetry in Equation 2.53, then

$$\Im(\lambda_f) = \sin(2\beta), \tag{2.108}$$

[d] $\mathcal{CP}$ Violation in the interference between decay and mixing was discussed in Section 2.2.5.

where λ_f was defined in Equation 2.49.

Between 1998 and 2000, the LEP general purpose experiments ALEPH and OPAL, and the CDF experiment at Fermilab, published measurements of $\sin(2\beta)$ [57–59]. Then in 2001, each of the BaBar and Belle collaborations published their first measurements of $\sin(2\beta)$ [60,61]. Both experiments updated their measurements again in 2001 and again in 2002 [25,26,62]. In particular, [25,26] were the first significant non-zero measurements of $\sin 2\beta$, therefore confirming the existence of $\mathcal{CP}$ Violation in the B-meson system.

$\sin(2\beta)$ is now becoming a precision measurement, with the latest values of $\sin(2\beta)$ from BaBar and Belle in 2002(2003) based upon 81(140) fb^{-1} of data collected between 1999 and 2002(2003) giving

- $\sin(2\beta) = 0.741 \pm 0.067\,(\text{stat}) \pm 0.034\,(\text{syst})$, BaBar (2002) [62]
- $\sin(2\beta) = 0.733 \pm 0.057\,(\text{stat}) \pm 0.028\,(\text{syst})$, Belle (2003) [63].

These two measurements combined give an average value of $\sin(2\beta)$ as

- $\sin(2\beta) = 0.736 \pm 0.049$ [56,63].

All measurements of $\sin(2\beta)$ are summarised in Table 2.1.

2.8.3 Indirect measurements

There exists a standard analysis which is used to constrain the apex of the unitarity triangle in the $\overline{\rho}$-$\overline{\eta}$ plane. This is illustrated in Figure 2.10. The three main ingredients to this analysis are:

- Exclusive and inclusive semi-leptonic B decays due to $b \to c\ell\overline{\nu_\ell}$ and $b \to u\ell\overline{\nu_\ell}$ quark level transitions measure the quantities $|\text{V}_{\text{ub}}|$ and $|\text{V}_{\text{cb}}|$, thereby fixing a circle of radius R_b around (0, 0),
- B^0_q–$\overline{\text{B}^0_\text{q}}$ ($q \in \{d, s\}$) fixes a circle of radius R_t around (1, 0),

Pre "B-factory measurements"			
Experiment	Date	$\sin(2\beta)$	Reference
ALEPH	2000	$0.84\ ^{+0.82}_{-1.04}$ (stat) $\pm$ 0.16 (syst)	[57]
CDF	2000	$0.79\ ^{+0.41}_{-0.44}$ (stat and syst combined)	[59]
OPAL	1998	$3.2\ ^{+1.8}_{-2.0}$ (stat) $\pm$ 0.5 (syst)	[58]
Past "B-factory measurements"			
Experiment	Date	$\sin(2\beta)$	Reference
BaBar	2001	0.34 ± 0.20 (stat) $\pm$ 0.05 (syst)	[60]
BaBar	2001	0.59 ± 0.14 (stat) $\pm$ 0.05 (syst)	[25]
Belle	2001	$0.58\ ^{+0.32}_{-0.34}$ (stat)$^{+0.09}_{-0.10}$ (syst)	[61]
Belle	2001	0.99 ± 0.14 (stat) $\pm$ 0.06 (syst)	[26]
Current "B-factory measurements"			
Experiment	Date	$\sin(2\beta)$	Reference
BaBar	2002	0.741 ± 0.067 (stat) $\pm$ 0.034 (syst)	[62]
Belle	2003	0.733 ± 0.057 (stat) $\pm$ 0.028 (syst)	[63]

Table 2.1: *Summary of past and present* $\sin(2\beta)$ *results.*

- The parameter ϵ_K from indirect $\mathcal{CP}$ Violation in the neutral kaon system defines a hyperbola,

where the variables R_b and R_t were defined in Figure 2.9 and ϵ_K was defined in Equation 2.37. A strategy to deal with the current experimental values and range of theoretical parameters is the Frequentist statistical fitting approach developed in [52] and illustrated in Figure 2.11. In this so called Rfit method one maximises the likelihood $\mathcal{L}(y_{th}) = \mathcal{L}_{exp}(x_{exp} - x_{th}\,(y_{th}))\cdot\mathcal{L}_{th}(y_{th})$, where measurements x_{exp} and theoretical predictions x_{th}, depending on parameters y_{th} enter the experimental part $\mathcal{L}_{exp}$. The theoretical part $\mathcal{L}_{th}$ equals unity if the set of parameters are within an allowed range of predictions and vanish otherwise. The typical ranges of α, β and γ that are implied by this strategy are

$$83^\circ \leq \alpha \leq 109^\circ, \quad 21.8^\circ \leq \beta \leq 24.8^\circ, \quad 48^\circ \leq \gamma \leq 73^\circ. \tag{2.109}$$

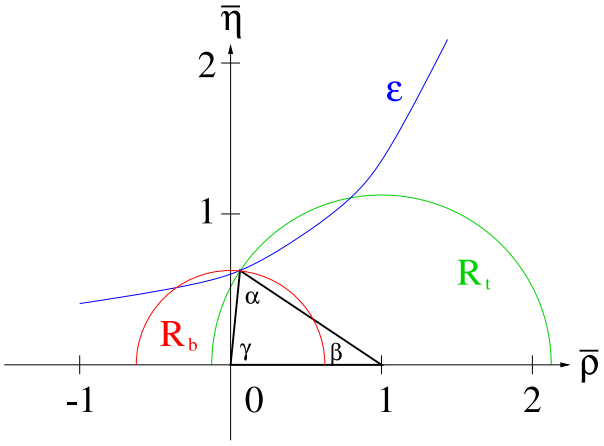

Figure 2.10: *Contours to determine the unitarity triangle in the $\overline{\rho}$-$\overline{\eta}$ plane . [41]*

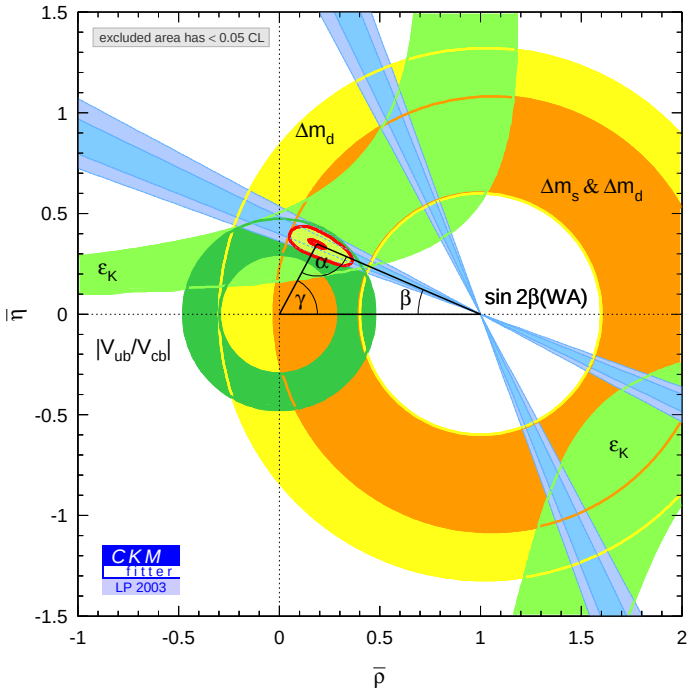

Figure 2.11: *Two dimensional representation in the $\overline{\rho}$-$\overline{\eta}$ plane illustrating confidence limits and numerical results for the CKM matrix elements ($|\mathrm{V_{ub}}|$ and $|\mathrm{V_{cb}}|$), and $\mathcal{CP}$-violating and mixing observables parameters ϵ_K, Δm_d, Δm_s and the current world-average of $\sin(2\beta)$, denoted here by $\sin(2\beta)_{WA}$. The unitarity triangle (Figure 2.9) is superimposed upon this representation [56].*

The current values of the elements $|V_{ub}|$, $|V_{cb}|$, $|V_{td}|$ and $|V_{ts}|$ of the CKM matrix are listed in Section 2.8.1 and are measurements which are sensitive only to the sides of the unitarity triangle through semi-leptonic B decays and B^0_d-$\overline{B^0_d}$ mixing. These values allow an indirect or "sides" measurement of $\sin(2\beta)$ via Equation 2.92. From [48], the value obtained via this indirect method is $\sin(2\beta) = 0.695 \pm 0.055$. The values of $\sin(2\beta)$ obtained via direct and indirect measurements are seen to be in very good agreement showing that the Standard Model currently gives a very consistent picture.

In Section 2.4 the fact that in the CKM picture of the three generation Standard Model, there are four fundamental parameters that need to be experimentally determined, was discussed. In Section 2.5.2 the Wolfenstein parameterisation, with real parameters λ, A, ρ and η was introduced. Of these parameters, λ and A are well measured. The value of the parameter λ has been precisely determined from measurements of $|V_{ud}|$ via nuclear beta decay, and has previously been stated in Equation 2.106. The parameter A has also been determined precisely, but from measurements of V_{cb} via inclusive and exclusive B decays [64]. The value of A has been determined from measurements of $|V_{cb}|$ to be $A = 0.83 \pm 0.02$ [48]. Conversely the parameters ρ and η are poorly known. Using the value of $\lambda = 0.2229 \pm 0.0022$ then the current values of the parameters $\overline{\rho}$ and $\overline{\eta}$ (defined in Equations 2.98 and 2.99 respectively) are [37, 52]

$$\overline{\rho} = 0.22 \ \pm \ 0.10 \quad \text{and} \quad \overline{\eta} = 0.35 \ \pm \ 0.05. \tag{2.110}$$

2.9 Future prospects

There are a number of channels which will be probed using the BaBar, Belle, CDF and D0 detectors before the LHC starts running. These are the so-called 'benchmark modes" i.e they are modes which have been well established in literature as being B^0_d and B^0_s decay channels in which to first explore $\mathcal{CP}$ Violation and to extract measurements of the angles of the unitarity triangles α, β and γ [50]. The potential for these modes at the B factories and at the Tevatron are well documented in [65] and [66]. Physics with

B_s^0 mesons is unique to the Tevatron until the start of the LHC in 2007 but since the current luminosity at the Tevatron is a factor of two lower than planned, it is expected that results until the start of the LHC will be dominated by $B^{\pm}$ and B_d^0 decays from the B factories.

Both BaBar and Belle are well on their way to collecting of the order of 500 fb^{-1} by 2007. [67] notes that the statistical error on $\sin(2\beta)$, σ_{stat} has improved versus the integrated luminosity $\int \mathcal{L}\,dt$ since both experiments have been able to perform better than $\sigma_{\text{stat}}^{-2} \propto \int \mathcal{L}\,dt$ by improving their reconstruction, calibration and selections. As a result, one can expect a statistical error on $\sin(2\beta)$ of approximately ± 0.03 given a 500 fb^{-1} sample by the start of the LHC. Channels used to measure $\sin(2\beta)$ will include decays such as $B_d^0 \to J/\psi\pi^0$, $B_d^0 \to \phi K_S^0$ and $B_d^0 \to \eta' K_S^0$.

It is also anticipated that improvements will be made towards measuring α through channels such as $B_d^0 \to \pi^+\pi^-$ and $B_d^0 \to \rho^+\rho^-$. The modes $B_d^0 \to \pi^0\pi^0$ and $B_d^0 \to \rho^0\rho^0$ can be used to limit the effect of unknown contributions from penguin diagrams, often referred to as "penguin pollution" [68]. Strategies to disentangle penguin contributions from the tree diagrams generally require very large data sets or involve hard to quantify theoretical uncertainties [66].

It will be experimentally very difficult to place limits on the angle γ at the B-factories. This is mainly due to the fact that many channels which are sensitive to γ will suffer from low statistics at both the B-factories and at the Tevatron. Studies to extract the angle γ is the subject of Chapter 3.

With respect to mixing measurements, the current world average B_d^0 oscillation frequency is dominated by the results from the B factories which will continue to improve the precision on Δm_d. This measurement will eventually be limited by the uncertainty on the B_d^0 lifetime [48]. The interest in mixing at the Tevatron, and at the LHC will lie in the measurement of B_s^0 oscillations.

The LHCb TDR [69] and the LHCb Reoptimisation TDR [70] also provide a comprehensive list of channels of interest, with emphasis on those that will be explored at

LHCb. [69] and [70] contain results of studies of the expected physics reach and sensitivity studies to the unitarity triangles expected to be achievable using the LHCb detector.

Figure 2.12 shows the expected $\overline{\rho}$-$\overline{\eta}$ plane as of 2010. The changes in Figure 2.12 compared to that of Figure 2.11 will be due to measurements of $\sin(2\beta)$ with a reduced statistical uncertainty, first measurements of α and γ due to increased statistics in both B^0_d and B^0_s channels and first measurements of Δm_s. The smallness of $\mathcal{CP}$-violating effects in the Kaon sector compared to that in the B sector, is an impediment to progress within kaon physics. However before 2010, the experiments KOPIO (Brookhaven) [71] and KAMI (Fermilab) [72] are expected to measure the branching ratios of the rare decays $K^+ \to \pi^+ \nu\overline{\nu}$ and $K_L \to \pi^0 \nu\overline{\nu}$ [52].

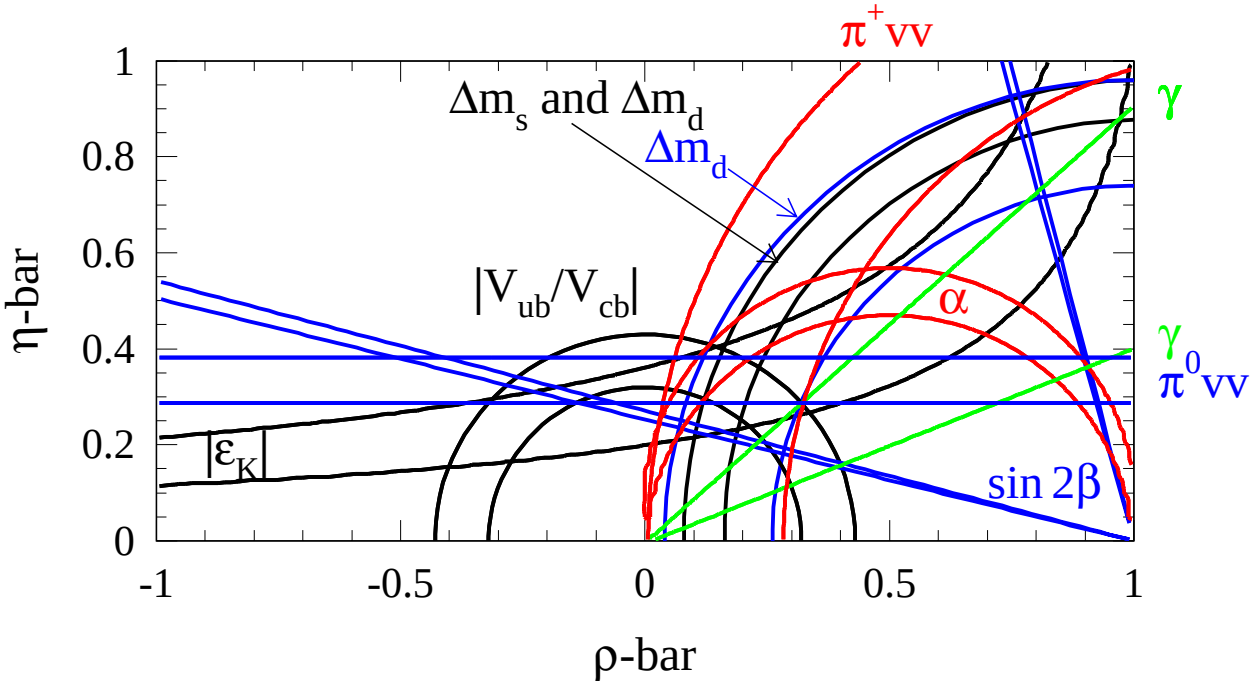

Figure 2.12: *Expected ρ-η plane as of 2010. [52, 56]*

Chapter 3

Extracting γ from $B \to DD$ decays

It is anticipated that precise studies of the CKM angle γ will be first achieved with the LHCb detector. Unlike the Tevatron and the current B-factories, LHCb will not be restricted by low statistics and will have access to a full spectrum of B-mesons. Many proposed methods to determine γ require both B^0_d and B^0_s decay channels to be accessible. One such method is that proposed by Fleischer using the U-spin symmetry-related $B^0_d \to D^+D^-$ and $B^0_s \to D^+_s D^-_s$ decays [73]. In addition a theoretical formalism has been proposed in which the $B^+_c \to D^+_s \overline{D}^0$ channel could also be used to extract γ [74]. The $B_{d(s)} \to D^+_{(s)} D^-_{(s)}$ channels have both tree and penguin contributions to their decay amplitudes whereas the $B^+_c \to D^+_s \overline{D}^0$ channel only has tree contributions. Should it be feasible that these channels can be studied at LHCb and that studies of γ are then possible, new physics may be visible through presence of the penguin contributions. Comparing the values of γ from the $B^0_{d(s)} \to D^+_{(s)} D^-_{(s)}$ and $B^+_c \to D^+_s \overline{D}^0$ (collectively referred to as the $B \to DD$ channels in the rest of this thesis) would be a good test of the Standard Model. This motivates the three physics analyses presented in Chapters 6-8.

The rest of this Chapter discusses the two methods of extracting γ from $B \to DD$ decays. The current knowledge of γ and an overview of possible methods to measure γ are also presented.

3.1 Current knowledge of γ

Current knowledge of the CKM parameters was discussed in Section 2.8 where it was stated that the CKM angle γ (defined in Equation 2.92) will remain unmeasured or known only with a large statistical uncertainty until the LHC comes into operation. The Belle collaboration has published the first results of their studies to measure γ using a Dalitz analysis of the three-body D^0 decay from the $B^0_d \rightarrow D^0K$ process [75]. The quoted 90% confidence interval for γ is $61^\circ < \gamma < 142^\circ$. This may be compared with the current limits on γ from indirect measurements. Recent studies carried out by the CKM Fitter Group show that the most likely values of $\overline{\rho}$ and $\overline{\eta}$ ($\overline{\rho} = 0.22 \pm 0.10$ and $\overline{\eta} = 0.35 \pm 0.05$ [37, 52]) correspond to $48^\circ < \gamma < 73^\circ$ [56]. A further Standard Model analysis using the current values of $|V_{ub}|$, $|V_{cb}|$, $|V_{td}|$ and $\sin(2\beta)$, predicts $\gamma \sim 65^\circ$ [48].

BaBar has not published a measurement of γ but simulation studies reported in the BaBar Physics Book [65] indicates that an integrated luminosity of $\sim$300 fb^{-1} will be needed in order to reach a sensitivity to γ in the range $\sigma(\gamma) = 10$ - 20°. BaBar accumulated 164.8 fb^{-1} of data up to January 2004 and is expected to accumulate $\sim$500 fb^{-1} in total by the start of the LHC.

Simulation studies prior to the start of Tevatron Run-II indicate that a resolution of 15° on γ could be achieved assuming that the branching ratio of the $B^+ \rightarrow K^+D^0$ decay could be determined with a 20% precision [66]. Current studies predict that $\sigma(\gamma) = \pm 10^\circ(\text{stat}) \pm 3^\circ(\text{theory})$ with the $B^0_d \rightarrow \pi^+\pi^-$ and $B^0_s \rightarrow K^+K^-$ channels could be achievable by the end of the current data-taking period (Run IIa) which is due to end in 2005 [76].

3.2 Overview of the methods to measure γ

Methods for measuring γ can be categorised into four groups, involving respectively: time-dependent asymmetries, time-integrated amplitude relations, isospin symmetry relations and U-spin symmetry relations. Sensitivity studies for all these cases are being carried out in LHCb.

1. Time-dependent asymmetries.

A theoretically clean way to extract the quantity $-\chi + \gamma$ is to mix the two tree diagrams $\overline{\mathrm{b}} \to \overline{\mathrm{u}} + \mathrm{W}^+$ and $\overline{\mathrm{b}} \to \overline{\mathrm{c}} + \mathrm{W}^+$. This can be done for example by studying the time-dependent rates of $\mathrm{B_s^0}$ decaying into $\mathrm{D_s^+K^-}$ and $\mathrm{D_s^-K^+}$ and their $\mathcal{CP}$-conjugated processes [43, 77]. χ is the Standard Model phase of $\mathrm{B_s^0}$–$\overline{\mathrm{B_s^0}}$ oscillations, which can be obtained from the time-dependent $\mathcal{CP}$ asymmetry of $\mathrm{B_s^0}$ and $\overline{\mathrm{B_s^0}}$ decaying into $\mathrm{J}/\psi\phi$ (or other $\mathcal{CP}$ eigenstates produced by the b$\to$ c + W^- and $\overline{\mathrm{b}} \to \overline{\mathrm{c}} + \mathrm{W}^+$ tree processes). Recent studies by the LHCb collaboration show that after one year of data-taking $\sigma\,(\gamma)$ = 14-15° for $55° < \gamma + \chi < 105°$ using these channels [78].

The $\mathrm{B_d^0}$ counterpart of $\mathrm{B_s^0} \to \mathrm{D_s^\pm K^\mp}$ is $\mathrm{B_d^0} \to \mathrm{D^{(*)\pm}}\pi^\mp$ from which the angle γ can be determined from the CKM combination $2\beta + \gamma$. This requires that the angle β is known, for example from studies of the $\mathrm{B_d^0} \to \mathrm{J}/\psi\mathrm{K_S}$ channel. [50].

2. Time-integrated amplitude relations.

A second way in which to determine γ is to observe the interference between the two tree processes $\overline{\mathrm{b}} \to \overline{\mathrm{u}} + \mathrm{W}^+$ and $\overline{\mathrm{b}} \to \overline{\mathrm{c}} + \mathrm{W}^+$, by measuring the three time-integrated decay rates for $\mathrm{B_d^0} \to \mathrm{D^0K^{*0}}$, $\mathrm{B_d^0} \to \overline{\mathrm{D}}^0\mathrm{K^{*0}}$, $\mathrm{B_d^0} \to \mathrm{D_{CP}^0K^{*0}}$ and their $\mathcal{CP}$-conjugated processes, where $\mathrm{D_{CP}^0} = (\mathrm{D^0} + \overline{\mathrm{D}}^0)/\sqrt{2}$ denotes the $\mathcal{CP}$-even eigenstate of the $\mathrm{D^0}$–$\overline{\mathrm{D}}^0$ system [79]. The value of γ extracted is sensitive to any new physics which may appear through $\mathrm{D^0}$–$\overline{\mathrm{D}}^0$ mixing. A recent LHCb study shows that $\sigma\,(\gamma)$ = 7-8° for $55° < \gamma < 105°$ after one year of data-taking, is possible using this method [80]. Analogous to this method is

that proposed to extract γ from $B_c^+ \to D_s^+ \overline{D}^0$ [74]. This is described in Section 3.4.

3. Isospin symmetry relations.

Studies of the $B^+ \to \pi^+ K_S$ and $B_d^0 \to \pi^- K^+$ and their charge-conjugates were proposed in [81–83]. This method makes use of the fact that the general phase structure of the corresponding decay amplitudes is known reliably within the Standard Model and uses the $SU(2)$ isospin symmetry of strong interactions to relate the QCD penguin contributions. This method is a promising one for future B experiments such as LHCb since it requires only time-independent measurements of branching ratios at $\mathcal{O}(10^{-5})$ level. Studies of the $B^+ \to \pi^+ K$ and $B_d^0 \to \pi^- K^+$ modes are currently underway within the LHCb collaboration.

4. U-spin symmetry relations.

Both $\overline{b} \to \overline{u} + W^+$ tree and $\overline{b} \to \overline{d} + g(\gamma, Z^0)$ penguin processes contribute to the decay $B_d^0 \to \pi^+\pi^-$. By replacing all the d and $\overline{d}$ quarks by s and $\overline{s}$ quarks, respectively, the tree and penguin processes generate the analogous decay $B_s^0 \to K^+K^-$. Assuming that the strong interaction dynamics remain invariant under this exchange (U-spin symmetry), the relative contributions of the penguin process with respect to the tree process are identical for both decay modes. Under this assumption, γ can be determined from the time-dependent $\mathcal{CP}$ asymmetry using the β and χ values obtained from the $\mathcal{CP}$ asymmetries measured with B_d^0, $\overline{B_d^0} \to J/\psi K_S$ and B_s^0, $\overline{B_s^0} \to J/\psi\phi$ respectively [84,85]. Studies performed by LHCb have shown that $\sigma(\gamma) = 4$-6° from one year of LHCb data-taking assuming U-spin symmetry [86]. Similar to this is the proposed method using the U-spin symmetry-related $B_d^0 \to D^+D^-$ and $B_s^0 \to D_s^+D_s^-$ decays.

In summary, of the methods listed above, 3 and 4 are both concerned with decays which have tree and penguin contributions, and so, unlike Methods 1 and 2, may show signs of new physics through the penguin contributions.

Two methods will now be discussed, first the U-spin symmetry relation method proposed by Fleischer [73] using the $B^0_{d(s)} \to D^+_{(s)}D^-_{(s)}$ channels and secondly the time-integrated amplitude relation method proposed by Fleischer and Wyler [74] using the $B^+_c \to D^+_s\overline{D}^0$ channel.

3.3 Extracting γ from $B^0_{d(s)} \to D^+_{(s)}D^-_{(s)}$ decays

This U-spin symmetry relation method of extracting γ requires three observables $\mathcal{A}^{dir}_{CP}$, $\mathcal{A}^{int}_{CP}$ and $\mathcal{A}_{\Delta\Gamma}$ to be extracted from a fit to the time-dependence of the tagged $B^0_d \to D^+D^-$ $\mathcal{CP}$ asymmetry which is normalised through the untagged $\mathcal{CP}$-averaged $B^0_s \to D^+_sD^-_s$ rate [73]. At the LHC the production fraction of $b \to B^0_s$ is $\sim$4 times smaller than the production fraction $b \to B^0_d$ [37]. However this is compensated by the fact that the $B^0_d \to D^+D^-$ events must be tagged whereas the $B^0_s \to D^+_sD^-_s$ events to be used should be untagged.

3.3.1 U-spin symmetry

The decays $B^0_d \to D^+D^-$ and $B^0_s \to D^+_sD^-_s$ are related to one other through the U-spin flavour symmetry of strong interactions (i.e. through the interchanging of all down and strange quarks). U-spin symmetry is the SU(2) subgroup of flavour SU(3) which relates the s and the d quark. It is known from hadron spectroscopy that U-spin symmetry is violated, which at the parton level originates from the different masses of the d and s quarks. However since the hadronic final states of the B^0_d and B^0_s meson have masses well above that of the d and s quarks, the U-spin limit is assumed to be valid [87].

3.3.2 Formalism

The decays $B^0_{d(s)} \to D^+_{(s)}D^-_{(s)}$ originate from b $\to c\bar{c}d$ quark level decays shown in Figures 3.1 and 3.2.

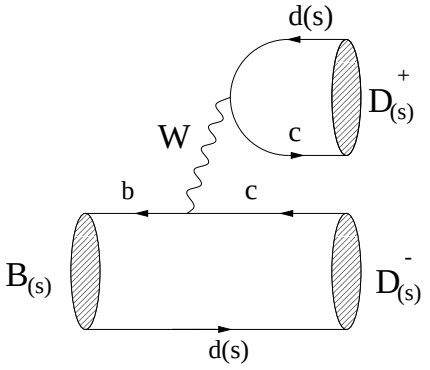

Figure 3.1: *Tree diagram contributions to the decays* $\mathrm{B^0_{d(s)} \to D^+_{(s)} D^-_{(s)}}$

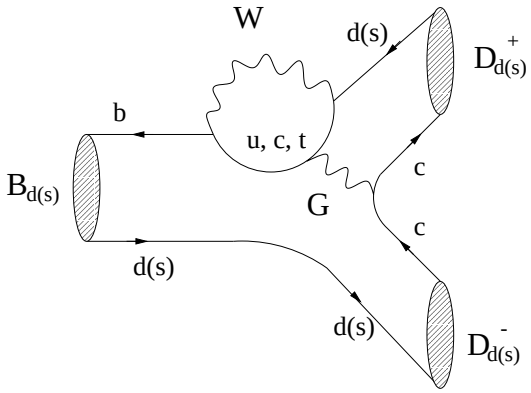

Figure 3.2: *Penguin contributions to the decays* $\mathrm{B^0_{d(s)} \to D^+_{(s)} D^-_{(s)}}$

The transition amplitude for the decay $\mathrm{B^0_s \to D^+_s D^-_s}$ is:

$$A(\mathrm{B^0_s \to D^+_s D^-_s}) = \lambda_{\mathrm{c}}{}^{(\mathrm{s})}\ (\mathrm{A}^{c'}_{\mathrm{cc}}\ +\ \mathrm{A}^{c'}_{\mathrm{pen}})\ +\ \lambda_{\mathrm{u}}{}^{(\mathrm{s})}\mathrm{A}^{u'}_{\mathrm{pen}}\ +\lambda_{\mathrm{t}}{}^{(\mathrm{s})}\mathrm{A}^{t'}_{\mathrm{pen}} \tag{3.1}$$

where $\mathrm{A}^{c'}_{\mathrm{cc}}$ denotes the amplitude of the $\mathrm{B^0_s \to D^+_s D^-_s}$ current-current ("tree") processes and $\mathrm{A}^{q'}_{\mathrm{pen}}$ denotes the contribution to $\mathrm{B^0_s \to D^+_s D^-_s}$ for penguin processes with internal quarks q, (q $\in\{u, c, t\}$). Denoting the CKM factors by $\lambda_{\mathrm{q}}{}^{(\mathrm{s})} \equiv \mathrm{V_{qs}V^*_{qb}}$, then invoking the unitarity of the CKM matrix (Equation 2.80) and by applying the Wolfenstein parametrisation in a form generalised to include non-leading order terms in λ, then the transition amplitude for the $\mathrm{B^0_s \to D^+_s D^-_s}$ decay can be re-expressed as

$$A(\mathrm{B^0_s \to D^+_s D^-_s}) = (1-\lambda^2/2)\ \overline{\mathcal{A}}'\ [1+\frac{\lambda^2}{1\ -\ \lambda^2}\overline{a}'\, e^{i\theta}e^{i\gamma}], \tag{3.2}$$

where

$$\overline{\mathcal{A}}' \equiv \overline{\mathcal{A}}\lambda^2\ (\mathrm{A}^{c'}_{\mathrm{cc}}\ +\ \mathrm{A}^{ct'}_{\mathrm{pen}}), \tag{3.3}$$

$$\mathrm{A}^{ct'}_{\mathrm{pen}} \equiv \mathrm{A}^{c'}_{\mathrm{pen}}\ -\ \mathrm{A}^{t'}_{\mathrm{pen}}, \tag{3.4}$$

and

$$\overline{a}'\, e^{i\theta} \equiv \mathrm{R_b}\ (1-\lambda^2/2)\ \left(\frac{\mathrm{A}^{ut'}_{\mathrm{pen}}}{\mathrm{A}^{c'}_{\mathrm{cc}}+\mathrm{A}^{ct'}_{\mathrm{pen}}}\right). \tag{3.5}$$

These steps are explained more fully in Appendix A. The relevant CKM factors are:

$$\lambda = |\mathrm{V_{us}}| = 0.2229 \pm 0.0022, \tag{3.6}$$

$$\overline{\mathcal{A}} \equiv \frac{1}{\lambda^2}\,|\mathrm{V_{cb}}| \;= 0.81 \pm 0.06, \tag{3.7}$$

and

$$\mathrm{R_b} \equiv \frac{1}{\lambda}\,|\mathrm{V_{ub}\,V_{cb}}| \;= 0.41 \pm 0.07. \tag{3.8}$$

The values of λ, $|\mathrm{V_{cb}}|$ and $\mathrm{R_b}$ are taken from [37].

In a similar manner, the transition amplitude for $\mathrm{B^0_d} \rightarrow \mathrm{D^+D^-}$ can be written in terms of the above CKM factors as

$$A(\mathrm{B^0_d} \rightarrow \mathrm{D^+D^-}) = (-\lambda)\,\overline{\mathcal{A}}\;\left[1 - \overline{a}e^{i\theta}e^{i\gamma}\right] \tag{3.9}$$

where

$$\overline{\mathcal{A}} \equiv \lambda^2 \mathrm{A}(\mathrm{A^c_{cc}} \;+\; \mathrm{A^{ct}_{pen}}) \tag{3.10}$$

and

$$\overline{a}e^{i\theta} \equiv \mathrm{R_b}\;(1 - \lambda^2/2)\;\left(\frac{\mathrm{A^{ut}_{pen}}}{\mathrm{A^c_{cc}} + \mathrm{A^{ct}_{pen}}}\right). \tag{3.11}$$

$\mathrm{A^c_{cc}}$ denotes the amplitude of the $\mathrm{B^0_d} \rightarrow \mathrm{D^+D^-}$ current-current ("tree") processes and $\mathrm{A^q_{pen}}$ denotes the contribution to $\mathrm{B^0_d} \rightarrow \mathrm{D^+D^-}$ for penguin processes with internal quarks q, (q $\in\{u, c, t\}$). Again these steps are explained more fully in Appendix A.

The time-dependent $\mathcal{CP}$ asymmetry $\mathcal{A}_{CP}(t)$ defined in Equation 2.50 can be re-expressed in terms of the time-dependent decay amplitudes $A(t)$ so that

$$\mathcal{A}_{CP}(t) \equiv \frac{|\,A(t)|^2 - |\,\overline{\mathrm{A}(t)}|^2}{|\,A(t)|^2 + |\,\overline{\mathrm{A}(t)}|^2} = 2e^{-\Gamma t}\frac{\mathcal{A}^{dir}_{CP}\cos(\Delta M t) \;+\; \mathcal{A}^{int}_{CP}\sin(\Delta M t)}{e^{-\Gamma_{\mathrm{H}} t} \;+\; e^{-\Gamma_{\mathrm{L}} t} \;+\; \mathcal{A}_{\Delta\Gamma}(e^{-\Gamma_{\mathrm{H}} t} \;-\; e^{-\Gamma_{\mathrm{L}} t})} \tag{3.12}$$

where $\Delta M \equiv m_{\mathrm{H}} \;-\; m_{\mathrm{L}} > 0$ is the mass difference between the B mass eigenstates (Equation 2.61) and $\Gamma_{\mathrm{H,L}}$ denotes their decay widths (Equation 2.62). The instantaneous

decay amplitudes take the form

$$\mathrm{A} = \mathcal{N}\left\{1 - b\, e^{i\rho} e^{i\gamma}\right\} \quad \text{and} \quad \overline{\mathrm{A}} = \eta\mathcal{N}\left\{1 - b\, e^{i\rho} e^{-i\gamma}\right\}, \tag{3.13}$$

where $\eta = \pm 1$ and $\mathcal{N}$ is a normalisation constant. As in Equation 2.50, $\mathcal{A}_{CP}^{dir}$ represents the direct $\mathcal{CP}$ violating component and $\mathcal{A}_{CP}^{int}$ the component describing $\mathcal{CP}$ violation in the interference. $\mathcal{A}_{CP}^{dir}$, $\mathcal{A}_{CP}^{int}$ and $\mathcal{A}_{\Delta\Gamma}$ are defined in [73] as

$$\mathcal{A}_{CP}^{dir} \equiv \frac{2\, b\, \sin\rho\, \sin\gamma}{1 - 2\, b\, \cos\rho\, \cos\gamma + b^2}, \tag{3.14}$$

$$\mathcal{A}_{CP}^{int} \equiv +\eta \left\{ \frac{\sin\phi - 2\, b\, \cos\rho\, \sin(\phi+\gamma) + b^2\, \sin(\phi+2\gamma)}{1 - 2\, b\, \cos\rho\, \cos\gamma + b^2} \right\}, \tag{3.15}$$

$$\mathcal{A}_{\Delta\Gamma} \equiv -\eta \left\{ \frac{\cos\phi - 2\, b\, \cos\rho\, \cos(\phi+\gamma) + b^2\, \cos(\phi+2\gamma)}{1 - 2\, b\, \cos\rho\, \cos\gamma + b^2} \right\}. \tag{3.16}$$

where

$$(\mathcal{CP})\,|f\rangle = \eta|f\rangle, \qquad \eta^2 = 1, \tag{3.17}$$

is the equation satisfied by the evolution of an initially tagged B_q^0 or $\overline{\mathrm{B}_\mathrm{q}^0}$ into a final $\mathcal{CP}$ eigenstate $|f\rangle$.

The three observables in Equations 3.14, 3.15, and 3.16 are related via

$$(\mathcal{A}_{CP}^{dir})^2 + (\mathcal{A}_{CP}^{int})^2 + (\mathcal{A}_{\Delta\Gamma})^2 = 1. \tag{3.18}$$

As with Equation 2.51, Equation 3.12 shows that the direct and interference $\mathcal{CP}$ violation contributions to the CP asymmetry $\mathcal{A}_{CP}(t)$ are separate. The direct $\mathcal{CP}$ violation contribution is independent of the $\mathrm{B}_\mathrm{q}^0 - \overline{\mathrm{B}_\mathrm{q}^0}$ mixing phase.

The observables $\mathcal{A}_{CP}^{dir}$, $\mathcal{A}_{CP}^{int}$ and $\mathcal{A}_{\Delta\Gamma}$ can be obtained experimentally from the time evolution of the time-dependent decay amplitudes $\mathrm{A}(t)$ via a likelihood fit similar to that described in [86]. Within this fit the experimentally observed decay rate for each channel is parameterised taking into account the following:

- flavour tagging,
- the presence of background,
- the signal acceptance as a function of the proper time after the trigger and offline-selection, and
- the resolution on the proper time measurement.

In the case that f is a $\mathcal{CP}$ eigenstate then the observed decay rates for events tagged as $\mathrm{B^0_q}$ and $\overline{\mathrm{B^0_q}}$ respectively can be written as

$$R_f(t) = \int \left[(1\ -\omega)\, k\Gamma_{B\to f}\,(\tau)\ +\ \omega k\Gamma_{\overline{B}\to f}\,(\tau)\right] \epsilon\,(\tau)\, G\,(\tau - t)\ d\tau\ + \frac{1}{2} B\,(t) \qquad (3.19)$$

and

$$\overline{R}_f(t) = \int \left[\omega k\Gamma_{B\to f}\,(\tau)\ +\ (1\ -\omega)\, k\Gamma_{\overline{B}\to f}\,(\tau)\right] \epsilon\,(\tau)\, G\,(\tau - t)\ d\tau\ + \frac{1}{2} B\,(t) \qquad (3.20)$$

where ω is the wrong tag fraction, $\epsilon(t)$ is the acceptance as a function of proper time t and $G(\Delta t)$ is a function describing the proper time resolution. Suitable parameterisations for these functions are as follows [86]:

$$\epsilon(t) = \frac{a}{1\ +\ \exp(t\ \times \mathrm{ps}^{-1})^b} \qquad (3.21)$$

where a and b are constants to be fitted.

The proper time resolution function $G(\Delta t)$ can be described by a double Gaussian with standard deviations $\sigma\Delta t_1$ and $\sigma\Delta t_2$:

$$G(\Delta t) = \frac{f}{\sqrt{2\pi}\sigma_{\Delta t_1}} \exp\left(-\frac{\Delta t^2}{2\sigma^2{}_{\Delta t_1}}\right) + \frac{(1-f)}{\sqrt{2\pi}\sigma_{\Delta t_2}} \exp\left(-\frac{\Delta t^2}{2\sigma^2{}_{\Delta t_2}}\right) \qquad (3.22)$$

where $\Delta t = t_{rec}$ - t_{true}. t_{rec} is the reconstructed proper time and t_{true} is the true proper time. The function $B(t)$ is an effective function describing the proper time dependence of the background rate. Its functional form for combinatorial background can be

determined from data by studying the proper time distribution in the mass sideband spectrum. If n_B is the number of tagged background events then $B(t)$ can be written as

$$B(t) = n_B\, b(t) \tag{3.23}$$

where $b(t)$ is the normalised rate for combinatorial background events and is taken to have the same form as that of the untagged signal rate. It can be written as

$$b(t) = \frac{\exp^{-\eta t}}{1\ +\ \exp(\mathrm{t}\ \times \mathrm{ps}^{-1})^{\delta}} \Big/ \int \frac{\exp^{-\eta t}}{1\ +\ \exp(\mathrm{t}\ \times \mathrm{ps}^{-1})^{\delta}} \tag{3.24}$$

The constant k in Equations 3.19 and 3.20 is obtained by noting that the sum of the integrals of the two signal rates must give the total number of tagged signal events n_f:

$$\begin{aligned} \int\int \left[(1\ -\omega)\, k\Gamma_{B\to f}\,(\tau)\ +\ \omega k\Gamma_{\overline{B}\to f}\,(\tau)\right] \epsilon\,(\tau)\, G\,(\tau - t)\ d\tau dt \\ +\ \int\int \left[\omega k\Gamma_{B\to f}\,(\tau)\ +\ (1\ -\omega)\, k\Gamma_{\overline{B}\to f}\,(\tau)\right] \epsilon\,(\tau)\, G\,(\tau - t)\ d\tau dt = n_f. \end{aligned} \tag{3.25}$$

The signal mass distribution can be described with a single Gaussian

$$g_S(m) = \frac{1}{\sqrt{2\pi}\sigma_m} \exp\left(-\frac{(m\ -\overline{m})^2}{2\sigma_m^2}\right) \tag{3.26}$$

and the combinatorial mass distribution is assumed to have an exponential shape of the form

$$g_B(m) = \frac{\mu \exp(-\mu m)}{\exp\left(-\mu m_{min}\right) - \exp\left(-\mu m_{max}\right)}, \tag{3.27}$$

where m_{min} and m_{max} are the minimum and maximum mass values accepted by the trigger. Both $g_S(m)$ and $g_B(m)$ must be normalised to 1:

$$\int g_S(m) dm = \int g_B(m) dm = 1. \tag{3.28}$$

Also to be entered into such a fit are values of parameters to determined from studies of the $\mathrm{B_{d(s)}} \rightarrow \mathrm{D^{+}_{(s)}D^{-}_{(s)}}$ channel, for example the background-to-signal ratio (B/S), the

tagging efficiency $\epsilon_{\rm tag}$ and the proper time resolutions $\sigma\Delta t_1$ and $\sigma\Delta t_2$.

By construction the $\mathcal{CP}$ observables fitted would be $\Re\left(\lambda_f\right)$ and $\Im\left(\lambda_f\right)$ which are related to the observables $\mathcal{A}_{CP}^{dir}$, $\mathcal{A}_{CP}^{int}$ and $\mathcal{A}_{\Delta\Gamma}$ by

$$\begin{aligned} \mathcal{A}_{CP}^{dir} &= \frac{1-\left|\lambda_f\right|^2}{1+\left|\lambda_f\right|^2}, \\ \mathcal{A}_{CP}^{int} &= \frac{-2\Im(\lambda_f)}{1+\left|\lambda_f\right|^2}, \\ \text{and} \quad \mathcal{A}_{CP}^{\Delta\Gamma} &= \frac{-2\Re(\lambda_f)}{1+\left|\lambda_f\right|^2}. \end{aligned} \tag{3.29}$$

In practise the values, uncertainties and correlations of $\mathcal{A}_{CP}^{dir}$ and $\mathcal{A}_{CP}^{int}$ would then be determined from $\Re\left(\lambda_f\right)$ and $\Im\left(\lambda_f\right)$ by some analytic procedure.

Theoretically the $\mathcal{CP}$ violating asymmetries $\mathcal{A}_{CP}^{dir}$ and $\mathcal{A}_{CP}^{int}$ allow the fixing of two contours (one each for the $\pm$ sign in the following equation) in the γ-a plane which are described by

$$a = \sqrt{\frac{1}{k}\left[l \pm \sqrt{l^2-hk}\right]}, \tag{3.30}$$

where

$$\begin{aligned} l \;=\; & 2 - \left\{\frac{\eta\,\mathcal{A}_{CP}^{int} - \sin\phi}{\eta\,\mathcal{A}_{CP}^{int}\,\cos\gamma - \sin\left(\phi+\gamma\right)}\right\}\left\{\frac{\eta\,\mathcal{A}_{CP}^{int} - \sin\left(\phi\,+\,2\gamma\right)}{\eta\,\mathcal{A}_{CP}^{int}\,\cos\gamma - \sin\left(\phi+\gamma\right)}\right\} \\ & - \left(\frac{\mathcal{A}_{CP}^{dir}}{\sin\gamma}\right)^2\left\{1 - \frac{\left(\eta\,\mathcal{A}_{CP}^{int} - \sin\phi\right)\cos\gamma}{\eta\,\mathcal{A}_{CP}^{int}\,\cos\gamma - \sin\left(\phi+\gamma\right)}\right\}\left\{1 - \frac{\left(\eta\,\mathcal{A}_{CP}^{int} - \sin\left(\phi\,+\,2\gamma\right)\right)\cos\gamma}{\eta\,\mathcal{A}_{CP}^{int}\,\cos\gamma - \sin\left(\phi+\gamma\right)}\right\}, \end{aligned} \tag{3.31}$$

$$h = \left\{\frac{\eta\,\mathcal{A}_{CP}^{int} - \sin\phi}{\eta\,\mathcal{A}_{CP}^{int}\,\cos\gamma - \sin\left(\phi+\gamma\right)}\right\}^2 + \left(\frac{\mathcal{A}_{CP}^{dir}}{\sin\gamma}\right)^2\left\{1 - \frac{\left(\eta\,\mathcal{A}_{CP}^{int} - \sin\phi\right)\cos\gamma}{\eta\,\mathcal{A}_{CP}^{int}\,\cos\gamma - \sin\left(\phi+\gamma\right)}\right\}^2 \tag{3.32}$$

and

$$k = \left\{\frac{\eta\,\mathcal{A}_{CP}^{int} - \sin\left(\phi\,+\,2\gamma\right)}{\eta\,\mathcal{A}_{CP}^{int}\,\cos\gamma - \sin\left(\phi+\gamma\right)}\right\}^2 + \left(\frac{\mathcal{A}_{CP}^{dir}}{\sin\gamma}\right)^2\left\{1 - \frac{\left(\eta\,\mathcal{A}_{CP}^{int} - \sin\left(\phi\,+\,2\gamma\right)\right)\cos\gamma}{\eta\,\mathcal{A}_{CP}^{int}\,\cos\gamma - \sin\left(\phi+\gamma\right)}\right\}^2 \tag{3.33}$$

A third contour can be plotted in the γ-a plane. This described by

$$a = \sqrt{\frac{H \; - \; 1 \; + \; u\,(1 \; + \; \epsilon H)\,\cos\gamma}{1 \; - \; v\,(1 \; + \epsilon H)\cos\gamma \; - \; \epsilon^2 H}} \tag{3.34}$$

where u and v are given by

$$u \; = \; \frac{\eta \mathcal{A}_{\Delta\Gamma} \; + \; \cos\phi}{\eta \mathcal{A}_{\Delta\Gamma}\cos\gamma \; + \; \cos\left(\phi \; + \gamma\right)} \qquad \text{and} \qquad v \; = \; \frac{\eta \mathcal{A}_{\Delta\Gamma} \; + \; \cos\left(\phi \; + \; 2\gamma\right)}{\eta \mathcal{A}_{\Delta\Gamma}\cos\gamma \; + \; \cos\left(\phi \; + \gamma\right)}. \tag{3.35}$$

In terms of the experimentally deduced parameters then H is given by

$$\epsilon\, H = \frac{\mathcal{A}_{CP}^{dir}(\mathrm{B_s^0} \to \mathrm{D_s^+ D_s^-})}{\mathcal{A}_{CP}^{dir}(\mathrm{B_d^0} \to \mathrm{D^+ D^-})}, \tag{3.36}$$

and as a theoretical parameterisation,

$$H = \frac{1 - 2\,a\,\cos\theta\,\cos\gamma \; + \; a^2}{1 + 2\,\epsilon a^{'}\cos\theta^{'}\cos\gamma \; + \; \epsilon^2 a^{'2}}. \tag{3.37}$$

The general expressions for the observables $\mathcal{A}_{CP}^{dir}$, $\mathcal{A}_{CP}^{int}$ and $\mathcal{A}_{\Delta\Gamma}$ in Equations 3.14, 3.15 and 3.16 and the theoretical parameterisation of H in Equation 3.37 simplify considerably if only terms which are linear in a and $a^{'}$ are kept. If U-spin symmetry holds then setting $a = a^{'}$ allows the approximate result

$$\tan\gamma \; \approx \; \frac{\sin\phi \; - \; \eta \mathcal{A}_{CP}^{int}}{(1 \; - \; H)\cos\phi} \; = \; \left(\frac{-\eta \mathcal{A}_{CP}^{int}}{1 \; - \; H}\right)\Bigg|_{\phi \,=\, 0}. \tag{3.38}$$

Equations 3.30 and 3.34 describe contours which may be plotted in the γ-a plane. If U-spin symmetry holds then $a = a^{'}$ in Equation 3.37 and the contours described by Equations 3.30 and 3.34 may be plotted in the same γ-a plane with the intersection of these contours fixing the values of both γ and a. Figures 3.3 and 3.4 show the γ-a plane with contours plotted using the values $a = 0.1$, $\theta = 210°$, $\gamma = 76°$, and the $\mathrm{B_d^0} - \overline{\mathrm{B_d^0}}$ mixing phase, $\phi_\mathrm{d} = 2\beta = 53°$ (Figure 3.3) or $127°$ (Figure 3.4) which is obtained from taking $\sin(2\beta) = 0.8$. On each figure, the two physical solutions of γ, $\gamma = 76°$ and $\gamma = 104°$, are shown. The fact that two values of γ are shown in each of Figures 3.3

and 3.4 is due to the two-fold ambiguity[a] in the extraction of 2β. It is thought that this two-fold ambiguity can be resolved in future experiments like LHCb.

In practise the contours in Figures 3.3 and 3.4 would appear as confidence region bands obtained by projecting the confidence regions from the space of the observables ($\mathcal{A}_{CP}^{dir}$, $\mathcal{A}_{CP}^{mix}$) to the corresponding space in the γ-a plane. However the experimental feasibility of determining γ from these channels is strongly dependent upon the size of the penguin contributions, the magnitude of which are difficult to predict theoretically.

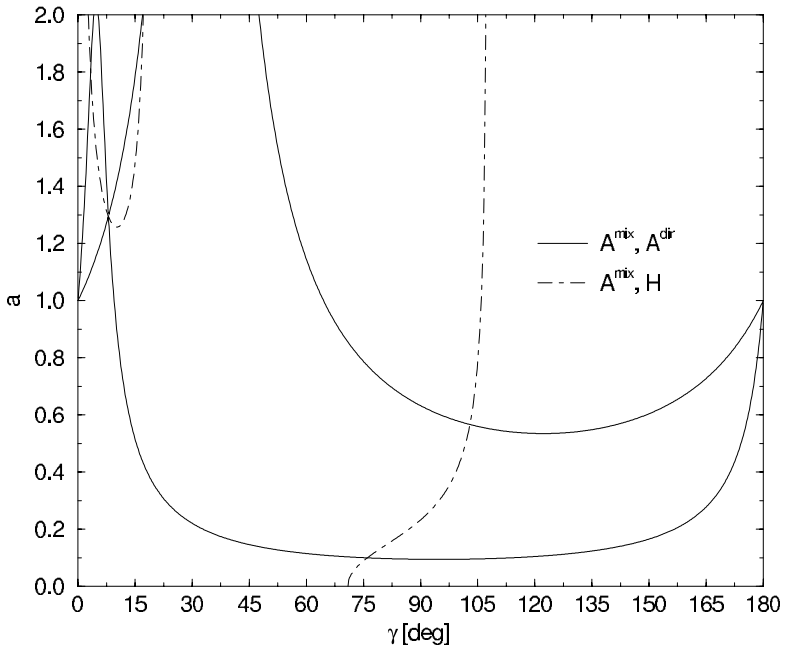

Figure 3.3: *Contours in the γ-a plane fixed through* $\mathrm{B}^0_{\mathrm{d(s)}} \to \mathrm{D}^+_{\mathrm{(s)}}\mathrm{D}^-_{\mathrm{(s)}}$ *with* $2\beta = 53^\circ$ *[73].*

[a]In any measured value of $\sin(2\beta)$ a discrete four-fold ambiguity for the extracted value of $\beta[\,0, 2\pi\,]$ remains. Current information on the CKM matrix elements reduces the allowed range, implying that 2β is in the first quadrant ($0 < \beta < \pi/4$) and reducing the four-fold ambiguity to a two-fold ambiguity.

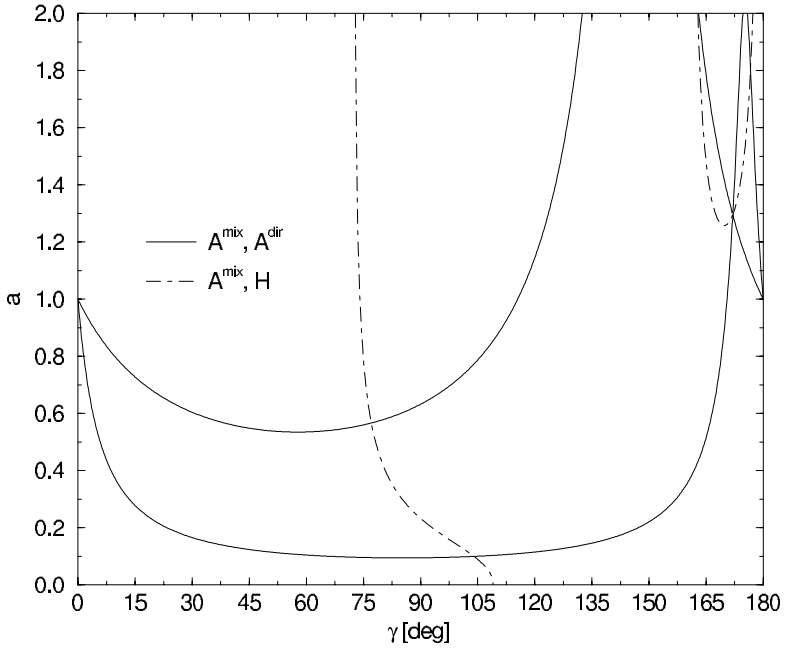

Figure 3.4: *Contours in the γ-a plane fixed through $B^0_{d(s)} \to D^+_{(s)}D^-_{(s)}$ with $2\beta = 127°$ [73]. The (solid line) contours in the γ-a plane related to Equation 3.30 are unaffected by U-spin symmetry breaking corrections where as the (dashed-dot line) contour described by Equation 3.34 relies on U-spin symmetry.*

3.4 Extracting γ from $B^+_c \to D^+_s\overline{D}^0$

It is proposed in [74] that the pure "tree" decays $B^\pm_c \to D^\pm_s D$ are suited to extract the CKM angle γ. Figures 3.5 and 3.6 show the Feynman diagrams contributing to the decays $B^+_c \to D^+_s D^0$ and $B^+_c \to D^+_s\overline{D}^0$. In order to make such a measurement, six decay amplitudes are needed: $B^+_c \to D^+_s D^0_+$, $B^+_c \to D^+_s D^0$, $B^+_c \to D^+_s\overline{D}^0$, $B^-_c \to D^-_s D^0_+$, $B^-_c \to D^-_s\overline{D}^0$ and $B^-_c \to D^-_s D^0$, where the $\mathcal{CP}$ eigenstate of the neutral D meson system D^0_+ is defined by

$$|\, D^0_+\rangle \;=\; \frac{1}{\sqrt{2}}\,(|\, D^0\rangle \;+\; |\,\overline{D}^0\rangle). \tag{3.39}$$

Experimentally this would be carried out in a similar manner to that of the $B^0_d \to D^0K^{*0}$ channel, studies of which are described in [80]. The $\mathcal{CP}$ eigenstate D^0_+ could be identified by its decay to K^+K^- or $\pi^+\pi^-$. The $D^0(\overline{D}^0)$ decays into $K^+\pi^-(K^-\pi^+)$ with the charge

of the kaon allowing the D^0 flavour to be tagged. $\mathcal{CP}$ Violation in the D system would be assumed to be negligible.

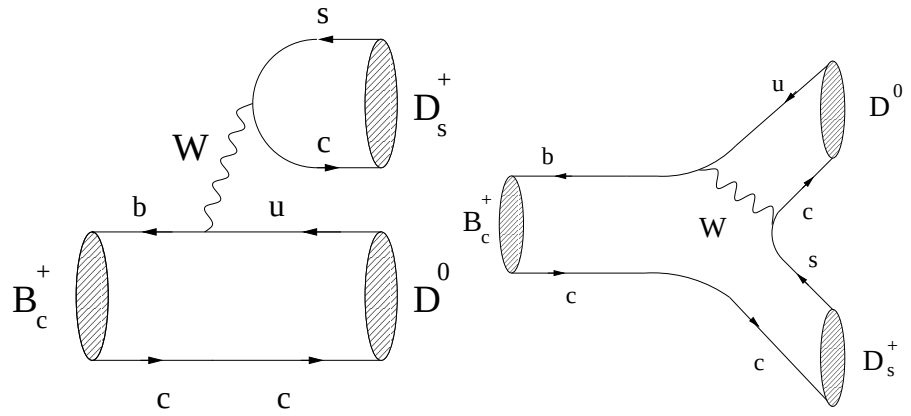

Figure 3.5: *Feynman diagrams contributing to the decay* $B_c^+ \to D_s^+ D^0$.

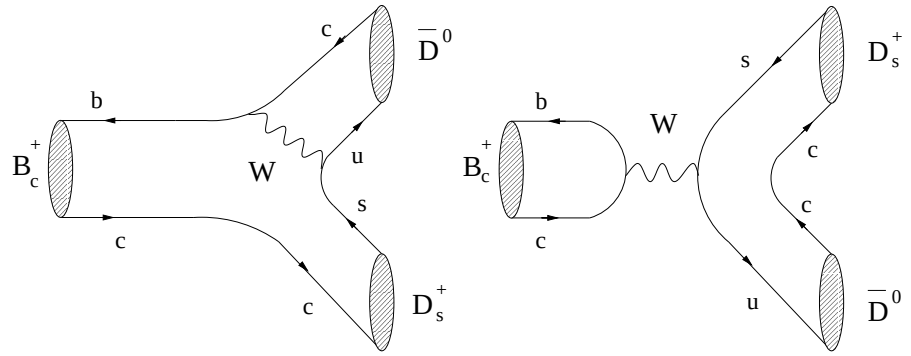

Figure 3.6: *Feynman diagrams contributing to the decay* $B_c^+ \to D_s^+ \overline{D}^0$.

For the decay $B_c^+ \to D_s^+ D_+^0$, two interfering amplitudes contribute. The first amplitude relation is

$$A(B_c^+ \to D_s^+ D_+^0) = \frac{1}{\sqrt{2}} \left[A\left(B_c^+ \to D_s^+ D^0\right) + A\left(B_c^+ \to D_s^+ \overline{D}^0\right) \right]. \tag{3.40}$$

Defining A_1, A_2 and $\frac{1}{\sqrt{2}}A_3$ as the magnitudes of the $B_c^+ \to D_s^+ D_+^0$, $B_c^+ \to D_s^+ D^0$ and $B_c^+ \to D_s^+ \overline{D}^0$ amplitudes then

$$A(B_c^+ \to D_s^+ D_+^0) = \frac{1}{\sqrt{2}} \left[A_1 + A_2 e^{i(\delta+\gamma)} \right] = \frac{1}{\sqrt{2}} A_3. \tag{3.41}$$

δ denotes the final state phase and the weak phase difference is the CKM angle γ. The second amplitude relation is given by the $\mathcal{CP}$ conjugate of the first amplitude relation.

$$\mathrm{A}(\mathrm{B}_\mathrm{c}^- \rightarrow \mathrm{D}_\mathrm{s}^- \mathrm{D}_+^0) \;=\; \frac{1}{\sqrt{2}} \left[\mathrm{A}\left(\mathrm{B}_\mathrm{c}^- \rightarrow \mathrm{D}_\mathrm{s}^- \mathrm{D}^0\right) \;+\; \mathrm{A}\left(\mathrm{B}_\mathrm{c}^- \rightarrow \mathrm{D}_\mathrm{s}^- \overline{\mathrm{D}}^0\right) \right]. \tag{3.42}$$

Again defining A_1, A_2 and $\frac{1}{\sqrt{2}}\mathrm{A}_4$ as the magnitudes of the $\mathrm{B}_\mathrm{c}^- \rightarrow \mathrm{D}_\mathrm{s}^- \mathrm{D}_+^0$, $\mathrm{B}_\mathrm{c}^- \rightarrow \mathrm{D}_\mathrm{s}^- \mathrm{D}^0$ and $\mathrm{B}_\mathrm{c}^- \rightarrow \mathrm{D}_\mathrm{s}^- \overline{\mathrm{D}}^0$ amplitudes then

$$\mathrm{A}(\mathrm{B}_\mathrm{c}^- \rightarrow \mathrm{D}_\mathrm{s}^- \mathrm{D}_+^0) = \frac{1}{\sqrt{2}} \left[\mathrm{A}_1 \;+\; \mathrm{A}_2 e^{i(\delta - \gamma)} \right] \;=\; \frac{1}{\sqrt{2}} \mathrm{A}_4. \tag{3.43}$$

Equations 3.40 to 3.43 have been written assuming that

$$\begin{aligned} \Gamma\left(\mathrm{B}_\mathrm{c}^+ \rightarrow \mathrm{D}_\mathrm{s}^+ \mathrm{D}_+^0\right) \;&\neq\; \Gamma\left(\mathrm{B}_\mathrm{c}^- \rightarrow \mathrm{D}_\mathrm{s}^- \mathrm{D}_+^0\right), \\ \Gamma\left(\mathrm{B}_\mathrm{c}^+ \rightarrow \mathrm{D}_\mathrm{s}^+ \mathrm{D}^0\right) \;&=\; \Gamma\left(\mathrm{B}_\mathrm{c}^- \rightarrow \mathrm{D}_\mathrm{s}^- \overline{\mathrm{D}}^0\right), \\ \Gamma\left(\mathrm{B}_\mathrm{c}^+ \rightarrow \mathrm{D}_\mathrm{s}^+ \overline{\mathrm{D}}^0\right) \;&=\; \Gamma\left(\mathrm{B}_\mathrm{c}^- \rightarrow \mathrm{D}_\mathrm{s}^- \mathrm{D}^0\right). \end{aligned} \tag{3.44}$$

$\Gamma\left(\mathrm{B}_\mathrm{c}^+ \rightarrow \mathrm{D}_\mathrm{s}^+ \mathrm{D}_+^0\right)$ and $\Gamma\left(\mathrm{B}_\mathrm{c}^- \rightarrow \mathrm{D}_\mathrm{s}^- \mathrm{D}_+^0\right)$ differ since they are expected to show $\mathcal{CP}$ violation. The two amplitude relations containing six decay amplitudes form two triangles. This is seen from the relations

$$\begin{aligned} \mathrm{A}_3^2 \;&=\; \mathrm{A}_1^2 \;+\; \mathrm{A}_2^2 \;+\; 2\mathrm{A}_1\mathrm{A}_2 e^{i(\delta + \gamma)}, \\ \mathrm{A}_4^2 \;&=\; \mathrm{A}_1^2 \;+\; \mathrm{A}_2^2 \;+\; 2\mathrm{A}_1\mathrm{A}_2 e^{i(\delta - \gamma)}, \end{aligned} \tag{3.45}$$

from which

$$\begin{aligned} \cos(\delta \;+\; \gamma) \;&=\; \frac{\mathrm{A}_3^2 \;-\; \mathrm{A}_1^2 \;-\; \mathrm{A}_2^2}{2\mathrm{A}_1\mathrm{A}_2}, \\ \cos(\delta \;-\; \gamma) \;&=\; \frac{\mathrm{A}_4^2 \;-\; \mathrm{A}_1^2 \;-\; \mathrm{A}_2^2}{2\mathrm{A}_1\mathrm{A}_2} \end{aligned} \tag{3.46}$$

These equations describe the two triangles shown in Figure 3.7.

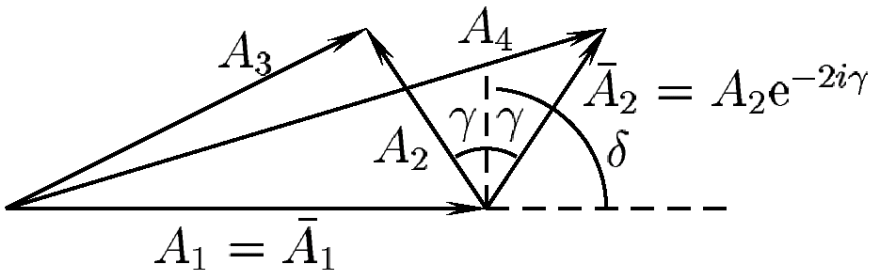

Figure 3.7: *The extraction of γ using the amplitude method.*

The amplitude (Equation 3.41) with the small CKM matrix element V_{ub} is not colour suppressed whereas the amplitude with the larger CKM matrix element V_{cb} is colour suppressed (Equation 3.43). This leads to the two amplitude relations in Equations 3.41 and 3.43 being of a similar magnitude. Therefore in the case of $B_c^{\pm} \rightarrow D_s^{\pm}\{D^0, \overline{D}^0, D_+^0\}$ decays, all the sides of the triangles in Figure 3.7 are of a similar size. Figure 3.8 shows how these two triangles are drawn for the $B_c^{\pm} \rightarrow D_s^{\pm}\{D^0, \overline{D}^0, D_+^0\}$ decays.

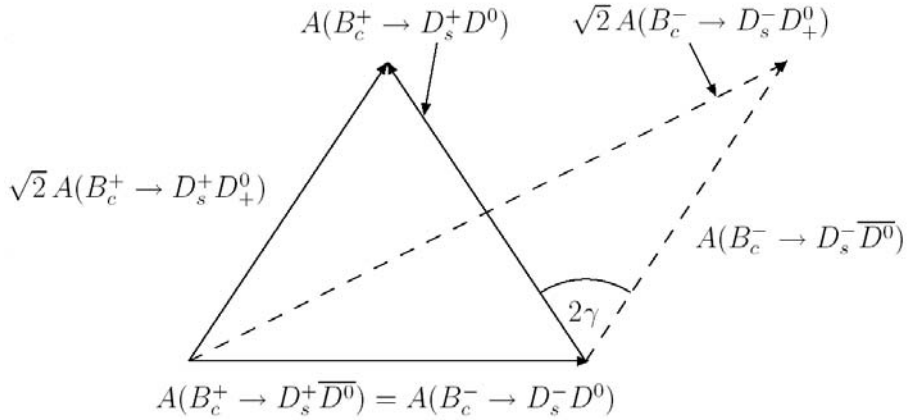

Figure 3.8: *The extraction of γ from $B_c^{\pm} \rightarrow D_s^{\pm}\{D^0, \overline{D}^0, D_+^0\}$ decays using the amplitude method.*

The relative orientation of the two triangles in Figure 3.8 are fixed via the relation

$$A(B_c^+ \rightarrow D_s^+ \overline{D}^0) \;=\; A(B_c^- \rightarrow D_s^- D^0). \tag{3.47}$$

The decay modes $B_c^+ \to D_s^+ D^0$ and $B_c^+ \to D_s^+ \overline{D}^0$ only receive contributions from tree-diagram-like topologies and only the $\overline{b} \to \overline{u}$ transition in Figure 3.5 involves γ in the Wolfenstein parametrisation of the CKM matrix (Equation 2.96). Theoretically this then should allow the CKM angle γ to be determined via the relationship

$$A(B_c^+ \to D_s^+ D^0) \;=\; e^{i2\gamma}\; A(B_c^- \to D_s^- \overline{D}^0). \tag{3.48}$$

3.5 Summary

Studies of the $B_d^0 \to D^+ D^-$, $B_s^0 \to D_s^+ D_s^-$ and $B_c^+ \to D_s^+ \overline{D}^0$ have been motivated by methods proposed by Fleischer and Wyler [73, 74] to determine the CKM angle γ which is expected to remain unmeasured, or known only with a large theoretical uncertainty until the start of the LHC in 2007. Methods which have been proposed to measure γ have been categorised into four groups; time-dependent asymmetries, time-integrated amplitude relations, isospin symmetry relations and U-spin symmetry relations.

The method proposed by Fleischer [73] to extract γ using $B_{d(s)}^0 \to D_{(s)}^+ D_{(s)}^-$ is one which depends upon U-spin symmetry relations. A similar method using the $B_{d(s)}^0 \to h^+h^-$ ($h = \pi$,K) channels has previously been studied [86] suggesting that should the event yields and background-to-signal (B/S) ratios be favourable in the $B_{d(s)}^0 \to D_{(s)}^+ D_{(s)}^-$ channels, these could prove to be both feasible and promising channels for γ studies at LHCb.

The theoretically clean method proposed by Wyler [74] is one which uses time-dependent amplitude relations and the $B_c^\pm \to D_s^\pm D$ channels to extract γ. A similar method has been successfully implemented as documented in [80]. However the B_c^+ estimated production fraction at the LHC of $<$1% (compared to $\sim$40% for both B_d^0 and B_s^0) may result in event yields that are too small and/or B/S ratios too large even after several years of data-taking to allow such a study to be carried out. In order to assess the potential for such studies Monte Carlo simulation studies of each of the $B_d^0 \to D^+ D^-$, $B_s^0 \to D_s^+ D_s^-$ and $B_c^+ \to D_s^+ \overline{D}^0$ channels have been carried out and the

results are presented in Chapters 6 to 8.

Chapter 4

The LHCb detector

In this chapter, the Large Hadron Collider (LHC) and the Large Hadron Collider Beauty Experiment (LHCb) for the precision measurements of $\mathcal{CP}$ violation and the study of rare decays will be introduced. Each of the LHCb sub-detector components will be described. Within section 4.4, the emphasis is placed upon describing the Ring Imaging Cherenkov (RICH) detectors as this is relevant for the work presented in Chapters 5 to 8.

4.1 The LHC

LHCb [69, 70], is one of the five planned experiments at the CERN LHC pp collider. LHCb is to be constructed at interaction point (I.P.) 8 in the LHC ring which until recently, was occupied by the LEP DELPHI experiment. Also at the LHC there will be two multi-purpose experiments; ATLAS [88] and CMS [89], and the heavy ion experiment ALICE [90], to be located at interaction points 1, 5 and 2 respectively. The location of these experiments are shown in Figure 4.1. The fifth experiment, TOTEM which is also located at I.P. 5, is designed to measure the total cross section, elastic scattering and diffractive processes at the LHC [91]. The LHC will start operating in 2007.

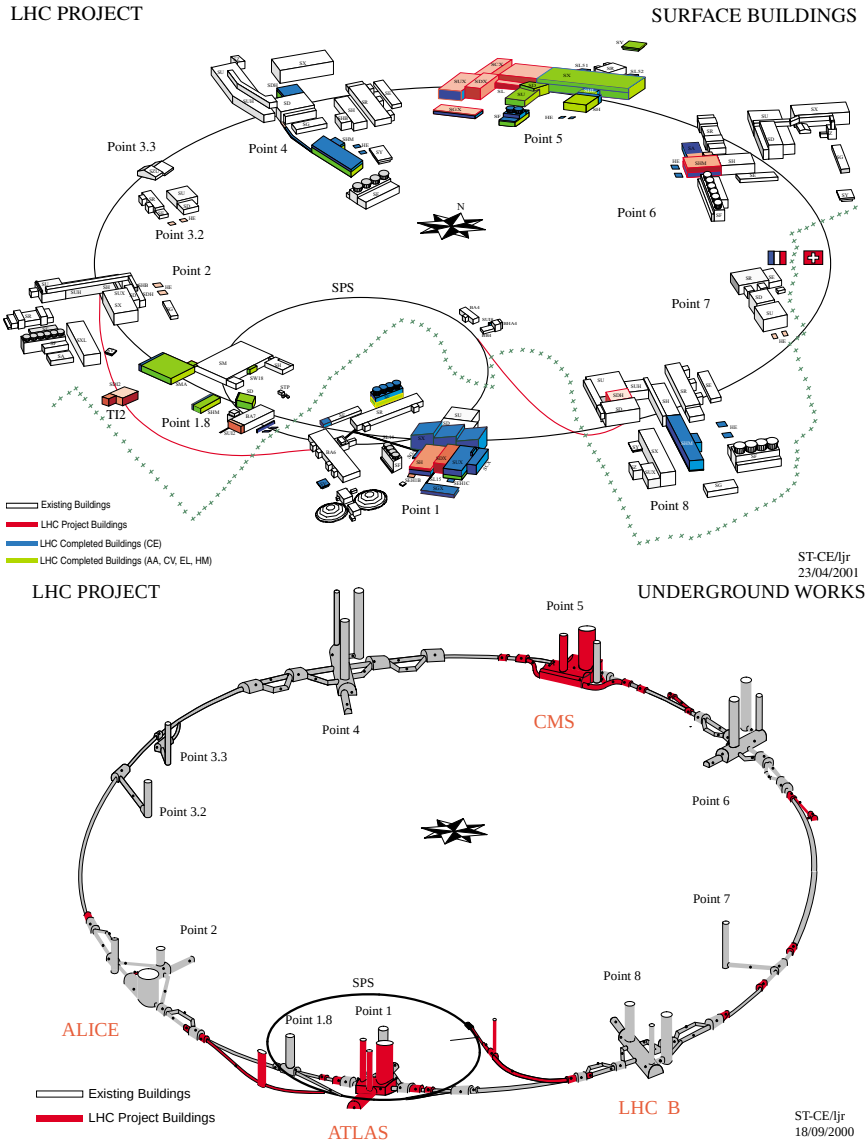

Figure 4.1: *Schematic diagrams of the LHC accelerator ring at the surface and underground. The general purpose experiments ATLAS and CMS are located at interaction points 1 and 5, the heavy ion experiment ALICE is located at interaction point 2, and the LHCb experiment is located at interaction point 8. TOTEM is also located at interaction point 5. Two bunches of protons will be accelerated progressively to 7 TeV in CERN's chain of accelerators, of which only the two largest, the SPS (Super Proton Synchrotron) and the LHC are shown.*

At the LHC, bunches of protons will be collided with a centre-of-mass energy of $\sqrt{s} = 14$ TeV[a] and an inelastic pp cross-section, $\sigma_{\text{inelastic}}$ of ~80 mb [69]. In each of the two LHC rings, there will be 2808 bunches with 1.1×10^{11} protons per bunch, at a bunch spacing of 7.48 m and at a bunch separation of 24.95 ns [92].

The LHC will take three years to reach its design luminosity of $10^{34}\,\text{cm}^{-2}\text{s}^{-1}$ from a starting luminosity of $10^{33}\,\text{cm}^{-2}\text{s}^{-1}$. However, the luminosity at LHCb will be locally controlled by defocussing the beams at the LHCb interaction point such that it will have a mean value of $\mathcal{L}_{av} = 2 \times 10^{32}\,\text{cm}^{-2}s^{-1}$[b]. The choice of $2 \times 10^{32}\,\text{cm}^{-2}\text{s}^{-1}$ as the LHCb design luminosity is motivated by the following.

The number of pp interactions occurring in a given bunch crossing n, follows the Poisson distribution

$$P(\mu, n) = \frac{\mu^n}{n} e^{-\mu}, \tag{4.2}$$

where μ denotes the average number of pp interactions (known as collisions) per pp bunch crossing. μ is described by the following equation,

$$\sigma_{\text{inelastic}} = \mathcal{L} \cdot f_{LHC} \cdot \epsilon_{filled} \cdot \mu, \tag{4.3}$$

where $\sigma_{\text{inelastic}}$ denotes the inelastic $b\bar{b}$ cross-section, $\mathcal{L}$ is the integrated luminosity[c], f_{LHC} is the LHC pp bunch crossing frequency of 40 MHz, and $\epsilon_{filled} = 0.744$ is the fraction of non-empty bunch crossings.

Figure 4.2 shows the probability as a function of LHC luminosity, of the proportion of events with $n = 0$, 1, 2, 3 and 4 pp interactions per pp bunch crossing. In order that decay distances of the B mesons may be measured accurately, it is important that

[a] In a pp collider, the actual centre-of-mass energy, $\sqrt{s'}$ is given by

$$\sqrt{s'} = x_1 \cdot x_2 \sqrt{s} \tag{4.1}$$

where x_1 and x_2 are the fraction of momenta carried by the interacting partons, and $\sqrt{s} = 14$ TeV.

[b] The luminosity is assumed to decrease exponentially with a 10 hour luminosity lifetime during the course of 7-hour fills with an average value of $2 \times 10^{32}\,\text{cm}^{-2}\text{s}^{-1}$, which implies that the luminosity $\sim 2.8(1.4) \times 10^{32}\text{cm}^{-2}\text{s}^{-1}$ at the start(end) of the fill.

[c] $\mathcal{L} = \int L(t)\,dt$ where $L(t)$ is the instantaneous luminosity at time t.

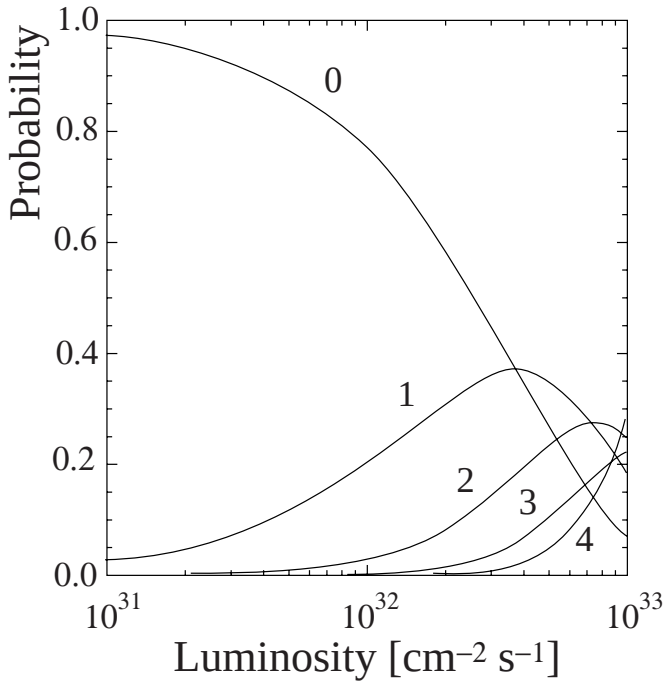

Figure 4.2: *Probability distribution as a function of LHC luminosities for the proportion of events with 0,1,2,3 and 4 interactions(inelastic collisions) per bunch crossing, assuming an inelastic* $\mathrm{b\overline{b}}$ *cross-section of* $\sigma_{\mathrm{inelastic}} = 80$ *mb. [93]*

the primary vertex co-ordinates are determined to the best precision possible. This is best achieved in events which have only a single interaction ($n = 1$). From Figure 4.2, assuming that $\sigma_{\mathrm{inelastic}} = 80$ mb, then the probability of this is greatest when the LHCb luminosity is $\sim 4 \times 10^{32}\mathrm{cm}^{-2}\mathrm{s}^{-1}$. However, running at this luminosity coincides with increasing numbers of multiple interactions ($n > 1$). The compromise solution is to run at $2 \times 10^{32}\,\mathrm{cm}^{-2}\mathrm{s}^{-1}$ which means that the detector occupancies in the tracking detectors will be lower and radiation damage (particularly in the VELO) will be reduced. The LHCb sub-detectors and the data-acquisition system have been designed to cope with luminosities up to $5 \times 10^{32}\,\mathrm{cm}^{-2}\mathrm{s}^{-1}$.

4.2 Bottom Production at the LHC

In pp collisions, $b\bar{b}$ pairs are produced by flavour creation, splitting or excitation as shown in Figure 4.3.

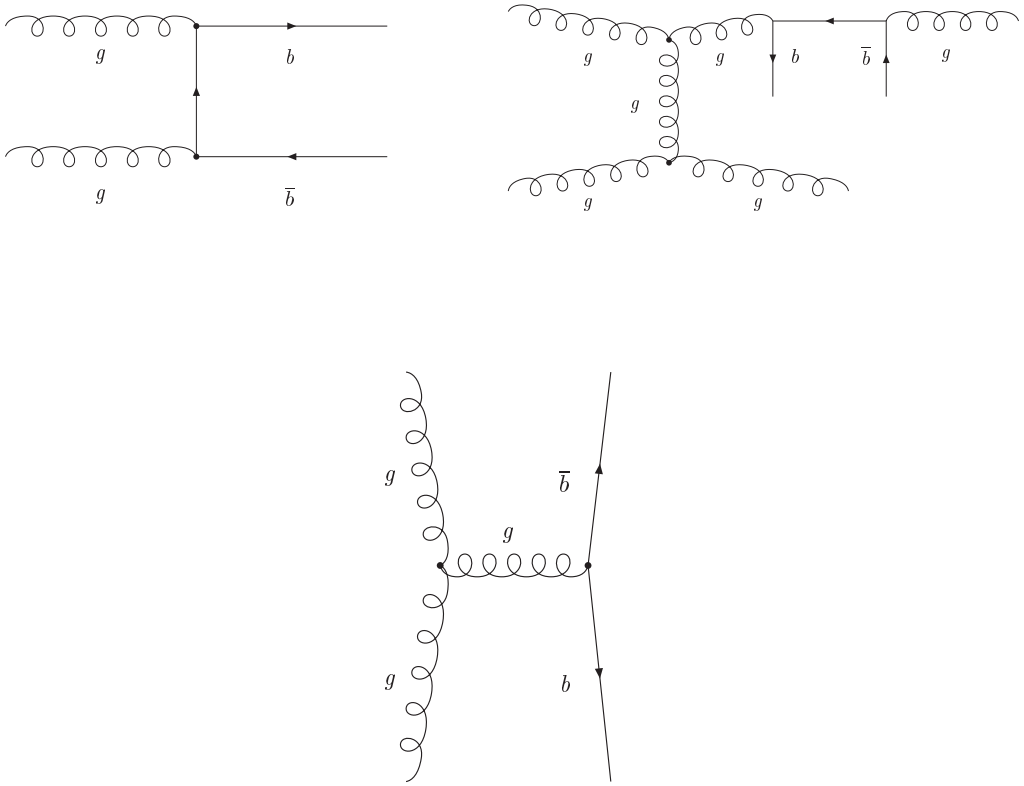

Figure 4.3: *Feynman diagrams of the dominant* $b\bar{b}$ *production mechanisms at lowest order* (α_s^2)*(left to right : creation, splitting and excitation). Light partons within the incoming protons collide and produce the heavy quark-antiquark* $b\bar{b}$ *pair via elementary strong interaction vertices [94].*

At LHC energies, the parton distribution functions of the proton (quark or gluon) are such that it is most likely that partons with very different momenta interact. This results in both the b and the $\bar{b}$ being predominantly produced in the same forward cone, as shown in Figure 4.4 and that the B-hadrons are highly boosted at production. This "forward cone" polar angle distribution motivates the design of the LHCb detector,

which is described in Section 4.3.

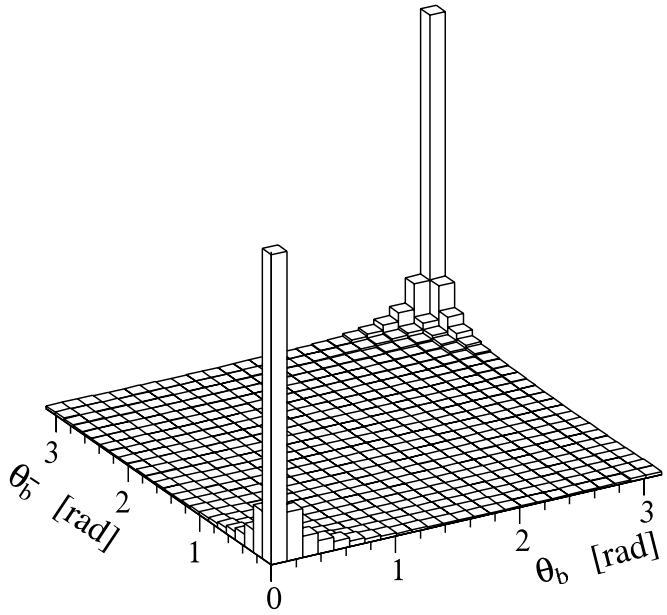

Figure 4.4: *The polar angle (θ) distribution of* b *and* $\overline{\text{b}}$ *hadrons due to a* $\sqrt{s}$ *= 14 TeV pp interaction as calculated by the PYTHIA event generator [69, 95]. The polar angle is the angle between the particle track and the beam line in the particle centre-of-mass frame.*

The expected cross-section for the production of $\text{b}\overline{\text{b}}$ pairs at the LHC is $\sigma_{\text{b}\overline{\text{b}}} = 500\,\mu\text{b}$ providing 10^{12} $\text{b}\overline{\text{b}}$ pairs produced per year (10^7 s) of running at the LHCb mean luminosity value $\mathcal{L}_{av}$. The LHC will also be a source of the full spectrum of B-hadrons, $\text{B}^{\pm}$, B^0_{d}, B^0_{s} and $\text{B}^{\pm}_{\text{c}}$, Λ_{b} and others, enabling LHCb to measure $\mathcal{CP}$ violating observables with high statistics in many different decay channels.

Forward versus Central Geometry

The relatively low luminosity of the first three years of LHC, as discussed earlier, will allow the ATLAS and CMS experiments to carry out most of their B-physics programme. The achievable precision will be better than in the e^+e^- B-factories and at the Tevatron, and even in a few cases competitive with LHCb. This is however strongly dependent on the success of the trigger strategies adopted by ATLAS and CMS. The most obvious difference between the three detectors is that ATLAS and CMS are central detectors

while LHCb is a forward detector. It should be emphasised that although the LHCb detector is the only LHC detector which is specifically optimised for B physics, there are several issues for which either forward or central geometry has an advantage. The forward geometry is able to utilise the correlated $b\bar{b}$ production which peaks in the forward and backward cone. However the minimum bias events will also peak in the same forward and backward cone, the presence of which will be minimised at LHCb by dedicated high p_T triggers.

Figure 4.5 is a plot of b hadron pseudorapidity η versus the b hadron transverse momentum p_T. The p_T-η ranges covered by the ATLAS/CMS experiments compared to that covered by LHCb are shown. The pseudorapidity η is defined as

$$\eta = -\ln(\tan\theta/2)\,, \tag{4.4}$$

where θ is the polar angle relative to the beam line.

By design, the forward geometry is much more open, simplifying the mechanical design and maintenance requirements of LHCb compared to that at ATLAS or CMS. LHCb will be able to obtain much better vertex resolution than the central detectors since the forward geometry allows the vertex detector to be placed much closer to the interaction point than it would in a central geometry configuration. Neither ATLAS or CMS have dedicated detectors for hadron identification although a limited π/K separation will obtained by using the dE/dx energy loss in the ATLAS straw tracker.

Just for comparison, the BTeV experiment at Fermilab, also with a forward detector geometry, was approved as a single-arm spectrometer in 2002 [32]. It is planned to run at a luminosity of between 1.3 - 2×10^{32} cm^{-2}s^{-1} but with an increased bunch-spacing (decreased bunch crossing frequency) of between 132-396 ns resulting in 2-6 interactions per bunch-crossing. Since the Tevatron operates at a collision energy of 2 TeV, then the $b\bar{b}$ cross-section would be a factor of five smaller than that of LHCb ($\sigma_{b\bar{b}} \approx 100\ \mu$b).

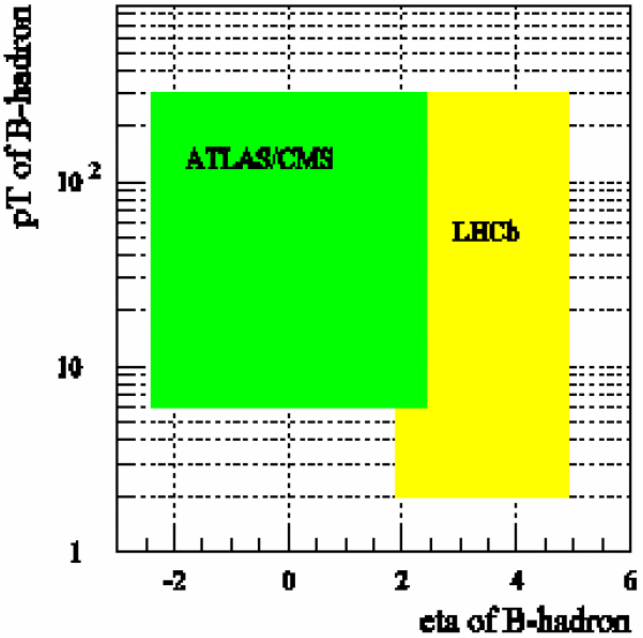

Figure 4.5: *B-hadron pseudorapidity η, versus B-hadron transverse momentum p_T, showing the p_T-η ranges covered by the ATLAS and CMS experiments compared to that covered by LHCb. ATLAS and CMS are so-called "central-coverage" detectors and cover the pseudorapidity range $|\eta| < 2.5$, whereas LHCb is a "forward-coverage" detector, and covers the pseudorapidity range $\sim 1.9 < \eta < 4.9$ [96].*

4.3 LHCb

LHCb is a single-arm spectrometer covering the forward region for pp interactions. The detector covers the polar angle range $\theta = 10$ mrad up to 300 mrad in the x-z plane[d], and from 10 mrad up to 250 mrad in the y-z plane. Figure 4.6 is a plan view of the LHCb detector in the y-z plane with the main sub-detector components labelled.

The features of the LHCb detector which are in particular optimised for a B physics environment are:

[d]LHCb uses a right handed coordinate system with the z axis pointing from the interaction point toward the muon chamber along the beam line. The y-axis is pointing upward. The $x(y)$-z plane is also referred to as the horizontal (vertical) plane. The magnet (described later in Section 4.7.1) is orientated so that the charged tracks are curved in the x-z plane (therefore also known as the bending plane), but not curved in the y-z plane (non-bending plane).

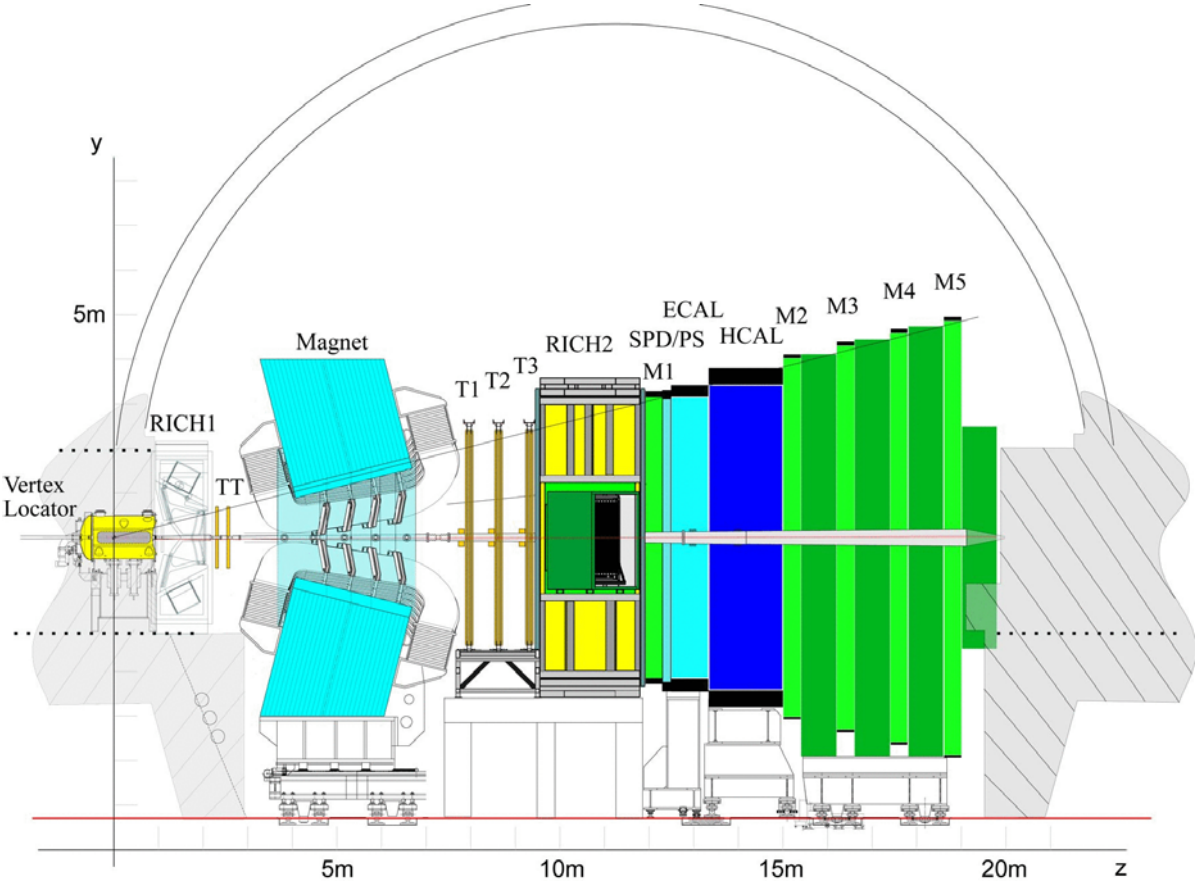

Figure 4.6: *y-z plane view of the LHCb detector. The main sub-detector components are labelled - these are the Vertex Locator (VELO), the two RICH counters (RICH-1 and RICH-2), the four tracking stations (TT and T1-T3), the magnet, the Scintillating Pad Detector (SPD), PreShower (PS). Electromagnetic (ECAL) and Hadronic (HCAL) Calorimeters, and the five muon stations (M1-M5).*

- **Vertexing and decay time resolution:** Excellent time resolution is required for studying the rapidly oscillating B_s mesons, and in particular their $\mathcal{CP}$ asymmetries. Good vertex reconstruction is a fundamental requirement since displaced secondary vertices are a distinctive feature of b-hadron decays.

- **Precise mass reconstruction:** This is required in order to reject so-called combinatorial background - background due to random combinations of tracks. Precise mass reconstruction requires that the tracks should be reconstructed with a good momentum resolution.

- **Particle Identification:** This can be subdivided into two categories, that of hadron (π/K) identification and lepton (e/μ) identification:
  - Hadron identification is required for kaon tagging and also to discriminate between many different decay modes which have almost identical topologies and which are useful for measuring different $\mathcal{CP}$ physics parameters. For example,
    - Reconstructed $B^0_d \to \pi^+\pi^-$ decays which are used to measure the unitarity triangle α are heavily contaminated by $B^0_d \to K^\pm\pi^\mp$, $B^0_s \to K^\mp\pi^\pm$ and $B^0_s \to K^\pm K^\mp$ decays;
    - Reconstructed $B^0_s \to D^\pm_s K^\mp$ decays which are used to measure the unitarity angle χ, where the main background comes from $B^0_s \to D^\pm_s\pi^\mp$ with a branching fraction $\sim$10 times larger than that of $B^0_s \to D^\pm_s K^\mp$. $B^0_s \to D^\pm_s\pi^\mp$ can itself be used to measure the B^0_s mixing parameter Δm_s.
  - Lepton identification is used in the Level-0 trigger and for the tagging of semi-leptonic decays.
- **Triggering:** A high-performance trigger is needed which is able to distinguish minimum bias events from events with B mesons. This is achieved by triggering on particles with large transverse momentum and displaced decay vertices.

Detector Reoptimisation

The LHCb detector underwent an extensive reoptimisation phase during 2001-2003, and hence there are some significant changes from the LHCb detector described in the Technical Proposal of 1998 [69]. These changes are described in the "Reoptimised LHCb Detector Design and Performance" Technical Design Report [70] which was completed in September 2003. The LHCb detector, as described in [69], is shown in Figure 4.7. The reasons for reoptimisation and a brief summary of changes due to the reoptimisation procedure, are given below.

There were two objectives in reoptimising the LHCb detector. The first was to reduce the amount of material in the detector, and the second was to improve the

trigger performance.

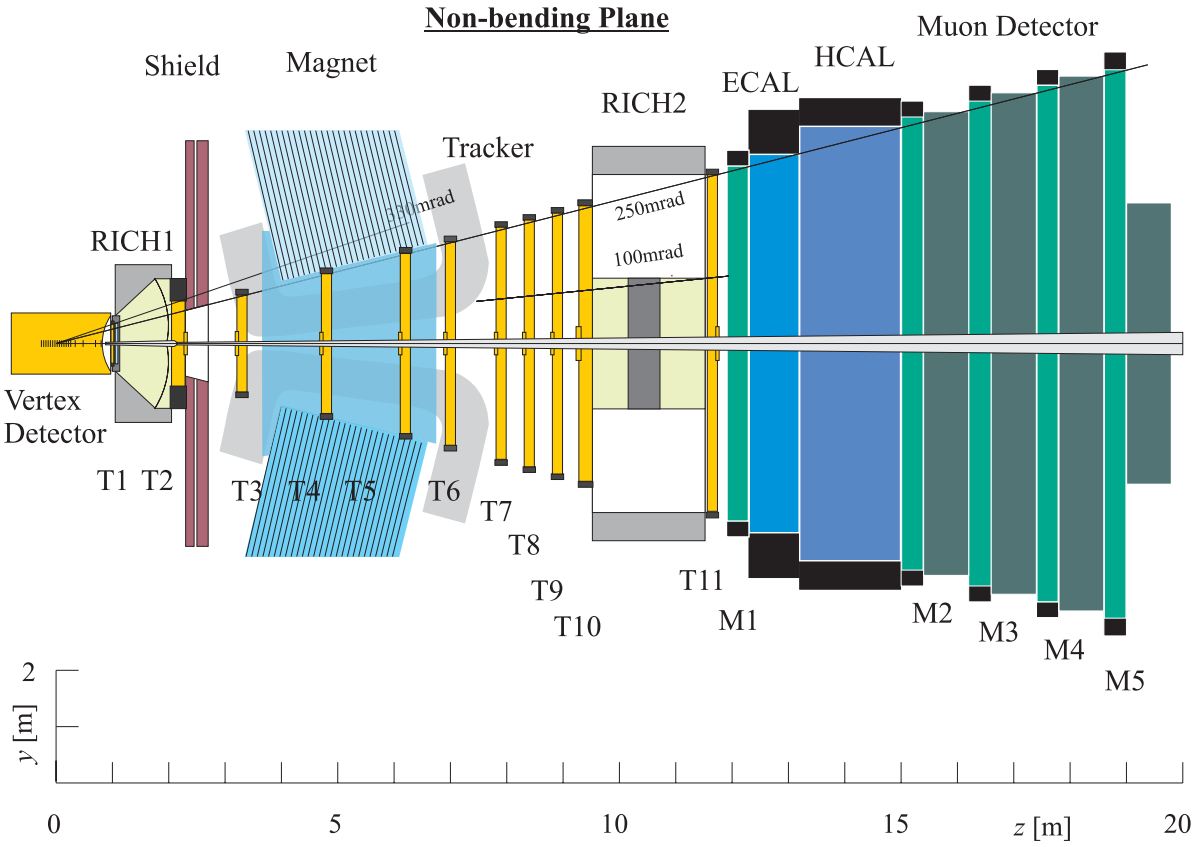

Figure 4.7: *y-z plane view of the LHCb detector, as of the LHCb Technical Proposal (2000) [69].*

- **Reduction of material budget:** As of the Technical Proposal in 1998 [69], the material budget up to the RICH-2 detector was $0.4X_0$ ($0.1\lambda_0$) where X_0 and λ_0 are the total radiation and interaction lengths respectively of the whole detector. This was found to have increased to $0.6X_0$ ($0.2\lambda_0$) by late 2001 as the detector design and accompanying software framework became more realistic. The presence of additional material deteriorates the detection capability of $e^{\pm}$ and γ, increases the occupancies of the tracking stations, and increases the amount of multiple scattering of charged particles. The increase in X_0 before RICH-2 meant that more kaons and pions would interact before traversing all of the tracking stations, resulting in a decrease in the track reconstruction efficiency and especially affect

the physics performance in decay channels with high-multiplicity final states.

- **Improvement of trigger:** It was realised that the performance of the trigger could be made more robust by adding p_T information to tracks with a large impact parameter. This could be achieved by associating the high-p_T calorimeter clusters and muons found at Level-0 to the tracks found in the VELO.

Some of the changes made due to the reoptimisation can be seen pictorially in the differences between Figures 4.6 and 4.7. Note that prior to the start of the reoptimisation procedure, the tracking stations labelled as T4 and T11 in Figure 4.7 had already been removed from the design for reasons of redundancy.

- **Reduction of material budget:** In each of the VELO, beam-pipe and RICH-1, lighter materials have been used. In the VELO, the thickness of the Si sensors (300 to 200μm) and the number of stations (25 to 21) has been reduced, the first section of the beam pipe is now made from beryllium (Be) instead of a Be-Al alloy and the RICH-1 mirrors are now constructed from a carbon composite.

- **Removal of the magnetic shield:** The shielding plate shown in Figure 4.7 was designed to shield RICH-1 and the Vertex Detector from the magnetic field. Removing this shield now allows the B-field to extend to the Vertex Detector and therefore provide p_T information to the trigger.

- **Reorganised tracking strategy:** Referring to the notation in Figure 4.7, T1 was removed, T2 is now called TT (Trigger Tracking station, described in Section 4.6.2.1) and T3, T5 and T6 have been removed. Downstream of the magnet, stations T7 to T10 were replaced by new stations known as T1 to T3, with the new T1 and T3 located at the positions of T7 and T10, and the new T2 located halfway between T1 and T3.

From the above list, there appear to have been many changes to the LHCb detector during the reoptimisation period. However, unless explicitly mentioned, the chosen technologies for the different components of the detector have remained the same.

The remainder of this chapter describes the reoptimised LHCb detector as illustrated in Figure 4.6. For organisational purposes, the components of the detector are sub-divided into four categories; particle identification, tracking, trigger and other components (e.g. beam pipe, magnet and computing). These are discussed in turn in Sections 4.4, 4.5, 4.6, and 4.7 respectively. Each of the detector components are discussed in detail in their respective Technical Design Reports [97–105].

4.4 Particle Identification

In LHCb, particle identification is required over a wide momentum range for many different types of particles. It is provided by the electromagnetic calorimeter (ECAL) for electrons, photons and π^0s, the hadronic calorimeter (HCAL) for hadrons, the Ring-Imaging-Cherenkov (RICH) system for π/K separation, and the muon system. Each of these sub-detectors are now discussed in turn.

4.4.1 Muon detector

The muon system [100] is used to provide muon identification in event reconstruction, muon information for the high p_{T} Level-0 trigger and the suppression of the muon background in many B-decays of interest to LHCb. For example, the decays $\mathrm{B}^0_{\mathrm{d}} \to J/\psi(\mu^+\mu^-)\mathrm{K_S}$, $\mathrm{B}^0_{\mathrm{s}} \to J/\psi(\mu^+\mu^-)\phi$ and $\mathrm{B}^0_{\mathrm{s}} \to \mu^+\mu^-$. Background muons arise from four processes; muons produced by the decay of pions and kaons, muons produced in hadronic showers, low-energy electrons produced in the calorimeters and the muon system, and muons from the beam halo [100]. Of these, muons produced in pion and kaon decays dominate.

The muon system consists of five multi-wire proportional chamber (MWPC) stations known as M1-M5, which are placed along the beam axis at increasing z away from the interaction point. The first station (M1) is placed in front of the calorimeter system and is specifically used to provide a high p_{T} measurement which is then used in the Level-0

trigger. The other stations (M2-M5) are located downstream of the calorimeters and are interleaved with three iron filters which attenuate all photons, hadrons, electrons and are used to suppress the muon backgrounds previously listed. Downstream of station M5 is a steel plate which acts to protect the last detector station from particles emerging from the LHC tunnel.

4.4.2 Calorimeters

The LHCb calorimeter system consists of a scintillator pad detector (SPD), a PreShower detector (PS), an electromagnetic calorimeter (ECAL), and a hadron calorimeter (HCAL), each of which is divided into regions with different cell sizes. This lateral segmentation as illustrated in Figure 4.8, increases in number (decreases in cell size) closer to the beam line corresponding to the expected increase in particle flux in this region. A complete description of the calorimeter system is found in the calorimeter TDR [98].

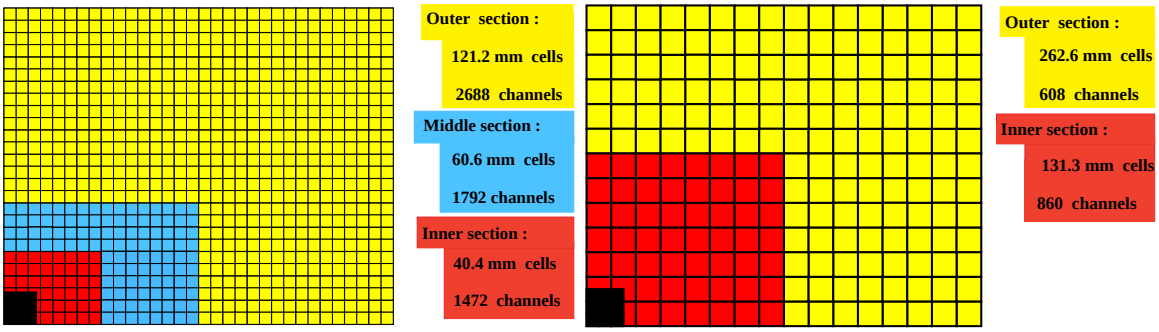

Figure 4.8: *Lateral segmentation of the SPD, PS and ECAL cells and lateral segmentation of the HCAL. In both figures, one quarter of the detector front face is shown.*

The purpose of the calorimeter system is to provide identification of hadrons (including neutral pions), electrons and photons, and the measurement of their energies and positions. This information is used in the L0 trigger (as described in Section 4.5), offline analysis, and also for the reconstruction of electrons, neutral pions and photons.

The first elements of the calorimeter system are the SPD and the PS. A particle

entering the calorimeter system first encounters an SPD which registers the presence of charged particles. This is followed by the PS which consists of 12 mm of lead followed by a second 10 mm-thick SPD which detects showering from electromagnetic particles ($e^{\pm}$ and γ). In both cases the SPD's are divided into three regions of different cell granularity to maintain low detector occupancy. Wavelength shifting (WLS) fibres transport the photons from the scintillator to the photodetectors. The baseline photodetector is the 16-pixel Hamamatsu H6568 photomultiplier. The function of the PS is to discriminate between $e^{\pm}$ and photons and reject background from pions. This is achievable knowing that photons deposit much more energy in the second SPD than in the first, and that hadronic particles deposit little energy in either the SPD or the PS.

Following the PS and SPD is the electromagnetic calorimeter (ECAL) which will be built using the Shashlik[e] design of 66 alternating 4 mm-thick scintillator/2 mm-thick lead block cells with, as in the case of the PS/SPD, WLS fibres transporting the scintillator photons to photo-multipliers at the rear of the structure. The electromagnetic particles ($e^{\pm}$,γ) shower in the ECAL whereas the hadrons (e.g. pions and protons) will shower later in the HCAL. This electromagnetic showering provides an energy measurement of the showering particle, and in conjunction with the PS/SPD, is then used to provide p_T information for the Level-0 trigger.

The expected energy resolution of the ECAL over the range 1 up to 200 GeV/c^2 is given by

$$\frac{\sigma(E)}{E} = \frac{10\%}{\sqrt{E\ (GeV)}} \oplus 1.5\% \tag{4.5}$$

where the first term is a statistical term coming from fluctuations in the shower creation process, and the second term is systematic in origin. This is in comparison to the expected energy resolution of the hadron calorimeter (HCAL), which is given by

$$\frac{\sigma(E)}{E} = \frac{80\%}{\sqrt{E\,(GeV)}} \oplus 5\%. \tag{4.6}$$

The HCAL searches for high p_{T} hadrons which are used in the Level-0 trigger. It is

[e]So named because the scintillator tiles are pierced by the WLS fibres as on a skewer.

constructed from scintillator tiles placed parallel to the beam direction and embedded in an iron structure, with on average 4 mm scintillator thickness for every 16 mm of iron. As is the case for the PS/SPD and ECAL, to maintain a low occupancy, the HCAL has cells of different sizes. This is illustrated in Figure 4.8. Again, as for the ECAL, scintillator photons are collected with WLS fibres to photomultiplier tubes.

4.4.3 Ring Imaging Cherenkov (RICH) Detectors

The role of the Ring Imaging Cherenkov (RICH) detectors in LHCb is that of particle identification, in particular π/K separation. There are two RICH detectors in LHCb, referred to as RICH-1 and RICH-2. Particles with momentum up to $\sim$60 GeV/c are identified by the RICH-1 detector which is located downstream of the magnet. As mentioned in Section 4.3, RICH-1 was redesigned as part of the reoptimisation procedure, and so differs significantly from that described in the RICH TDR (2000) [99]. An addendum to the RICH TDR was recently published and described in detail the redesigned RICH-1 [106]. The RICH-2 detector covers higher momentum particles, up to $\sim$100 GeV/c and differs little from that described in the RICH TDR. A more recent and detailed description of RICH-2 is found in the RICH-2 Engineering Design Review Report (EDR) [107]. Before the RICH-1 and RICH-2 detectors are described in detail, the physics of Cherenkov radiation, and the principles behind the RICH detector are introduced.

4.4.3.1 Cherenkov Radiation

Cherenkov Radiation is an effect discovered by P.A Cherenkov in 1934 while studying the effects of gamma rays on liquids [108,109] and was subsequently explained in 1937 by I.E. Tamm and I.M. Frank [110]. Experimental verification soon followed in 1938 [111] and again in 1943 [112].

When a charged particle passes through an optical medium of refractive index n at

a velocity v, then the surrounding atoms polarise and subsequently depolarise causing a weak electromagnetic wave to spread out from the instantaneous position of the particle. If the particle is travelling at a velocity v greater than the local speed of light ($v > c/n$), then the wave-fronts originating at different times can overlap constructively leading to a significant observable signal. This is illustrated in Figure 4.9. The necessary condition $v > c/n$ implies that $\beta n > 1$, where $\beta = v/c$.

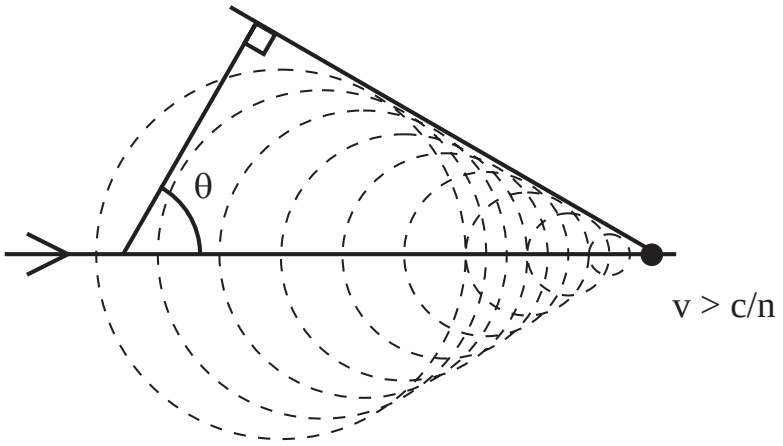

Figure 4.9: *Huygens construction for the Cherenkov radiation emitted by a particle travelling with a velocity v greater than c/n, the speed of light in the medium.*

The Huygens construction of Figure 4.9 implies that for $\theta = \theta_c$ then

$$\cos\,\theta_c = \frac{1}{\beta n} \tag{4.7}$$

where θ_c is the polar angle (Cherenkov angle) at which photons are radiated relative to the particle direction. The azimuthal emission angle ϕ has a flat distribution between 0 and 2π. The photon emission probability is uniform along the particle's track and the energy radiated per unit length is given as a function of the angular frequency of the radiated light ω,

$$\frac{dE}{dl} = \frac{e^2}{c^2}\int (1 - \frac{1}{(\beta n(\omega))^2})\;\omega\;.\;d\omega. \tag{4.8}$$

When calculating the expected number of photoelectrons from a radiating particle, then the following experimental parameters must be considered: the assumed coverage of the

photodetector active area (G), the transmission efficiency of the radiator (T) and the photodetector quantum efficiency (Q). These parameters are related via

$$N_{\text{photoelectrons}} = \left(\frac{\alpha}{\hbar c}\right)\ L\ G \int (1 - \frac{1}{(\beta n(E))^2})\ T(E)\ Q(E)\ .\ dE \tag{4.9}$$

where α is the fine structure constant and L is the radiator length in centimetres. $\alpha/\hbar c$ is a constant with the value 370 $\text{eV}^{-1}\text{cm}^{-1}$. Assuming that n is constant, then the number of photoelectrons expected per particle is

$$N_{\text{photoelectrons/particle}} = 370\ L\ \sin^2\theta_{\text{c}}\ G \int\ T(E)\ Q(E)\ .\ dE. \tag{4.10}$$

4.4.3.2 RICH detectors

The first RICH detector was demonstrated in 1977 using mirror focusing and gas phase ionisation detectors [113]. All RICH counters built for particle physics experiments, for example DELPHI, WA89 and HERA-B, have since followed a similar design [114–116]. The basic principle of a RICH detector is illustrated in Figure 4.10.

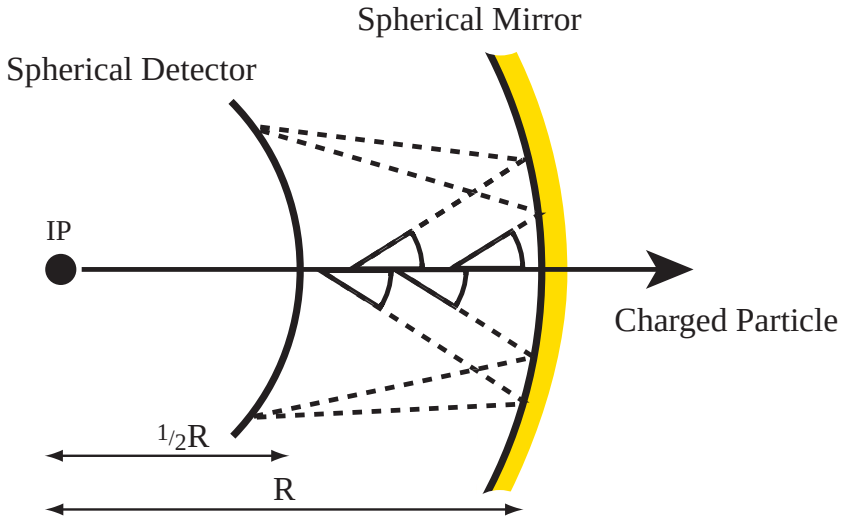

Figure 4.10: *Schematic showing the basic principle of a RICH detector: In a focused system, light that is emitted at a common azimuthal angle ϕ and polar angle θ_{c} is imaged at the same position on the detector, independent of where along the charged particle track, the photon was emitted.*

A charged particle enters the RICH system, consisting of a spherical mirror of radius R and focal length f,

$$f = \frac{R}{2}; \tag{4.11}$$

and a spherical photosensitive surface with radius of curvature $R/2$, between which is contained a Cherenkov radiating medium. When a charged particle (produced at the interaction point IP) interacts with this medium, photons are emitted at different points along its straight line trajectory. These photons are focused by the reflective mirror to produce a circular ring image of radius r on the photosensitive detector [117, 118]. At the detector surface, the radius of the ring is given by

$$r = f\theta_{\mathrm{c}} = \frac{R}{2}\theta_{\mathrm{c}}. \tag{4.12}$$

By measuring r, then with R known, the Cherenkov angle can be determined using equation 4.12. This then allows the precise determination of the velocity of a particle β from the angle θ_{c} (Equation 4.7) which is measured in the RICH detector. Since the momentum of the particle, $\underline{p}$ is determined in the tracking system, the mass of the particle m, can be determined using

$$m = \frac{|\underline{p}|}{c\ \gamma\ \beta} \tag{4.13}$$

where

$$\gamma = \frac{1}{\sqrt{1-\beta^2}}. \tag{4.14}$$

4.4.3.3 Determining the momentum range for hadron particle identification

The momentum range over which particle identification is required in LHCb can be determined by examining the momentum spectra of low and high multiplicity decays. Figure 4.11(a) shows the momentum spectra of the low multiplicity decay $\mathrm{B}^0_{\mathrm{d}} \to \pi^+\pi^-$ and the high multiplicity decay $\mathrm{B}^0_{\mathrm{s}} \to \mathrm{D}^+_{\mathrm{s}}\pi^+\pi^-\pi^-$. To define the upper momentum limit, it is found that in about 90% of $\mathrm{B}^0_{\mathrm{d}} \to \pi^+\pi^-$ decays, neither of the pion tracks

have a momentum greater than 150 GeV/c over the whole detector acceptance [119].

The identification of kaons from the accompanying b hadron in a selected decay provides a clean mechanism for determining the charge of the primary b quark. These kaons typically are of a low momentum, as illustrated in Figure 4.11(b). This, combined with the fact that in about 90% of $B_s^0 \to D_s^+\pi^+\pi^-\pi^-$ decays (Figure 4.11(a)) none of the final state tracks have a momentum less than 1 GeV/c over the whole detector acceptance, defines the lower momentum limit for RICH particle identification to be approximately 1 GeV/c.

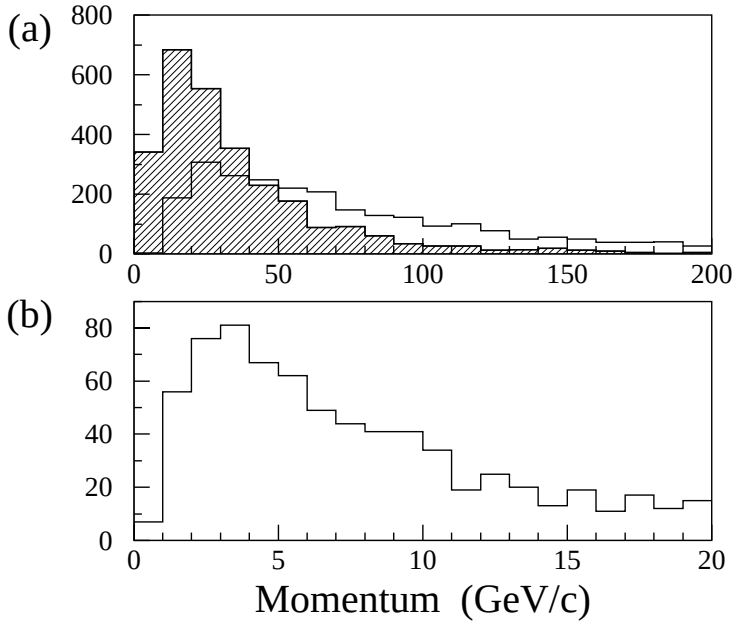

Figure 4.11: *(a) Momentum distributions for the highest momentum pion from simulated* $B_d^0 \to \pi^+\pi^-$ *events (unshaded) and* $B_s^0 \to D_s^+\pi^+\pi^-\pi^-$ *(shaded). (b) Momentum distribution for tagging kaons.*

4.4.4 The RICH detector system

Figures 4.12 and 4.13 show the two RICH detectors, RICH-1 and RICH-2. Each detector consists of a plane mirror, a spherical mirror, a photodetector plane and either two (as in

RICH-1) or one (as in RICH-2) radiators of Cherenkov radiating material with different refractive indices n.

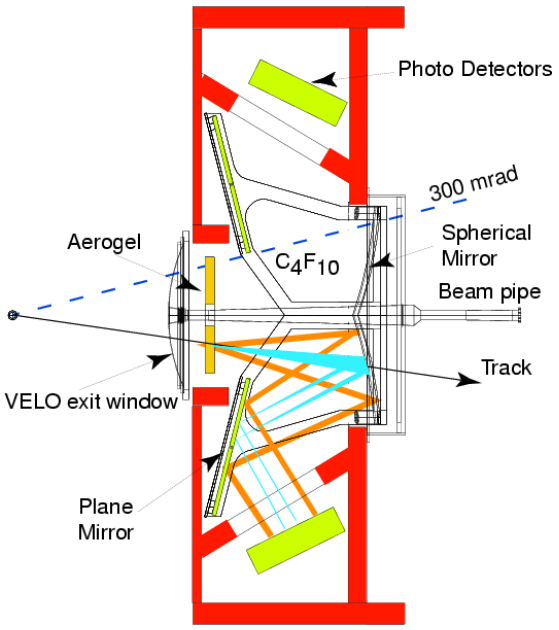

Figure 4.12: *y-z plane schematic diagram of RICH-1. The aerogel and* C_4F_{10} *radiators, and the photodetector planes are shown.*

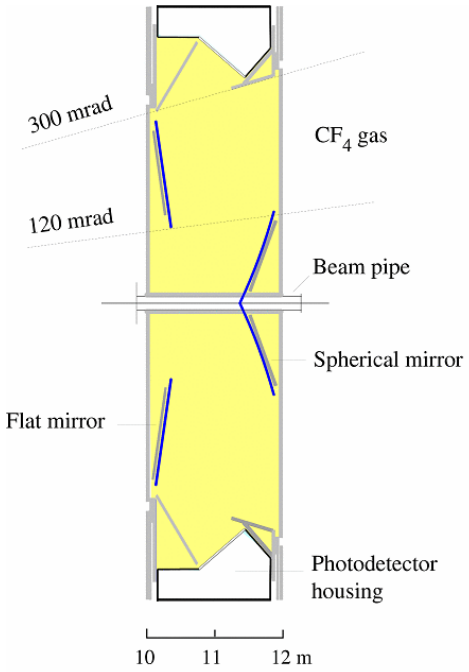

Figure 4.13: *x-z plane schematic diagram of RICH-2. The* CF_4 *radiator and photodetector planes are shown.*

RICH-1 is located upstream of the magnet and covers the full acceptance of LHCb (10 - 300 mrad in both x and y projections). It is designed to detect and identify low-to-intermediate momentum particles that are swept out of the acceptance of LHCb. To achieve this, RICH-1 contains both a 5 cm-thick silica aerogel radiator that is suitable for detection of the lowest momentum tracks, and a gaseous ∼95 cm long C_4F_{10} radiator for the intermediate momentum tracks. The removal of the shield between the RICH-1 and the magnet which allows an enhanced fringe field between the VELO and the Trigger Tracker means that there is a B-field of ∼60 mT in the region of RICH-1. This has required the design of an iron shielding house internal to RICH-1 for shielding the photodetectors from the B-field, and also a vertical optical layout so that the photon detectors are located above and below the beam.

RICH-2 is shown in Figure 4.13 and is a downstream detector containing a ∼180cm long CF_4 radiator, which compliments RICH-1 by analysing higher momentum tracks. In comparison to RICH-1, RICH-2 has a reduced acceptance (10-120 mrad in x and 10-100 mrad in y projections). To shorten the overall length of both RICH-1 and RICH-2, the image from the spherical mirror is reflected by a second flat mirror to the detector planes.

Figure 4.14 shows the polar angle θ as a function of momentum of all charged tracks in simulated $B^0_d \rightarrow \pi^+\pi^-$ events and highlights the region covered by RICH-1 and RICH-2. In both of the RICH detectors, Cherenkov photon rings are produced when charged particles traverse the radiator materials. The momentum thresholds above which charged particles which produced these rings may be identified, is defined by a threshold for Cherenkov light emission (Section 4.4.3.1). For a particle of mass m traversing a radiator with refractive index n, then the Cherenkov angle θ_c is given by

$$\cos\theta_c = \frac{1}{n\,\beta} = \frac{1}{n}\sqrt{1+\left(\frac{m}{p}\right)^2} \;\leq\; 1 \tag{4.15}$$

so that

$$p_{thresh} \geq \frac{m}{\sqrt{n^2-1}}. \tag{4.16}$$

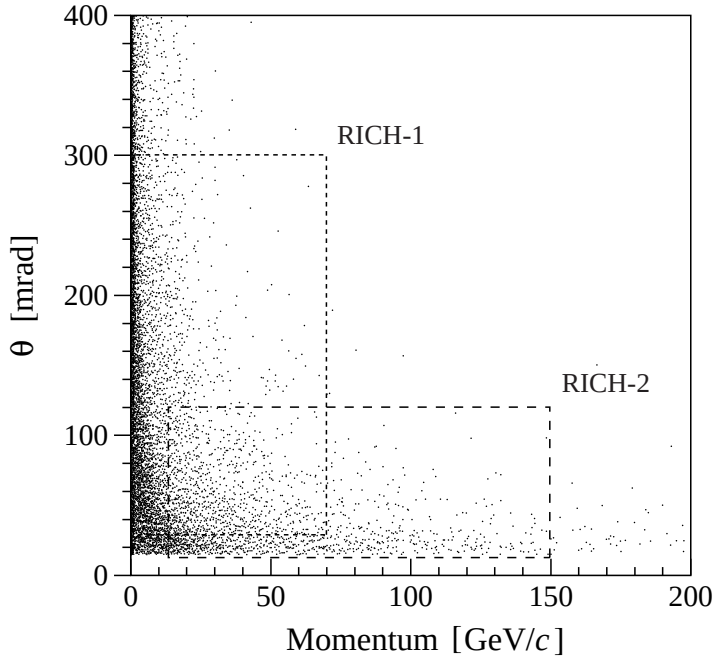

Figure 4.14: *Polar angle θ versus momentum for all tracks in simulated $\mathrm{B}^0_\mathrm{d} \to \pi^+\pi^-$ events. The acceptance of the RICH-1 and RICH-2 detectors are superimposed.*

Figure 4.15 shows θ_c as a function of particle momentum, for each particle mass hypothesis and each of the three RICH radiator materials. Table 4.1 lists the momentum thresholds for pions and kaons, $p_\mathrm{thresh}(\pi)$ and $p_\mathrm{thresh}(\mathrm{K})$ above which, if the charged particle passing through the radiator material has momentum, $p > p_\mathrm{thresh}(\pi)$ and $p > p_\mathrm{thresh}(\mathrm{K})$, then Cherenkov photons will be produced enabling that charged particle to be identified as a π or K. Also in Table 4.1, θ_c^{max} is the maximum Cherenkov angle at which Cherenkov photons will be produced in each radiator and these are labelled on Figure 4.15 for each of the three radiators. $\theta_\mathrm{accept}^{min}$ and $\theta_\mathrm{accept}^{max}$ are the minimum and maximum acceptance angles covered by the three radiators in the two RICH detectors. After production, the Cherenkov rings are focused by mirrors onto photodetector planes, positioned outside of the LHCb acceptance.

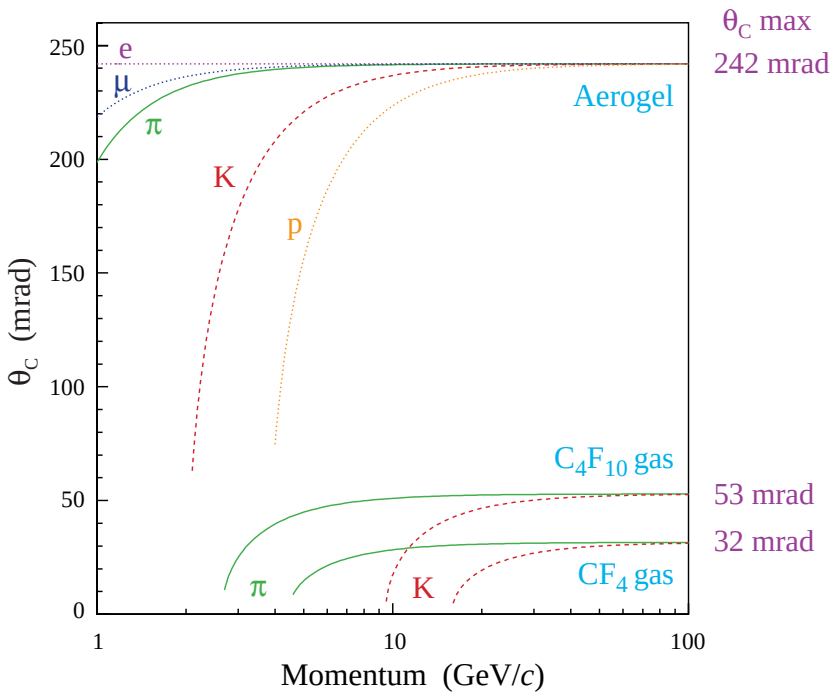

Figure 4.15: *Cherenkov angle θ_c for different mass hypotheses as a function of particle momentum .*

Detector	RICH-1	RICH-1	RICH-2
Radiator Material	Aerogel	C_4F_{10}	CF_4
Refractive index, n	1.03	1.0014	1.0005
$p_{\text{thresh}}(\pi)$ $[\frac{GeV}{c}]$	0.6	2.6	4.4
$p_{\text{thresh}}(\text{K})$ $[\frac{GeV}{c}]$	2.0	9.3	15.6
θ_c^{max} [mrad]	242	53	32
$\theta_{\text{accept}}^{min}$ [mrad]	25	50	10
$\theta_{\text{accept}}^{max}$ [mrad]	330	330	120

Table 4.1: *Characteristics of the three radiator materials used in the RICH detectors.*

4.4.5 RICH Particle Identification

Figure 4.16 is a typical event display showing ring images due to charged particles passing through RICH-1 and through RICH-2.

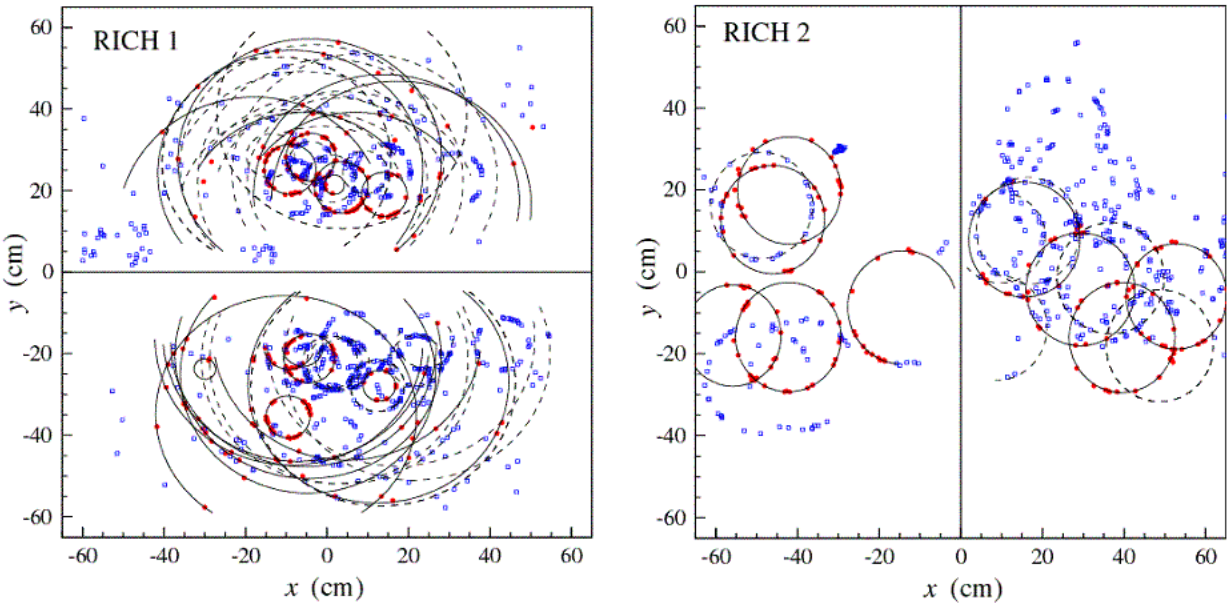

Figure 4.16: *Event display of a simulated* $B_d^0 \to \pi^+\pi^-$ *event. The dots mark the positions of detected Cherenkov photons. The red dots (fitted with the black line) are photons which via a pattern recognition algorithm are found to be associated with a track and therefore have particle identification. In the RICH-1 display, the larger rings are due to Cherenkov photons from the aerogel radiator while the smaller rings are due to Cherenkov photons from the* C_4F_{10} *gas radiator. In both figures, the Cherenkov photons in blue are due to simulated backgrounds such as secondary particles from the beampipe, tracks which may not have been reconstructed by the tracking system, or electronic and detector noise.*

RICH particle identification is carried out as follows: for each track, a probability is assigned in the form of a log likelihood $\mathcal{L}$ for each of the possible particle identities of e, μ, π, K or p of that track. For each track, the Gaussian sigma separation $\Delta\sigma$ between different particle assignments, changes the log likelihood by an amount $\Delta \ln\mathcal{L}$ given by

$$\Delta\sigma = \sqrt{2 \mid \Delta \ln\mathcal{L} \mid}. \tag{4.17}$$

If the likelihood of the hypothesis is more than 3σ separated from other hypotheses then a particle is positively identified [120]. Figure 4.17 shows as a function of momentum, the

mean number of sigma separation between π and K hypotheses for true pions, denoted by $\langle \Delta\sigma(\pi - K) \rangle$. It shows that at least 3σ separation exists for π-K identification between $\sim$3 and $\sim$80 GeV.

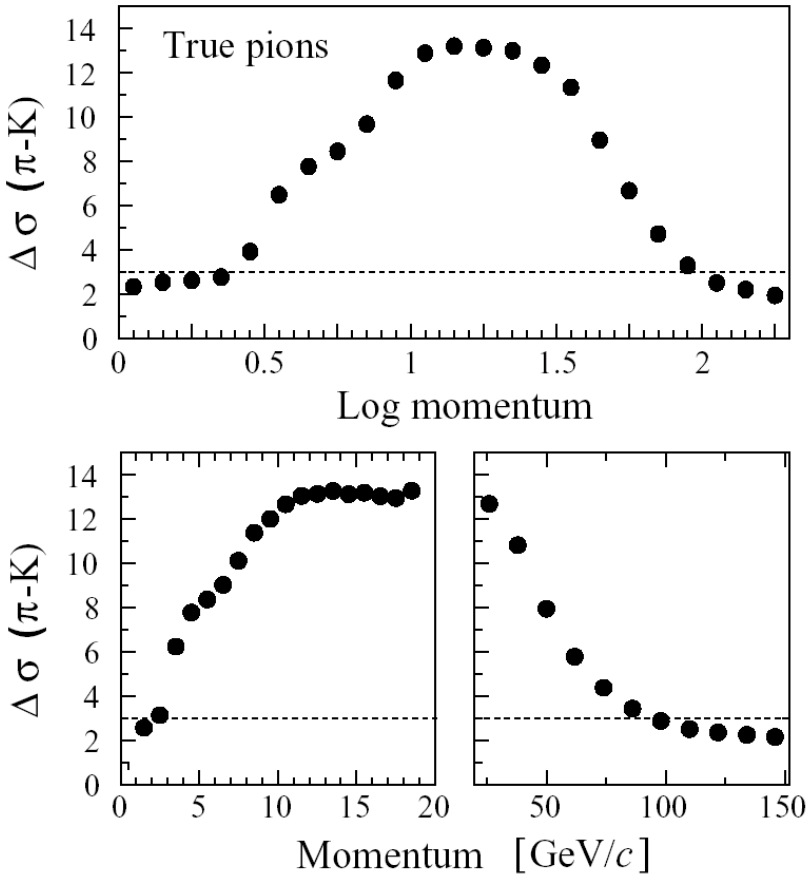

Figure 4.17: *Mean number of sigma separation between K/π hypothesis for true pions as a function of pion momentum - shown on logarithmic and linear scales. The dashed horizontal line represents a 3σ separation.*

At low momentum, the thresholds of the RICH radiators become important since Table 4.1 shows that a π(K) with momentum below 0.6 (2.0) GeV cannot be positively identified since it does not radiate Cherenkov light in any of the radiators. For particles below these radiator thresholds, the RICH operates in so-called "veto mode" i.e. the particle can only be identified as not being a π(K). RICH particle identification is used in the analyses presented in Chapters 6 to 8, and will be discussed in further detail there.

4.4.6 RICH Photon Detectors

Since the time of the LHCb Technical Proposal in 1998 [69], two detector technologies have been candidates for the RICH photon detectors. These are the hybrid photon detector (HPD) (with either the pixel [121] or pad silicon detector [122]) and the multianode photomultiplier (MaPMT) [123]. The pixel HPD, which will be the subject of Chapter 5, was chosen as the baseline option at the time of the LHCb-RICH Technical Design Report [99] in September 2000 with the Multi-Anode PhotoMuliplier Tube (MAPMT) chosen as the backup solution. In October 2003, the HPD was formally chosen as the RICH photon detector technology [106].

The choice of photon detector technology for the LHCb RICH must satisfy a number of requirements. The photodetector planes of the RICH detector cover a total area of 2.8 m^2 [106], over which it is required that single photons be detected with the maximum possible efficiency and with a spatial granularity of 2.5×2.5 mm^2. The photon detectors should be sensitive to Cherenkov photons over the UV and visible wavelength range of 200 to 600 nm and have a time resolution compatible with the LHC bunch-crossing rate of 25 ns. The photon detector readout electronics are required to cope with a RICH occupancy rate of up to 8%, the high level-0 trigger rate of 1 MHz and the level-0 latency of 4 μs. Finally the photon detectors will have to be tolerant to the magnetic fringe fields of up to 2.5 mT due to the spectrometer magnet, and be radiation hard to a level of up to 3 kRad/year.

4.4.7 The Hybrid Photon Detector (HPD)

Figure 4.18 is a schematic illustrating the component parts of the pixel HPD tube. The main components are the optical window, the electrodes, the anode and the vacuum tube. The anode consists of a silicon pixel array which is solder bump bonded to a binary electronics readout chip and encapsulated inside the vacuum tube envelope. The photoelectrons released by a single photon incident on the photocathode are accelerated onto the silicon sensor by an applied voltage of -20 kV, resulting in a signal of $\simeq$ 5000 e

in the silicon.

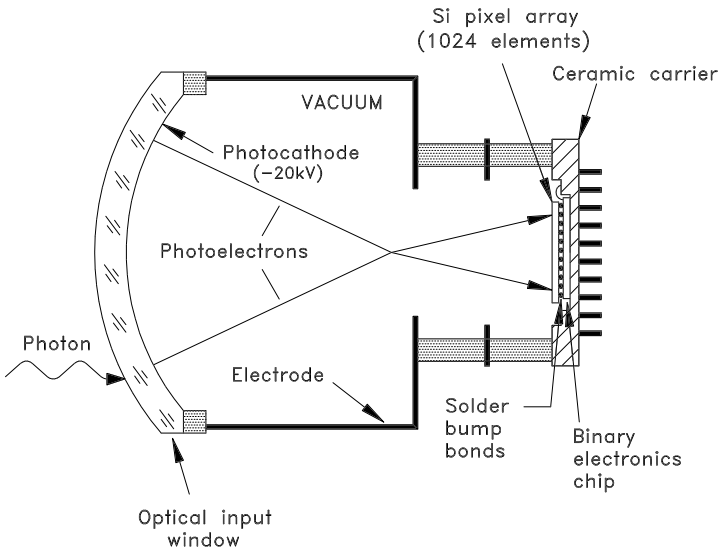

Figure 4.18: *Schematic illustrating the component parts of the pixel-HPD.*

The HPD has a diameter of 83 mm. The curved quartz optical input window is 7 mm thick with a 72 mm active diameter and a radius of curvature of 55 mm. The photocathode is coated on the inside of the window. When the photocathode is illuminated parallel to the tube axis, its active diameter is increased by ∼3 mm by refraction at the edges of the window. This results in an active area ratio of $\left(\frac{75}{83}\right)^2 = 81.7\%$. The anode active diameter is 18 mm. The pixel HPD is described in more detail in Chapter 5.

4.5 Trigger

At the LHC, the $b\overline{b}$ cross-section is 500 μb compared to the inelastic cross-section of 80 mb. These figures show that at LHCb it is necessary to have an optimal trigger where events containing B decays can be distinguished from the large minimum bias background.

Figure 4.19 provides an illustrative overview of the three LHCb trigger levels and the sub-detector components that are associated with them [105]. The three levels are

known as Level-0 (L0), Level-1 (L1) and the Higher Level Triggers (HLT) and have the combined effect of reducing the event rate from that of the LHC bunch-crossing frequency of 40 MHz, to the rate at which the events are eventually to be stored, which is 200 Hz.

The three levels are implemented through five hardware sub-systems (four L0 sub-systems and one sub-system for L1 and the HLT combined). The four L0 sub-systems are the Calorimeter Triggers, the Muon Trigger, the Pile-Up Trigger and the L0 Decision Unit (L0DU). The L1 and the HLT are referred to as one hardware sub-system since they share the same event building network and processor farm.

Level-0

The Level-0 (L0) trigger is the lowest level trigger in LHCb and through hardware implementation, reduces the event rate from 40 MHz to a maximum output rate of 1 MHz with a latency of 4 μs. Information at L0 is collected by the Level-0 decision unit (L0DU) which receives information from each of the Calorimeter, Muon and Pile-Up sub-triggers at 40 MHz.

The large boost given to the b-hadron and, to a lesser extent, its large mass means that b hadrons decay to large E_T leptons, hadrons or photons. Therefore, at L0 information is collected about the highest E_T lepton, hadron and photon clusters, and the two highest p_T clusters in the muon chambers. Secondly, to ensure that selection of events is based on signatures of b-hadrons rather than those of the large combinatorial background, events can also be rejected based upon so-called global event variables such as charged track multiplicities and the number of interactions per event.

The L0DU combines all of these signatures into one decision per event and then accepts events where at least one of the largest E_T e, γ, ${\pi^0}_{local}$, ${\pi^0}_{global}$, hadrons or muons is above threshold provided that the pile-up veto detects less than three tracks coming from a secondary vertex. Events are also accepted if the sum of the E_T of the two muons with the largest transverse energy are above a threshold $E_T^{\mu\mu}$, irrespective of the pile-up veto result. Once the L0DU decision has been made, then the decision is passed to the

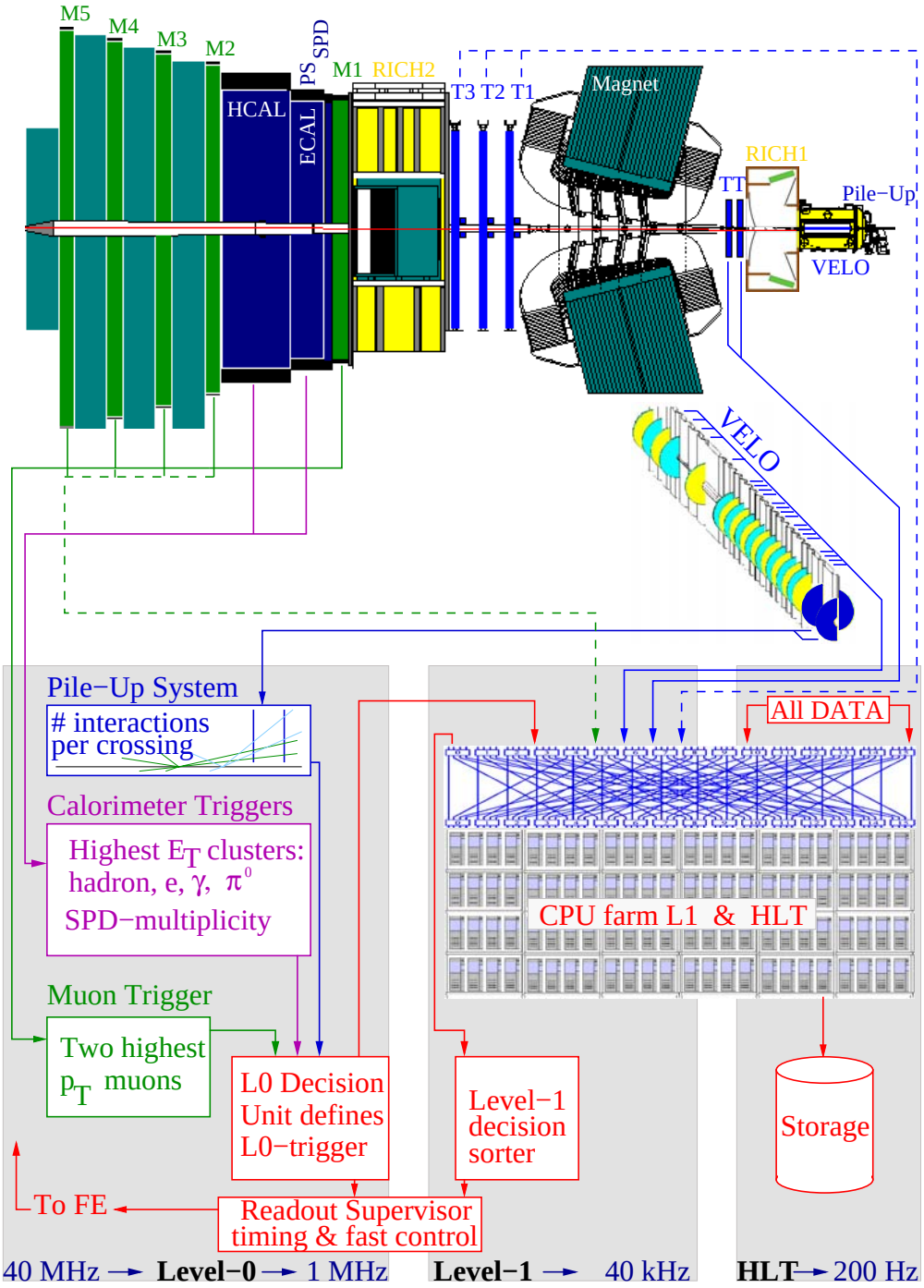

Figure 4.19: *An overview of the three trigger levels and the sub-detector components associated with them is shown. The three trigger levels are Level-0 (L0), Level-1 (L1) and the Higher Level Trigger (HLT).*

Readout Supervisor which transmits it to the Front-End electronics. Tables 4.2 and 4.3 list the complete set of cuts implemented at Level-0.

L0 Trigger	E_T^{hadron}	E_T^{μ}	$E_T^{electron}$	E_T^{γ}	$E_T^{\mu\mu}$	$E_T^{\pi^0 local}$	$E_T^{\pi^0 global}$
Threshold (GeV)	3.6	1.1	2.8	2.6	1.1	4.5	4.0

Table 4.2: *List of Level-0 trigger cuts [105].*

Global Cuts	Value
Tracks in the 2nd vertex	3
Pile-Up Multiplicity	112 hits
SPD Multiplicity	280 hits
E_T	5.0 GeV

Table 4.3: *List of Level-0 trigger cuts on global event variables [105].*

Level-1

The second trigger level, Level-1 (L1) reduces the event rate from 1 MHz to an output rate of 40 kHz using information from the VELO, TT, T1-T3 and the summary information from the L0DU. The L1 algorithm reconstructs tracks in the VELO, matches them to L0 muon and L0 calorimeter trigger candidates and then measures their momenta using the fringe field of the magnet between the VELO and TT. Events are then selected based upon tracks with a large p_T and a large impact parameter with respect to the primary vertex. Both L1 and the HLT are executed on a 1200 node CPU farm, with L1 taking priority over the HLT due to its smaller latency ($\sim$50 ms compared to $\sim$200 ms).

Higher Level Trigger (HLT)

The HLT uses all the detector information and selects events which are associated with specific b-hadron decay modes. It starts by reconstructing the VELO tracks and the

primary vertex rather than having this information transmitted from L1. A fast pattern recognition algorithm then links the VELO tracks to the tracking stations T1-T3, after which a set of selection cuts dedicated to specific final states are applied. Studies at the time of the Technical Proposal (1998) [69] found that the events reaching the HLT stage consist of $b\overline{b}$, $c\overline{c}$ and light quark events in a ratio of about 1:2:1, however HLT studies using the reoptimised detector description are currently in progress.

The HLT has a latency of ∼200 ms and a suppression factor of 1/25 - reducing the L1 output rate (HLT input rate) from 40 kHz to 200 Hz. At 200 Hz the remaining events are fully reconstructed and particle identification applied before written to storage using a 200 node CPU farm.

4.6 Tracking

The principle task of the tracking system is to provide efficient reconstruction of charged-particle tracks and precise measurements of their momenta. It also has to provide measurements of track directions for the reconstruction of Cherenkov rings in the RICH detectors. The tracking detectors in LHCb are the silicon vertex detector (Vertex Locator (VELO) and pile-up veto), the Trigger Tracker (TT) located between RICH-1 and the magnet, and the three stations (T1-T3) located between the magnet and RICH-2. Each of T1-T3 are divided into two components, known as the inner tracker (IT) and the outer tracker (OT). The tracking strategy is described in Section 6.4.

4.6.1 Silicon Vertex Detector

The silicon vertex detector consists of two components, the VELO and a pile-up veto counter.

The VELO shown in Figure 4.20 has the task of providing precise measurements of track co-ordinates close to the interaction region [101]. These track co-ordinates are

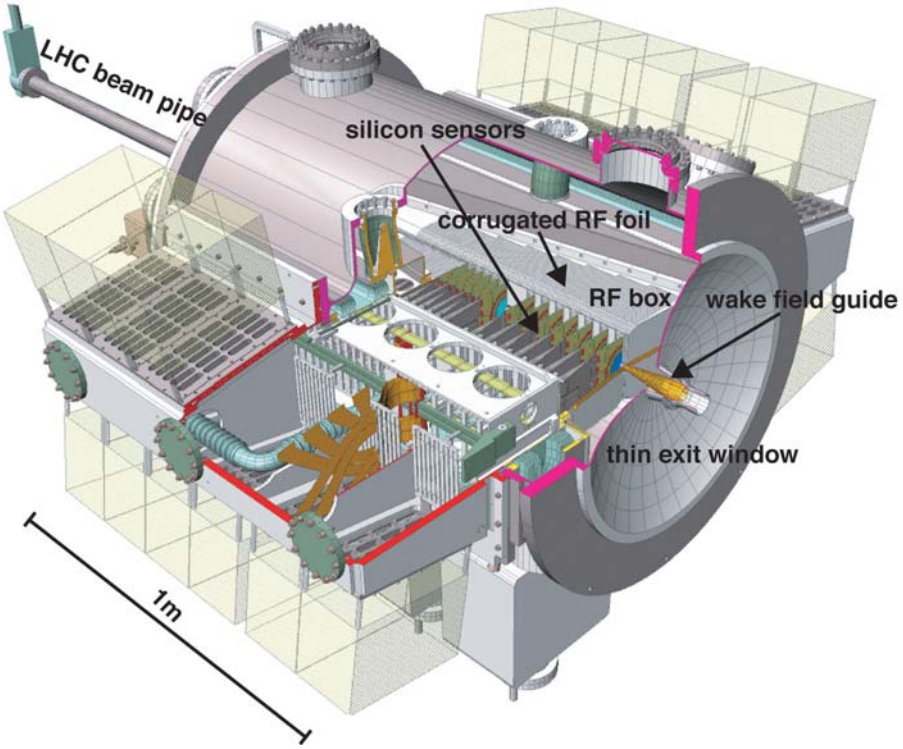

Figure 4.20: *VELO vacuum vessel. The main components are the silicon sensor stations, the corrugated RF foils, the RF box, the wakefield guides and the exit window. The LHC beam pipe is also shown [70].*

then used to reconstruct production and decay vertices of beauty- and charm-hadrons, to provide an accurate measurement of their decay lifetimes, and to measure the impact parameter of particles used in flavour tagging. The VELO also provides vertex information for use in the Level-1 trigger.

Figure 4.21 shows the layout of the VELO and pile-up veto silicon stations. The VELO consists of 21 stations interspersed over $\sim$1 m parallel to the beam direction. The stations closest to the interaction region are required in order to reconstruct tracks with angles up to 390 mrad. The most downstream stations are required to reconstruct low angle tracks down to 15 mrad. Six of these stations in between are not strictly required for covering the LHCb acceptance but are present in order to minimise the extrapolation distance of tracks towards the vertex and for redundancy reasons. Each station consists of two planes of 220 μm silicon strips as illustrated in Figure 4.22. One

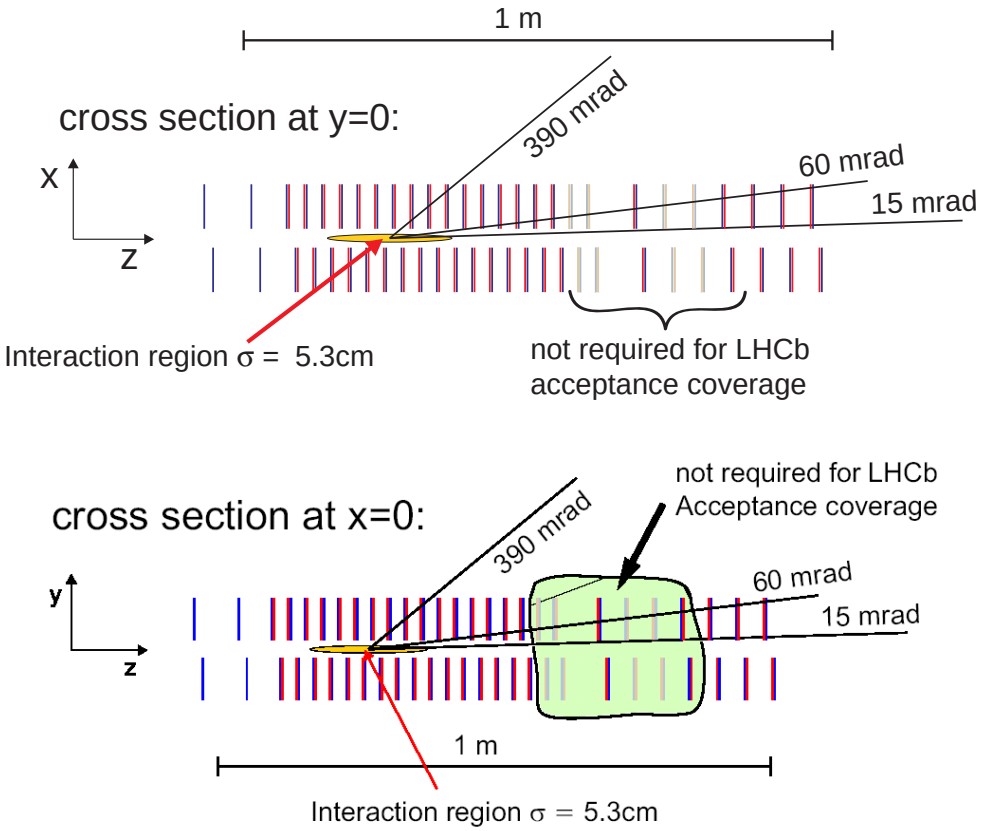

Figure 4.21: *Pile-up veto counter and VELO station setup shown in the x-z and y-z planes. The pile-up veto consists of two single plane silicon stations nearest the interaction point. The VELO consists of 21 stations, with each station consisting of two planes of silicon. [70]*

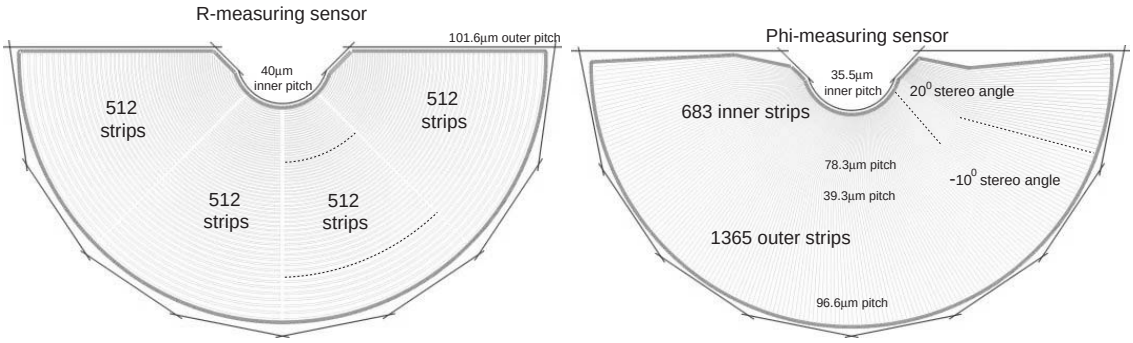

Figure 4.22: *Each VELO station consists of two silicon planes. One plane measures radial co-ordinates (r-measuring sensor) and the other measures azimuthal coordinates (ϕ-measuring sensor) [70].*

plane is designed to measure radial position co-ordinates (referred to as the r-detector plane) and the other to measure azimuthal coordinates (referred to as the ϕ-detector plane). The stations closest to the interaction point are needed in order to reconstruct low angle tracks down to 15 mrad; and the stations further away are used to reconstruct tracks with angles up to 390 mrad.

The two planes of silicon detector which are placed upstream of the main VELO, act as a pile-up veto. This is used in the Level-0 trigger to suppress events that contain multiple pp interactions in a single bunch crossing. By counting the number of primary vertices, the pile up veto counter will be able to reject 80% of multiple interactions while retaining 95% of single interactions. Figure 4.2 shows that there is a finite probability of multiple interactions at the LHCb luminosity of $2\times10^{32}\mathrm{cm}^{-2}\mathrm{s}^{-1}$.

4.6.2 Tracking Stations

4.6.2.1 Trigger Tracker (TT)

The purpose of the Trigger Tracker (TT) is two-fold. Firstly, it is used to reconstruct the trajectories of low momentum particles that are bent out of the detector acceptance before reaching the tracking stations T1-T3. Secondly, it is used in the Level-1 trigger to assign p_T information to large impact-parameter tracks.

The Trigger Tracker covers a rectangular area of approximately 140 cm in width and 120 cm in height. It consists of four planes of silicon strip detectors with strip pitch of 198 μm, which are split into two pairs of planes separated by 30cm. The first and the fourth plane have vertical readout strips, with the second and third layers having readout strips rotated by a stereo angle of +5° and -5° respectively. The first two layers (TTa) are centred around z = 232 cm, and the last two (TTb) around z = 262 cm. These are illustrated in Figure 4.23.

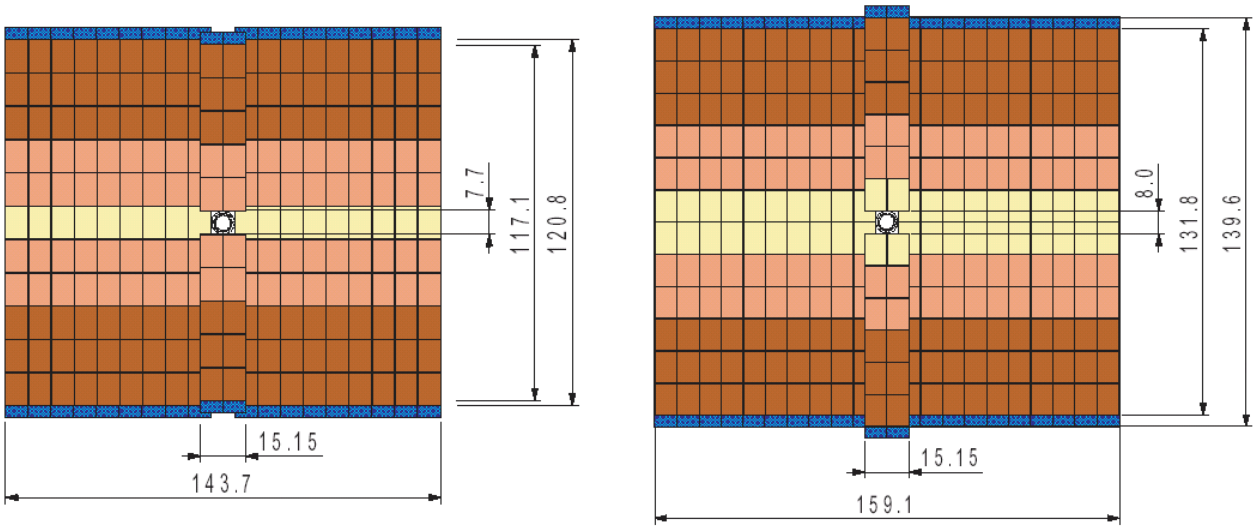

Figure 4.23: *Layout of x-layer in TTa (left) and in TTb (right). Dimensions are in cm.*

4.6.2.2 Tracking Stations T1-T3

Owing to the variation in particle flux with polar angle, each of the tracking stations T1, T2 and T3 are split into two regions - an inner tracker (IT) [104] and an outer tracker (OT) [102], each of which uses a different technology.

The inner tracker covers a cross-shaped area ∼120 cm in width and 40 cm in height around the LHC beam pipe, where particle densities are highest (particle fluxes of $\sim 3.5\times 10^6$ cm^{-2}s^{-1} are expected). The technology used is the same as that used in the Trigger Tracker, namely single-sided silicon strip detectors.

The outer tracker covers the rest of the T1-T3 stations where expected particle fluxes are $< 1.4\times 10^5$ cm^{-2}s^{-1}, which is low enough to use straw-tube drift chambers with a 5 mm cell diameter. Precise coordinates are obtained in the x-z bending plane from straw tubes located at 0° and ±5° with respect to the vertical.

4.7 Other Components

4.7.1 Magnet

The LHCb magnet [97] consists of two aluminium trapezoidal coils as shown in Figure 4.24, bent at 45° on the two transverse sides and arranged inside an iron yoke. This is shown schematically in Figure 4.25. Each aluminium coil is composed of fifteen individual so-called pancakes which are themselves individually wound from 290 m lengths before being connected electrically in series. Since the tracking detectors located about the magnet have to provide a momentum measurement for charged particles with a precision of about 0.4% for momenta up to 200 GeV/c, this requires the presence of an integrated field of $\int \underline{B}.d\underline{l} = 4$ Tm for tracks originating near the primary interaction point.

Figure 4.24: *The two LHCb magnet trapezoidal coils.*

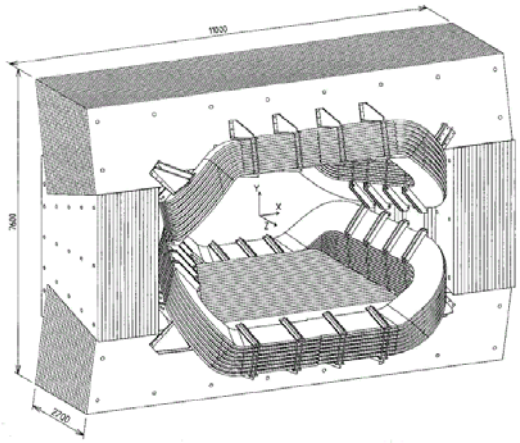

Figure 4.25: *Schematic of the magnet coil inside the soft iron yoke.*

4.7.2 Beam Pipe

The proposed LHCb beam-pipe is illustrated in Figure 4.26 and is described in detail in reference [70]. The first section (labelled UX85/1) is 1840 mm in length, made of 1mm-thick beryllium and consists of a 25 mrad cone followed by a 10 mrad cone which are connected by a 250 mm long cylindrical section. The second and third sections (labelled

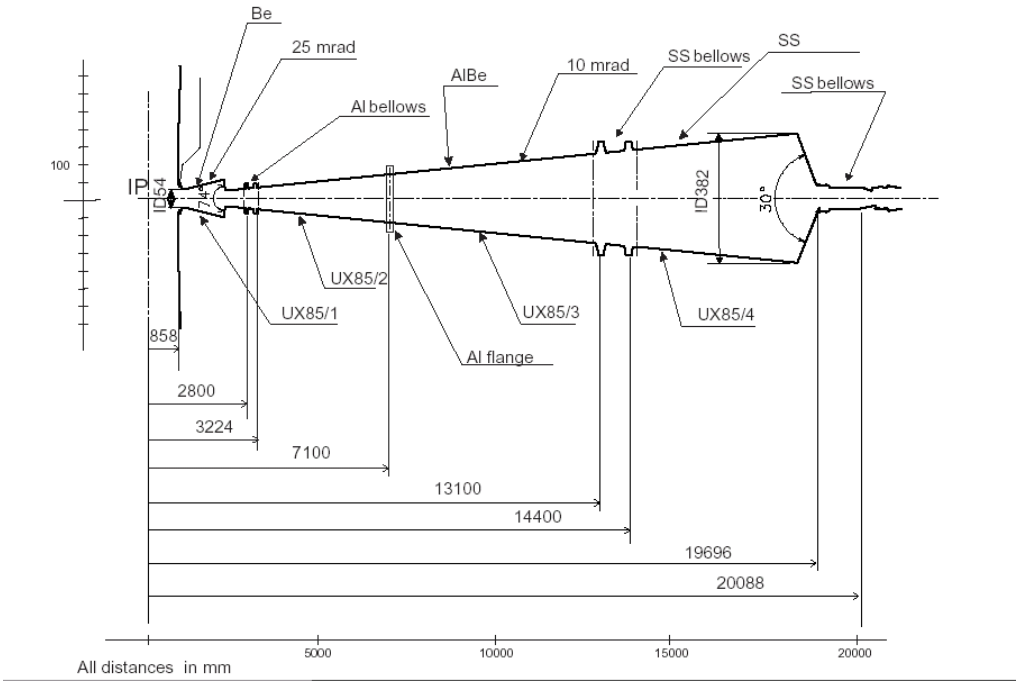

Figure 4.26: *The LHCb beam pipe consists of three sections - a thin exit window sealed to the VELO vacuum tank, followed by two conical parts with apertures of 25 mrad and 10 mrad respectively. All lengths are measured in mm.*

UX85/2 and UX85/3) consists of a 10 mrad aluminium/beryllium alloy cones of lengths 3876 mm and 6000 mm, which are connected by flanges located at 7100 mm from the interaction point (IP). A second transition located at 13100 mm connects UX85/3 with the last section of the beam pipe (labelled UX85/4), which consists of a 10 mrad ∼4 mm thick - stainless steel (SS) cone.

4.7.3 Data Acquisition (DAQ)

The role of the LHCb Online System (Data Acquisition and Experimental Control) [103] is to read and buffer data from the front-end electronics following the Level-1 trigger, to assemble complete events and to provide storage facilities for event data and for calibration and monitoring information. Following the Level-1 trigger, Front-End multiplexers (FEM) multiplex the zero-suppressed data from many detector channels onto the

Front-end links (FEL), with at least one FEL allocated to each detector segment. The Readout Units (RU) receive fragments from several FELs and assemble them into larger sub-events. Once assembled, each sub-event is then transferred via the readout network to the Sub-Farm Controller (SFC) which then assembles all the sub-events arriving via the readout network into complete events. Once the complete event is assembled and processed via the higher level triggers (HLT), the SFC then dispatches the accepted events via the readout network to the storage sub-system.

DAQ also includes the Detector Control System (DCS) which will be used to monitor and control the operational state of the LHCb detector, and the associated experimental equipment such as the gas systems, high voltages and readout electronics. The DCS is designed so that it is able to operate the experiment from the control room during data-taking, but also allows the operation of the different sub-systems in stand-alone mode, if necessary. The DCS is also able to store data from the detector such as temperatures or positions, so that they can be accessed by both the reconstruction and physics analysis programs.

4.7.4 Computing

All of the physics results presented in this thesis were obtained with the aid of computer simulations. Until 2001, all studies, including those presented in the LHCb Technical Proposal [69] were carried out using the FORTRAN based program, SICB which carried out the tasks of event generation, detector simulation, reconstruction and analysis [124].

Since 2001, work has been ongoing to re-implement this using the Object-Orientated (OO) C++ framework, Gaudi [125]. Currently all tasks, except that of the detector simulation, are now fully implemented within this framework. The tasks that were previously carried out using SICB have been broken down into different stand-alone programs. Monte Carlo production is carried out using DIRAC (Distributed Infrastructure with Remote Agent Control) [126], simulation using Gauss [127], digitisation using Boole [128], reconstruction using Brunel [129] and physics analyses using DaVinci [130].

Present computing developments will mean that future physics analyses will be performed using the Loki or the Python-based Bender tools and greater use will be made of GRID technologies such as Ganga (Grid to Gaudi interface) [131]. These will be described in the Computing TDR which will be written in 2004.

Chapter 5

Hybrid Photon Detectors for the LHCb RICH

5.1 Introduction

One of the main features of the LHCb detector is that of particle identification and, in particular, excellent π/K separation over a wide momentum range. This will be achieved using the RICH detectors which were described in Section 4.4.3 with the Hybrid Photon Detector (HPD) as the chosen photodetector technology.

The subject of this chapter is the calculation of the efficiency of a prototype pixel HPD for detecting single photoelectrons. The chapter begins with an overview of the HPD project, including a detailed description of the HPD and its component parts, expanding upon the brief description in Section 4.4.7. The theory behind the measurements necessary for this calculation are explained, along with the experimental setup used to perform them. The efficiency of the prototype HPD to single photoelectrons is then determined, along with an estimate of the statistical and systematic errors. The chapter concludes with a brief summary of the photon detector project status to date. Part of this work presented in this chapter has previously been published in [1, 2].

5.2 The Hybrid Photon Detector

The 10 MHz HPD prototype that has been used to produce the results presented in this chapter is one in a series of HPDs manufactured as a result of long-standing collaboration between CERN and the company Delft Electronic Products (DEP)[a]. All measurements taken using this prototype were carried out at CERN. A photograph of this prototype is shown in Figure 5.1. Figure 5.2 (previously shown as Figure 4.18 in Chapter 4) is a schematic illustrating the component parts of a generic pixel HPD tube.

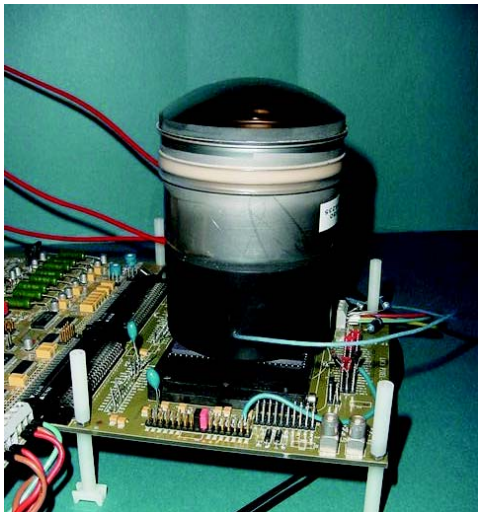

Figure 5.1: *Photograph of the full-scale 10 MHz HPD prototype. The HPD is shown mounted in the ZIF (zero-insertion-force) socket of the pixel carrier board (also referred to as the "daughterboard". The cables leading from the back of the HPD are for the high voltage (HV) supply.*

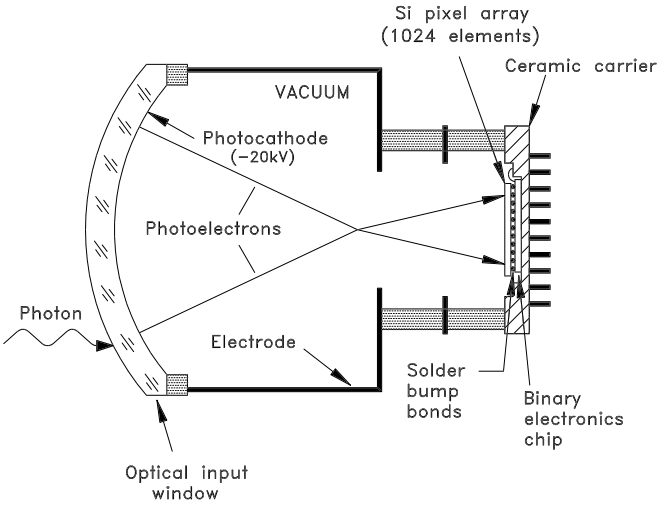

Figure 5.2: *Schematic illustrating the component parts of the pixel-HPD [69]. The main components of the HPD are the optical input window, the electrodes and the anode consisting of a silicon pixel array bump-bonded to a binary readout chip. These components are described in the text.*

The program of HPD development has evolved from the "Imaging Silicon Pixel Array" (ISPA) tube [134], which was initially developed to read out small diameter scintillating fibres for particle tracking [135], and later shown to be useful detection tool for biomedical applications [136]. Figures 5.3 and 5.4 show the two types of HPD prototypes

[a]Delft Electronic Products (DEP) B.V. P.O. Box 60, Dwazziewegen 2, NL-9300 AB Roden, The Netherlands.

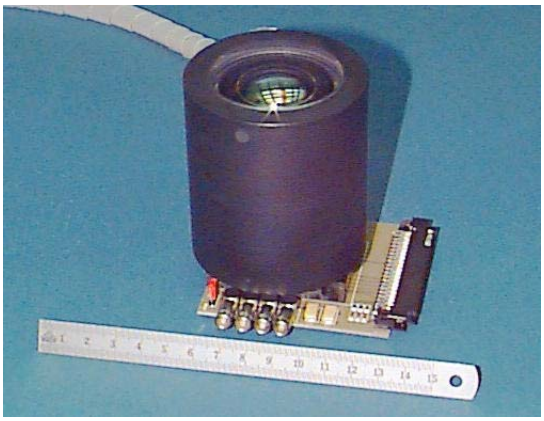

Figure 5.3: *Photograph of the half-scale (40:11) 2048-pixel HPD prototype [132, 133].*

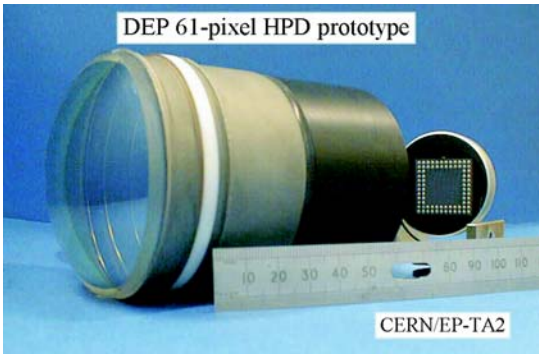

Figure 5.4: *Photograph of the full-scale (72:18) HPD prototype, fitted with a 61-pixel anode [132, 133].*

that have previously been manufactured. These were tested during the 1998 and 1999 test beam periods at the CERN X7 facility [132, 133]. Figure 5.3 shows the half-scale prototype with an input window to anode diameter ratio of 40:11 and a 2048 pixel anode. This prototype was manufactured as a test of fine-grained sensor encapsulation within a HPD casing. Figure 5.4 shows the full-scale prototype with an input window to anode diameter ratio of 72:18 and a 61 pixel anode. This prototype was manufactured as a test of an HPD with the required electron optics. Several of these full-scale prototypes were manufactured, one of which was equipped with a phosphor screen anode coupled to a CCD camera, in place of the pixels. The prototype studied here is the first full-scale HPD prototype to have an encapsulated fine-grain sensor.

5.2.1 Quartz optical input window

The curved quartz optical input window labelled in Figure 5.2 is 7 mm thick with a 72 mm active diameter and a radius of curvature of 55 mm. A S20 multi-alkali ($SbNa_2KCs$) photocathode is deposited on the concave side of the window surface. The combined quantum efficiency of the window and the photocathode coating as a function of the wavelength of normally incident light is shown in Figure 5.5 for several HPD prototypes up to and including the 10 MHz HPD studied here. The distribution corresponding to

this in Figure 5.5 is denoted by the label "Alice-LHCb HPD 1". The fractional transmission of the quartz optical window over the same wavelength range is also shown. These figures show that at long wavelengths the sensitivity of the photocathode is limited by the photoemission threshold of the S20 multi-alkali coating, whereas at short wavelengths, the detection efficiency is limited by the transmission properties of the window.

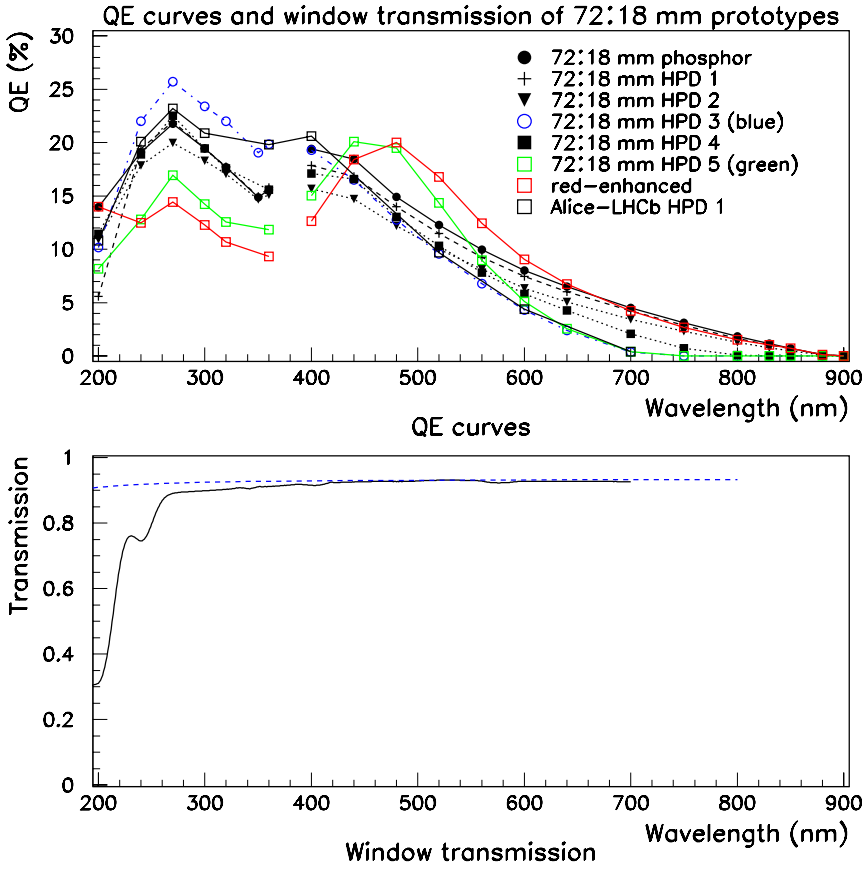

Figure 5.5: *Quantum efficiency and fractional transmittance of the HPD quartz optical input window as function of the wavelength of normally incident light.*

It is shown in Figure 5.2 that when a photon is incident upon the input window, a photoelectron is released from the inside of the photocathode at -20 kV, and is accelerated onto the anode assembly at 0 kV. The photoelectrons follow a cross-focused

path defined by the electron optics within the tube. This consists of two electrodes set at -19.7 kV and -15.8 kV. A simulation of the path followed by such a photoelectron is illustrated in Figure 5.6.

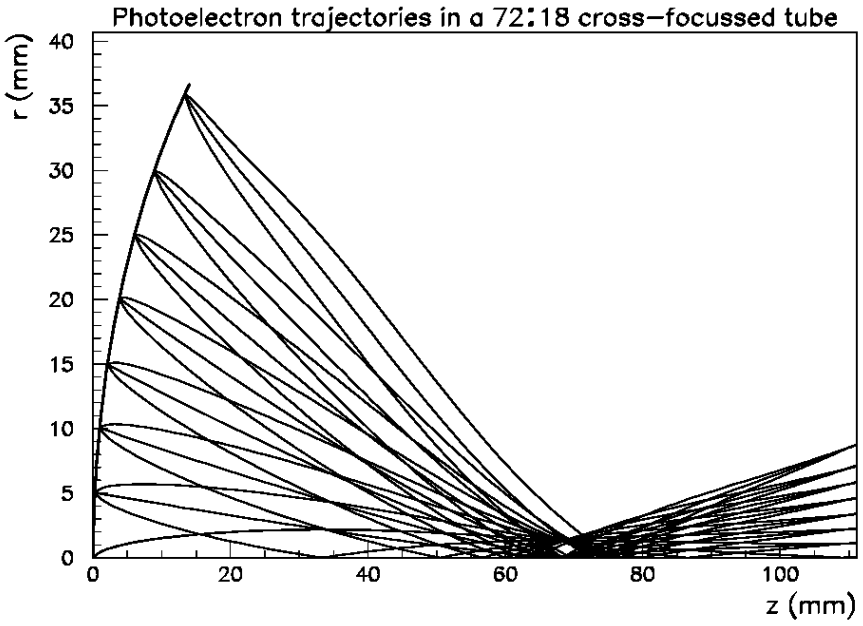

Figure 5.6: *Radial coordinate of the calculated photoelectron trajectories for nominal tube operation, illustrating the performance of the cross-focusing electron optics. The vertical axis is stretched for clarity [134].*

A second function of the electron optics is that of demagnification. The image formed by the incident photoelectrons at the cathode is demagnified onto the anode according to the demagnification law

$$r_{\mathrm{p}} = \alpha\, r_{\mathrm{c}} + \beta\, r_{\mathrm{c}}^2. \tag{5.1}$$

In Equation 5.1, r_{c} is the radial coordinate with respect to the tube axis of the emitted photoelectron at the photocathode and r_{p} is the radial coordinate with respect to the tube axis of the same photoelectron after demagnification at the anode. The constant α is the linear demagnification and the constant, β is related to the edge distortion. The on-axis (away from the edge of the anode) design values of α and β are 0.216 and $0.7{\times}10^{-3}\,\mathrm{mm}^{-1}$ respectively [134]. Since $\alpha \gg \beta$, the demagnification is said to be almost

linear across the photocathode surface.

The spatial resolution of the electron optics within the tube is described by the width of the Point Spread Function (PSF)[b] which measures the radial distribution of incident photoelectrons on the anode surface due to a point source of photoelectrons from the photocathode surface. Assuming a blue light illumination at 400 nm then the standard deviation of the PSF at the anode has been determined to be ∼33 μm (on-axis) and ∼65 μm (off-axis) which is much smaller than the anode pixel dimensions of $425\,\mu\text{m} \times 50\,\mu\text{m}$. Assuming a demagnification of 0.216 (on-axis) and 0.241 (off-axis) then this corresponds to a spatial resolution at the photocathode of ∼150 μm (on-axis) and ∼225 μm (off-axis) [134].

5.2.2 Anode

The anode is a hybrid structure consisting of a reverse-biased silicon (Si) 256 × 32 pixel array detector. Each pixel is solder-bump bonded to an ALICE1LHCb front-end binary pixel readout chip [137]. The Si detectors are patterned on a standard 300 μm-thick n-type silicon by the company Canberra Semiconductor[c]. The p^+-n junctions in the Si are formed by an array of 256 × 32 p^+ implants[d] in the n-bulk silicon. This is known as the junction side of the detector. The other side of the n-bulk silicon is doped[e] to form a 150 μm-thick n^+ implant "ohmic"(backplane) layer. This is the surface upon which the photoelectrons emitted from the photocathode are incident. Its thickness is chosen to minimise the energy loss by a photoelectron while traversing the Si sensor. It is also the surface from which an analogue (backpulse) signal is read. The mechanical and electrical connection between each of the p^+ implants on the Si detector and the individual pixels of the 750 μm thick ALICE1LHCb readout chip is made by a eutectic[f]

[b] In the spatial domain of an optical system, the PSF describes the degree to which an optical system blurs (spreads) a point of light.

[c] Canberra Semiconductors N.V., Lammerdries 25, 2250 Olen, Belgium.

[d] Boron at $5\times10^{16}\text{cm}^{-2}$.

[e] Arsenic at $5\times10^{15}\text{cm}^{-2}$

[f] A composition of two or more metals that melts at a single temperature and not over a range.

Sn-Pb solder bump-bond which is produced by the company VTT[g].

5.2.3 ALICE1LHCb pixel readout chip

The ALICE1LHCb binary readout chip has been developed as a common project between the LHCb and ALICE experiments [138]. In addition to its use in HPDs, the ALICE1LHCb readout chip is to be used in the silicon pixel detectors of the ALICE Inner Tracking System (ITS). In both cases, its function is to process the signal generated by photoelectrons incident upon a pixelated silicon detector, to compare them to a fixed threshold, and convert them to a bit pattern corresponding to the location of the hits. The readout chip used for photoelectron detection within the LHCb RICH must meet the following requirements [134, 139].

- **Operational threshold $<$ 2000 e^- :** The HPD photocathode is at -20 kV and the average energy required to create one electron-hole pair is 3.65 eV [37]. Assuming no losses in the n^+ ohmic layer, the most probable signal size created in the Si detector from one photoelectron is therefore $\sim$5000e^-. However the incident photoelectron may deposit its charge across two adjacent pixels, in which case the signal size can be reduced to $\sim$2500e^-. In addition there will be losses within the n^+ ohmic layer and so the readout chip must to be able to read signals of an even lower threshold.

- **Acceptance of large signals without saturation :** Large signals can be created in the Si detector by minimum-ionising particles ($\sim$ 22000 e^- [37]) or by Cherenkov light produced in the input window of the HPD [140]. The chip must be able to accept such large signals without saturation, and, when saturation does occur, be able to recover in a reasonable time.

- **Minimum power consumption :** The readout chip is vacuum-encapsulated within the HPD and so must consume a minimum amount of power. In [140] the

[g]VTT Electronics, P.O. Box 1101, FIN-02044 VTT, Finland.

total power consumption of the readout chip was estimated to be ~ 480 mW.

- **Time resolution :** For the readout chip to be compatible with the LHC bunch-crossing frequency, it must be able to read out the Si detector within 25 ns (referred to as the time resolution). It must be able to correctly discriminate between hits and also associate (i.e. time-tag) them with a specific bunch-crossing.

- **Radiation tolerance :** The chip must be able to withstand total-dose radiation levels of 30 kRad across 10 years of operation [140].

- **Compatibility with HPD manufacturing process :** The chip must be able to withstand and retain full functionality after undergoing the HPD manufacturing process where the anode undergoes vacuum encapsulation at 300-350 $^\circ$ C within the tube structure.

The readout chip has been fabricated using a commercial 0.25 μm CMOS (Complementary Metal Oxide Silicon) technology. A schematic plan of the chip is shown in Figure 5.7. The chip measures 14.0×15.0 mm^2, with an active area of 13.6×12.8 mm^2. The active area is divided into $32 \times 256 = 8192$ pixels each of size 425×50 μm^2. The chip is designed to operate in two modes, referred to as the ALICE and LHCb modes. When the chip is in its ALICE mode, then all of the 8192 pixels are read out individually. In the LHCb mode pixels are grouped together to form an array of $32 \times 32 = 1024$ super-pixels. Four pixels on the chip provide test points that can be used to verify the response of the different parts of the pixel matrix. These are located in the top row at column numbers 1, 9, 17 and 25.

The remainder of the chip consists of the peripheral control logic that controls the chip during data acquisition, biasing circuitry, a serial control and configuration interface (JTAG) [141] and the input/output pads. The JTAG interface controls the 42 on-chip digital-to-analogue converters (DACS) that provide voltage and current biases to the analogue and digital circuitry within each pixel cell. Each of the 8192 individual pixel cells is divided into an analogue and a digital part, as shown in Figure 5.8 [137].

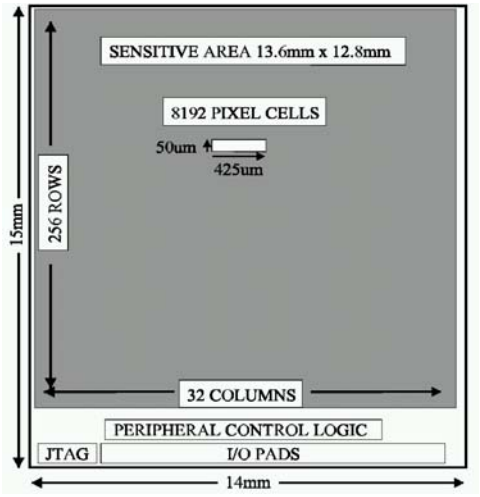

Figure 5.7: *Schematic of the ALICE1LHCb pixel chip.*

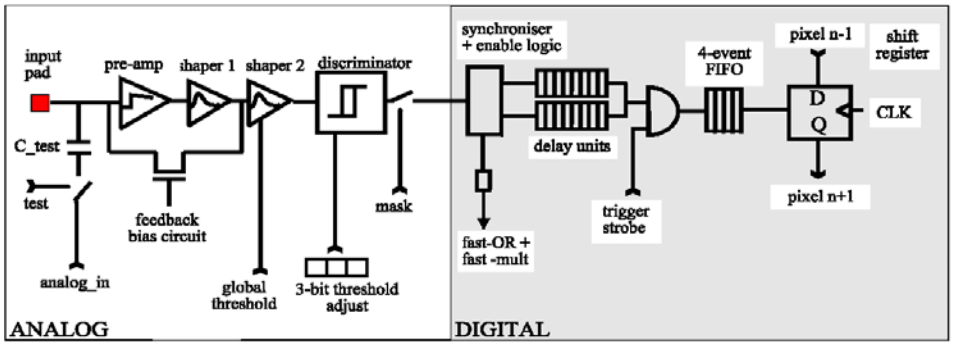

Figure 5.8: *Schematic diagram of the ALICE1LHCb pixel cell architecture. The pixel cell is divided into an analogue and a digital part.*

The analogue part consists of a pre-amplifier, followed by a shaper stage with a peaking time of 25 ns, and finally a discriminator. Both the pre-amplifier and the shaper are differential, with one input carrying the detector signal and the other tied to a reference. This improves the noise suppression of the circuit. The discriminator transforms the analogue signal into a digital signal by comparing the output of the shaper with a threshold, which is fixed globally across the chip via the control and configuration (JTAG) interface.

The LHCb experiment requires that the global threshold be < 2000 e$^-$, with a pixel-to-pixel RMS spread of < 200 e$^-$. To improve pixel-to-pixel uniformity, there is a 3-bit threshold adjust which allows this global threshold to be fine tuned (over a range of $\sim$960 e$^-$) on a pixel-by-pixel basis. Each pixel can be individually addressed for electrical testing and for masking. To perform electrical tests, it is possible to apply a test input to the pre-amplifier using a voltage step applied across a capacitor $C_{\text{test}} \sim 16$ pF. The size of the voltage step is controlled by two DC voltage levels applied to the chip. A mask flip-flop[h] allows an individual pixel to be disabled should it be defective or noisy, preventing it from injecting spurious information into the data stream [142].

The discriminator output is fed into the digital part of the cell. This consists of two digital delay units, a trigger strobe, a FIFO[i] and a shift register. The digital delay units store a hit for a time which is set to that of the trigger latency . Each delay unit registers a single hit and is then unavailable to register further hits during the trigger latency. In order that inefficiencies are not introduced there must be sufficient delay units available per channel to accommodate the total number of hits expected per channel during the trigger latency. This limits the maximum channel occupancy that can be handled. The hit is stored in a buffer which is implemented as a FIFO memory.

Figure 5.9 shows how the chip is configured to comprise of 32×32 super-pixels. Each super-pixel is formed from eight row-wise pixels when their discriminator outputs are OR-ed together and their sixteen delay units configured as an array. Four of the 4-event FIFOs are connected together to form a a 16-event FIFO which can be written to by any of the 16 delay units within the 8 pixels in the super-pixel. The output of the 16-event FIFO is then loaded into the flip-flop of the top pixel in the super-pixel, bypassing the other seven pixels during readout. Data is then shifted out of the pixel cell (and out of all the pixels cells in the chip) by a shift register[j] in time with the system clock. There were two main limitations to the performance of the chip. First

[h] A device that may assume either of two reversible, stable states.

[i] A queueing discipline in which entities in a queue leave the queue in the same order in which they arrive.

[j] A storage device, in which a serially ordered set of data may be moved as a unit into a discrete number of storage locations.

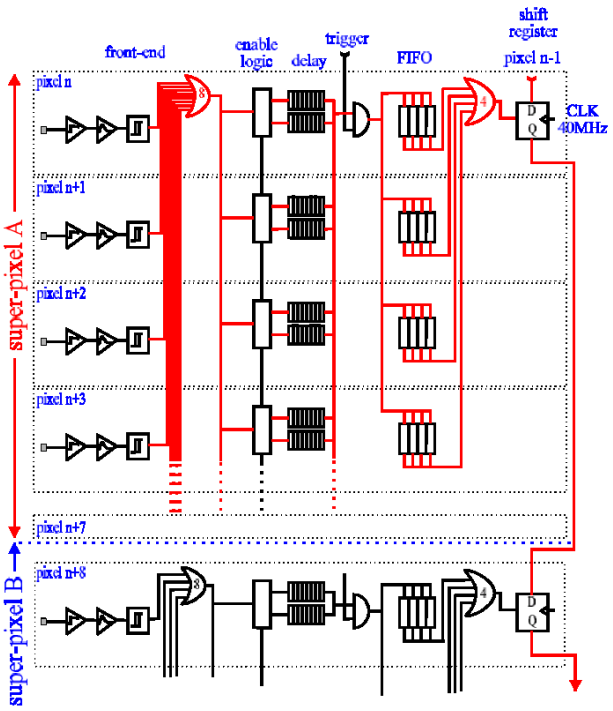

Figure 5.9: *Pixel cell configuration in the LHCb mode of the ALICE1LHCb chip.*

the digital circuitry of the chip was found to be limited to a maximum clock frequency of 15 MHz. The biggest factor causing this was that of power supply drops due to mechanical constraints caused by the pixel size. Second, the performance of the test pulser designed for electrical testing and calibration of the chip was limited because of the effects of parasitic capacitance and the non-uniformity of the pulse size across the pixel matrix. The test pulser was designed to supply a step signal of 50 mV across the capacitor C_{test} in the analogue part of each pixel chip. This step signal would simulate the instantaneous injection of a charge equivalent[k] to 5000e$^-$.

Within the chip the pulser step signal output is distributed to each of the 8192 pixels through a long line of interconnection lines and the parasitic capacitance associated with each line is $\sim$ 90 pF. The effect of this parasitic capacitance is to change the shape of the pulse reaching pixel from an ideal step function. The pixels on the chip are connected

[k]Given that the average energy required to create on electron-hole pair in Silicon is 3.65 eV, then for this to be achieved over all of the 8192 pixels, 3.65 eV $\times$ 8192 pixels $\simeq$ 5000e$^-$ would need to be injected.

to the output of the pulser through different RC paths meaning that the size of the pulse at the input of each pixel is not uniform across the pixel matrix. These effects are shown in Figure 5.10. Figure 5.11 shows the systematic variation of the threshold of the chip across the pixel matrix when a test pulse is injected. The test pulser non-uniformity meant that it could not be used to perform certain calibration and cross-check measurements such as calculating the fraction of working ALICE1LHCb readout pixels.

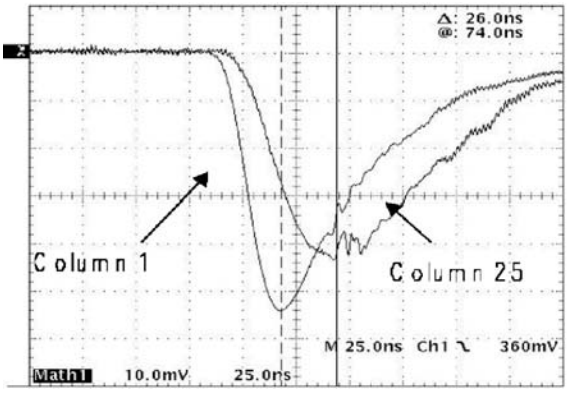

Figure 5.10: *The test pulse shape as seen at the output of shaper2 according to test pixels located at the top of columns 1 and 25. [143]*

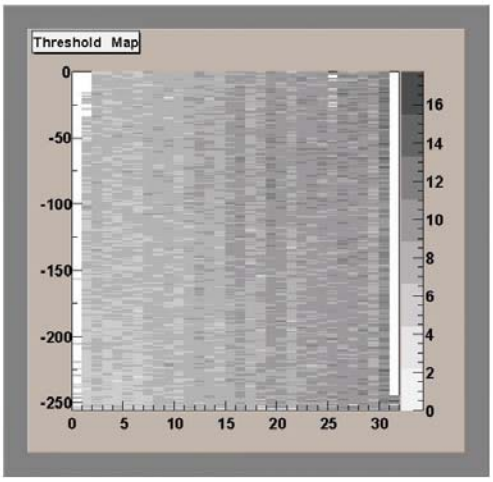

Figure 5.11: *Pixel threshold map of the ALICE1LHCb chip when test pulse is applied.*

5.2.4 Other components

The ALICE1LHCb readout chip is mounted and gold-wire bonded to a ceramic pin grid array (PGA) carrier, which is manufactured by the Kyocera[l] company. The anode and carrier are shown in Figure 5.12 mounted in the ZIF socket of the LHCb "daughtercard". The data from the anode is transmitted out of the HPD by means of vacuum-tight feed throughs. The HPD outer tube casing and the electrodes are made of Kovar[m] metal.

[l]Kyocera Corporation, Japan

[m]Kovar is a vacuum melted low expansion alloy with composition Ni (29.0 %), Fe (53.0 %), Co (17.0 %), C (0.04 % max), Mn (0.50 % max), Si (0.20 % max), Al (0.10 % max), Cr (0.20 % max), Mg (0.10 % max), Zr (0.10 % max), Ti (0.10 % max), Cu (0.20 % max) and Mo (0.20 % max).

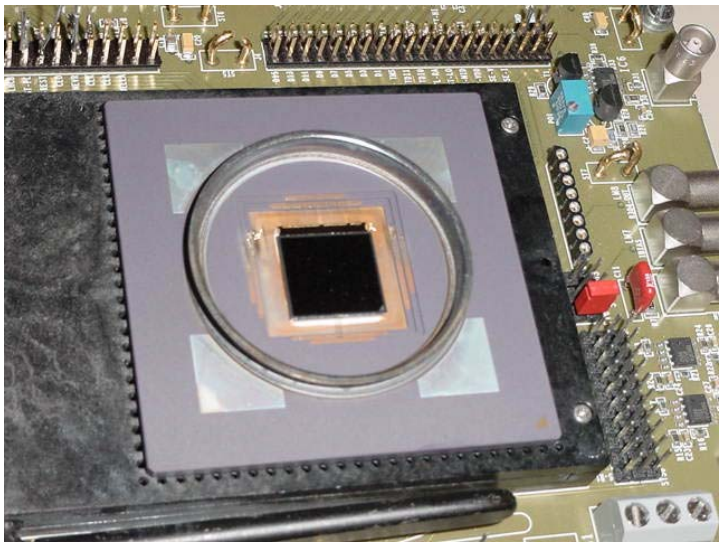

Figure 5.12: *The ALICE1LHCb readout chip is shown mounted and gold wire-bonded onto a ceramic pin grid array.*

5.3 Performance in magnetic fields

The HPDs will lie within the non-uniform fringe fields of the LHCb magnetic field. Extensive magnetic field tests have been carried out using the phosphor screen anode and a Helmholtz coil [144]. The aim of these tests was to determine the effect of magnetic field distortions on the functionality of the electron optics within the HPDs. The Helmholtz coil was able to provide fields of up to 36 Gauss, the maximum field strength expected in the photodetector volume of the upstream RICH system. The phosphor anode tube was tested in two configurations one where its axis transverse to the Helmholtz coil axis (transverse B field) and one where the phosphor tube axis was parallel to the Helmholtz coil (longitudinal B field). The distortions at the anode of the image of an LED cross pattern for longitudinal or transverse magnetic fields up to 30 Gauss were noted. Figures 5.13 and 5.14 show the images of the LED cross pattern on the unshielded HPD with a phosphor anode, with and without the presence of a 30 Gauss longitudinal

and transverse applied magnetic field respectively.

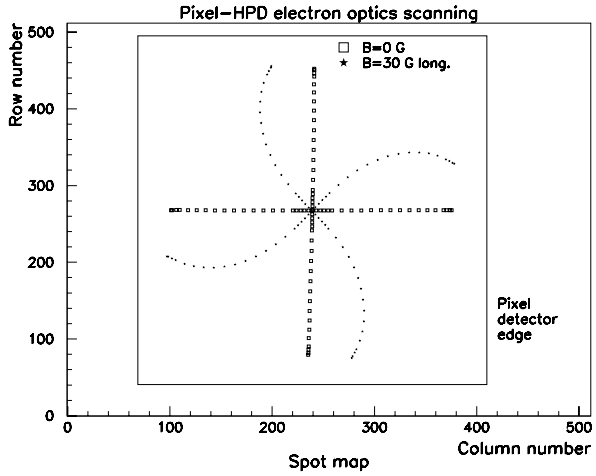

Figure 5.13: *The image of a cross as seen on a phosphor anode, with and without a longitudinal B field of 3 mT (30 Gauss).*

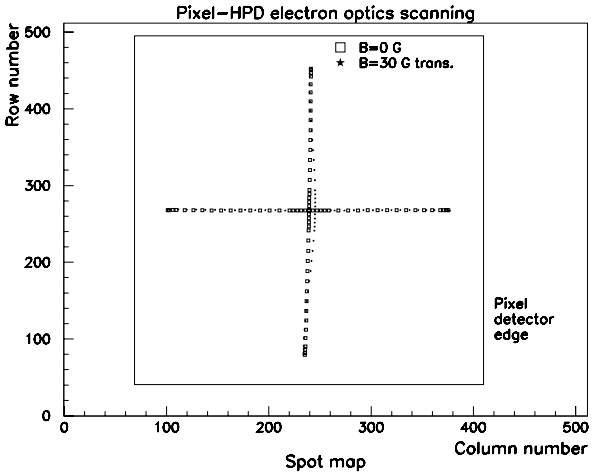

Figure 5.14: *The image of a cross as seen on a phosphor anode, with and without a transverse B field of 3 mT (30 Gauss).*

It is seen that in the presence of a longitudinal B field, the LED image becomes stretched and rotated. However, in the presence of a transverse B field, a non-uniform shift is introduced in the direction perpendicular to the field orientation. In both Figures 5.13 and 5.14, it is seen that the cross remains within the area of the Si sensor (this area is marked by the square box), thus these image distortions due to magnetic field effects can be corrected offline.

5.4 Local magnetic shielding and Photon detector mounting

Each HPD is to be surrounded by a magnetic shield which is a 0.9 mm thick μ-metal[n]cylinder, 86 mm in diameter and 140 mm in length. The shielding is to extend 20 mm beyond the HPD entrance window. Figure 5.15 is an outline drawing of the pixel

[n] μ-metal is an iron-nickel alloy which is used in the shielding of low magnetic fields

HPD and its magnetic shield. The HPDs will be arranged in a hexagonal close-packed array arrangement within a metal support structure at the photodetector plane, as illustrated in Figure 5.16. The packing fraction of a hexagonal close-packing arrangement is 90.7 % and the distance between the tube centres is 87 mm. The active diameter of each HPD is 75 mm and therefore the active fraction of the surface area covered by the HPDs, ϵ_a is

$$\epsilon_a = 0.907 \times \left(\frac{75\ \text{mm}}{87\ \text{mm}}\right)^2 = 0.67. \tag{5.2}$$

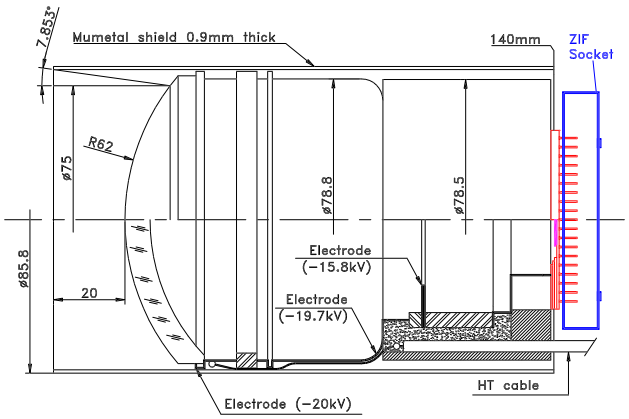

Figure 5.15: *Outline drawing of the pixel HPD and the μ-metal magnetic shield. The high voltage (HV) cable and the ZIF socket are shown.*

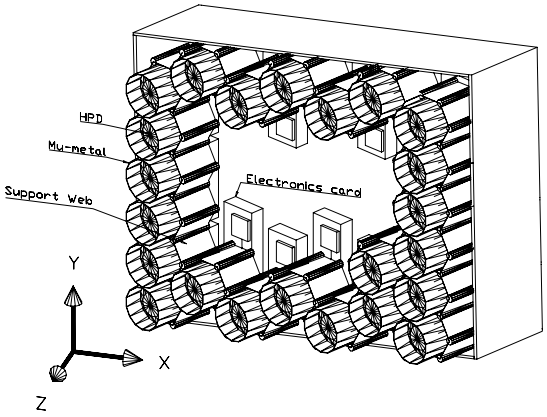

Figure 5.16: *Part of the photodetector array for one quadrant in RICH-1. The HPDs are to be arranged in a hexagonal close-packed arrangement. The individual Level-0 interface electronics boards, μ-metal shields and the HPD support web are also shown [99].*

5.5 Test setup

The apparatus to perform the measurements for the calculation of the efficiency of a prototype pixel HPD to single photoelectrons consists of the following components.

Light Source: Measurements were carried out in a light-tight box with a low in-

tensity blue light-emitting diode (LED) as a light source. The LED was operated in pulsed mode at a rate of 1 μs, with the duration of each pulse being 5 ns. The LED was powered by a voltage supply set at 110 V.

High voltage (HV) source: The high voltages for the photocathode and focusing electrodes of the HPD are provided using a commercial low-ripple[o] Matsusada K7-20N supply which is mounted on the outside of the light-tight box [145]. By design this provides an output voltage of -20 kV d.c. Figure 5.17 shows the HPD voltage supply scheme and bleeder resistor chain which monitor and control the HPD HV source using the voltage range 0 to 10 V.

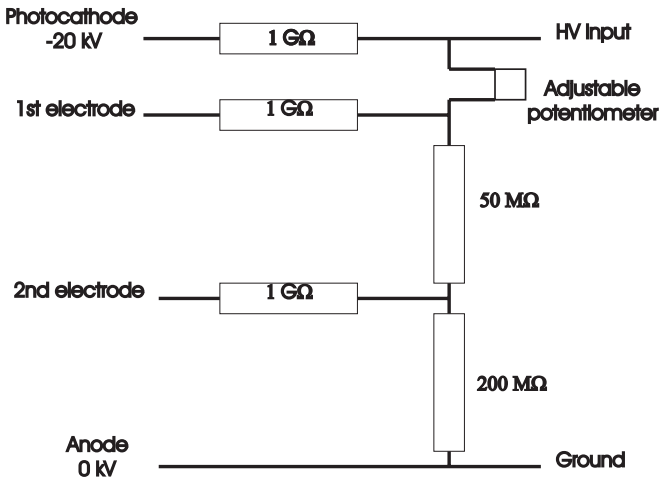

Figure 5.17: *Schematic of the HPD voltage supply scheme and bleeder resistor chain.*

Resistor bleeder chain: A 250 MΩ potential divider consisting of one 200 Ω and one 50M Ω resistor, and an adjustable potentiometer set at 3.5 MΩ sets the three different high voltages (-20 kV, -19.7 kV and -15.83 kV) at which the photocathode, first and second electrodes respectively are designed to be operated. Damping resistors of size 1 GΩ are inserted between the divider and the tube. This results in a high voltage input measured at the photocathode of -19.35 ± 0.01 kV when the photocathode is set at -20

[o] In a dc voltage, the alternating component that is coupled into a circuit from a source of interference.

kV. The first and second electrodes will then typically have value of ∼-19.06 kV and ∼-15.22 kV respectively with the anode at 0 kV.

Temperature monitoring: The pixel chip temperature is recorded during operation using a Pt100 temperature sensor [146]. The temperature sensor and the HV control are interfaced to a PC using a National Instruments (NI) 6035E multi-purpose data-acquisition card [147]. Labview software is used for monitoring and control [148].

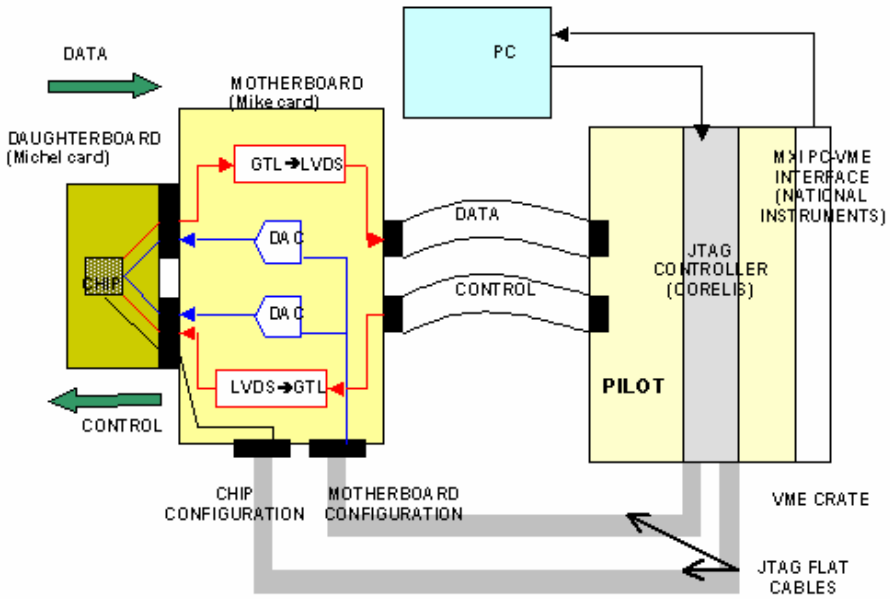

Figure 5.18: *The ALICE1LHCb pixel detector readout system [149]. The main components are the DAQ VME crate, the DAQ adapter board ('motherboard') and the pixel carrier board ('daughterboard').*

Pixel detector readout: This is illustrated in Figure 5.18. The main components are the DAQ VME crate, the DAQ adapter board ('motherboard') and the pixel carrier board ('daughterboard'). A PC is connected to the VME crate by a National Instruments MXI connection [150] and is used to control the readout and storage of data from the chip via a National Instruments Labview interface [148]. The VME crate contains a JTAG control module, a MXI control module and a PILOT readout module board. The JTAG control module has two channels, one is used for the configuration of the readout

chip and the other is used to control the motherboard. Two channels are used to reduce the risk of a faulty readout chip impeding the correct function of the motherboard. The PILOT board controls how the chip is read [151]. It also zero suppresses and encodes the data so that the amount of data to be stored in an output buffer is reduced. The motherboard contains DACs that are configured using the PC via the JTAG controller in the VME crate. It also contains circuitry for power and bias supplies. The daughterboard is the interface between the readout chip and the rest of the pixel detector readout system.

5.6 Photoelectron response

The HPD prototype is characterised by the efficiency of its anode in detecting single photoelectrons when a light source such as a pulsed LED, is incident upon the HPD photocathode. This quantity $\epsilon_{\text{p.e.}}$ is measured purely for research and development and is required to be $\simeq 85\,\%$. $\epsilon_{\text{p.e.}}$ is determined from quantities derived from measuring the two different signals that are able to be read out from the HPD. The two signals and the information that can be derived from them are as follows.

Binary signal: The binary signal is read via the ALICE1LHCb chip and shows the response of each of the 8192 pixels (0 = pixel doesn't respond, 1 = pixel does respond) to the LED pulse incident upon the silicon detector surface of the HPD anode. From this signal the average number of firing pixels $\mu^{'}$ per LED pulse is determined.

Analogue signal: The analogue ('backpulse') signal is read from the n^{+} backplane of the silicon detector anode. In the test setup this signal provides global analogue information from which the average number of photoelectrons μ per LED pulse incident upon the silicon detector surface of the HPD anode is determined. Once the HPD is mounted in the RICH photodetector array as shown in Figure 5.16 the analogue signal is not read out as it is not needed for the detection of Cherenkov rings.

The number of photons per LED pulse follows the Poisson distribution [152]. Therefore the number of photoelectrons incident upon the silicon detector surface per LED pulse, and the number of firing pixels per LED pulse will both obey the Poisson distribution with means μ and $\mu^{'}$ respectively. The probability of one pixel being hit by two or more photoelectrons is negligible ($< 10^{-6}$) [153]. The HPD single photoelectron efficiency $\epsilon_{\text{p.e.}}$, is given by

$$\epsilon_{\text{p.e.}} = \frac{\mu^{'}}{\mu}. \tag{5.3}$$

where the values of μ and $\mu^{'}$ are obtained from data taken at the same values of HPD High Voltage (HV) and bias voltage V_{bias} applied across the silicon detector within the anode.

5.7 Binary data

Binary data is read from the HPD using the ALICE1LHCb chip when the PILOT board receives an external trigger from the LED. The DAQ adapter board and PILOT board have been synchronised with the pulsed LED light source prior to data-taking so that the number of external triggers received by the PILOT board corresponds directly to the number of LED pulses. The length of time over which a set of binary data is collected is specified by the number of external triggers which is set using the PC via the Labview interface.

Each set of binary data is collected at a specific HPD HV and V_{bias} and with the ALICE1LHCb chip set in the ALICE readout mode. The HPD HV value noted is the value at which the photocathode is set rather than a HV value that could be measured at the photocathode. The following information is obtained for each set of data:

- Number of LED pulses. This is equal to the number of external triggers applied to the PILOT board.

- Number of empty triggers. This is the number of LED pulses to which no pixel on the readout chip responded.
- Number of LED pulses which caused at least one readout chip pixel to respond.
- An efficiency ϵ which is defined as

$$\epsilon = \frac{\#\text{ external triggers to which } \geq 1 \text{ readout pixels fire}}{\#\text{ external triggers applied}} \tag{5.4}$$

5.7.1 Charge-sharing

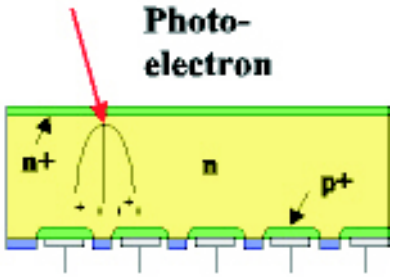

Figure 5.19: *Schematic illustrating charge-sharing at the silicon diode surface. Due to charge-sharing in the lateral direction, one photoelectron may cause more than one anode pixel to fire [154].*

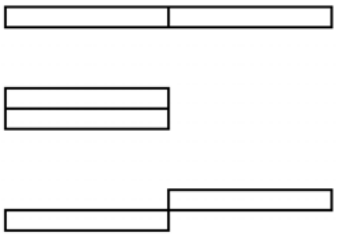

Figure 5.20: *One photoelectron incident upon the anode may for example, cause two pixels to fire in any one of the horizontal, vertical or diagonal two-pixel cluster configurations shown.*

Holes are created at the n^+ ohmic layer of the silicon detector part of the anode. These drift across the 300 μm-thick silicon, but simultaneously diffuse laterally and their charge is shared among the other pixels. This is illustrated in Figure 5.19. This charge-sharing effect means that for each photoelectron emitted from the photocathode one or more of the anode pixels may respond and so a signal may be read from more than one of the readout chip pixels. As a consequence it is more convenient to consider groups of pixels ("clusters") which respond to one photoelectron incident upon the anode rather than to consider individual pixels that respond. For example one photoelectron may result in a signal from two neighbouring pixels from the readout chip in any of the horizontal, vertical or diagonal configurations shown in Figure 5.20.

5.7.2 Estimating $\mu^{'}$ using binary data.

$\mu^{'}$ can be estimated in two ways. Assuming that the number of readout chip pixels from which a signal was read per LED pulse follows Poisson statistics with mean $\mu^{'}$, then the probability that no signal was read from a pixel due to a particular LED pulse is

$$P(0) = e^{-\mu^{'}} = 1 - \epsilon. \tag{5.5}$$

ϵ is the efficiency value from Equation 5.4 determined online at the end of each set of binary data-taking. Therefore the first estimate of $\mu^{'}$ is given by

$$\mu_1^{'} = \ -\ln(1-\epsilon). \tag{5.6}$$

$\mu^{'}$ can also be estimated by

$$\mu_2^{'} = \frac{\#\ clusters\ due\ to\ all\ external\ triggers}{total\ \#\ external\ triggers}. \tag{5.7}$$

The estimate for $\mu^{'}$ given by Equation 5.6 does not account for clustering in that it does not account for the number of photoelectrons which caused a signal to be read. This is accounted for in the estimate for $\mu^{'}$ given by Equation 5.7.

For a measured tube HPD high voltage of -19 kV, the silicon detector bias voltage $V_{\rm bias}$ was scanned over the range 27.5 V to 80 V in 2.5 V intervals. A second scan was then carried out, where, at a constant silicon detector bias voltage of 80 V, the HPD high voltage was varied from -5 kV to -19 kV in 1 kV intervals. From each of these sets of data, two estimates of $\mu^{'}$ were calculated using Equations 5.6 and 5.7. These values are listed in Tables 5.1 and 5.2. These values are seen to be consistent with each other within errors at all values of HV and $V_{\rm bias}$ showing that the effect of charge sharing is small.

Figure 5.21 shows $\mu_1^{'}$ as a function of silicon detector bias (for a HPD high voltage of -19 kV). The incident photoelectrons are stopped within the first few μm of the silicon

H.V. (kV)	$\mu_1^{'} \pm \sigma_1$	$\mu_2^{'} \pm \sigma_2$
5.0 ± 0.1	0.00049 ± 0.00003	0.00049 ± 0.00003
6.0 ± 0.1	0.0094 ± 0.0001	0.0094 ± 0.0001
7.0 ± 0.1	0.1118 ± 0.0005	0.1121 ± 0.0005
8.0 ± 0.1	0.456 ± 0.001	0.457 ± 0.001
9.0 ± 0.1	0.850 ± 0.002	0.850 ± 0.002
10.0 ± 0.1	1.123 ± 0.002	1.121 ± 0.002
11.0 ± 0.1	1.307 ± 0.002	1.304 ± 0.002
12.0 ± 0.1	1.444 ± 0.003	1.444 ± 0.003
13.0 ± 0.1	1.552 ± 0.003	1.550 ± 0.003
14.0 ± 0.1	1.642 ± 0.003	1.641 ± 0.003
15.0 ± 0.1	1.719 ± 0.003	1.715 ± 0.003
16.0 ± 0.1	1.774 ± 0.003	1.773 ± 0.003
17.0 ± 0.1	1.823 ± 0.003	1.822 ± 0.003
18.0 ± 0.1	1.857 ± 0.003	1.859 ± 0.003
19.0 ± 0.1	1.901 ± 0.003	1.903 ± 0.003

Table 5.1: $\mu^{'}$ *as a function of HPD high voltage.*

V_{bias} (V)	$\mu_1^{'} \pm \sigma_1$	$\mu_2^{'} \pm \sigma_2$
25.0 ± 0.1	0.00017 ± 0.00002	0.00017 ± 0.00002
27.5 ± 0.1	0.00023 ± 0.00002	0.00029 ± 0.00002
30.0 ± 0.1	0.0258 ± 0.0002	0.0268 ± 0.0002
32.5 ± 0.1	0.3012 ± 0.0008	0.3547 ± 0.0010
35.5 ± 0.1	0.781 ± 0.002	0.917 ± 0.002
35.0 ± 0.1	1.229 ± 0.002	1.296 ± 0.002
37.5 ± 0.1	1.499 ± 0.003	1.508 ± 0.003
40.0 ± 0.1	1.613 ± 0.003	1.613 ± 0.003
42.5 ± 0.1	1.664 ± 0.003	1.666 ± 0.003
45.0 ± 0.1	1.704 ± 0.003	1.701 ± 0.003
47.5 ± 0.1	1.723 ± 0.003	1.722 ± 0.003
50.0 ± 0.1	1.737 ± 0.003	1.738 ± 0.003
52.5 ± 0.1	1.759 ± 0.003	1.753 ± 0.003
55.0 ± 0.1	1.754 ± 0.003	1.755 ± 0.003
57.5 ± 0.1	1.767 ± 0.003	1.764 ± 0.003
60.0 ± 0.1	1.762 ± 0.003	1.765 ± 0.003
62.5 ± 0.1	1.761 ± 0.003	1.765 ± 0.003
65.0 ± 0.1	1.762 ± 0.003	1.765 ± 0.003
67.5 ± 0.1	1.761 ± 0.003	1.765 ± 0.003
70.0 ± 0.1	1.769 ± 0.003	1.768 ± 0.003
72.5 ± 0.1	1.768 ± 0.003	1.765 ± 0.003
75.0 ± 0.1	1.751 ± 0.003	1.757 ± 0.003
77.5 ± 0.1	1.754 ± 0.003	1.755 ± 0.003
80.0 ± 0.1	1.747 ± 0.003	1.748 ± 0.003

Table 5.2: $\mu^{'}$ *as a function of silicon detector bias voltage* V_{bias}.

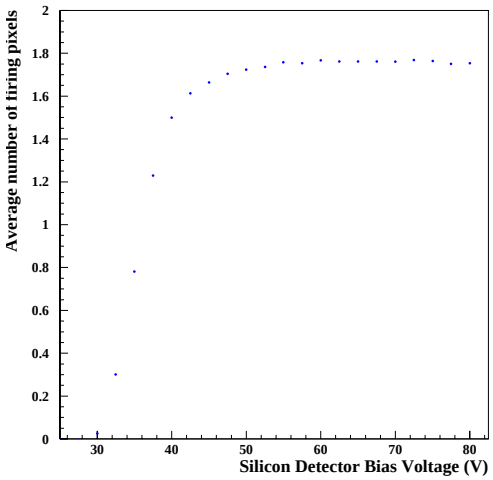

Figure 5.21: *Average number of firing pixels per LED pulse as a function of silicon detector bias voltage. The HPD high voltage is -19 kV.*

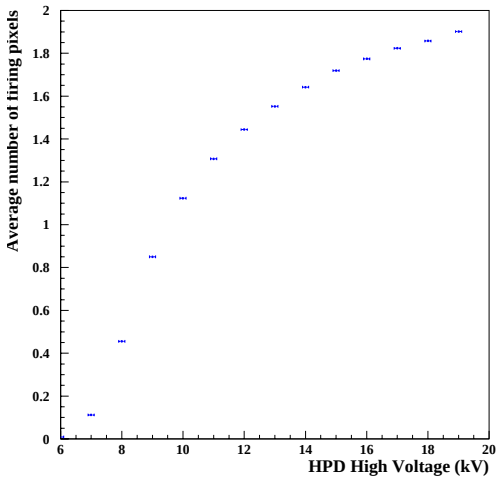

Figure 5.22: *Average number of firing pixels per LED pulse as a function of HPD high voltage, while at 80V silicon detector bias voltage.*

detector which first becomes sensitive to photoelectrons when it has been fully depleted by the applied $V_{\rm bias}$. This is seen to occur at $V_{\rm bias} \sim 30.0$ V. Above $V_{\rm bias} = 30.0$ V the silicon detector becomes over-depleted and this results in a large increase in efficiency. The distribution reaches a plateau at ~ 50 V. Beyond this value the charge collection time will decrease with increasing bias voltage and is reduced further by operating the detector with an increased overbias. $V_{\rm bias}$ is limited to a maximum value of 80 V because of the risk of avalanche breakdown within the silicon.

Figure 5.22 shows $\mu_1^{'}$ as a function of HPD high voltage (for a silicon detector bias of 80 V). The data shows the detector becoming sensitive at about -6 kV with the efficiency still increasing below -19 kV. The detector insensitivity below $\sim$ -6 kV is consistent with simulations presented in [153] of the energy loss within the n^+ ohmic backplane of the silicon detector. No plateau is reached since an increased high voltage and therefore a larger charge deposit will increase the probability of detecting backscattered photoelectrons.

The HPD is designed to be operated at a high voltage of -19/-20 kV and a $V_{\rm bias}$ of 80 V. Table 5.3 lists the calculated PDG weighted mean values and associated statistical

errors [37] of $\mu_1^{'}$ and $\mu_2^{'}$ at -19 kV and $V_{\rm bias}$ of 80 V. The statistical errors on $\mu_1^{'}$ and $\mu_2^{'}$ are too small to cover the variation found in the separate $V_{\rm bias}$ and H.V. scans (Table 5.3). An estimate of the systematic errors is taken as half the difference between the $V_{\rm bias}$ and H.V. scan values for $\mu_1^{'}$ and $\mu_2^{'}$.

$V_{\rm bias}$ = 80 V, H.V. = -19 kV	$\mu_1^{'} \pm \sigma_1$	$\mu_2^{'} \pm \sigma_2$
With variable $V_{\rm bias}$	1.747 ± 0.003	1.748 ± 0.003
With variable H.V.	1.901 ± 0.003	1.903 ± 0.003
Averaged value	1.817 ± 0.002 (stat) ± 0.079 (syst)	1.820 ± 0.002 (stat) ± 0.078 (syst)

Table 5.3: *Average number of firing pixels per LED pulse at 80 V $V_{\rm bias}$ and -19 kV high voltage.*

The value of $\mu^{'}$ at 80 V $V_{\rm bias}$ and -19 kV high voltage to be used later in the efficiency calculation is

$$\mu^{'} = 1.820 \pm 0.002\,(\text{stat}) \pm 0.079\,(\text{syst})$$

since this does not assume that the photoelectrons are produced exactly according to Poisson statistics.

5.7.3 Double pixel clusters

Figures 5.23(a) and (b) show the fraction of double pixel clusters as a function of HPD high voltage (HV), and as a function of silicon detector bias $V_{\rm bias}$. In both of these figures the vertical double pixel clusters are seen to be the most common type of double pixel clusters. Vertical double pixel clusters share a long pixel side (425 μm), the horizontal double pixel clusters share the short pixel side (50 μm) and the diagonal double pixel clusters touch only at one corner point. The vertical two-pixel clusters are much more common due to the increased probability of sharing the charge along the long pixel side rather than the short side or at a point. The shape of Figure 5.23(a) is similar to that of Figure 5.22 with no plateau being reached since the increased high voltage and therefore

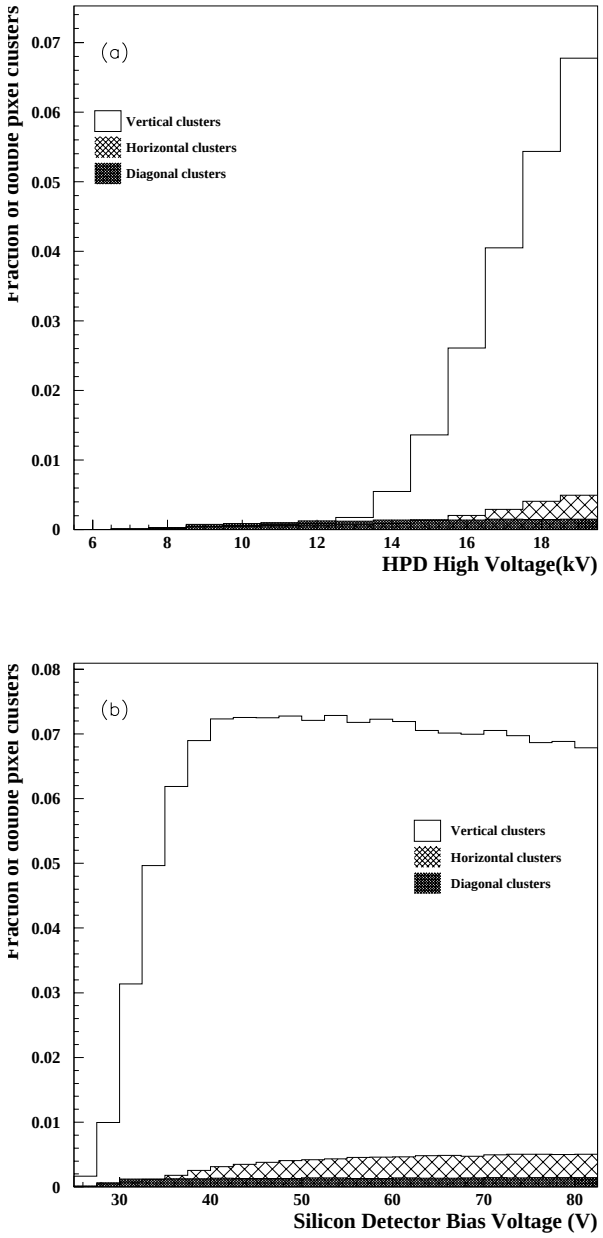

Figure 5.23: *(a) Fraction of double pixel clusters as a function of HPD high voltage. The silicon detector bias voltage is at 80V. (b) Fraction of double pixel clusters as a function of silicon detector bias voltage. The HPD high voltage is at -19 kV.*

larger charge deposit has caused an increased probability of detecting backscattered photoelectrons. The shape of Figure 5.23(b) is similar to that of Figure 5.21 with a

plateau reached at ~ 50 V. Beyond this value the decreasing charge collection time causes a decrease in the charge-sharing/clustering. The ratio of the number of vertical to number of horizontal two pixel clusters is ~ 15 at 80 V, -19 kV compared to the ratio of the sides of the long:short pixel edges which is ~ 8. This is consistent with previous prototypes [153].

5.7.4 Comparator threshold of the ALICE1LHCb chip

The LHCb requirement upon the global threshold of the HPD pixel readout chip is 2000 e^- with a pixel-to-pixel RMS spread of < 200 e^-. At the time that this HPD was manufactured there was no procedure in place for the testing and selection of the readout chip. A number of anodes were produced from available readout chips and after a series of tests [155, 156] upon these anodes, one was chosen to produce the 10 MHz HPD. A consequence of this is that the readout chip used in this HPD was probably not the best available at that time. A standard procedure for testing readout chips prior to their manufacture into anodes has since been implemented [157].

Figure 5.24 shows the number of readout pixels which respond as a function of the HPD high voltage setting. This reflects the global threshold distribution of the readout chip. The lower part of this distribution involving $\sim 53\%$ of the readout pixels has a Gaussian shape with a mean of 6.76 kV (~ 1880 e^-) and a standard deviation of 0.82 kV (~ 230 e^-). A non-Gaussian tail in the high threshold region is clearly visible. This behaviour is consistent with that of the half-scale prototype shown in Figure 5.3, studies of which are documented in [153]. The binary data taken at 80 V, -19 kV indicate that $\sim 58\%$ of the pixels in the anode are being read. $\sim 3\%$ of the readout pixels have too low a threshold and produce a signal due to their own electronic noise. These pixels are electrically masked prior to data taking. Niavely it could then be concluded that the remaining $\sim 39\%$ pixels have too high a threshold and are insensitive to single photoelectrons, or do not work. The study presented in [153] shows $\sim 71\%$ of the pixels being sensitive to single photoelectrons, $\sim 12\%$ of pixels have too low a threshold and

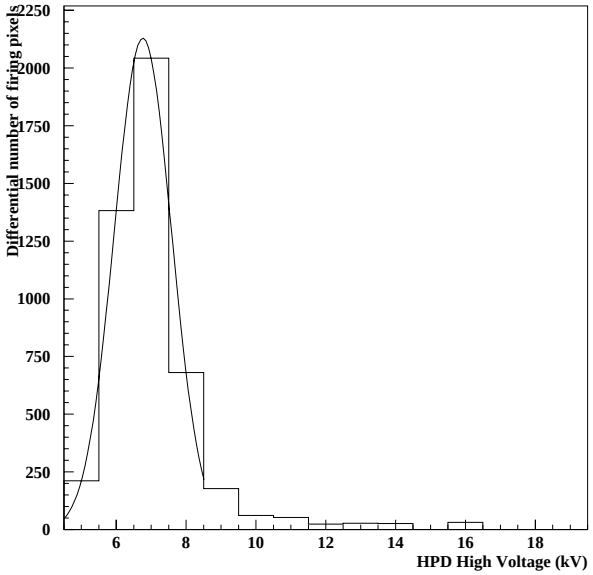

Figure 5.24: *Differential number of responding readout chip pixels as a function of HPD high voltage. The detector bias voltage is 80 V. A Gaussian fit to this distribution yields a mean of 6.76 kV (∼ 1880 e^-) and a standard deviation of 0.82 kV (∼ 230 e^-).*

were masked, and ∼ 17% have too high a threshold, with no allowance made for non-working pixels. However during the manufacture of the 10 MHz prototype a significant fraction of the bump bonds connecting the silicon detector and the readout chip became detached during the 300-350°C bakeout cycle and so the number of non-responding pixels due to detached bump-bonds is larger than in previous prototypes.

5.7.5 Bump-bonding

Figure 5.25 shows the distribution of readout pixels responding across the 256×32 pixel matrix in response to a Sr^{90} source of energy 2.25 MeV and ∼ 63000e^-. This was taken with the readout chip already bump-bonded to the silicon detector, but before the anode had been encapsulated to form the HPD. The energy of the Sr^{90} source corresponds to approximately the signal of three minimum ionising particles (MIPs) in 300 μm silicon

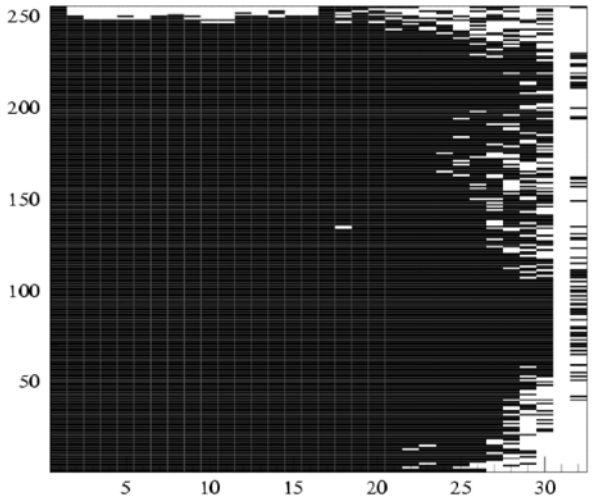

Figure 5.25: *Anode (prior to encapsulation) response to a Sr^{90} source of energy 2.25 MeV and ∼ 63000*e$^-$*. The non-working pixels are distributed along the top and right hand edges of the anode.*

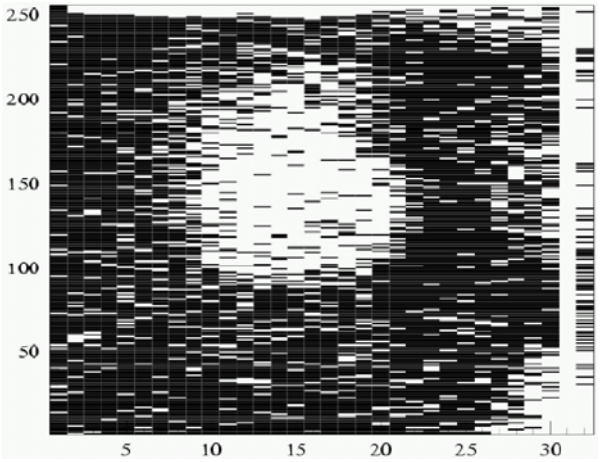

Figure 5.26: *HPD anode response to an Am^{241} source of energy 59.9 keV and ∼16,000*e$^-$*. The additional non-working pixels to those shown in Figure 5.25 are predominantly located at the centre of the anode.*

(∼63000e$^-$) and so all non-responding pixels here are assumed to be non-working pixels. These non-working pixels correspond to ∼ 5.7% of the pixel matrix. Once encapsulated in the HPD tube, Figure 5.26 shows the distribution of the same readout pixels in response to a Am^{241} source of energy 59.9 keV and ∼16,000e$^-$ which is ∼8.5 times that

of the ALICE1LHCb chip threshold. $\sim 29.2\%$ of the pixels in Figure 5.26 do not respond to this source of which from Figure 5.25 $\sim 5.7\%$ are estimated to be non-working. The difference is attributed solely to the bump-bond detachment that occurred during the anode encapsulation. This effect had not been observed with any of the previous HPD prototypes. The effect of bump-bond detachment were later confirmed by simulating the bake-out process on three similar anodes and comparing their responses to either Sr^{90} or Cd^{109} [p] sources before and after bake-out. Prior to bake-out, $0.8\%(Sr^{90})$, $0.3\%(Sr^{90})$ and $7.6\%(Cd^{109})$ of the 8192 pixels of each of these assemblies were non-responding. After bake-out, $21.4\%(Sr^{90})$, $33.9\%(Sr^{90})$ and $58.9\%(Sr^{90})$ of the pixels were found to be non-responsive [158].

5.8 Analogue data

The analogue signal discussed in this section provides global information from the n^+ backplane of the silicon detector. This is in contrast to the binary signal discussed in the previous section which provides information from each of the 8192 pixels of the readout chip. The analogue signal is read using an electronics chain consisting of a Eurorad PR 304 pre-amplifier [159], an ORTEC 579 CR-RC fast-filter amplifier with time constants of 100ns (RC) and 200ns (CR) [160], and an ORTEC 926 multi-channel analyser (MCA)[q]. By design, the MCA accepts pulses in the voltage range, 0 to 12 V, and has a maximum resolution of 8192 channels [162]. An analogue-to-digital (ADC) converter within the MCA, converts each pulse into a channel number, so that each channel corresponds to a range of $\sim$1.46 mV.

The resulting spectrum is known as the backpulse spectrum and is displayed as a graph whose horizontal axis represents the size of the analogue voltage (expressed in

[p]The Cd^{109} source has energy 22 keV ($\sim$6100e$^-$).

[q]The MCA is an instrument which sorts and counts events, where here, an event is one photoelectron incident upon the silicon detector surface. The sorting is based upon some characteristic of these events, in this case, the size of the analogue voltage signal. The events are then grouped together into channels for counting purposes [161].

terms of ADC channel numbers), and whose vertical axis represents the number of events at that particular channel number. Figure 5.27 is the backpulse spectrum obtained in between the taking of the two sets of binary data discussed in Section 5.7.

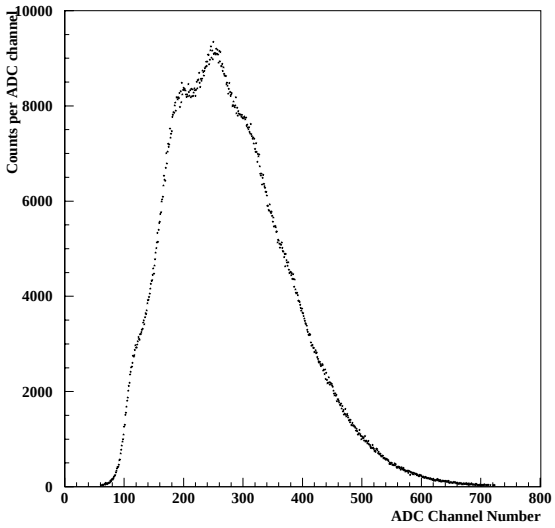

Figure 5.27: *Backpulse spectrum taken at -19 kV, 80 V* V_{bias}.

5.8.1 Backscattering at the silicon detector surface

A photoelectron that is incident upon the surface of the silicon detector part of the anode will either stop within the first few μm of the silicon, or backscatter from the surface. The probability α that a photoelectron will be backscattered is known as the backscattering coefficient [163]. α is a function of the angle of photoelectron incidence, the specimen atomic number Z, and to a lesser extent, the photoelectron energy. Assuming that the photoelectrons are incident normal to the surface of the Si diode, then based upon [164, 165] a value of $\alpha = 0.18 \pm 0.02$ is chosen as the value of the backscattering coefficient for photoelectrons with energy $\sim$20 keV.

During the backscattering process a photoelectron can transfer to the anode a factor $0 < \mathrm{q} < 1$ of its incident energy E_0 [165]. The model proposed in [153] to describe the

energy released in the anode is a triangular distribution with a base of length E_0, area $0.18 \cdot E_0$ and which peaks at $0.4 \cdot \mathrm{E}_0$. Using this triangular distribution then the average energy deposited by a backscattering photoelectron is $0.467 \cdot \mathrm{E}_0$. This model is known to be a good approximation of the experimental results for the energy range 5-20 keV [163] which from Figure 5.22 corresponds to the high voltage range covered by the HPD. The model assumes that the non-backscattered electrons release their full energy when incident on the anode and can therefore be represented by a δ-function of height (1-α) at E_0.

5.8.2 Light spectra sum rule model

The light spectra sum rule model described in [152] was applied to the data shown in Figure 5.27 using the MINUIT function minimisation and error analysis package [166]. The backpulse spectrum is modelled as a Poisson distribution composed of discrete Gaussian peaks (labelled n = 0,1,2,...) plus a continuous background. Within the light spectra sum model a single electron response (S.E.R) function $r(x;\underline{a})$ is used to represent the probability density function ($p.d.f.$) of one photoelectron having a signal of amplitude x. In this application the model proposed in the previous section to describe the energy released in the anode is used for $r(x;\underline{a})$. Within this the variable x represents the number of counts per channel of the multi-channel analyser (MCA) and the variable $\underline{a}$ represents a set of detector dependent parameters: μ_{ped}, σ_{ped}, σ_{sig}, μ and α.

μ_{ped} and σ^2_{ped} are the mean and variance of the pedestal ($n = 0$) distribution due only to the noise of the electronics readout chain. This pedestal is modelled as a Gaussian distribution. σ^2_{sig} is the variance of the signal ($n > 0$) distribution which is also described as a Gaussian. Within the model σ^2_{sig} includes the noise of the electronics readout chain σ^2_{el} and the effect of statistical fluctuations in photoelectron energy deposition in the silicon ${\sigma_{\mathrm{i}}}^2$. σ^2_{el} arises from the noise of the preamplifier in the analogue part of the readout chip and from the input capacitance seen by the preamplifier [135]. The input capacitance seen by the preamplifier depends on the bias voltage V_{bias} across the silicon detector, the coupling of the silicon detector to the readout chip and the pixel size. The

electronic noise has therefore in part been minimised by the small size of the silicon detector/readout pixels and their direct bump-bonding to one another. A response function $g(x;\underline{b})$ covering both the pedestal and the signal parts of the spectrum is used to describe these effects.

α is the backscattering coefficient and μ is the average number of photoelectrons detected at the backplane per LED pulse. d_{chan} is the distance (in numbers of ADC channels) between the peaks of the photoelectron spectrum which assumes that the MCA behaviour is linear over its input voltage range. N_{meas} is an overall normalisation coefficient which is set to be the number of events observed within the backpulse spectrum.

The model assumes that the path of the photoelectrons during acceleration toward the anode are independent of one another. This assumption allows the $p.d.f.$ for n photoelectrons with a signal of amplitude x to be recursively obtained via an n-fold convolution of $r(x;\underline{a})$:

$$r^{*n}(x;\underline{a}) = \int_0^\infty r^{*(n-1)}(y;\underline{a})r(x-y;\underline{a})dy. \tag{5.8}$$

The $p.d.f.$ of observing a signal of amplitude x from n photoelectrons when an average number of photoelectrons, μ is expected, is

$$s(x\,,n;\mu,\underline{a}) = e^{-\mu}\frac{\mu^n}{n!}r^{*n}(x;\underline{a}). \tag{5.9}$$

Within the model the backpulse spectrum $s(x,n;\mu,\underline{a},\underline{b})$ is given by $s(x,n;\mu,\underline{a})$ convoluted with $g(x;\underline{b})$,

$$s(x,n;\mu,\underline{a},\underline{b}) = \left(\sum_{n=0}^{\infty} e^{-\mu}\frac{\mu^n}{n!}r^{*n}(x;\underline{a})\right) * g(x;\underline{b}). \tag{5.10}$$

5.8.3 Fit to the backpulse spectrum

The result of the MINUIT fit using the light spectra sum model is shown in Figure 5.28. The backpulse spectrum shown has lower peak-to-valley ratio than spectra taken using previous prototypes which makes the separate photoelectron peaks much less distinguishable [167, 168]. This could mean that there was a relatively high level of electronic noise when the measurement was taken. However since this was the backpulse spectrum taken under the same conditions as the binary data discussed in Section 5.7 from which the value of $\mu^{'}$ at 80 V $V_{\rm bias}$ and -19 kV H.V. was calculated, then this should be the spectrum from which the value of μ to be used in the efficiency calculation (Equation 5.3) should be deduced.

The lower part of the pedestal region was neglected from the fit. This was as a result of the behaviour of the analogue-to-digital (ADC) signal conversion within the multi-channel analyser (MCA) where an increased dead-time prevented the ADC from converting actual pulses of interest at low channel number. Within the fit the $n = 0$, $e^{-\mu}$ term is weighted by a factor which is determined within the fit to account for the truncation at low channel values.

Parameter	MINUIT fit value
$\mu_{\rm ped}$	121.510 ± 0.002
$\sigma_{\rm ped}$	0.737 ± 0.002
$\sigma_{\rm sig}$	0.43 ± 0.001
μ	2.7246 ± 0.0002
$d_{\rm chan}$	63.966 ± 0.001
Weight	1.4667 ± 0.004

Table 5.4: *Fit parameters when the backpulse spectrum is fitted using the light spectra sum model. The errors are obtained from the MINUIT fitting package and are thought to be a significant underestimate.*

The parameters μ, $\mu_{\rm ped}$, $\sigma_{\rm ped}$, $\sigma_{\rm sig}$, $d_{\rm chan}$ and $N_{\rm meas}$ are listed in Table 5.4. The value of μ at 80 V $V_{\rm bias}$ and -19 kV high voltage to be used in the efficiency calculation is

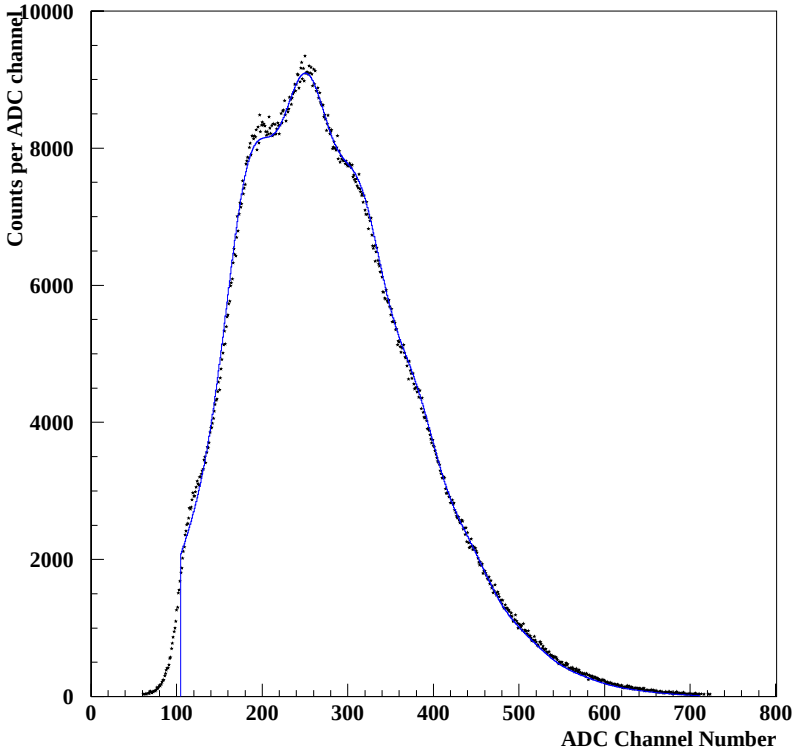

Figure 5.28: *Backpulse spectrum taken at -19 kV, 80 V V_{bias}. The data has been fitted according to the model described in [152].*

$$\mu \;=\; 2.7246 \;\pm\; 0.0002\,(\text{stat}).$$

N_{meas} was calculated at the start of the fit procedure rather than being a result of the fitting procedure itself. The value of α was fixed to be 0.18 ± 0.02. The values of σ_{sig} and σ_{ped} obtained are inconsistent with one another in that σ_{sig} is smaller than σ_{ped}. This discrepancy is attributed to the behaviour of the analogue-to-digital (ADC) signal conversion about the pedestal region and the validity of the assumptions in the light spectra sum model that both the pedestal and signal peaks can accurately be described by Gaussian distributions.

5.9 Correction factors

A number of correction factors are applied to the value of $\mu^{'}$ obtained from the binary data. These are applied to account for a number of inefficiencies within the HPD. The correction factors considered as as follows:

5.9.1 Correction due to charge-sharing at the pixel boundaries

The similarity of the estimates for $\mu^{'}$ in Table 5.3 suggests that the effect of charge-sharing is small. However whether the effect is small enough to be neglected when calculating the ratio $\mu^{'}/\mu$ is unclear. In order to quantify this the amount of charge-sharing has been estimated using a method outlined in [134] and equations derived in [169]. The electric field inside the fully depleted n-bulk silicon is given by the solution to Poisson's Equation. In one-dimension this is

$$E\left(x\right) = \frac{\left(V_{\text{bias}} - V_d\right)}{d} + \frac{2 \cdot V_d \cdot x}{d^2} \tag{5.11}$$

where V_{bias} is the applied Silicon bias voltage, V_d is the magnitude of the depletion voltage ($V_{\text{bias}} > V_d$ for depletion to occur), and d = 300 μm is the thickness of the n-bulk silicon. The time that it takes for the charge generated at point x = x_0 to drift to the p^+ implants located at x = d is obtained by integrating the following relationship between the drift velocity, v and the electric field, E(x).

$$v = \frac{dx}{dt} = \mu_{\text{d}} \cdot E(x) \tag{5.12}$$

where μ_{d} = 450 $\text{cm}^2\text{V}^{-1}\text{s}^{-1}$ is the drift mobility of the collected charge carriers. The result is

$$t(x_0) = -\frac{d^2}{2\mu_{\text{d}} V_d} \ln\left(1 - \frac{2V_d\left(d - x_0\right)}{(V_{\text{bias}} + V_d)d}\right). \tag{5.13}$$

Assuming that the depletion voltage V_d is the voltage at which the silicon detector appears to become sensitive to photoelectrons then the hole transit time t, can be calculated

for different silicon detector bias voltages $V_{\rm bias}$. At $x_0 = 0$, Equation 5.13 becomes

$$t(x=0) = -\frac{d^2}{2\mu_{\rm d} V_d} \ln\left(1 - \frac{2V_d \cdot d}{(V_{\rm bias} + V_d)d}\right). \tag{5.14}$$

It is assumed that charges which are created at a point on the n^+ backplane will upon diffusion, appear as a Gaussian distribution on the p^+ junction side of the silicon detector with a standard deviation

$$\sigma = \sqrt{2D_{\rm p}t} \tag{5.15}$$

where $D_{\rm p} = 12.3\ {\rm cm^2 V^{-1} s^{-1}}$ is the hole diffusion coefficient. Taking V_d to be 30 V from Figure 5.21 then Figures 5.29 and 5.30 show how t and σ as described by Equations 5.14 and 5.15 vary with $V_{\rm bias}$. The values of t and σ at $V_{\rm bias}$ = 80 V are 26.3 ns and 8.0 μm respectively. The value of σ is much smaller than the sides of each pixel (50 μm and 425 μm).

It is assumed that a pixel becomes inefficient if 50% of its charge is lost to an adjacent pixel. This can be described by the error function formula as shown in Equation 5.16. When charge has diffused by an amount 0.001σ away from the pixel boundary, then $\sim$50% of the charge will be collected by an adjacent pixel. The correction to $\mu^{'}$ is therefore given by

$$f = \frac{[50 - (2 \times 0.001\sigma)] \times [425 - (2 \times 0.001\sigma)]}{50 \times 425}. \tag{5.16}$$

Taking σ = 8.0 μm, then $f = 0.9996$. A correction due to charge-sharing at the pixel boundaries can therefore be neglected.

5.9.2 Correction due to the number of sensitive pixels

The value of μ does not account for the fraction of sensitive pixels in the readout chip. In principle the percentage of sensitive pixels ($\sim$ 58%) for this HPD could be confirmed by measurements using the readout chip test pulser. As described in [153] the amplitude of the test signal could be varied until ($\sim$ 58%) of the pixels respond. Then assuming a

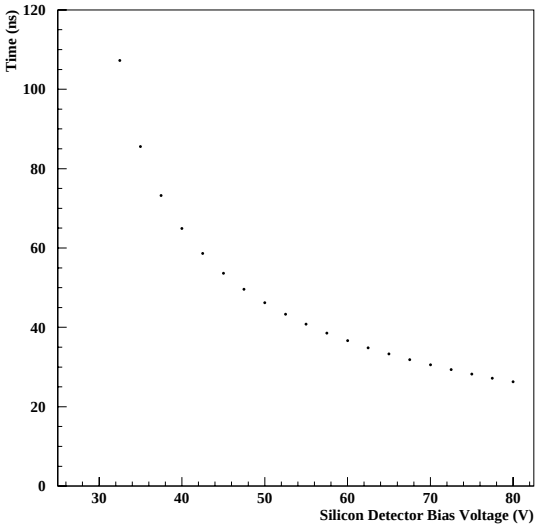

Figure 5.29: *Hole transit time t as a function of* V_{bias}.

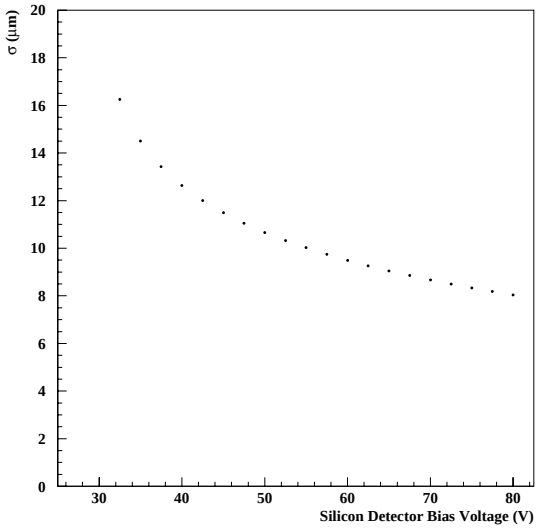

Figure 5.30: *Standard deviation of charge distribution* σ *as a function of* V_{bias}

value for the test capacitance of $C_{\mathrm{test}} = 16$ pF in the analogue part of each pixel chip the magnitude of the signal injected to the readout chip could be calculated and should be to within a reasonable agreement to the analogue signal for one photoelectron obtained from the n^+ backplane of the silicon detector [134]. However due to the problems with

the test pulser described earlier, this cannot be carried out. It is thought that the figure of $\sim$ 58% sensitive pixels is an underestimate due to the detached bump-bonds and so correcting the value of μ obtained earlier by a factor $\sim$0.58 would lead to an underestimation of μ by an unknown amount.

Instead the approach used to correct μ for the fraction of sensitive readout pixels is as follows. A region of the HPD anode was chosen where the effect of the missing bump-bonds would be a minimum. It was assumed that the sensitivity of the pixels in this chosen region would be an accurate representation of the sensitivity of the pixels over the whole anode should the bump-bonding degradation not have occurred. Figure 5.31 is a 2-D pixel map of the binary data from the readout chip when the LED was focused on the lower right of the anode surface. Figure 5.32 shows column numbers 18 to 26 and row numbers 45 to 135.. An estimate is made of the fraction of sensitive pixels in the region of 270 pixels covering column numbers 22 to 25 and row numbers 45 to 135. In this area 249 out of 270 (92.2$\pm$2%) pixels were seen to respond. Therefore the correction to $\mu^{'}$ due to the fraction of sensitive pixels is taken to be 0.92 ± 0.02 (syst).

5.9.3 Correction due to backscattering and the discriminator threshold.

Is is assumed that each photoelectron has an energy of $(19.35{\times}10^3/3.65) \simeq 5300e^-$ prior to contact with the HPD anode. This is above the ALICE1LHCb discriminator threshold shown in Figure 5.24 of $1880e^-$. According to the triangular model described in Section 5.8 the non-backscattered photoelectrons will deposit all of this $\sim 5300e^-$ into the anode and will all contribute to the backpulse spectrum and to the measurement of μ. This energy is above the ALICE1LHCb chip threshold and so all the non-backscattered photoelectrons will contribute to the binary data and to the measurement of $\mu^{'}$.

According to the triangular model the backscattered photoelectrons will deposit an average of $\sim 0.467 \times 5300 \simeq 2475e^-$ into the anode. However this model also shows that $\sim$30.6 % of these backscattered photoelectrons will have an energy below that of the

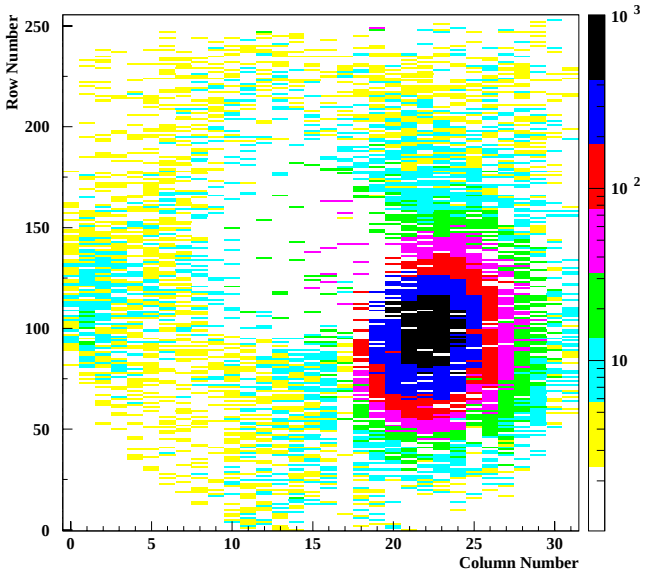

Figure 5.31: *2-D pixel map of the binary data from the readout chip with the LED focused on the lower right of the anode surface.*

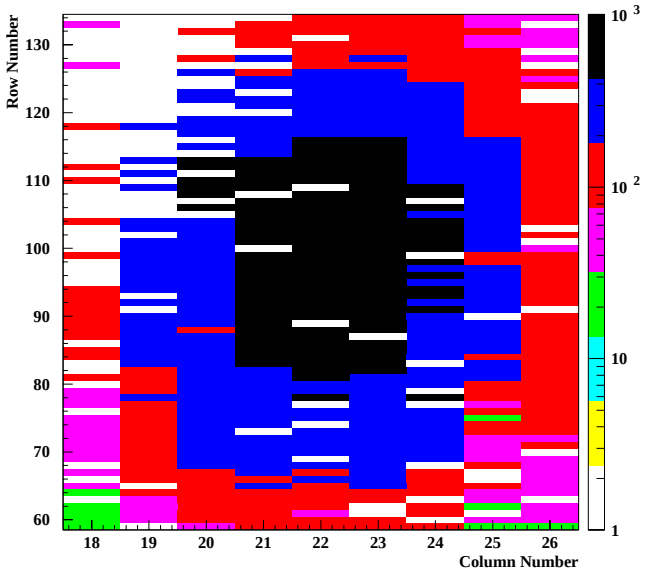

Figure 5.32: *Column numbers 18 to 26 and row numbers 45 to 135 of the 2-D pixel map shown in Figure 5.31.*

ALICE1LHCb chip threshold. These contribute to the backpulse spectrum and to the measurement of μ but are of too low a threshold to contribute to the binary data and so do not contribute to the measurement of $\mu^{'}$. In summary there will be three catagories of photoelectrons:

- Non-backscattered photoelectrons: Corresponds to 82 % of all photoelectrons incident on the anode.
- Backscattered electrons below threshold: Corresponds to (30.6 % of 18 %) 5.5 % of all photoelectrons incident on the anode.
- Backscattered electrons above threshold: Corresponds to (69.4 % of 18 %) 12.5 % of all photoelectrons incident on the anode. These are assumed to deposit ~0.467 of their energy to the anode.

The correction factor is therefore (1 - α) + (0.125×0.467) = 0.88 ± 0.02 (syst), where $\alpha = 0.18 \pm 0.02$ (syst).

5.10 HPD efficiency to single photoelectrons

From Section 5.7.2 the average number of responding ALICE1LHCb readout pixels per LED pulse $\mu^{'}$ was determined to be

$$\mu^{'} = 1.820 \pm 0.002\,(\text{stat}) \pm 0.079\,(\text{syst}) \tag{5.17}$$

In Section 5.8.3 the average number of photoelectrons per LED pulse incident upon the silicon detector surface of the HPD anode μ, was found to be

$$\mu = 2.7246 \pm 0.0002\,(\text{stat}). \tag{5.18}$$

A number of corrections were applied to the value of μ to account for inefficiencies within the HPD. These accounted for the fraction of sensitive pixels within the ALICE1LHCb

readout chip, backscattering and the ALICE1LHCb readout chip discriminator threshold as follows:

- Correction due to the fraction of sensitive pixels within the ALICE1LHCb readout chip:

$$0.92 \pm 0.02\,(\text{syst}). \tag{5.19}$$

- Correction due to backscattering and the ALICE1LHCb readout chip discriminator threshold:

$$0.88 \pm 0.02\,(\text{syst}). \tag{5.20}$$

The inefficiency due to charge-sharing at the pixel boundaries was found to be negligible assuming that a pixel became inefficient only when 50 % of its charge was lost to an adjacent pixel. Applying the correction factors in Equations 5.19 and 5.20 multiplicatively to μ (Equation 5.18) then the corrected value of μ is

$$\mu = 2.20 \pm 0.03\,(\text{syst}) \pm 0.0002\,(\text{stat}). \tag{5.21}$$

Combining this value of μ with the value of $\mu^{'}$ from Equation 5.17 then this results in an efficiency to single photoelectrons of

$$\epsilon_{\text{p.e.}} = \frac{\mu^{'}}{\mu} = 0.827 \pm 0.001\,(\text{stat}) \pm 0.037\,(\text{syst}). \tag{5.22}$$

The required LHCb specification for the HPD is that it has an efficiency of $\sim 85\,\%$ [99] and can be read out at 40 MHz. The significant bump-bond loss during manufacture and a binary read out limited to 10 MHz mean that this prototype has failed these requirements.

No correction has been made to the value of $\epsilon_{\text{p.e.}}$ due to the energy loss within the n^{+} ohmic backplane of the silicon detector. Simulations in [153] of the energy loss within a 500 μm-thick ohmic layer show that as much as 1.2 keV of the energy of a 20 keV photoelectron can be lost. However the 10 MHz (and all subsequent) prototypes have a

thinner (150 μm-thick) layer in order that this energy loss is minimised. No simulations assuming a 150 μm-thick layer have been reported.

Several HPDs were later manufactured using the 40 MHz LHCPIX readout chip [170] and anodes where $< 1\%$ loss in bump-bonds occurred during the HPD bake-out cycle [171]. A test beam period was held in August 2003 at the CERN X7 test beam area where HPD efficiency values of ~ 88 % were determined using the 40 MHz HPDs with 10 GeV/c pion/electron beam [171, 172]. The analyses presented in [171] show that there is no loss in the photoelectron detection efficiency when binary data is taken in the LHCb super-pixel mode compared to when taken in the ALICE mode. The HPD was confirmed as the photon detector technology choice in October 2003. The bump-bond degradation in the 10 MHz HPD was found to have been caused by a formation of a crust on the surface of the bump-bonds prior to formation of the anode as shown in Figure 5.33 [173]. A change in composition of the Sn-Pb solder bump-bond composition, a change in the bump-bonding process and an incompatibility of the new Sn-Pb solder bump-bond composition with the HPD bake-out cycle were also key factors [174].

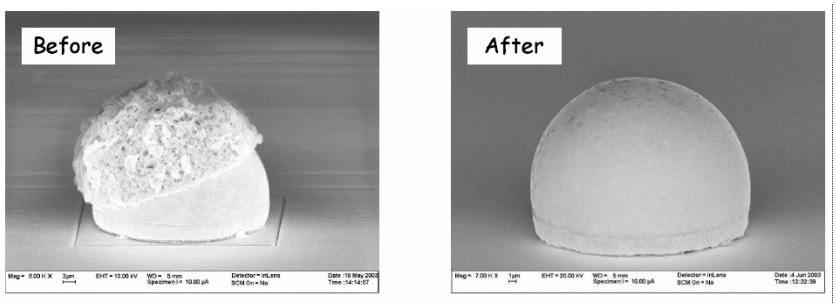

Figure 5.33: *(Left) A bump-bond of the type used in the 10 MHz HPD (with crust) and (right) without the crust. [173].*

Between now and November 2006, approximately 500 HPDs (168 for RICH-1 and 262 for RICH-2 plus spares [99]) must be manufactured and tested. The installation of these HPDs into RICH-1 and RICH-2 is scheduled to begin in November 2005.

Chapter 6

Event Reconstruction

This chapter is the first of three chapters discussing the Monte Carlo simulation studies of the $B_d^0 \to D^+(\pi^+\pi^+K^-)\, D^-(\pi^-\pi^-K^+)$, $B_s^0 \to D_s^+(\pi^+K^+K^-)\, D_s^-(\pi^-K^+K^-)$ and $B_c^+ \to D_s^+(\pi^+K^+K^-)\, \overline{D}^0(\pi^-K^+)$ decays, collectively referred to as $B \to DD$ decays. The motivation for studying these $B \to DD$ channels was the subject of Chapter 3. This particular chapter describes the event generation, detector simulation and software framework with which studies of these decay modes were performed.

6.1 Event Generation

Generation of Monte Carlo events is carried out using the LHCb GEANT-3 based FORTRAN simulation package [175], SICBMC. Within SICBMC, minimum bias proton-proton interactions at $\sqrt{s} = 14$ TeV are generated using the PYTHIA 6.2 program [95] which is tuned on CDF and UA5 data. The predefined option `MSEL = 2` in PYTHIA allows the inclusion of interactions such as hard QCD processes, single diffraction, double diffraction and elastic scattering in the Monte Carlo generation. However an elastic scattering interaction only very rarely produces tracks within the detector.

Several parton-parton interactions can occur in one proton-proton collision. Within

PYTHIA this is described by the parameter $p_T^{\min}$ that represents the minimum transverse momentum of the parton-parton interaction. Studies described in [70] and references therein obtain

$$p_T^{\min} = 3.47 \pm 0.17 \frac{\text{GeV}}{c} \text{ at } \sqrt{s} = 14 \text{ TeV}. \tag{6.1}$$

Other samples of events are obtained by filtering this minimum bias data-set. For example a subset of $b\overline{b}$ events are obtained by selecting the minimum bias events with at least one b- or $\overline{b}$-hadron. The total inelastic and $b\overline{b}$ production cross-sections obtained in this way are $\sigma_{\text{inelastic}} = 79.2$ mb and $\sigma_{b\overline{b}} = 633$ μb respectively [70]. $\sigma_{b\overline{b}}$ and $\sigma_{\text{inelastic}}$ are experimentally not well measured parameters and instead the conservative values of $\sigma_{\text{inelastic}} = 80$ mb and $\sigma_{b\overline{b}} = 500$ μb respectively are used in all LHCb calculations and are the values used in this thesis. Within the SICB package, the decay of all unstable B mesons are simulated with the QQ program [176]. This program was originally developed by the CLEO collaboration, and uses a decay table from CDF which includes B_s^0 and b-baryon decays [70]. Within QQ, the B_d^0 and B_s^0 oscillation parameters as defined in Equations 2.66 and 2.67 are set to $x_d = 0.755$ and $x_s = 20$ respectively.

Several inelastic proton-proton collisions may occur in the same bunch crossing and this is known as pile-up[a]. This is included in the simulated events assuming that the number of inelastic proton-proton interactions follows a Poisson distribution with a mean μ given by Equation 4.3.

6.2 Detector Simulation

Generated particles are tracked through the detector material and surrounding environment using the GEANT-3 package [175]. The geometry of the LHCb detector, both active (detection components and their front-end electronics) and passive (frames, sup-

[a]In practise, only so-called visible collisions contribute to the pile-up. Visible collisions are the ones that produce at least two charged particles which are reconstructible as long tracks (Section 6.4) which are tracks which give hits in each of the VELO, TT and T1→T3 tracking stations. These visible collisions correspond to (79.1±0.2)% of the inelastic cross-section $\sigma_{\text{inelastic}}$ [70].

ports beam-pipe and shielding elements) are described in detail. The low-energy particles such as hadrons, photons and electrons that are mainly produced due to secondary interactions, are tracked up to energy cut-off points of 10 MeV, 1 MeV and 1 MeV respectively.

The detector response simulation program registers the entry and exit points of a particles which has traversed a sensitive detector layer. The energy loss by a particle within that sensitive layer, and the time-of-flight of the particle with respect to its interaction time with the layer is also recorded. This information is used to generate digitised data which takes into account the sensitivities of each of the detector components. The resolutions and detection efficiencies obtained from this are then adjusted using test-beam results from prototype components, and corrections due to electronics noise and cross-talk are added. Finally for any bunch-crossing occurring at time t, the effect from the two proceeding (t=-50, $t=-25$ ns) and the one following ($t=+25$ ns) bunch-crossings are added according to the sensitivities of the detector components. This effect is known as "spillover". The results of this simulated detector response is then used for event reconstruction.

6.3 Event Reconstruction

The Brunel[b] [129] event reconstruction takes as its input the results of the detector response simulation as described in Section 6.2. This data is processed as if it were from real events with no reference to Monte Carlo "truth information" except in the case when the reconstruction performance is monitored.

To minimise the time spent on high multiplicity events, the reconstruction algorithm first searches the Vertex Locator (VELO) for charged particle trajectories, and should such an event not be found, the remaining tracking algorithms are not applied. Since most of these events are rejected by the trigger, this strategy is thought not to

[b] *Brunel, Isambard Kingdom* (1806-1859). 19th Century Engineer.

significantly affect the event yields in any physics channels. For the non high multiplicity events, reconstructed track parameters obtained from the tracking system (TT and T1→T3), combined with information from the Cherenkov photons which are detected as photoelectrons in the RICH system, are used to calculate probabilities of the charged particle being a $e^{\pm}$, $\mu^{\pm}$, $\pi^{\pm}$, $K^{\pm}$ or $p(\overline{p})$. Muons are separately reconstructed using the muon system while electromagnetic and hadronic clusters are reconstructed using the calorimeter system.

6.4 Tracking

Figure 6.1 is a schematic of the main tracking system and the various track types as defined within LHCb. As described in Section 4.6, the tracking system consists of the silicon vertex detector (Vertex Locator - VELO and pile-up veto) and four tracking stations; the Trigger Tracker (TT) and stations T1, T2 and T3. Figure 6.1 also shows that there five different defined track types which differ according to the section(s) of the tracking system: long, upstream, downstream, VELO and T tracks in which the track generates hits.

In particular long tracks are those which generate hits in all parts of the tracking system. With the exception of K^0_S and Λ studies, these are the only track types used in the current physics studies within LHCb. The V→TT tracks (also known as upstream tracks) are in general, low momentum tracks which do not traverse the magnet and so leave hits in the VELO and TT stations only. These tracks are useful for understanding photon backgrounds in the particle identification system of the RICH since these tracks pass through the RICH-1 detector and may generate Cherenkov photons. These can be useful for some physics analyses but with a reduced momentum resolution.

Figure 6.2 shows the momentum distributions of kaons ((a) and (b)) and pions ((c) and (d)) for the decay channel $B^0_d \rightarrow D^+D^-$. The figures are subdivided into those which may be reconstructed as upstream ((a) and (c)); and as long tracks ((b) and (d)).

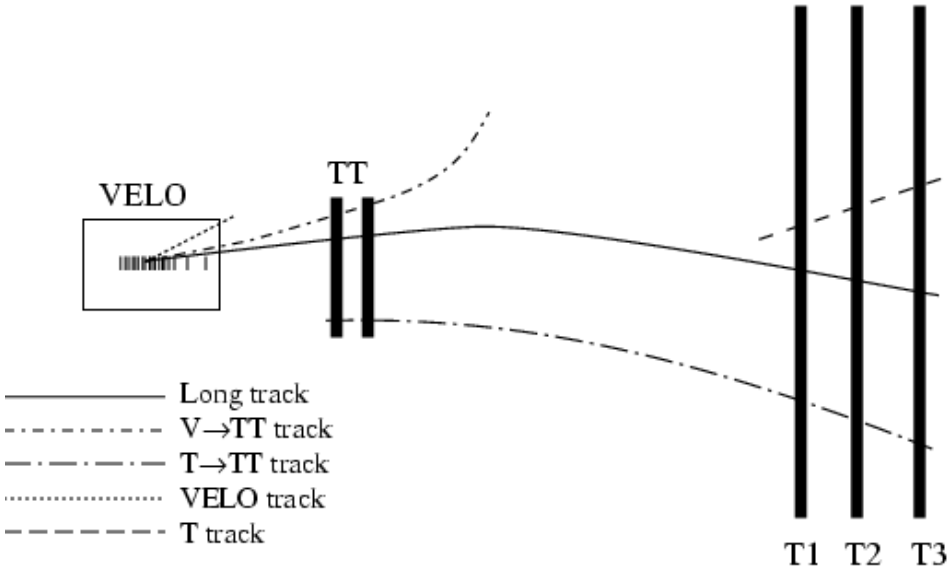

Figure 6.1: *A schematic of the main tracking systems and the various track types as defined within the LHCb experiment. The track types are long tracks, upstream (V→TT) tracks, downstream (T→TT) tracks, VELO tracks and T tracks [70].*

The upstream tracks are seen to be of a predominantly lower momentum than the long tracks. Since each of the B → DD channels are of a high multiplicity, the proportion of tracks that are reconstructed as upstream tracks is expected to be greater than for other channels studied at LHCb. Therefore in the B → DD analyses, upstream and long tracks are used.

Figures 6.3(a) and (b) show the momentum resolution respectively of long and upstream tracks. Figure (a) shows that the average long track momentum resolution is 0.37% and that the average upstream track resolution is ∼17%. These are comparable with the long and upstream momentum resolutions presented in [70]. The relatively poor upstream track momentum resolution is attributed to the fact that upstream tracks see only a small fraction of the total B-field integral.

The other track types shown on Figure 6.1 are the VELO, T→TT (downstream) and T tracks. The VELO tracks are typically large angle or backward tracks, which leave

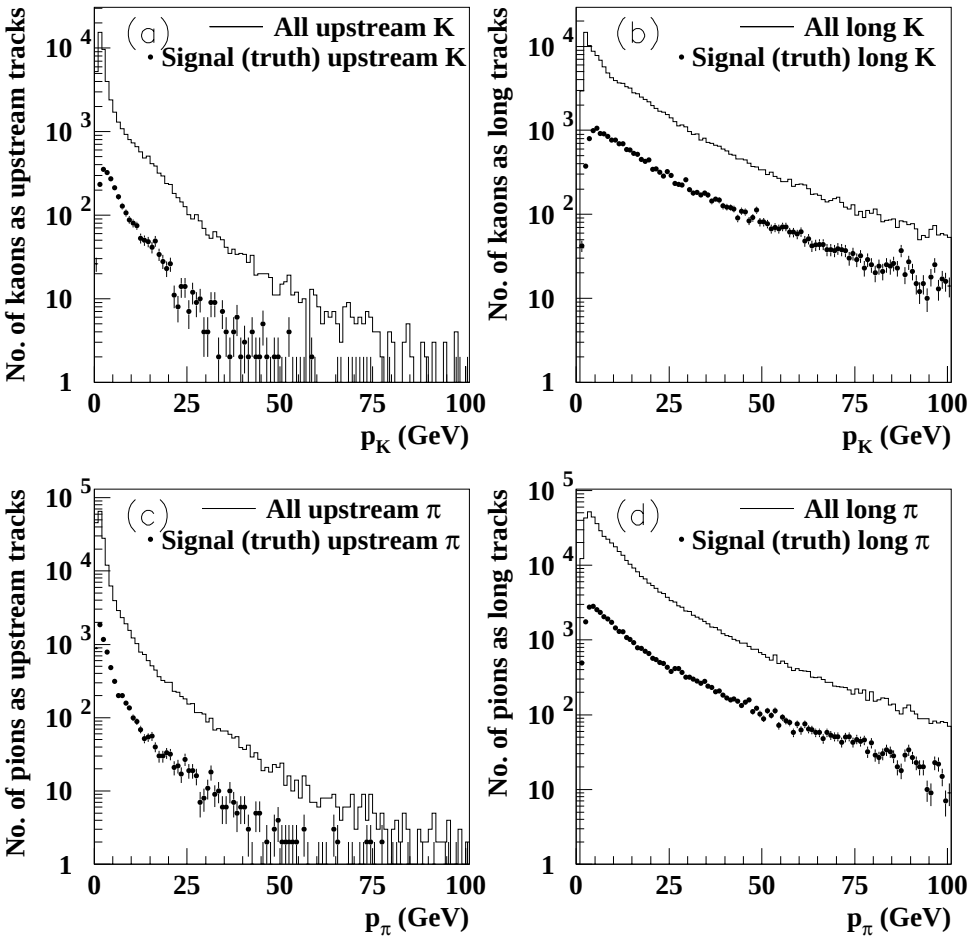

Figure 6.2: *Momentum plots of final state K and π from 47.5 k* $\mathrm{B^0_d} \to \mathrm{D^+D^-}$ *Monte Carlo events subdivided into (a) upstream K (b) long K (c) upstream π and (d) long π. Superimposed upon each plot is the corresponding distribution for final state K and π which (from looking at MC truth information) are known to originate from the* $\mathrm{B^0_d} \to \mathrm{D^+D^-}$ *decay.*

hits only in the VELO and are used in the primary vertex reconstruction. The T→TT tracks leave hits in the TT and T stations only. These are mainly the decay products of $\mathrm{K^0_S}$ or Λ particles that have decayed outside of the VELO. Finally the T tracks are those which leave hits only in the T1→T3 stations and are typically produced in secondary interactions.

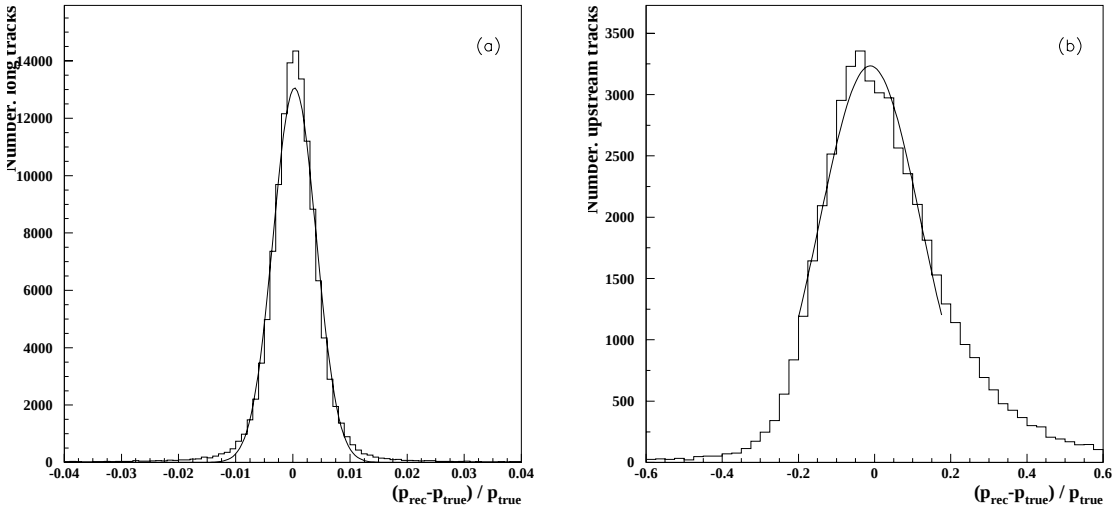

Figure 6.3: *Momentum resolution of (a) long tracks identified as kaons and (b) upstream tracks identified as kaons from* $B_d^0 \to D^+D^-$ *Monte Carlo. Both distributions are fitted with a single Gaussian with (a)* $\sigma = 0.0037$ *and (b)* $\sigma = 0.17$ *respectively.*

The term "reconstructible events" is used to describe the fraction of the generated signal events which have the potential to be reconstructed given the information available about that event from the detector. A reconstructible event is one in which all final state tracks from the decay of interest are reconstructible. Of these reconstructible events, the term "reconstructed" is applied to those events which have been successfully reconstructed. More specifically "reconstructible" and "reconstructed" can be defined in terms of the track types illustrated in Figure 6.1 as follows.

Reconstructible: For a long track to be considered reconstructible, then the particle must be reconstructible as both a VELO and a T track. For a VELO→TT track to be considered reconstructible, then the particle must be reconstructible as both a VELO and a TT track. The reconstructibility requirements for each of the VELO, TT and T tracks are as follows:

– for VELO tracks the particle must give at least 3 r and 3 ϕ hits in the VELO stations,

– for TT tracks, the particle must give at least three hits in TT,

– for T tracks, the particle must give at least 1 x and 1 stereo hit in each of T1→T3.

Reconstructed: To be considered as "successfully reconstructed" a VELO or T track must have at least 70% of its associated hits originating from a single Monte Carlo particle [70]. In addition, an upstream (VELO → TT) track must have a correct TT hit assigned. For a long track to be considered as "successfully reconstructed", it must have successfully reconstructed each of the VELO, TT and T(T1→T3) segments.

The search for low momentum tracks is known to be more difficult than that for higher momentum tracks. This is because the multiple scattering angle of a particle is inversely proportional to its momentum and so the relatively larger search window[c] required within the track-finding and pattern recognition algorithms for lower momentum tracks increases the probability of including either a track hit corresponding to another signal particle, or a so-called "ghost" hit, which does not correspond to any generated MC particle. It is for this reason that for low momentum tracks a reduced reconstruction efficiency is observed. This is illustrated in Figures 6.4 and 6.5. Figures 6.4(a) and 6.5(a) show the long and upstream track reconstruction efficiencies as a function of the momentum of the generated particle. Figure 6.4(b) shows the long track ghost rate as a function of the momentum of the generated particle and Figure 6.5(b) shows the upstream track ghost rate of tracks with a momentum greater than p_{cut}.

More specifically, for long tracks with p > 10 GeV/c, then the average long track reconstruction efficiency is 94% and for the V→TT (upstream) tracks, an average track reconstruction efficiency of ∼75% with the reconstruction procedure for long tracks achieving a higher efficiency due to the fact that track segments are able to be measured at both sides of the dipole magnet [70]. Using the same reasoning, a higher ghost rate is observed when studying low momentum tracks. From [70] the average long and V→TT (upstream) track ghost rates are quoted as 9% and 15%.

[c] A name given to the area of the detector plane about a projected reconstructed track trajectory within which track "hits" are searched for.

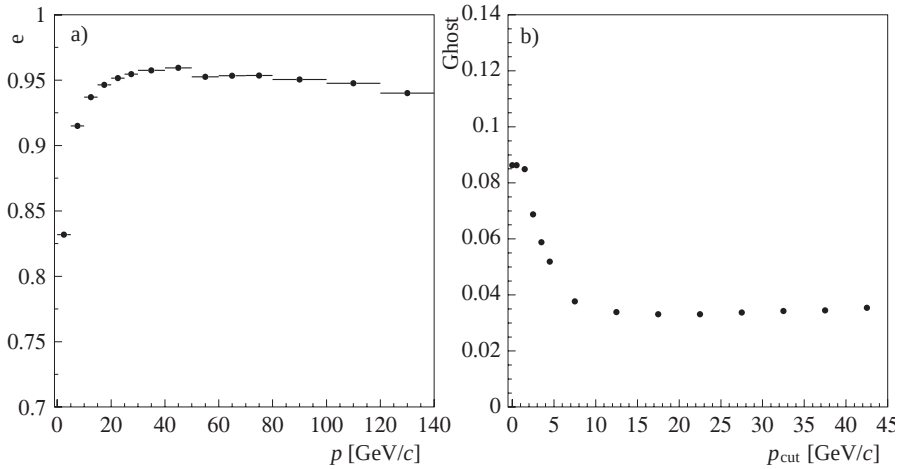

Figure 6.4: *(a) Long track reconstruction efficiency as a function of the momentum of the generated particle. (b) Long track ghost rate for tracks of momentum p greater than* p_{cut} *[70] .*

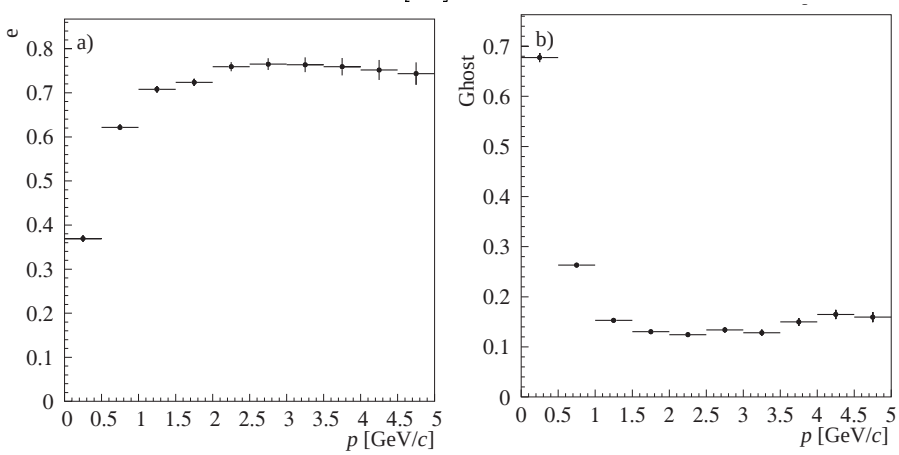

Figure 6.5: *(a) Upstream track reconstruction efficiency as a function of the momentum of the generated particle. (b) Upstream track ghost rate as a function of the momentum of the generated particle [70].*

6.5 Data Samples and Analysis Tools

The analyses presented here were carried out on Monte Carlo samples of size ∼50 k events in each of the $\mathrm{B_d^0} \to \mathrm{D^+D^-}$, $\mathrm{B_s^0} \to \mathrm{D_s^+D_s^-}$ and $\mathrm{B_c^+} \to \mathrm{D_s^+}\overline{\mathrm{D}}^0$ channels. The charmed meson decays included intermediate ϕ and $\mathrm{K^*}$ resonances according to probabilities given in [37]. This is denoted by the symbol "⇒" in the remainder of this thesis. The branching ratios for the B → DD channels are listed in Table 6.1.

Decay	Branching fraction		Reference
$\mathcal{BR}(\mathrm{B_d^0} \to \mathrm{D^+D^-})$	4×10^{-4}	$(*)$	[55]
$\mathcal{BR}(\mathrm{B_d^0} \to \mathrm{D^+D^-})$	$(2.46 \pm 0.61_{\mathrm{stat}} \pm 0.42_{\mathrm{syst}}) \times 10^{-4}$		[63]
$\mathcal{BR}(\mathrm{B_s^0} \to \mathrm{D_s^+D_s^-})$	8×10^{-3}	$(*)$	[73]
$\mathcal{BR}(\mathrm{B_c^+} \to \mathrm{D_s^+}\overline{\mathrm{D}}^0)$	10^{-5} - 10^{-6}	$(*)$	[74]
$\mathcal{BR}(\mathrm{B_c^+} \to \mathrm{D_s^+}\overline{\mathrm{D}}^0)$	4.8×10^{-6}		[177, 178]
$\mathcal{BR}(\mathrm{D^\pm} \to \mathrm{K^\mp}\pi^\pm\pi^\pm)$	0.088 ± 0.006	$(*)$	[37]
$\mathcal{BR}(\mathrm{D_s^+} \to \mathrm{K^+K^-}\pi^+)$	0.044 ± 0.012	$(*)$	[37]
$\mathcal{BR}(\overline{\mathrm{D}}^0 \to \mathrm{K^+}\pi^-)$	0.038 ± 0.012	$(*)$	[37]

Decay	Total branching fraction
$\mathcal{BR}(\mathrm{B_d^0} \to \mathrm{D^+}(\Rightarrow \pi^+\pi^+\mathrm{K^-})\ \mathrm{D^-}(\Rightarrow \pi^-\pi^-\mathrm{K^+}))$	$(3.1 \pm 1.2) \times 10^{-6}$
$\mathcal{BR}(\mathrm{B_s^0} \to \mathrm{D_s^+}(\Rightarrow \pi^+\mathrm{K^+K^-})\ \mathrm{D_s^-}(\Rightarrow \pi^-\mathrm{K^+K^-}))$	$(15.0 \pm 8.0) \times 10^{-6}$
$\mathcal{BR}(\mathrm{B_c^+} \to \mathrm{D_s^+}(\Rightarrow \pi^+\mathrm{K^+K^-})\ \overline{\mathrm{D}}^0 \to (\pi^-\mathrm{K^+}))$	$(0.017 \pm 0.005) \times 10^{-6}$

Table 6.1: *Branching fractions for relevant B and D meson decay channels. The branching fraction values used to calculate the total branching fraction values in the lower half of the table are indicated with (∗). The value of* $\mathcal{BR}(\mathrm{B_c^+} \to \mathrm{D_s^+}\overline{\mathrm{D}}^0)$ *is taken to be* 10^{-5} *in all calculations.*

Approximately $\mathcal{O}\left(10^7\right)$ inclusive $\mathrm{b\overline{b}}$ events were used for background rejection calculations and estimates of the background to signal (B/S) ratios for each channel and $\sim \mathcal{O}\,(21\,\mathrm{M})$ minimum bias events, of which $\sim \mathcal{O}\,(56\,\mathrm{k})$ were known to have passed the Level-0 and Level-1 trigger, were also studied.

The inclusive $\mathrm{b\overline{b}}$ Monte Carlo sample corresponds to ∼4 minutes of LHCb data-taking at the mean luminosity of $\mathcal{L} = 2\times 10^{32}\mathrm{cm^{-2}s^{-1}}$. In comparison, the signal Monte Carlo events correspond to ∼6 and ∼5 days for the $\mathrm{B_d^0}$ and $\mathrm{B_s^0}$ channels respectively and to $\sim 608 \times 10^3$ days ($\sim$ 1665 years !) for the $\mathrm{B_c^+}$ channel. Assuming a total inelastic cross-section of 80 mb then the sample of $\sim \mathcal{O}\,(21\,\mathrm{M})$ minimum bias events corresponds to ∼1.4 seconds of LHCb data-taking.

In each of the signal and inclusive $\mathrm{b\overline{b}}$ samples, a cut is imposed at the generator level such that the particle must have a true polar angle (as defined in Section 4.3) of less than 400 mrad. This avoids the tracking and reconstruction of many events where not all of

the decay products would be in the LHCb detector acceptance. For the signal samples, the cut is imposed on the signal $\overline{\mathrm{b}}$ of the decaying B-meson and has an efficiency of $\epsilon_{\mathrm{gen}}^{\mathrm{signal}} = (34.71 \pm 0.03)\%$. For the inclusive $\mathrm{b\overline{b}}$ sample, the cut is applied to one of the b-hadrons and has an efficiency of $\epsilon_{\mathrm{gen}}^{\mathrm{b\overline{b}}} = (43.21 \pm 0.04)\%$. Therefore, the Monte Carlo samples sizes quoted are those after this cut at the generator level has been applied. No cut is imposed at the generator level for the minimum bias sample [70].

The analyses presented here were carried out using the LHCb analysis program DaVinci[d] [130]. Figure 6.6 shows the general structure of the DaVinci framework.

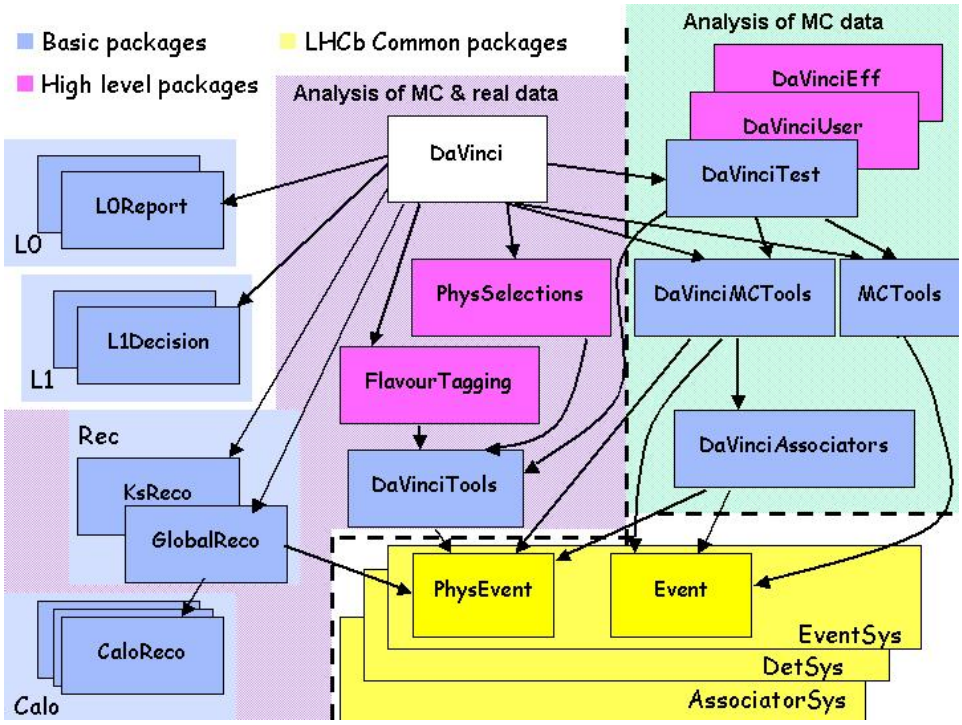

Figure 6.6: *DaVinci general package structure and contents [130].*

DaVinci is comprised of three main components (basic packages, higher level packages and LHCb component packages) which are controlled by the main application, also called DaVinci. Within these packages the programs (and their tasks) which are of direct relevance to the analyses presented are:

[d] *DaVinci, Leonardo* (1452-1519). Italian High Renaissance Painter and Inventor

- **Rec/PrimVtx:** This package reconstructs primary vertices using an iterative search and fit procedure described in [70].

- **PhysSelections(PhysSel):** This package contains decay channel-specific analysis algorithms. Each of the algorithms in the PhysSel/B2DD package were written for the analyses presented in this thesis.

- **DaVinciTools:** This package contains software tools that are used within the analysis algorithms, for example tools to calculate impact parameters and to perform vertex fitting.

- **DaVinciAssociators:** This package allows the user to look at the MC "truth" information for a particular reconstructed particle during cut optimisation, although the final selection algorithms contained in the PhysSel package have no explicit dependence on this MC truth information

- **L0Report** and **L1Decision:** are the two packages used to retrieve the Level-0 and Level-1 trigger decisions for an event. The L1Decision package can be applied to any event irrespective of whether the event has passed or failed at Level-0.

- **DaVinciEff:** This package evaluates the performance of the selection algorithms contained within the PhysSel packages. For example, the performance of the $B^0_d \to D^+(\pi^+\pi^+K^-)\ D^-(\pi^-\pi^-K^+)$ selection algorithms contained in PhysSel/B2DD are evaluated using PhysSelEff/EffBd2DD.

- **FlavourTagging:** This package applies and evaluates the effect of flavour tagging on events (triggered or untriggered) which have been selected using the PhysSel package.

6.6 Detection and Reconstruction Efficiencies

The number of tracks available for analysis in each event depends upon several factors; the angular acceptance of the detector as compared to the topology of the event, the

potential of the decay-of-interest within the event to be reconstructed, and finally the performance of the tracking in reconstructing these decays. These factors can be quantitatively evaluated by defining a detection efficiency $\epsilon_{\rm det}$ and a reconstruction efficiency $\epsilon_{\rm rec/det}$ as follows.

When discussing signal Monte Carlo a detection efficiency $\epsilon_{\rm det}$ can be defined which includes:

- the generator-level cut on the polar angle of the b-hadron, $\epsilon_{\rm gen}^{\rm signal}$
- the fraction of the Monte Carlo events that are reconstructible by the detector, $\epsilon_{\rm accept}$ according to the definition of reconstructible given in Section 6.4.

If there are $N_{\rm gen}^{sig}$ generated signal Monte Carlo events per decay channel of which:

- $N_{\rm rec'ble}$ is the number of events from $N_{\rm gen}^{sig}$ that are reconstructible according to the definition of reconstructible given in Section 6.4,
- $N_{\rm rec'ted}$ is the number of events from $N_{\rm gen}^{sig}$ that are reconstructed according to the definition of reconstructed given in Section 6.4. This number is dependent upon the efficiency of the reconstructed-truth association.
- $N_{\rm rec}$ is the number of signal Monte Carlo events from $N_{\rm gen}^{sig}$ that are reconstructible and reconstructed. This is dependent upon the definition of reconstructible and upon the efficiency of the reconstructed-truth association.

$\epsilon_{\rm det}$ is defined as

$$\epsilon_{\rm det} = \epsilon_{\rm gen}^{\rm signal} \times \epsilon_{\rm accept}\,, \tag{6.2}$$

where $\epsilon_{\rm accept}$ is defined as

$$\epsilon_{\rm accept} = \frac{N_{\rm rec'ble}}{N_{\rm gen}^{sig}} \times \frac{N_{\rm rec'ted}}{N_{\rm rec}}. \tag{6.3}$$

The second term in Equation 6.3 is a correction term which accounts for inefficiencies in the definition of reconstructible and the effect of the reconstructed-truth association. It is these two factors which allow $N_{\rm rec'ted} > N_{\rm rec}$ as shown in Table 6.2.

A reconstruction efficiency $\epsilon_{\mathrm{rec/det}}$ is defined to describe the fraction of reconstructible particles that are successfully reconstructed - this quantity is dependent both upon the momentum of the particle and the track types as illustrated in Figures 6.4 and 6.5. Using the previously stated definitions of N_{rec} and $N_{\mathrm{rec'ble}}$ then $\epsilon_{\mathrm{rec/det}}$ is defined as

$$\epsilon_{\mathrm{rec/det}} = \frac{N_{\mathrm{rec}}}{N_{\mathrm{rec'ble}}}. \tag{6.4}$$

The values of ϵ_{det} and $\epsilon_{\mathrm{rec/det}}$ are collected together in Table 6.2.

	$B_d^0 \to D^+D^-$	$B_s^0 \to D_s^+D_s^-$	$B_c^+ \to D_s^+\overline{D}^0$
N_{gen}^{sig}	47500	48000	48750
$N_{\mathrm{rec'ble}}$	8335	8962	10088
$N_{\mathrm{rec'ted}}$	6064	6260	7958
N_{rec}	5882	6116	7762
$\epsilon_{\mathrm{det}}[\%]$	6.29 ± 0.09	6.61 ± 0.09	7.36 ± 0.09
$\epsilon_{\mathrm{rec/det}}$ [%]	70.4 ± 0.5	68.5 ± 0.5	76.9 ± 0.4

Table 6.2: *Detection and reconstruction efficiencies* ϵ_{det} *and* $\epsilon_{\mathrm{rec/det}}$. *The errors are statistical only.*

Chapter 7

Event Selection

In this chapter the particle identification, event selection and trigger performance of the $B \to DD$ channels are discussed. The offline analyses were performed using the LHCb analysis program DaVinci and channel-specific software written for the PhysSel/B2DD package as described in Section 6.5. The event selection for the $B \to DD$ analyses were carried out in two stages. The aim of the initial step was to produce smaller and therefore more manageable sets of signal and inclusive $b\overline{b}$ events to analyse. This required that a preliminary set of cuts were determined which in the second stage would be refined and added to. The aim of the second stage was to maintain a high efficiency for the signal while providing a very large rejection factor for the combinatorial background. These two stages are described in Sections 7.3 and 7.4. The background studies for these channels are described later in Section 8.3.

7.1 Particle Identification

At the beginning of the selection for each event the reconstructed tracks are assigned a particle identification (PID) based upon information from the different subdetectors. PID is provided by the Ring-Imaging Cherenkov (RICH) counters (π/K/p), the Electromagnetic Calorimeter (ECAL) and the Hadronic Calorimeter (HCAL) ($e^{\pm}$, γ and

hadrons) and the muon system ($\mu^{\pm}$).

In Section 4.4.5 it was described how information from the RICH detectors can be used to assign a probability for each track in the form of a log likelihood $\mathcal{L}$ for each of the possible particle identities of e, μ, π, K or p. Using this information each track is then assigned a "best PID" which corresponds to the identity of the particle of which the assigned probability was highest. This assigned probability is referred to later in Chapter 7 as a "confidence limit"(C.L.).

Since all of the B $\rightarrow$ DD final states are kaons and pions, classification of the tracks follows a convention adopted in [69, 70, 99] where tracks are classified as either "light" (best PID = $e^{\pm}$, $\mu^{\pm}$ or $\pi^{\pm}$) or "heavy" (best PID = $\mathrm{K}^{\pm}$ or $p(\overline{p})$). The "light" tracks are then taken to be $\pi^{\pm}$ candidates and the "heavy" tracks are taken to be $\mathrm{K}^{\pm}$ candidates. Unless explicitly stated otherwise, the notation $\pi^{\pm}$ and $\mathrm{K}^{\pm}$ is used in the remainder of this thesis to denote $\pi^{\pm}$ ($e^{\pm}$, $\mu^{\pm}$ or $\pi^{\pm}$) and $\mathrm{K}^{\pm}$ ($\mathrm{K}^{\pm}$ or $\mathrm{p}(\overline{\mathrm{p}})$) candidates.

Figure 7.1 shows the kaon identification (identifying true kaons as "heavy") and pion misidentification (not identifying true pions as "light") efficiency as a function of particle momentum. The visible fluctuations observed in the kaon mis-id efficiency occur at the RICH-1 and RICH-2 radiator thresholds (2.0 GeV/c, 9.3 GeV/c and 15.6 GeV/c for the aerogel, C_4F_{10} and CF_4 radiators respectively) above which the RICH is able to identify kaons. The average efficiency for kaon identification between 2 and 100 GeV/c is 88% and the average pion misidentification rate between 2 and 100 GeV/c is 3%.

7.2 Primary Vertex Reconstruction

Within the event reconstruction, the primary vertex search and fit is performed using the following iterative procedure. A histogram of the z-coordinate of the point of closest approach to the beam line for all (long, upstream and VELO) tracks measured in the VELO is constructed with a bin width of 1 mm. The highest bin of this histogram is used, together with its 4 neighbours on each side, to define a cluster of tracks from which

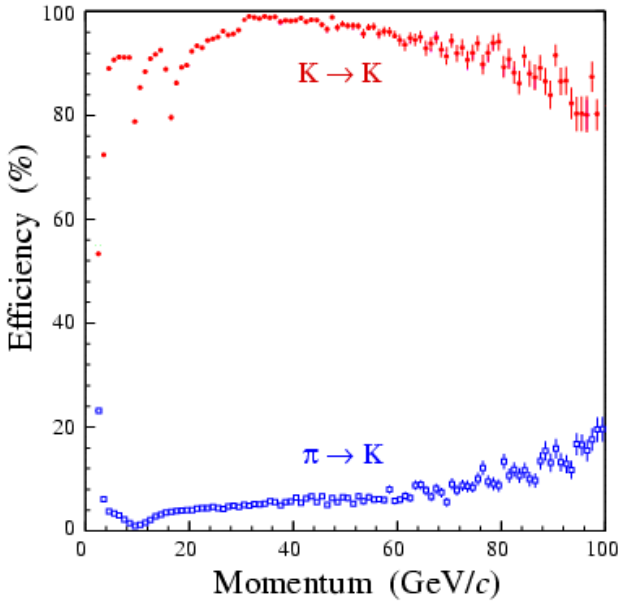

Figure 7.1: *Kaon identification and pion misidentification efficiency as a function of particle momentum.*

the mean value computed is used as the z of an original vertex (located on the beam axis). Tracks with a large χ^2 contribution to the vertex (> 225 for the first iteration and > 9 afterwards) are eliminated from the cluster, and the remaining tracks in the cluster are fitted to a new common vertex. This step is iterated until no further tracks are rejected. If at least six tracks were used in the last iteration, the vertex is kept as a primary vertex, these tracks are removed from the overall set of tracks, and the whole search procedure is restarted to find additional primary vertices. If less than six tracks were used then the vertex is discarded and the search is stopped. In the case that no primary vertex has been found, the original vertex obtained from the histogram peak is kept as the only primary vertex of the event.

This procedure was developed in order to optimise the efficiency for finding the $b\overline{b}$ production vertex, which is on average 98 %. In the case of the $B \to DD$ channels, Table 7.1 shows that in approximately only 0.01 % of events is there no primary vertex reconstructed. The events in which this is the case are neglected from the analyses.

When there is more than one primary vertex found in an event, then the first one that had been reconstructed using the Rec/PrimVtx package (Section 6.5) is used. From Table 7.1 it is seen that approximately 27 % of the B $\rightarrow$ DD events have more than one primary vertex reconstructed.

Figure 7.2 shows the resolution of the $B_d^0 \rightarrow D^+D^-$ primary vertices in directions transverse (x,y) and longitudinal (z) to the beam. These resolutions were obtained by plotting the difference between the reconstructed and Monte Carlo truth values in the events that the B-meson was selected using the final selection cuts discussed later in Section 7.4 and before any trigger was applied. Each distribution is fitted with a double Gaussian with a common central value. The core Gaussian resolutions are $\sim$45 μm in x,y and $\sim$7.5 μm in z with 25-35 % of events in the second Gaussian which is two to three times wider. The same is found for the primary vertices reconstructed in the $B_s^0 \rightarrow D_s^+D_s^-$ and $B_c^+ \rightarrow D_s^+\overline{D}^0$ channels and are comparable to that quoted for the primary vertex reconstruction performance in [70]. A small but significant 8 μm bias in z is caused by decay products of b- or c- hadrons that cannot be separated from the primary vertex by the χ^2 cut within the iterative search and fit procedure. This shift is known not to be present in minimum bias events.

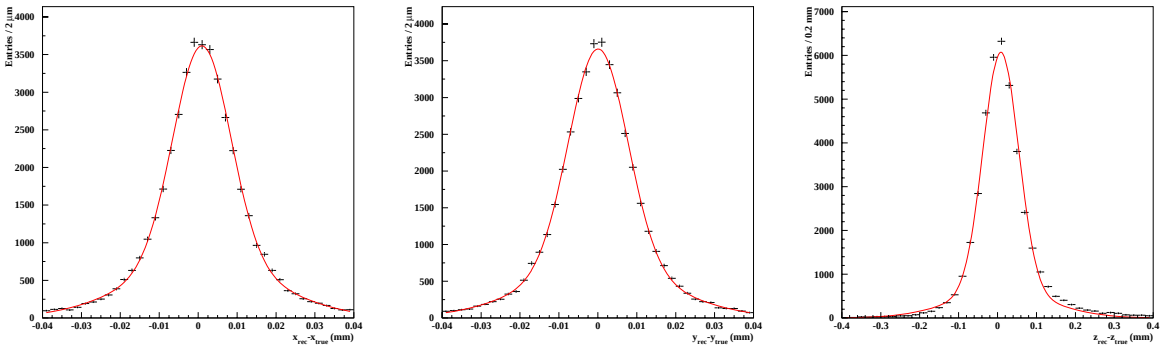

Figure 7.2: $B_d^0 \rightarrow D^+D^-$*: Primary vertex position resolutions in (left-to-right) x, y and z.*

7.3 Pre-selection criteria

A summary of the initial set of selection cuts applied for each of the B $\rightarrow$ DD channels is summarised in Table 7.2. For each channel the cuts are categorised into three groups and are applied in the algorithms summarised below. Within each of these three groups the cuts are applied in the order listed in Table 7.2.

- $B_d^0 \rightarrow D^+D^-$:
  - Cuts on $K^\pm$ and $\pi^\pm$ (`D2KPiPi.cpp/h`).
  - Cuts on $K^\mp\pi^\pm\pi^\pm$ combinations (`D2KPiPi.cpp/h`).
  - Cuts on D^+D^- combinations (`Bd2DD.cpp/h`).
- $B_s^0 \rightarrow D_s^+D_s^-$:
  - Cuts on $K^\pm$ and $\pi^\pm$ (`Ds2KKPi.cpp/h`).
  - Cuts on $K^\pm K^\mp\pi^\pm$ combinations (`Ds2KKPi.cpp/h`).
  - Cuts on D_s^+/D_s^- combinations (`Bs2DsDs.cpp/h`).
- $B_c^+ \rightarrow D_s^+\overline{D}^0$:
  - Cuts on $K^\pm$ and $\pi^\pm$ (`Ds2KKPiForBc2DsD0.cpp/h` and `D0Bar2KPiForBc2DsD0.cpp/h`).
  - Cuts on $K^+K^-\pi^+$ (`Ds2KKPiForBc2DsD0.cpp/h`) and $K^+\pi^-$ combinations (`D0Bar2KPiForBc2DsD0.cpp/h`).
  - Cuts on $D_s^+/\overline{D}^0$ combinations (`Bc2DsD0.cpp/h`).

The different B meson decay channels studied are all treated in the same way. In nearly all cases the same set of cut variables are used, and the selections differ only by the choice of the values at which the cuts are made.

Cuts were first made on final state particles which differed in value depending upon whether the final state particle had been classified as a pion or kaon candidate. Cuts

are applied on the transverse momentum and upon the impact parameter significance[a] with respect to the chosen primary vertex in that event. From the kaons and pions which pass these cuts, the appropriate D meson candidates are formed. For example in the `D2KKPi.cpp` algorithm the D^+ candidates are formed by taking two different π^+ candidates and one K^- candidate. Similarly the D^- candidates are formed by taking two different π^- candidates and one K^+ candidate.

When a D meson candidate has been formed, a loose mass cut is applied about the true D meson mass. This is to remove the D meson candidates that lie well away from the true D meson mass and should increase the effectiveness of the cuts that are applied to the remaining D meson candidates. The tracks which form each remaining D meson candidate are fitted to a common vertex but no mass constraint is applied. The D meson candidate must then pass cuts based upon the following criteria:

- χ^2 of the unconstrained vertex fit : This cut is not normalised to the number of degrees of freedom and so this cut does not represent a cut on the χ^2 probability,
- a minimum transverse momentum,
- a minimum impact parameter significance with respect to the chosen primary vertex, and
- a tighter mass window about the true D meson mass. This supersedes the loose mass cut discussed above.

It was previously stated that the signal D mesons were generated so as to decay via various intermediate ϕ and K^* resonances. In the $B^0_d \rightarrow D^+D^-$ channel, the $D^\pm \Rightarrow \pi^\pm\pi^\pm K^\mp$ decay has been generated such that the $D^\pm$ decays to $\pi^\pm\pi^\pm K^\mp$ in the following proportions:

[a]The impact parameter (I.P) is the closest distance of approach of a track to a vertex. The impact parameter significance is calculated as $\mathrm{I.P}/\sigma_{\mathrm{IP}}$ where the error on the impact parameter σ_{IP} is calculated from the error on the vertex position and the error on the track parameters.

$K^{*0}(892)$: $K^{*0}(1430)$: non-resonant

10.5 % 18.9 % 70.6 %

In the $B_s^0 \to D_s^+ D_s^-$ channel the $D_s^\pm \Rightarrow \pi^\pm K^\pm K^\mp$ decay has been generated such that the $D_s^\pm$ decays to $\pi^\pm K^\pm K^\mp$ in the following proportions:

$K^{*0}(892)$: $\phi(1020)$: non-resonant

45.2 % 36.3 % 18.5 %

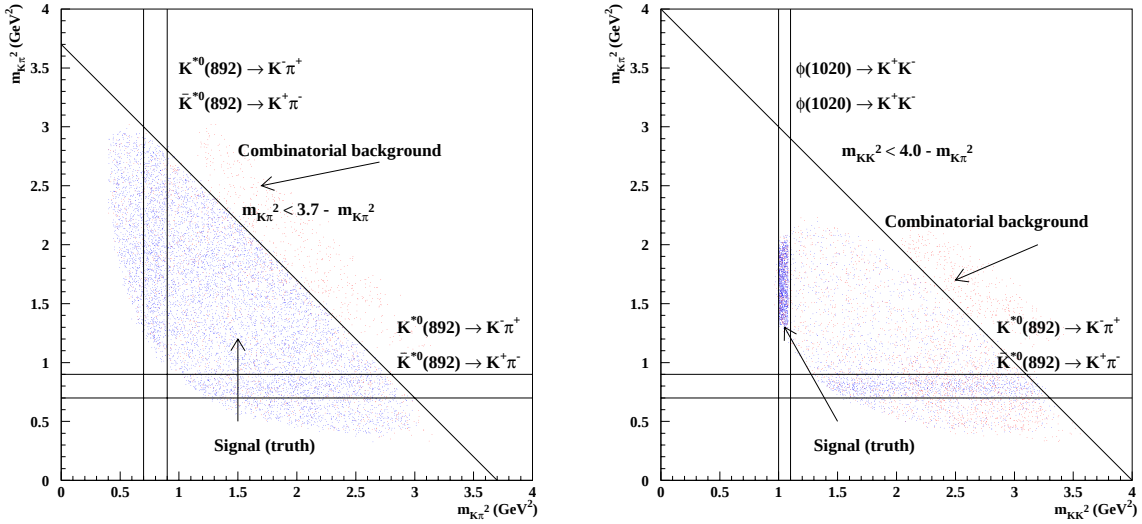

Figure 7.3: *(a)* $D^+ \Rightarrow \pi^\pm\pi^\pm K^\mp$ *:* $m^2_{K\pi_1}$ [GeV/c^2] *plotted against* $m^2_{K\pi_2}$ [GeV/c^2]. *The* $K^{*0}(892)$ *resonance bands are indicated. The selection cut* $m^2_{K\pi_1} < 3.7 - m^2_{K\pi_2}$ *is also labelled. (b)* $D_s^+ \Rightarrow K^\pm K^\mp \pi^\pm$ *:* $m^2_{K^+K^-}$ [GeV/c^2] *plotted against* $m^2_{K^-\pi^+(K^+\pi^-)}$ [GeV/c^2]. *The* $K^{*0}(892)$ *and* $\phi(1020)$ *resonance bands are indicated. The selection cut* $m^2_{K^+K^-} < 4.0 - m^2_{K^-\pi^+(K^+\pi^-)}$ *is also labelled.*

However, in this analysis none of the $D^\pm$, $D_s^\pm$ or D_s^+ ($B_c^+ \to D_s^+ \overline{D}^0$) candidates have been formed explicitly via any of the resonant states[b]. When the Dalitz plot of the

[b]The Monte Carlo for the $B_s^0 \to D_s^\pm K^\mp$ and $B_s^0 \to D_s^+\pi^-$ studies also had the $D_s^\pm$ decays generated in the way as for the $B_s^0 \to D_s^+ D_s^-$ channel. In neither of these analysis were the intermediate resonance states used [179].

$D^{\pm} \Rightarrow \pi^{\pm}\pi^{\pm}K^{\mp}$ and $D_s^{\pm} \Rightarrow \pi^{\pm}K^{\pm}K^{\mp}$ is made, the intermediate $\phi(1020)$ (width = 4.26 $\pm$ 0.05 MeV) and $K^{*0}(892)$ (width = 50.7 $\pm$ 0.9 MeV) resonances are visible, as shown in Figures 7.3(a) and (b). The contributions from true signal $K\pi/KK$ combinations and from combinatorial background $K\pi/KK$ combinations within the signal Monte Carlo. The $K^{*0}(1430)$ resonance is too broad (width = 294 $\pm$ 23 MeV) to be seen in Figure 7.3(a).

From Figure 7.3(a) and the above numbers, excluding all but the resonant $K\pi\pi$ combinations would result in a loss of $\sim$70 % of the true signal. Instead a cut has been made to exclude all combinations which are found in the unphysical region of the Dalitz plot. In Figure 7.3 (b) it is apparent that excluding all but the resonant $KK\pi$ combinations and in addition, excluding the uphysical region of the Dalitz plot would be the optimal method, resulting in only $\sim$20 % of the true signal being lost. In the first instance only a cut which excluded the uphysical region of the Dalitz plot was applied and after the analysis had been completed, should the background-to-signal (B/S) ratio (discussed later in Section 8.3.2) have been found to be much larger than other channels studied then a further study of the $D_s^{\pm} \Rightarrow K^{\pm}K^{\mp}\pi^{\pm}$ Dalitz plot would have been carried out.

A study using $B_s^0 \rightarrow D_s^{\pm}K^{\mp}$ and $B_s^0 \rightarrow D_s^{+}\pi^{-}$ events has shown that applying cuts about the resonance masses and relaxing existing cuts does not decrease the B/S ratio [180]. For the analyses presented here it is acknowledged that when more inclusive $b\overline{b}$ events become available and more precise background/signal estimates are able to be made, a full study of the $D_s^{\pm} \Rightarrow K^{\pm}K^{\mp}\pi^{\pm}$ and also the $D^{\pm} \Rightarrow \pi^{\pm}\pi^{\pm}K^{\mp}$ Dalitz plot should be made.

In summary, the cuts on the Dalitz plots are as follows:

- `D2KPiPi.cpp` : $m^2_{K\pi_1} < 3.7 - m^2_{K\pi_2}$, where $m_{\pi_1} > m_{\pi_2}$[c]

[c]The notation used here is that π_1 and π_2 represent two different $\pi^{\pm}$ candidates which along with a $K^{\mp}$ in the event are used to form a $D^{\pm}$ candidate. Therefore m_{π_1} and m_{π_2} can take any of the values $m_{e^{\pm}}$, $m_{\mu^{\pm}}$ or $m_{\pi^{\pm}}$. The condition $m_{\pi_1} > m_{\pi_2}$ then has no effect if both π_1 and π_2 are true pions.

- `Ds2KKPi.cpp` : $m^2_{\mathrm{K^+K^-}} < 4.0 - m^2_{\mathrm{K^-}\pi^+(\mathrm{K^+}\pi^-)}$
- `Ds2KKPiForBc2DsD0.cpp` : $m^2_{\mathrm{K^+K^-}} < 4.0 - m^2_{\mathrm{K^-}\pi^+}$

B meson candidates are formed using combinations of the previously found $\mathrm{D^+/D^-}$, $\mathrm{D_s^+/D_s^-}$ and $\mathrm{D_s^+/\overline{D}^0}$ candidates. At this point there is no limit placed upon the number of B meson candidates allowed per event. A loose mass window is first applied about about the true B meson mass. The two D mesons which form each B meson candidate are then fitted to a common vertex with no mass constraint applied. The B meson candidate must then pass a cut based upon the following criteria:

- χ^2 of the unconstrained vertex fit : This cut is also not normalised to the number of degrees of freedom.

In addition, the following cuts were placed upon the $\mathrm{B_c^+}$ candidate.

- minimum transverse momentum,
- maximum impact parameter significance with respect to the chosen primary vertex

The reasoning behind the application of these additional cuts in the $\mathrm{B_c^+ \to D_s^+\overline{D}^0}$ initial selection rather than in the refined selection to be discussed in the next section, was that this allowed a sufficient enough reduction factor to allow running over the entire sample of $\sim\mathcal{O}(10^7)$ inclusive $\mathrm{b\overline{b}}$ events which had been generated for physics studies in 2003 [181]. Not including these cuts in the $\mathrm{B_d^0 \to D^+D^-}$ and $\mathrm{B_s^0 \to D_s^+D_s^-}$ initial selection algorithms only allowed $\sim$80% and $\sim$50% respectively of the available inclusive $\mathrm{b\overline{b}}$ events to be used.

The number of inclusive $\mathrm{b\overline{b}}$ events to which these initial cuts were applied and the number of $\mathrm{b\overline{b}}$ events remaining are shown in Table 7.3. Also listed are the number of signal events for each $\mathrm{B \to DD}$ channel before and after the initial cuts are applied.

7.4 Final selection

In order to fully reconstruct the $B_d^0 \to D^+D^-$, $B_s^0 \to D_s^+D_s^-$ and $B_c^+ \to D_s^+\overline{D}^0$ decays, the same procedure is used as described in the previous section. A refined set of selection cuts were determined using the signal and inclusive $b\overline{b}$ events produced as described in Section 7.3. These cuts are listed in Table 7.4 and are organised in the same way as the initial cuts in Table 7.2. The refined set of cuts listed in Table 7.4 were tuned such that the inclusive $b\overline{b}$ background contribution became as small as possible while maximising the signal efficiency. The number of kaon/pion and D meson combinations at each stage of these cuts are tabulated[d] as follows:

- Table 7.5 : shows the number of $K^{\mp}\pi^{\pm}\pi^{\pm}$ and D^+D^- combinations at each stage of the $B_d^0 \to D^+D^-$ analysis.
- Table 7.6 : shows the number of $K^{\pm}K^{\mp}\pi^{\pm}$ and $D_s^+D_s^-$ combinations at each stage of the $B_s^0 \to D_s^+D_s^-$ analysis.
- Table 7.7 : shows the number of $K^+K^-\pi^+/K^+\pi^-$ and $D_s^+\overline{D}^0$ combinations at each stage of the $B_c^+ \to D_s^+\overline{D}^0$ analysis.

The mass, vertex and proper time resolutions resulting from these selection are discussed in the following sections. Only events in which the B meson was selected are considered.

[d]By looking at the "truth" information associated with each reconstructed particle, it is possible to monitor the number of true (reconstructed matches truth information) and fake signal combinations formed using the signal Monte Carlo. These fake combinations have been labelled as **some-signal** and **non-signal** in Tables 7.5, 7.6 and 7.7. When discussing $K\pi\pi/KK\pi/K\pi$ combinations a signal combination is one which has each contributing particle originating from the $B \to DD$ decay of interest. Therefore a non-signal combination is one which has at least one contributing particle which does not originate from the $B \to DD$ decay of interest. When discussing D^+/D^-, D_s^+/D_s^-, $D_s^+/\overline{D}^0$ combinations, a signal DD combination is one which consists of two signal combinations, a some-signal DD combination is one which consists of one signal and one non-signal combination and a non-signal DD combination is one which consists of two non-signal combinations.

7.5 Mass, Vertex and Proper Time Resolutions

7.5.1 Mass Resolutions

The invariant mass distributions of the D and B mesons in each of the B $\rightarrow$ DD decay channels are shown in Figures 7.4, 7.5 and 7.6. The D meson distributions are shown for events where a B meson was selected where the cuts discussed in Section 7.4 were applied and before any trigger.

Figures 7.4(a) and 7.5(a) are fitted with a single Gaussian. The remaining figures are fitted with a double Gaussian with the same mean value. The fit parameters and the percentage of events covered by each Gaussian are listed in Table 7.8. The resolutions on the B_d^0, B_s^0 and B_c^+ invariant mass distributions in Figures 7.4(b), 7.5(b) and 7.6(c) are consistent with those of the channels discussed in [70].

7.5.2 Vertex Resolutions

Unlike primary vertices which are reconstructed prior to analysis and about which information can be retrieved without carrying out the vertex fit during the analysis procedure, secondary vertices have to be reconstructed as required within each event. For example in the `Bd2DD.cpp` algorithm in which a candidate B_d^0 meson is reconstructed from a D^+ and a D^-, the vertex is obtained by fitting the D^+ and the D^- candidate to a common vertex.

Figures 7.7, 7.8 and 7.9 show resolutions of the B_d^0, B_s^0 and B_c^+ vertices in directions transverse (x,y) and longitudinal (z) to the beam. As with the primary vertices, each distribution is fitted with a double Gaussian with a common central value. The core Gaussian resolutions are $\sim$18-20 μm in x,y and $\sim$270 μm in z with 20-25 % of events in the second Gaussian which is three to four times wider.

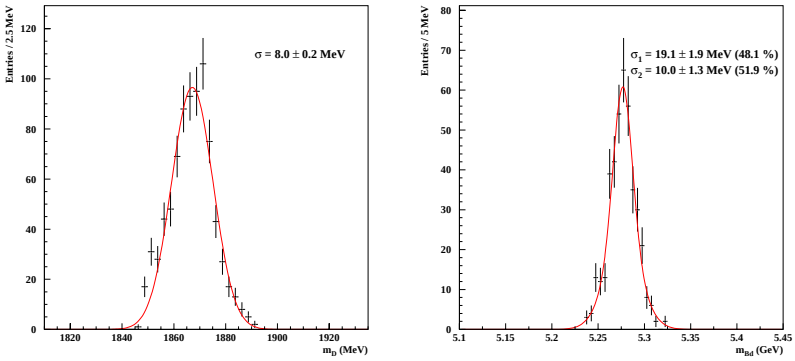

Figure 7.4: *Invariant mass distributions of selected* $D^{\pm} \Rightarrow K^{\mp}\pi^{\pm}\pi^{\pm}$ *and* $B_d^0 \rightarrow D^+D^-$ *mesons*

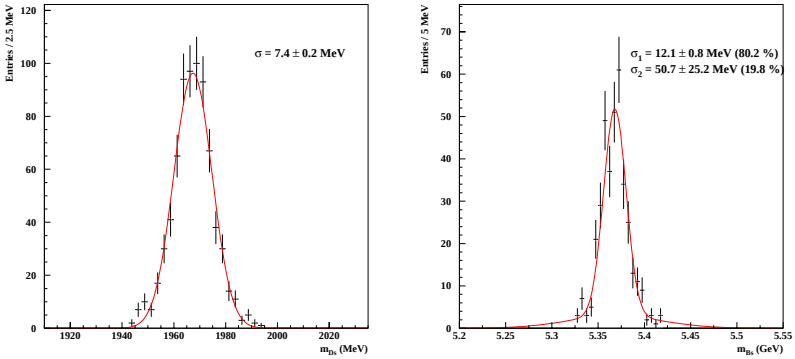

Figure 7.5: *Invariant mass distributions of selected* $D_s^{\pm} \Rightarrow K^{\pm}K^{\pm}\pi^{\mp}$ *and* $B_s^0 \rightarrow D_s^+D_s^-$ *mesons*

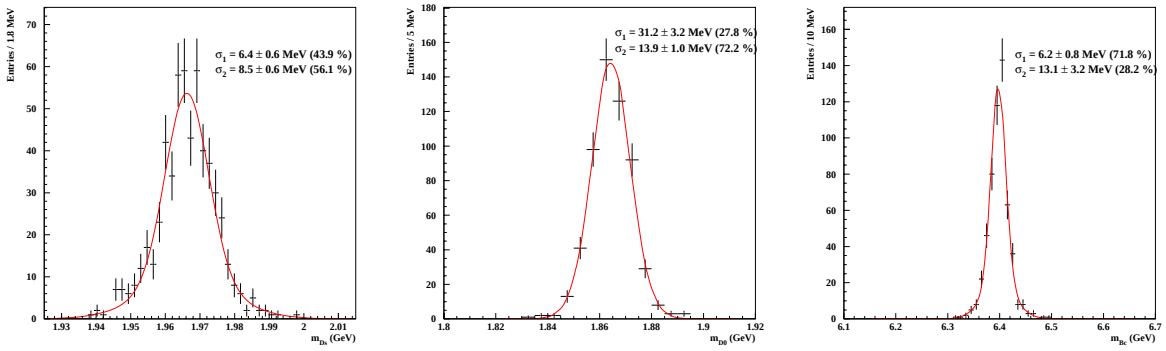

Figure 7.6: *Invariant mass distributions of selected* $D_s^+ \Rightarrow K^+K^-\pi^+$, $\overline{D}^0 \rightarrow K^+\pi^-$ *and* $B_c^+ \rightarrow D_s^+\overline{D}^0$ *mesons*

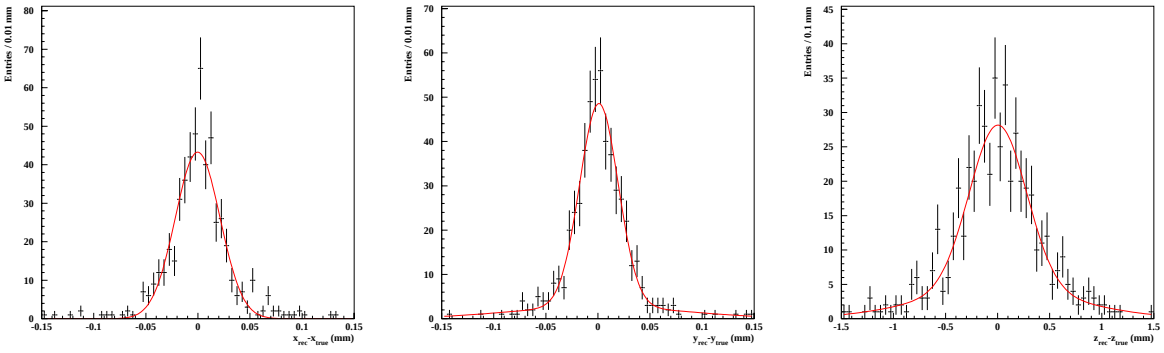

Figure 7.7: $B_d^0 \to D^+D^-$: B_d^0 *vertex resolutions in (left-to-right) x, y and z.*

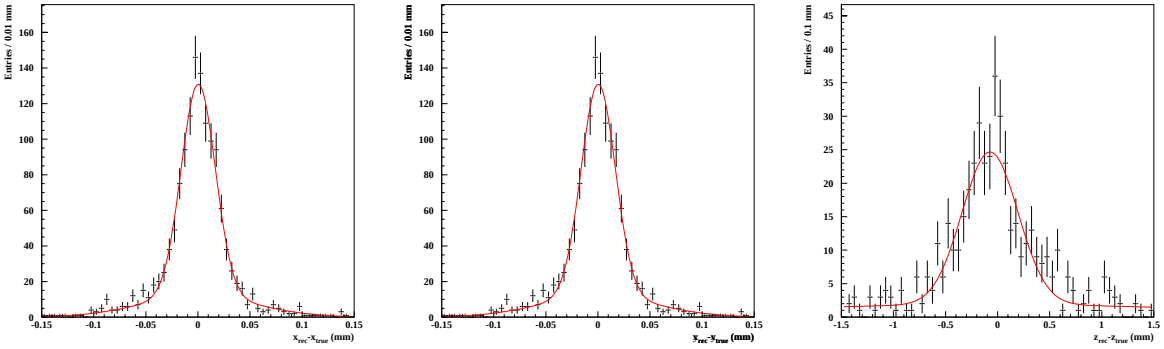

Figure 7.8: $B_s^0 \to D_s^+D_s^-$: B_s^0 *vertex resolutions in (left-to-right) x, y and z.*

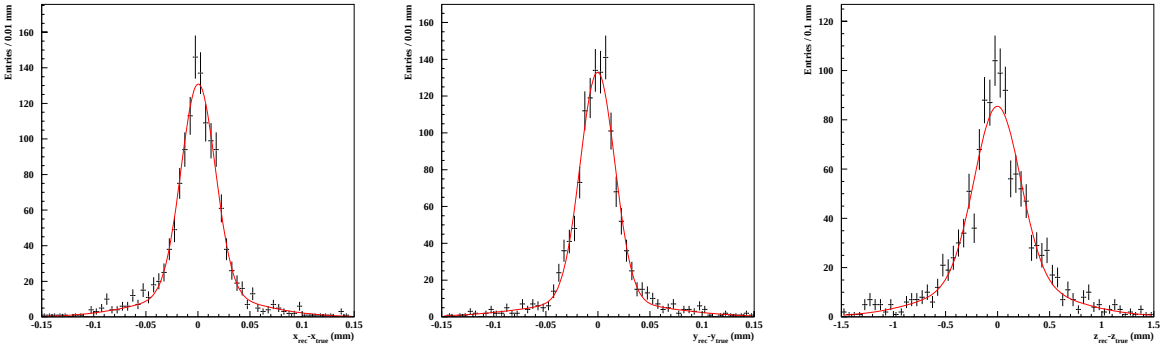

Figure 7.9: $B_c^+ \to D_s^+\overline{D}^0$: B_c^+ *vertex resolutions in (left-to-right) x, y and z.*

7.5.3 Proper Time Resolutions

In the measurement of the $\mathcal{CP}$-violating asymmetry $\mathcal{A}_{\mathcal{CP}}(t)$, the resolution on the proper time measurement is one of the factors to be included in a parameterisation of the ex-

perimentally observed decay rate for each channel. This was discussed in Section 3.3.2.

The proper time τ satisfies

$$\tau = \frac{t}{\gamma} \tag{7.1}$$

where t is the B meson lifetime in the laboratory. The B meson decay length, $\underline{L}$ is given by

$$\underline{L} = \underline{x}_{P.V.} - \underline{x}_{S.V.} = c \cdot \beta \cdot t \tag{7.2}$$

where β is the relative velocity of the particle with respect to c, the speed of light and $\underline{x}_{P.V.}$ and $\underline{x}_{S.V.}$ are the primary vertex and B meson decay vertex co-ordinates respectively. The B meson proper time, τ is calculated as

$$\tau = m_B \cdot \frac{\underline{p}_B \cdot \underline{L}}{|\underline{p}_B|^2} \tag{7.3}$$

with $\underline{p}_B$ being the reconstructed B meson momentum, and m_B being the true B meson mass.

The proper time resolution of the reconstructed B meson from $B_d^0 \to D^+D^-$ and $B_s^0 \to D_s^+D_s^-$ are shown in Figures 7.10 (a) and (b). These distributions are fitted using a double Gaussian with a common mean μ and standard deviations σ_1 and σ_2. The fit parameters are listed in Table 7.9. In particular the proper time resolution of the selected B_s^0 mesons is seen to be comparable to that of the $B_s^0 \to D_s^{\pm}K^{\mp}$ and $B_s^0 \to D_s^-\pi^+$ channels, studies of which are presented in [179]. In [179] the proper time resolution for the selected B_s^0 mesons is fitted with a double Gaussian where the first Gaussian has a width of 33 ± 1 fs and describes 69 % of the entries while the rest of the entries are described by a Gaussian of width 67 ± 3 fs. The first $B_s^0 \to D_s^+D_s^-$ Gaussian width is 33 ± 5 fs corresponding to 53 % of the entries while the rest of the entries are described by a Gaussian of width 120 ± 30 fs.

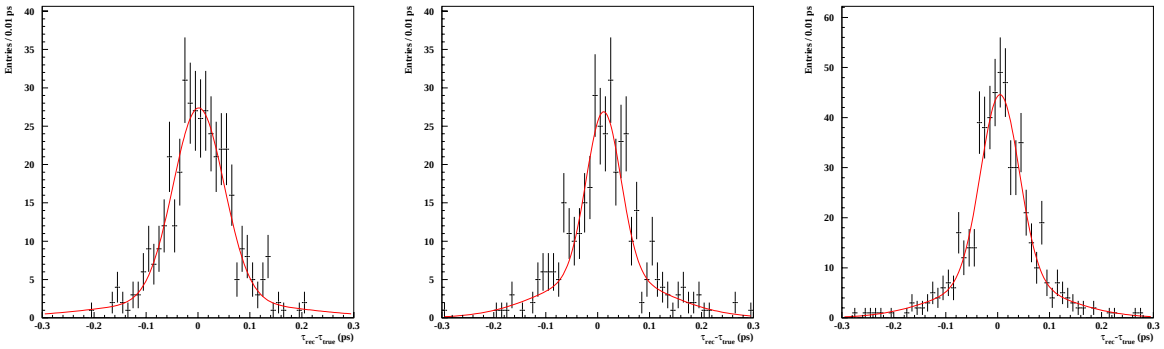

Figure 7.10: *Proper time resolution of selected B mesons from (left-to-right)* $B_d^0 \to D^+D^-$, $B_s^0 \to D_s^+D_s^-$ *and* $B_c^+ \to D_s^+\overline{D}^0$ *decays.*

7.5.4 Selection Efficiency, $\epsilon_{\text{sel/rec}}$

A selection efficiency $\epsilon_{\text{sel/rec}}$ is defined to describe the fraction of reconstructible and reconstructed signal Monte Carlo particles that pass the offline selection cuts listed in Table 7.4. As in Section 6.6 N_{rec} is the number of signal Monte Carlo events from N_{gen}^{sig} that are reconstructible and reconstructed. $\epsilon_{\text{sel/rec}}$ is defined as

$$\epsilon_{\text{sel/rec}} = \frac{N_{\text{sel}}^{sig}}{N_{\text{rec}}} \tag{7.4}$$

where N_{sel}^{sig} is the number of signal Monte Carlo events which pass the offline selection cuts. The values of $\epsilon_{\text{sel/rec}}$ for each channel are given in Table 7.10. None of the events selected contained decays which were composed of a ghost track. In Section 6.4 a ghost was defined as a track which does not correspond to any generated Monte Carlo particle.

7.6 Trigger

The LHCb trigger consists of three levels; Level-0 (L0), Level-1 (L1) and the Higher Level Trigger (HLT) and was described in Section 4.5. Within the DaVinci framework, the L0 and L1 trigger decisions can be evaluated. The HLT efficiency is not considered

here since there is currently no existing software with which to evaluate its performance. The software is expected to become available within the next year. However in principle, the HLT should be fully efficient on all selected events.

To quantitatively evaluate the trigger performance, a combined Level-0 (L0) and Level-1 (L1) trigger efficiency on the offline selected events, $\epsilon_{\text{trigger/sel}}$ is defined. If for a particular channel, there were N_{sel}^{sig} events which passed the offline selection cuts, N_{L0} of which passed the L0 trigger, and N_{trigger} of which passed both the L0 and L1 trigger, then the L0 trigger efficiency of the offline selected events is $N_{L0}/N_{\text{sel}}^{sig}$, the L1 trigger efficiency on offline selected events which have passed L0 is $N_{\text{trigger}}/N_{L0}$. The combined L0 and L1 trigger efficiency on offline selected events $\epsilon_{\text{trigger/sel}}$ is therefore

$$\epsilon_{\text{trigger/sel}} = \frac{N_{L0}}{N_{\text{sel}}^{sig}} \times \frac{N_{\text{trigger}}}{N_{L0}} = \frac{N_{\text{trigger}}}{N_{\text{sel}}^{sig}}. \tag{7.5}$$

Table 7.10 lists the values of N_{sel}^{sig}, N_{L0}, N_{L1} and $\epsilon_{\text{trigger/sel}}$ for each channel. The trigger efficiencies for each B $\rightarrow$ DD channel are comparable to those of other hadronic channels.

Decay Channel	Number of PV per event					
	0	1	2	3	4	5
$B_d^0 \to D^+D^-$	0.015 ± 0.006 %	73.3 ± 0.2 %	24.4 ± 0.2 %	2.25 ± 0.07 %	0.032 ± 0.008 %	-
$B_s^0 \to D_s^+D_s^-$	0.010 ± 0.005 %	73.3 ± 0.2 %	24.4 ± 0.2 %	2.23 ± 0.07 %	0.07 ± 0.01 %	-
$B_c^+ \to D_s^+\overline{D}^0$	0.010 ± 0.005 %	73.5 ± 0.2 %	24.1 ± 0.2 %	2.31 ± 0.07 %	0.07 ± 0.01 %	0.002 ± 0.002 %
All $B \to DD$ events	0.0118 ± 0.003 %	73.4 ± 0.1 %	24.3 ± 0.1 %	2.26 ± 0.04 %	0.055 ± 0.006 %	0.0007 ± 0.0007 %

Table 7.1: *Number of primary vertices (P.V.) reconstructed per event expressed as a percentage of the total number of* $B_d^0 \to D^+D^-$, $B_s^0 \to D_s^+D_s^-$ *and* $B_c^+ \to D_s^+\overline{D}^0$ *events, and then averaged over all* $B \to DD$ *events.*

Decay channels			
$B_d^0 \to D^+D^-, D^\pm \Rightarrow K^\mp\pi^\pm\pi^\pm$	$B_s^0 \to D_s^+D_s^-, D_s^\pm \Rightarrow K^\pm\pi^\pm\pi^\mp$	$B_c^+ \to D_s^+\overline{D}^0, D_s^+ \Rightarrow K^+\pi^+\pi^-, \overline{D}^0 \to K^-\pi^+$	
$D^\pm \Rightarrow K^\mp\pi^\pm\pi^\pm$	$D_s^\pm \Rightarrow K^\pm\pi^\pm\pi^\mp$	$D_s^+ \Rightarrow K^+\pi^+\pi^-$	$\overline{D}^0 \to K^+\pi^-$
Cuts on kaons and pions			
$p_{T\,K}$ [GeV] > 0.25	$p_{T\,K}$ [GeV] > 0.25	$0.25 < p_{T\,K}$ [GeV] < 15.0	$p_{T\,K}$ [GeV] < 1000.0
$p_{T\,\pi}$ [GeV] > 0.20	$p_{T\,\pi}$ [GeV] > 0.20	$0.15 < p_{T\,\pi}$ [GeV] < 10.0	$p_{T\,\pi}$ [GeV] < 1000.0
IP_K/σ_K w.r.t. P.V. > 0.9	IP_K/σ_K w.r.t. P.V. > 1.0	IP_K/σ_K w.r.t. P.V. > 0.9	-
IP_π/σ_π w.r.t. P.V. > 1.0	IP_π/σ_π w.r.t. P.V. > 1.2	IP_π/σ_π w.r.t. P.V. > 0.9	-
Cuts on $K\pi\pi/KK\pi/K\pi$ combinations			
$\lvert m_{K\pi\pi}$-$m_{D}\rvert < 200.0$ MeV	$\lvert m_{KK\pi}$-$m_{D_s}\rvert < 200.0$ MeV	$\lvert m_{KK\pi}$-$m_{D_s}\rvert < 200.0$ MeV	$\lvert m_{K\pi}$-$\rvert < 150.0$ MeV
χ^2 $K\pi\pi$ vertex < 40	χ^2 vertex < 50	χ^2 vertex < 250	-
$p_{T\,K\pi\pi} > 1.0$ GeV	$p_{T\,KK\pi} > 0.5$ GeV	-	-
$3.0 < \lvert\frac{x_{P.V.}-x_{S.V.}}{\sigma_{x_{P.V.}-x_{S.V.}}}\rvert < 500.0$	$\lvert\frac{x_{P.V.}-x_{S.V.}}{\sigma_{x_{P.V.}-x_{S.V.}}}\rvert > 2.0$	$0.0 < \lvert\frac{x_{P.V.}-x_{S.V.}}{\sigma_{x_{P.V.}-x_{S.V.}}}\rvert < 500.0$	$0.0 < \lvert\frac{x_{P.V.}-x_{S.V.}}{\sigma_{x_{P.V.}-x_{S.V.}}}\rvert < 2000.0$
$\lvert m_{K\pi\pi}$-$m_{D}\rvert < 30.0$ MeV	$\lvert m_{KK\pi}$-$m_{D_s}\rvert < 50.0$ MeV	$\lvert m_{KK\pi}$-$m_{D_s}\rvert < 50.0$ MeV	$\lvert m_{K\pi}$-$\rvert < 40.0$ MeV
$m^2_{K\pi_1} < 3.7 - m^2_{K\pi_2}$	$m^2_{K^+K^-} < 4.0 - m^2_{K^-\pi^+(K^+\pi^-)}$	$m^2_{K^+K^-} < 4.0 - m^2_{K^-\pi^+}$	-
$B_d^0 \to D^+D^-$	$B_s^0 \to D_s^+D_s^-$	$B_c^+ \to D_s^+\overline{D}^0$	
Cuts on D^+/D^-, D_s^+/D_s^-, $D_s^+/\overline{D}^0$ combinations			
$\lvert m_{D^+D^-} - m_{B_d^0}\rvert < 500$ MeV	$\lvert m_{D_s^+D_s^-} - m_{B_s^0}\rvert < 500$ MeV	$\lvert m_{D_s^+\overline{D}^0} - m_{B_c^+}\rvert < 500$ MeV	
χ^2 D^+D^- vertex < 10.5	χ^2 $D_s^+D_s^-$ vertex < 10.0	χ^2 $D_s^+\overline{D}^0$ vertex < 7.0	
-	-	$p_{T\,D_s^+\overline{D}^0} > 2.0$ GeV	
-	-	$\lvert\frac{x_{P.V.}-x_{S.V.}}{\sigma_{x_{P.V.}-x_{S.V.}}}\rvert < 100.0$	

Table 7.2: *Loose selection cuts applied prior to preparation of the inclusive* $b\overline{b}$ *sample.*

Decay channel	# Signal events		# Inclusive $b\overline{b}$ events	
	Before	After	Before	After
$B_d^0 \to D^+D^-$	47500	1489	8461350	79475
$B_s^0 \to D_s^+D_s^-$	48000	2356	5250000	72559
$B_c^+ \to D_s^+\overline{D}^0$	48750	1524	10947600	31863

Table 7.3: *Number of events after* $B_d^0 \to D^+D^-$, $B_s^0 \to D_s^+D_s^-$ *and* $B_c^+ \to D_s^+\overline{D}^0$ *loose selection cuts applied*

Decay channels			
$B_d^0 \to D^+D^-, D^\pm \Rightarrow K^\mp\pi^\pm\pi^\pm$	$B_s^0 \to D_s^+D_s^-, D_s^\pm \Rightarrow K^\pm\pi^\pm\pi^\mp$	$B_c^+ \to D_s^+\overline{D}^0, D_s^+ \Rightarrow K^+\pi^+\pi^-, \overline{D}^0 \to K^-\pi^+$	
$D^\pm \Rightarrow K^\mp\pi^\pm\pi^\pm$	$D_s^\pm \Rightarrow K^\pm\pi^\pm\pi^\mp$	$D_s^+ \Rightarrow K^+\pi^+\pi^-$	$\overline{D}^0 \to K^-\pi^+$
Cuts on kaons and pions			
$C.L_K > 0.5$	$C.L_K > 0.5$	-	$C.L_K > 0.5$
$C.L_\pi > 0.45$	$C.L_K > 0.5$	-	$C.L_K > 0.5$
$0.25 < p_{TK}\,[\text{GeV}] < 9.0$	$0.25 < p_{TK}\,[\text{GeV}] < 10.0$	$0.2 < p_{TK}\,[\text{GeV}] < 15.0$	$0.2 < p_{T\pi}\,[\text{GeV}] < 1000.0$
$0.20 < p_{T\pi}\,[\text{GeV}] < 7.0$	$0.20 < p_{T\pi}\,[\text{GeV}] < 6.0$	$0.15 < p_{TK}\,[\text{GeV}] < 10.0$	$0.3 < p_{T\pi}\,[\text{GeV}] < 1000.0$
$3.3 < IP_K/\sigma_K$ w.r.t. P.V. < 400.0	$3.1 < IP_K/\sigma_K$ w.r.t. P.V. < 600.0	IP_K/σ_K w.r.t. P.V. > 0.9	-
$2.2 < IP_\pi/\sigma_\pi$ w.r.t. P.V. < 350.0	$2.8 < IP_\pi/\sigma_\pi$ w.r.t. P.V. < 200.0	IP_π/σ_π w.r.t. P.V. > 0.9	IP_π/σ_π w.r.t. P.V. > 0.7
Cuts on K$\pi\pi$/$KK\pi$/$K\pi$ combinations			
$\lvert m_{K\pi\pi}\text{-}m_{D}\rvert < 200.0$ MeV	$\lvert m_{KK\pi}\text{-}m_{D_s}\rvert < 200.0$ MeV	$\lvert m_{KK\pi}\text{-}m_{D_s}\rvert < 200.0$ MeV	$\lvert m_{K\pi}\text{-}\rvert < 150.0$ MeV
χ^2 $K\pi\pi$ vertex < 20	χ^2 vertex < 25	χ^2 vertex < 25	χ^2 vertex < 20
$p_{TKK\pi\pi} > 1.6$ GeV	$p_{TKK\pi} > 1.1$ GeV	$p_{TKK\pi} > 2.0$ GeV	-
$3.0 < \lvert\frac{x_{P.V.}-x_{S.V.}}{\sigma_{x_{P.V.}-x_{S.V.}}}\rvert < 220.0$	$2.0 < \lvert\frac{x_{P.V.}-x_{S.V.}}{\sigma_{x_{P.V.}-x_{S.V.}}}\rvert < 200.0$	$3.0 < \lvert\frac{x_{P.V.}-x_{S.V.}}{\sigma_{x_{P.V.}-x_{S.V.}}}\rvert < 500.0$	$2.0 < \lvert\frac{x_{P.V.}-x_{S.V.}}{\sigma_{x_{P.V.}-x_{S.V.}}}\rvert < 2000.0$
$\lvert m_{K\pi\pi}\text{-}m_{D}\rvert < 30.0$ MeV	$\lvert m_{KK\pi}\text{-}m_{D_s}\rvert < 25.0$ MeV	$\lvert m_{K\pi\pi}\text{-}m_{D_s}\rvert < 30.0$ MeV	$\lvert m_{K\pi}\text{-}\rvert < 30.0$ MeV
$m^2_{K\pi_1} < 3.7 - m^2_{K\pi_2}$	$m^2_{K^+K^-} < 4.0 - m^2_{K^-\pi^+(K^+\pi^-)}$	$m^2_{K^+K^-} < 4.0 - m^2_{K^-\pi^+(K^+\pi^-)}$	-
Cut on DD combinations			
$\lvert m_{D^+D^-} - m_{B_d^0}\rvert < 150$ MeV	$\lvert m_{D_s^+D_s^-} - m_{B_s^0}\rvert < 150$ MeV	$\lvert m_{D_s^+\overline{D}^0} - m_{B_c^+}\rvert < 500$ MeV	
χ^2 D^+D^- vertex < 5.0	χ^2 $D_s^+D_s^-$ vertex < 4.0	χ^2 $D_s^+\overline{D}^0$ vertex < 7.0	
I.P. w.r.t. P.V. < 0.01 cm	I.P. w.r.t. P.V. < 0.02 cm	$\lvert\frac{x_{P.V.}-x_{S.V.}}{\sigma_{x_{P.V.}-x_{S.V.}}}\rvert < 100.0$	
$p_{TD^+D^-} > 5.0$ GeV	$p_{TD_s^+D_s^-} > 5.0$ GeV	$p_{TD_s^+\overline{D}^0} > 6.5$ GeV	
$\lvert m_{D^+D^-} - m_{B_d^0}\rvert < 40$ MeV	$\lvert m_{D_s^+D_s^-} - m_{B_s^0}\rvert < 50$ MeV	$\lvert m_{D_s^+\overline{D}^0} - m_{B_c^+}\rvert < 100$ MeV	

Table 7.4: *Optimised selection cuts for the* $B_d^0 \to D^+D^-$, $B_s^0 \to D_s^+D_s^-$ *and* $B_c^+ \to D_s^+\overline{D}^0$ *decay channels.*

Decay channel	$B_d^0 \to D^+D^-, D^\pm \Rightarrow K^\mp\pi^\pm\pi^\pm$					
	$D^+ \to K^-\pi^+\pi^+$			$D^- \to K^+\pi^-\pi^-$		
Number of $K^\mp\pi^\pm\pi^\pm$ combinations	Signal	Non-signal	$b\bar{b}$	Signal	Non-signal	$b\bar{b}$
Before K and π cuts	10135	28615687	252715625	10211	27823708	253416542
After K and π cuts	6648	1124342	20366951	6696	1073443	20364136
After K$\pi\pi$ cuts	3708	619	25620	3745	573	25118

	$B_d^0 \to D^+D^-$			
Number of D^+D^- combinations	Signal	Some-signal	Non-signal	$b\bar{b}$
Before D^+D^- cuts	511	94	107	13758
After D^+D^- cuts	403	1	1	0

Table 7.5: *Number of* $K^\mp\pi^\pm\pi^\pm$ *and* D^+D^- *combinations at each stage of the* $B_d^0 \to D^+D^-$ *analysis.*

Decay channel	$B_s^0 \to D_s^+D_s^-, D_s^\pm \Rightarrow K^\pm K^\mp\pi^\pm$					
	$D_s^+ \to K^+K^-\pi^+$			$D_s^- \to K^+K^-\pi^-$		
Number of $K^\pm K^\mp\pi^\pm$ combinations	Signal	Non-signal	$b\bar{b}$	Signal	Non-signal	$b\bar{b}$
Before K and π cuts	10058	18650704	126401985	10007	18420484	124928764
After K and π cuts	5123	656326	9907474	5334	663087	10061668
After KKπ cuts	3347	986	23109	3137	968	22984

	$B_s^0 \to D_s^+D_s^-$			
Number of $D_s^+D_s^-$ combinations	Signal	Some-signal	Non-signal	$b\bar{b}$
Before $D_s^+D_s^-$ cuts	469	303	330	22032
After $D_s^+D_s^-$ cuts	364	3	0	0

Table 7.6: *Number of* $K^\pm K^\mp\pi^\pm$ *and* $D_s^+D_s^-$ *combinations at each stage of the* $B_s^0 \to D_s^+D_s^-$ *analysis*

Decay channel	$B_c^+ \to D_s^+\overline{D}^0, D_s^+ \Rightarrow K^+\pi^+\pi^-$, $\overline{D}^0 \to K^-\pi^+$					
	$D_s^+ \to K^+K^-\pi^+$			$\overline{D}^0 \to K^+\pi^-$		
Number of $K^+K^-\pi^+/K^+\pi^-$ combinations	Signal	Non-signal	$b\overline{b}$	Signal	Non-signal	$b\overline{b}$
Before K and π cuts	4272	24895191	30081578	10013	1852914	1784134
After K and π cuts	3539	8337711	9854675	9098	675210	644288
After $KK\pi/K\pi$ cuts	1936	4761	2253	7638	4360	6816
	$B_c^+ \to D_s^+\overline{D}^0$					
Number of $D_s^+\overline{D}^0$ combinations	Signal	Some-signal		Non-signal	$b\overline{b}$	
Before $D_s^+\overline{D}^0$ cuts	1076	1045		458	1020	
After $D_s^+\overline{D}^0$ cuts	563	21		0	0	

Table 7.7: *Number of* $K^+K^-\pi^+/K^+\pi^-$ *and* $D_s^+\overline{D}^0$ *combinations at each stage of the* $B_c^+ \to D_s^+\overline{D}^0$ *analysis.*

Figure	m_{MC} [MeV/c^2]	μ [MeV/c^2]	σ_1 [MeV/c^2]		σ_2 [MeV/c^2]		χ^2/n.d.f
7.4(a)	1869.3 ± 0.5	1867.1 ± 0.2	8.0 ± 0.2	-	-	-	2.2
7.4(b)	5279.4 ± 0.5	5276.7 ± 0.2	19.1 ± 1.9	(48.1%)	10.0 ± 1.3	(51.9%)	1.0
7.5(a)	1968.5 ± 0.6	1967.4 ± 0.2	7.4 ± 0.2	-	-	-	1.1
7.5(b)	5369.6 ± 2.4	5368.1 ± 0.5	12.1 ± 0.8	(80.2%)	50.7 ± 25.2	(19.8%)	1.6
7.6(a)	1968.5 ± 0.6	1966.2 ± 0.2	6.2 ± 0.8	(71.8%)	13.1 ± 3.2	(28.2%)	1.0
7.6(b)	1864.5 ± 0.5	1864.4 ± 0.2	6.4 ± 0.6	(43.9%)	8.5 ± 0.6	(56.1%)	1.0
7.6(c)	6400 ± 400	6397.7 ± 0.5	31.2 ± 3.2	(27.8%)	13.9 ± 1.0	(72.2%)	1.1

Table 7.8: *Parameters of the fitted mass distributions of* $D^{\pm}$ *and* B_d^0, $D_s^{\pm}$ *and* B_s^0, *and* $D_s^{\pm}$, $\overline{D}^0$ *and* B_c^+ *mesons from* $B_d^0 \to D^+D^-$, $B_s^0 \to D_s^+D_s^-$ *and* $B_c^+ \to D_s^+\overline{D}^0$ *events. The distributions have either been fitted with a single Gaussian (μ, σ) or a double Gaussian with the same mean (μ, σ_1, σ_2) with χ^2/ndf as listed. The true mass of the particle m_{MC} is also given [37].*

Figure	μ [ps]	σ_1 [ps]		σ_2 [ps]		χ^2/n.d.f.
7.10 (left)	0.013 ± 0.003	0.05 ± 0.01	(76.0 %)	0.17 ± 0.48	(24.0 %)	0.86
7.10 (centre)	0.012 ± 0.003	0.033 ± 0.005	(53.3 %)	0.12 ± 0.03	(46.7 %)	1.17
7.10 (right)	0.005 ± 0.002	0.04 ± 0.01	(64.2 %)	0.11 ± 0.07	(35.8 %)	0.66

Table 7.9: *Proper time resolution of the reconstructed B mesons from* $B_d^0 \to D^+D^-$, $B_s^0 \to D_s^+D_s^-$ *and* $B_c^+ \to D_s^+\overline{D}^0$ *decays*

Decay Channel	$B_d^0 \to D^+ D^-$	$B_s^0 \to D_s^+ D_s^-$	$B_c^+ \to D_s^+ \overline{D}^0$
$N_{\rm rec}$	5882	6116	7762
$N_{\rm sel}^{sig}$	405	367	584
$N_{\rm sel}^{sig}$ events passing L0 trigger, N_{L0}	203	191	331
$N_{\rm sel}^{sig}$ events passing L0 & L1 trigger,$N_{\rm trigger}$	147	126	130
Selection efficiency, $N_{\rm sel}^{sig}/N_{\rm rec}$ [%]	6.7 ± 0.3	5.9 ± 0.3	7.3 ± 0.3
L0 trigger efficiency, $N_{L0}/N_{\rm sel}^{sig}$ [%]	50.1 ± 2.5	52.0 ± 2.6	56.7 ± 2.1
L1 trigger efficiency, $N_{\rm trigger}/N_{L0}$ [%]	72.4 ± 3.1	66.0 ± 3.4	39.3 ± 2.7
Combined trigger efficiency, $\epsilon_{\rm trigger/sel}$ [%]	36.3 ± 2.4	34.3 ± 2.5	22.3 ± 1.7

Table 7.10: *Selection efficiencies of reconstructed events* $\epsilon_{\rm sel/rec}$ *and trigger efficiencies* $\epsilon_{\rm trigger/sel}$*, of offline selected events. The uncertainties on* $\epsilon_{\rm sel/rec}$*,* $N_{L0}/N_{\rm sel}^{sig}$*,* $N_{\rm trigger}/N_{L0}$ *and* $\epsilon_{\rm trigger/sel}$ *are statistical.*

Chapter 8

Efficiencies, Event Yields and B/S ratios

8.1 Signal efficiencies

The total signal efficiency, $\epsilon_{\rm total}$, is the fraction of generated signal Monte Carlo events containing a signal B decay that are triggered, reconstructed, and selected with offline cuts for physics analysis. $\epsilon_{\rm total}$ can be written as the product of several previously defined contributing efficiencies,

$$\epsilon_{\rm total} = \epsilon_{\rm det} \times \epsilon_{\rm rec/det} \times \epsilon_{\rm sel/rec} \times \epsilon_{\rm trigger/sel}, \tag{8.1}$$

where

- $\epsilon_{\rm det}$ is the detection efficiency including the 400 mrad acceptance generator-level cut on the polar angle of the signal b-hadron ($\epsilon_{\rm gen}^{\rm signal}$) and the fraction of events that are reconstructible ($\epsilon_{\rm accept}$), i.e. $\epsilon_{\rm det} = \epsilon_{\rm gen}^{\rm signal} \times \epsilon_{\rm accept}$
- $\epsilon_{\rm rec/det}$ is the reconstruction efficiency on reconstructible events,
- $\epsilon_{\rm sel/rec}$ is the efficiency for the offline selection cuts on the reconstructed events,

- $\epsilon_{\rm trigger/sel}$ is the product of the L0 trigger efficiency on the offline-selected events and the L1 trigger efficiency for the offline-selected events passing L0. It is assumed that the HLT is fully efficient on these events.

The values of $\epsilon_{\rm det}$, $\epsilon_{\rm rec/det}$, $\epsilon_{\rm sel/rec}$, $\epsilon_{\rm trigger/sel}$ are collected together in Table 8.1 along with the calculated values of $\epsilon_{\rm total}$.

Decay Channel	$\epsilon_{\rm det}$ [%]	$\epsilon_{\rm rec/det}$ [%]	$\epsilon_{\rm sel/rec}$ [%]	$\epsilon_{\rm trigger/sel}$ [%]	$\epsilon_{\rm total}$ [%]
$B^0_d \to D^+D^-$	6.29 ± 0.09	70.4 ± 0.5	6.7 ± 0.3	36.3 ± 2.4	0.107 ± 0.09
$B^0_d \to D^+D^-$	6.61 ± 0.09	68.5 ± 0.5	5.9 ± 0.3	34.3 ± 2.5	0.091 ± 0.08
$B^+_c \to D^+_s\overline{D}^0$	7.36 ± 0.09	76.9 ± 0.4	7.3 ± 0.3	22.3 ± 1.7	0.093 ± 0.08

Table 8.1: *Efficiency values* $\epsilon_{\rm det}$, $\epsilon_{\rm rec/det}$, $\epsilon_{\rm sel/rec}$, $\epsilon_{\rm trigger/sel}$ *and* $\epsilon_{\rm total}$ *with statistical errors.*

8.2 Annual signal event yields

The number of triggered events per year of LHCb running for a given decay channel, N_{year}, can be written as

$$N_{year} = \underbrace{\int_{year} \mathcal{L}(t)\,dt \times \sigma_{b\overline{b}}}_{N_{b\overline{b}}} \times 2 \times f_q \times \prod_i \mathcal{BR}_i \times \epsilon_{\rm total} \tag{8.2}$$

where

- $N_{b\overline{b}}$ is the number of $b\overline{b}$ produced per year of LHCb operation = 1.0×10^{12}/year. This is calculated assuming an average luminosity at LHCb of $2{\times}10^{32}$ cm^{-2}s^{-1}, a $b\overline{b}$ cross-section of 500 μb and a 10^7s year.

- f_q is the probability of forming a B^0_q meson after producing a $\overline{b}$ quark.

- The factor 2 takes into account the production of both b and $\overline{\mathrm{b}}$ quarks.
- $\prod_i \mathcal{BR}_i$ is the product of all branching ratios involved in the b-hadron decay of interest (see Table 6.1).
- $\epsilon_{\mathrm{total}}$ is the total efficiency as defined in Section 8.1.

The values of f_q, $\prod_i \mathcal{BR}_i$, $\epsilon_{\mathrm{total}}$ and N_{year} with statistical errors are listed in Table 8.2.

Decay Channel	Production fraction, f_q [%]	$\prod_i \mathcal{BR}_i$ ($\times 10^{-6}$)	$\epsilon_{\mathrm{total}}$ [%]	N_{year} (k)
$\mathrm{B_d^0} \to \mathrm{D^+ D^-}$	$f_d = 38.8 \pm 1.3$ [37]	(3.1 ± 1.2)	0.107 ± 0.09	2.60 ± 0.21
$\mathrm{B_s^0} \to \mathrm{D_s^+ D_s^-}$	$f_s = 10.7 \pm 1.3$ [37]	(15.0 ± 8.0)	0.091 ± 0.08	2.8 ± 0.3
$\mathrm{B_c^+} \to \mathrm{D_s^+ \overline{D}^0}$	$f_c = 0.08 \pm 0.01$ [37]	(0.017 ± 0.005)	0.093 ± 0.08	$(24.8 \pm 0.2) \times 10^{-6}$

Table 8.2: *Production fractions f_q, product of relevant branching ratios $\prod_i \mathcal{BR}_i$, total efficiencies $\epsilon_{\mathrm{total}}$ and annual events yields N_{year} for each of the* $\mathrm{B} \to \mathrm{DD}$ *channels.*

8.3 Background Studies

For these analyses, and in all analyses presented in [70] it is assumed that the most significant contribution to the combinatorial background comes from inclusive $\mathrm{b\overline{b}}$ events. These are $\mathrm{b\overline{b}}$ events where at least one b-hadron is emitted within 400 mrad of the beam axis. Tracks from inclusive b-hadron decays are displaced from the primary vertex and, after minimum p_T requirements, have a much larger probability to form fake secondary vertices than tracks in $\mathrm{c\overline{c}}$ or light-flavour events. The currently available Monte Carlo background statistics of $\sim 10^7$ inclusive $\mathrm{b\overline{b}}$ events is insufficient to obtain a precise estimate of the background levels (except for channels with a relatively large visible branching ratio), and so upper limits are derived.

To prevent the signal from being obscured by the inclusive $\mathrm{b\overline{b}}$ background, it is necessary that the selection cuts listed in Table 7.4 remove all inclusive $\mathrm{b\overline{b}}$ events from

within the tight B-meson mass window. However, since the inclusive $b\overline{b}$ sample used to tune these selection cuts is the same as the one used to estimate the background-to-signal (B/S) ratio (Section 8.3.2), then the B/S estimate obtained is not unbiased.

In order to obtain a better estimate of the B/S ratio, the $b\overline{b}$ event sample size is artificially increased using the following procedure. The tight mass window about the true B meson mass is removed, and the loose mass window about the true B meson mass is increased to $\sim$10 times the size of the original tight mass window. The following assumptions are made:

- The inclusive $b\overline{b}$ distribution is flat in the loose mass window, and the number of $b\overline{b}$ events found there can then be scaled according to the ratio of the width of the loose mass window to the tight mass window.
- The kinematics and topologies of the $b\overline{b}$ events in the new loose mass window are compatible with those of the $b\overline{b}$ events in the tight mass window.

The choice of the size of the loose mass window was arbitrary, but is consistent with the procedure carried out in other analyses in LHCb.

8.3.1 Inclusive $b\overline{b}$ Background

Before the background-to-signal (B/S) ratio is calculated, the individually selected background events from the inclusive $b\overline{b}$ sample for each analysis are inspected in more detail. Background events that have a reconstructed invariant B mass within the loose mass window, but arise from a decay process containing neutral particles and would therefore not normally pass the selection cuts, are eliminated from the background calculation. Each $B \to DD$ decay is now considered in turn.

8.3.1.1 $B_d^0 \to D^+D^-$ selection

One $b\overline{b}$ event passes $B_d^0 \to D^+D^-$ selection cuts and lies within the loose B_d^0 mass window ($\pm$ 500 MeV of the true B_d^0 mass). This event also passes the Level-0 and Level-1 triggers. In this event the tracks used to form the B_d^0 candidate come from the decay chain:

- $\overline{B_d^0} \to D^*(2010)^+D^-$
- $D^*(2010)^+ \to D^+\pi^0$ where $D^+(\to \overline{K^*}_2(1430)^0(\to K^-\pi^+))\pi^+$
- $D^-(\to K^{*0}(892)(\to K^+\pi^-)\pi^-)$

The selection cuts correctly select the mesons from the B_d^0 decay and all six tracks come from a true B_d^0 meson which has a reconstructed mass of 5118.54 MeV. This reconstructed mass is lower than the true B_d^0 mass since the π^0 ($p_{\pi^0} = 1.234$ GeV) in the $\overline{B_d^0} \to D^*(2010)^+(\to D^+\pi^0)$ part of the decay chain has not been included in the reconstruction. This event is removed from the $B_d^0 \to D^+D^-$ B/S calculation.

8.3.1.2 $B_s^0 \to D_s^+D_s^-$ selection

Two $b\overline{b}$ events pass the $B_s^0 \to D_s^+D_s^-$ selection cuts within the loose B_s^0 mass window ($\pm$ 500 MeV of the true B_s^0 mass). These events also pass the Level-0 and Level-1 trigger. The tracks used to form these two B_s^0 candidates come from the following decay chains:

- $B_s^0 \to D_s^{*+}D_s^{*-}$
- $D_s^{*+} \to D_s^+\gamma$ where $D_s^+ \to K^-K^+\pi^+$
- $D_s^{*-} \to D_s^-\gamma$ where $D_s^- \to \phi(\to K^+K^-)\pi^-$

and

- $B_s^0 \to D_s^{*+}D_s^{*-}$

- $D_s^{*+} \to D_s^+\gamma$ where $D_s^+ \to \overline{K^*}(892)^0(\to K^-\pi^+)K^+$
- $D_s^{*-} \to D_s^-\gamma$ where $D_s^- \to K^{*0}(892)(\to K^+\pi^-)K^-$.

In both of these events all six tracks come from a true B_s^0 meson with a reconstructed mass of 5016.23 MeV and 4888.03 MeV respectively. In both events the two γ (with momenta p_γ= 8.516 GeV, 1.191 GeV and 4.097 GeV, 4.852 GeV) have not been included in the reconstruction and therefore the reconstructed B_s^0 masses are lower than the true B_s^0 mass. Therefore as for the $B_d^0 \to D^+D^-$ analysis, none of the selected $b\overline{b}$ events should be considered as background.

8.3.1.3 $B_c^+ \to D_s^+\overline{D}^0$ selection

No $b\overline{b}$ events pass the $B_c^+ \to D_s^+\overline{D}^0$ selection cuts within the loose mass window ($\pm$ 500 MeV about the true B_c^+ mass).

Table 8.3 summarises the number of selected $b\overline{b}$ events used in the estimate of the $b\overline{b}$ background levels for each channel. The following abbreviations are used.

- $N_{\rm sel}^{b\overline{b},\rm loose}$ is the number of $b\overline{b}$ background selected events within the specified loose mass windows, and
- $N_{\rm sel}^{b\overline{b},\rm tight}$ is the number of $b\overline{b}$ background selected events within the specified tight mass windows.

8.3.2 Estimate of the inclusive $b\overline{b}$ background.

For a given decay channel the background-to-signal B/S ratio after selection, but before any trigger, is given by

$$\frac{B}{S} = \frac{\epsilon_{\rm gen}^{b\overline{b}}}{\epsilon_{\rm gen}^{\rm signal}} \cdot \frac{1}{2 \times f_q \times \prod_i \mathcal{BR}_i} \cdot \frac{N_{\rm sel}^{b\overline{b}}/N_{\rm gen}^{b\overline{b}}}{N_{\rm sel}^{sig}/N_{\rm gen}^{sig}} \tag{8.3}$$

Decay Channel	$B_d^0 \to D^+D^-$	$B_s^0 \to D_s^+D_s^-$	$B_c^+ \to D_s^+\overline{D}^0$
Loose mass window [MeV]	$\pm$ 500	$\pm$ 500	$\pm$ 500
$N_{\rm sel}^{\rm b\overline{b},loose}$	1 (0)	2 (0)	0
Tight mass window [MeV]	$\pm$ 50	$\pm$ 50	$\pm$ 100
$N_{\rm sel}^{\rm b\overline{b},tight}$	0	0	0

Table 8.3: *Numbers of* $\rm b\overline{b}$ *background selected events within set loose and tight mass windows.The entries 1(0) and 2(0) indicate that although 1 and 2* $\rm b\overline{b}$ *events passed the* $B_d^0 \to D^+D^-$ *and* $B_s^0 \to D_s^+D_s^-$ *selection cuts, they were discounted for reasons explained in the text. None of these 3* $\rm b\overline{b}$ *events contained ghost tracks.*

where the values of each contribution are listed in Table 8.4 and are summarised below.

- $\epsilon_{\rm gen}^{\rm b\overline{b}}$ and $\epsilon_{\rm gen}^{\rm signal}$ are the efficiencies of the cuts imposed on the Monte Carlo at the generator level, as described in Section 6.5

- f_q and $\prod_i \mathcal{BR}_i$ are the production fraction and product branching ratios listed in Table 8.2.

- $N_{\rm gen}^{sig}$ is the number of signal Monte Carlo events generated per decay channel, of which $N_{\rm sel}^{sig}$ events pass the offline selection cuts.

- $N_{\rm gen}^{\rm b\overline{b}}$ is the number of inclusive $\rm b\overline{b}$ events studied per channel, of which $N_{\rm sel}^{\rm b\overline{b}}$ is the *projected* number passing the selection cuts in the tight mass window.
  $N_{\rm sel}^{\rm b\overline{b}}$ is given by

$$N_{\rm sel}^{\rm b\overline{b}} = \frac{\text{Tight mass window [MeV]}}{\text{Loose mass window [MeV]}} \times N_{\rm sel}^{\rm b\overline{b},loose}, \tag{8.4}$$

  where in the cases that $N_{\rm sel}^{\rm b\overline{b},loose} < 10$, $N_{\rm sel}^{\rm b\overline{b},loose}$ takes the 90% confidence level Poisson upper limit for n observed events within the loose mass window. In the case that $n = 0$ then this upper limit is 2.44.

Decay Channel	$B_d^0 \to D^+D^-$	$B_s^0 \to D_s^+D_s^-$	$B_c^+ \to D_s^+\overline{D}^0$
$\epsilon_{gen}^{b\bar{b}}[\%]$	43.21 ± 0.04		
$\epsilon_{gen}^{signal}[\%]$	34.71 ± 0.03		
$2 \cdot f_q \cdot \prod_i \mathcal{BR}_i$	$(2.4 \pm 0.9)\times10^{-6}$	$(3.1 \pm 1.7)\times10^{-6}$	$(267.52 \pm 73)\times10^{-12}$
N_{sel}^{sig}	405	367	584
N_{gen}^{sig}	47500	48000	48750
$N_{sel}^{b\bar{b}}$	$\frac{50}{500} \times 2.44$	$\frac{50}{500} \times 2.44$	$\frac{100}{500} \times 2.44$
$N_{gen}^{b\bar{b}}$	8461350	5250000	10947600
$\frac{B}{S}$	< 1.7	< 2.4	$< 17.3 \times 10^3$

Table 8.4: *Contributions to the B/S calculation for each* $B \to DD$ *decay channel.*

8.3.3 Exclusive B meson decay backgrounds

From the $b\bar{b}$ analysis described in Section 8.3.1, the possible sources of combinatorial specific backgrounds are b-hadron decays with similar topologies to that of the considered $B \to DD$ channel. These decays are high multiplicity B_d^0 and B_s^0 decays with hadronic final states. Of the two types of decays selected by the $B_d^0 \to D^+D^-$ and $B_s^0 \to D_s^+D_s^-$ selection cuts, only $B_s^0 \to D_s^{*+}(\gamma D_s^+(\Rightarrow K^+K^-\pi^+))D_s^{*-}(\gamma D_s^-(\Rightarrow K^+K^-\pi^-))$ Monte Carlo (50k) was available. None of these 50k events passed the selection cuts in either of the $B_d^0 \to D^+D^-$ or $B_s^0 \to D_s^+D_s^-$ analyses.

8.3.4 Other event types

None of the $\sim\mathcal{O}$ (56 k) triggered events discussed in Section 6.5 passed the $B_d^0 \to D^+D^-$, $B_s^0 \to D_s^+D_s^-$ or $B_c^+ \to D_s^+\overline{D}^0$ selection cuts (with $\pm$ 500 MeV window about the true B-meson mass). Since this corresponds to ~1.4 seconds of LHCb data-taking then this result is not unexpected. The sample of $\sim \mathcal{O}$ (21 M) minimum bias events from which these triggered events were produced is approximately two-thirds of the total minimum

bias events currently available for study.

8.4 Flavour Tagging

Identification of the initial flavour of reconstructed B^0_d and B^0_s mesons is necessary in order to study decays involving $\mathcal{CP}$ asymmetries as described in Section 3.3.2. However the analysis of γ using $B^0_{d(s)} \to D^+_{(s)}D^-_{(s)}$ does not require the $B^0_s \to D^+_s D^-_s$ events to be tagged. The statistical uncertainty on the measured $\mathcal{CP}$ asymmetries is directly related to the effective tagging efficiency $\epsilon_{\rm eff}$, which is defined as

$$\epsilon_{\rm eff} = \epsilon_{\rm tag}\, D^2 \;=\; \epsilon_{\rm tag}(1-2\omega)^2. \tag{8.5}$$

$\epsilon_{\rm tag}$ is the probability that the tagging procedure gives an answer, i.e. the tagging efficiency, D is the dilution term and ω is the wrong tag fraction. The probabilities $\epsilon_{\rm tag}$ and ω are defined as

$$\epsilon_{\rm tag} \;=\; \frac{R\,+\,W}{R\,+\,W\,+\,U} \qquad \omega \;=\; \frac{W}{R\,+\,W} \tag{8.6}$$

where R, W and U are the number of correctly tagged, incorrectly tagged, and untagged events, respectively. The mistagging of the initial flavour of the reconstructed B-meson can occur due to several reasons. There are many leptons from K,π and semi-leptonic charm decays that can give the wrong sign lepton. Also when the b-hadron providing the tag is a B^0_d or B^0_s, then it can oscillate before it decays, providing a wrong tag.

The flavour tagging algorithm uses two types of single particle tag algorithms; opposite-side tag, based on muons, electrons and kaons, which are used to tag B^0_d and B^0_s mesons and same-side tag based on kaons which are used to tag B^0_s mesons only. These are described in detail in [182].

The opposite-side tag algorithms determine the flavour of the b-hadron accompanying the reconstructed B meson under study. They use the charge of the lepton from

semileptonic b decay and of the kaon from the $b \to c \to s$ decay chain. They also use the charge of the inclusive secondary vertex reconstructed from b-decay products. The same-side tag algorithms determine directly the flavour of the signal B meson exploiting the correlation in the fragmentation decay chain and are used to tag B_s^0 mesons. If a B_s^0 ($b\bar{s}$) is produced in the fragmentation of a $\overline{b}$ quark, an extra $\overline{s}$ is available to form a K meson, which is a charged K in about 50% of the time and a neutral K in the remaining cases. In addition the inclusive reconstruction of the opposite b-hadron is performed in order to determine the b-hadron charge. A quantity, the vertex charge Q_{vtx} is defined as the sum of the charges of all tracks associated to the vertex.

The results of the two single particle tag algorithms and the inclusive reconstruction of the opposite b-hadron are combined to form a combined tag result for each event. In the case when there is only one tag available, the production flavour of the reconstructed B candidate is taken using the charge of the tagging particle, or the secondary vertex charge Q_{vtx}. If there is more than one tag available then Q_{vtx} is ignored and the final decision is taken as follows: both the muon and the electron tag are available, the one with the highest probability to come from a $b \to \ell$ decay, is used. If two single-track tags are available and they disagree, then the B candidate remains untagged. If three single-track candidates are available, then the decision taken by the majority of them is used.

Table 8.5 shows the performance of the combined tag for the $B_d^0 \to D^+D^-$ and $B_s^0 \to D_s^+D_s^-$ channels, using events passing both offline and trigger cuts. In particular Table 8.5 shows how the quantities defined in Equations 8.5 and 8.6 are calculated. The uncertainties given are statistical. The flavour tagging performance of the $B_d^0 \to D^+D^-$ and $B_s^0 \to D_s^+D_s^-$ channels are consistent with that of other channels studied i.e. an effective tagging efficiency ϵ_{eff} of ~2-5% for B_d^0 decays and ~5-9% for B_s^0 decays. An increased ϵ_{eff} for B_s^0 decays as compared to B_d^0 decays is seen because of the extra $\overline{s}$ available for (same-side) tagging [70].

Using the values of the untagged but triggered events yields listed in Table 8.2 and the values of ϵ_{eff} and ϵ_{tag} listed in Table 8.5, then the $B_d^0 \to D^+D^-$ and $B_s^0 \to D_s^+D_s^-$ annual

triggered and tagged event yields can be calculated. These are shown in Table 8.6.

Decay channel	$B_d^0 \to D^+D^-$	$B_s^0 \to D_s^+D_s^-$
Correctly tagged events, R	44	52
Incorrectly tagged events, W	28	24
Untagged events, U	75	50
Total number of events, $R + W + U$	147	126
Tagging efficiency, ϵ_{tag} [%]	49.0 ± 4.1	60.3 ± 4.4
Wrong tag fraction, ω [%]	38.9 ± 5.7	31.6 ± 5.3
Effective tagging efficiency, ϵ_{eff} [%]	2.4 ± 1.3	8.2 ± 2.4

Table 8.5: *Combined flavour tagging efficiency values of the tagging efficiency ϵ_{tag} and the effective tagging efficiency ϵ_{eff} for each of the $B_d^0 \to D^+D^-$ and $B_s^0 \to D_s^+D_s^-$. Uncertainties are statistical.*

Decay Channel	N_{year} (k)	ϵ_{eff} [%]	$N_{year} \cdot \epsilon_{\text{eff}}$ (/year)
$B_d^0 \to D^+D^-$	2.60 ± 0.21	2.4 ± 1.3	62.40 ± 0.03
$B_s^0 \to D_s^+D_s^-$	2.8 ± 0.3	8.2 ± 2.4	229.60 ± 0.07

Table 8.6: *Annual triggered and tagged $B_d^0 \to D^+D^-$ and $B_s^0 \to D_s^+D_s^-$ event yields with statistical uncertainties.*

8.5 Comparison with other channels studied by LHCb

Table 8.7 is a summary of the signal efficiencies, untagged annual signal yields and background-over-signal (B/S) ratios from inclusive $b\overline{b}$ events for channels studied in preparation for the LHCb Reoptimisation TDR [70]. For completeness the results of the three channels studied in this thesis have been added into the table. It is noted that the assumed branching ratios $\prod_i \mathcal{BR}_i$ of the $B_d^0 \to D^+D^-$ and $B_s^0 \to D_s^+D_s^-$ are of the same order of magnitude of the other B decays studied. However the $B_c^+ \to D_s^+\overline{D}^0$ channel has an expected branching ratio on average ∼10-100 times smaller than other channels. The other B_c^+ channel which has been studied is $B_c^+ \to J/\psi(\mu^+\mu^-)\pi^+$ [183]. Studies of this channel assume a branching ratio for the $B_c^+ \to J/\psi\pi^+$ part of the decay of 1% in

comparison to the PDG 90% upper limit of $<8.2\times10^{-5}$ [37] making a direct comparison of the B_c^+ decay performance difficult.

Except for channels in which the B meson decays to a neutral particle such as a π^0 or a γ then the total signal efficiency $\epsilon_{\rm total}$ is significantly lower for the B $\rightarrow$ DD channels than for other channels. $\epsilon_{\rm total}$ is the product of several contributing efficiencies; the detection efficiency $\epsilon_{\rm det}$, the reconstruction efficiency of detected events $\epsilon_{\rm rec/det}$, the selection efficiency of reconstructed events $\epsilon_{\rm sel/rec}$ and the trigger efficiency of selected events $\epsilon_{\rm trigger/sel}$ as specified in Equation 8.1. The lower $\epsilon_{\rm total}$ obtained for the B $\rightarrow$ DD decay channels is mainly due to the lower values of $\epsilon_{\rm sel/rec}$ compared to others studied. $\epsilon_{\rm sel/rec}$ is expected to be lower for higher multiplicity decays since tighter cuts are needed in order to reduce an increased combinatorial background to a B/S level comparable with other channels. The other six-final state decay shown in Table 8.7 is $B_s^0 \rightarrow \eta_c(1S)(\Rightarrow h^+h^-h^+h^-)\phi(1020)(\rightarrow K^+K^-)$ where $h = \pi$,K, has $\epsilon_{\rm sel/rec}$=15.8 %. The decay occurs via two narrow resonances and so will have a much cleaner signal, requiring less stringent cuts to be imposed.

The values of the detection efficiency $\epsilon_{\rm det} = \epsilon_{\rm gen}^{\rm signal} \times \epsilon_{\rm accept}$ is at the lower end of the $\epsilon_{\rm det}$ range as compared to other channels. $\epsilon_{\rm gen}^{\rm signal}$ is (an event-based) efficiency of the cut imposed on the signal $\overline{\rm b}$ of the decaying B-meson and so is the same for all channels. $\epsilon_{\rm accept}$ is the fraction of the Monte Carlo events that are reconstructible by the detector and is expected to be lower for higher multiplicity decays. Therefore the values of $\epsilon_{\rm det}$ obtained are not unexpected. The inclusion of the upstream tracks with average track reconstruction efficiency of $\sim$75% compared to an average long track reconstruction efficiency of 94% appears to have a minimal effect on the reconstruction efficiency of the B $\rightarrow$ DD channels. The values of $\epsilon_{\rm rec/det}$ are comparable to that obtained from studies of other high-multiplicity channels. The trigger efficiencies of the B $\rightarrow$ DD channels are comparable with those of other hadronic channels.

The selection cuts used to calculate these figures were determined in order to maintain a high efficiency for the signal while providing a very large rejection factor for the combinatorial background. The B/S values obtained are comparable with other chan-

nels. However the $\sim \mathcal{O}\left(10^7\right)$ inclusive $b\bar{b}$ Monte Carlo events used for this corresponds to only ~4 minutes of LHCb data-taking, and is insufficient to provide an accurate value of B/S.

8.6 Future improvements

The LHCb analysis techniques and tools have been recently developed since the analyses presented in this thesis were completed. Future improvements are therefore expected in the particle identification, primary vertex selection and background studies as outlined below.

The recently available tools for the combining of information from the RICH, calorimeter and muon detectors has led to the use of so-called Combined ParticleID in some analyses. In this method, log likelihood information obtained from the RICH is combined with information from the calorimeter and muon detectors as follows:

$$\mathcal{L}(\mathrm{e}) \;=\; \mathcal{L}^{\mathrm{RICH}}(\mathrm{e}) \times \mathcal{L}^{\mathrm{CALO}}(\mathrm{e}) \times \mathcal{L}^{\mathrm{MUON}}(\mathrm{non}{-}\mu) \tag{8.7}$$

$$\mathcal{L}(\mu) \;=\; \mathcal{L}^{\mathrm{RICH}}(\mu) \times \mathcal{L}^{\mathrm{CALO}}(\mathrm{non-e}) \times \mathcal{L}^{\mathrm{MUON}}(\mu) \tag{8.8}$$

$$\mathcal{L}(\mathrm{K},\pi,\mathrm{p}) \;=\; \mathcal{L}^{\mathrm{RICH}}(\mathrm{K},\pi,\mathrm{p}) \times \mathcal{L}^{\mathrm{CALO}}(\mathrm{non-e}) \times \mathcal{L}^{\mathrm{MUON}}(\mathrm{non}{-}\mu) \tag{8.9}$$

Particle candidates can be selected by cutting on a likelihood ratio between hypotheses or equivalently on the difference of a log likelihood. This has been shown to achieve considerable discriminating power for lepton-hadron separation [70]. This would be the preferred method of categorising particle candidates rather than the use of "light"-"heavy" should these $B \to DD$ channels be studied in the future. As an example, the use of only RICH information rather than the Combined ParticleID may be a contributing factor to the lower than expected values of $\epsilon_{\mathrm{sel/rec}}$ obtained in Section 7.5.4 since information from the calorimeter and muon detectors is useful in rejecting electron and muon candidates mistakenly identified as pions by the RICH.

In Section 7.2 it was described that if more than one primary vertex was found in an event, then the first one that had been reconstructed is used. This method of choosing which primary vertex to use leaves room for improvement since it has later been found that choosing the primary vertex in this way will result in the selection of the wrong primary vertex in approximately 35% of events. Other analyses for example [184], take the primary vertex to be the vertex with respect to which the B-meson candidate has the smallest impact parameter significance. This method of choosing the primary vertex has the consequence that the choice of vertex, and any cut related to it, can only be applied once the B-meson candidate has been formed.

A LHCb computing challenge is scheduled for the summer of 2004 during which $\sim \mathcal{O}\left(5 \times 10^7\right)$ inclusive $b\overline{b}$ events are to be generated [185]. The data challenge will allow a greater range of channels than those listed in Table 8.7 to be studied. In particular, the higher inclusive $b\overline{b}$ statistics and the generation of exclusive final state backgrounds for different channels will allow more realistic background studies to take place. It is expected that both the $B_d^0 \to D^+D^-$ and $B_s^0 \to D_s^+D_s^-$ channels will be studied in greater detail during this time.

8.7 Summary

A study of the $B_d^0 \to D^+D^-$, $B_s^0 \to D_s^+D_s^-$ and $B_c^+ \to D_s^+\overline{D}^0$ decay channels have been carried out using the LHCb object-orientated DaVinci analysis framework. Preliminary studies of the $B_d^0 \to D^+D^-$ and $B_s^0 \to D_s^+D_s^-$ channels without a background study had been carried out several years ago [50]. However these had been carried out using the previous LHCb detector design [69] and prior to the implementation of the more realistic object-orientated software. Studies of the $B_d^0 \to D^+D^-$ and $B_s^0 \to D_s^+D_s^-$ channels have shown that they can be detected, reconstructed, selected and triggered with efficiencies of $0.107 \pm 0.09\%$ and $0.091 \pm 0.08\%$ respectively. This results in annual triggered event yields of 2.6 ± 0.2 k/year and 2.8 ± 0.3 k/year. Assuming that inclusive $b\overline{b}$ events are the dominant source of combinatorial background then this allows the setting of an upper

limit to the background-to-signal ratio (B/S) of < 1.7 and < 2.4 respectively for the $B^0_d \to D^+D^-$ and $B^0_s \to D^+_s D^-_s$ channels. These results show that high multiplicity final state decays can be studied within a hadronic environment. The events yields and B/S obtained mean that it is feasible for the $B^0_{d(s)} \to D^+_{(s)}D^-_{(s)}$ channels to be used to determine the CKM angle γ as discussed in Chapter 3.

The study of the $B^+_c \to D^+_s \overline{D}^0$ decay channel has found that an event yield of $(24.8 \pm 0.2)\times10^{-3}$ and a B/S ratio of $< 17.3 \times 10^3$ is to be expected. Therefore these studies also show that it is very unlikely that the $B^+_c \to D^+_s \overline{D}^0$ channel can be used to study γ at LHCb. It is also unlikely that this channel could ever be used for studies of the B^+_c mass and lifetime.

Decay Channel	Factors (in %) forming $\epsilon_{\rm total}$ (in %) $\epsilon_{\rm det} \times \epsilon_{\rm rec/det} \times \epsilon_{\rm sel/rec} \times \epsilon_{\rm trigger/sel} = \epsilon_{\rm total}$					Assumed visible BR (in 10^{-6})	Annual signal yield (k)	B/S ratio from incl. $b\bar{b}$ back.
	$\epsilon_{\rm det}$	$\epsilon_{\rm rec/det}$	$\epsilon_{\rm sel/rec}$	$\epsilon_{\rm trigger/sel}$	$\epsilon_{\rm total}$			
$B_d^0 \to D^+D^-$	6.3	70.4	6.7	36.3	0.107	3.1	2.6	< 1.7
$B_s^0 \to D_s^+D_s^-$	6.6	68.5	5.9	34.3	0.091	15.0	2.8	< 2.4
$B_c^+ \to D_s^+\overline{D}^0$	7.4	76.9	7.3	22.3	0.093	0.017	0.0000248	$< 17.3 \times 10^3$
$B_d^0 \to \pi^+\pi^-$	12.2	91.6	18.3	33.6	0.688	4.8	26.0	< 0.7
$B_d^0 \to K^+\pi^-$	12.2	92.0	25.2	33.2	0.94	18.5	135.0	0.16 ± 0.04
$B_s^0 \to \pi^+K^-$	12.0	92.1	13.5	36.7	0.548	4.8	5.3	< 1.3
$B_s^0 \to K^+K^-$	12.0	92.5	28.6	31.1	0.988	18.5	37.0	0.31 ± 0.10
$B_d^0 \to \pi^+\pi^-\pi^0$	6.0	65.5	2.0	36.0	0.028	20.0	4.4	< 7.1
$B_d^0 \to D^{*-}\pi^+$	9.4	77.7	18.5	27.4	0.370	71.0	206.0	< 0.3
$B_d^0 \to \overline{D}^0(K\pi)K^{*0}$	5.3	81.8	22.9	35.4	0.354	1.2	3.4	< 0.5
$B_d^0 \to \overline{D}^0(KK)K^{*0}$	5.2	81.4	29.4	31.2	0.390	0.19	0.59	< 2.9
$B_s^0 \to D_s^-\pi^+$	5.4	80.6	25.0	31.1	0.337	120.0	80.0	0.32 ± 0.10
$B_s^0 \to D_s^{\mp}K^{\pm}$	5.4	82.0	20.6	29.5	0.269	10.0	5.4	< 1.0
$B_d^0 \to J/\psi(\mu\mu)K_S^0$	6.5	66.5	53.5	60.5	1.39	19.8	216.0	0.80 ± 0.10
$B_d^0 \to J/\psi(ee)K_S^0$	5.8	60.8	17.7	26.5	0.164	20.0	25.6	0.98 ± 0.21
$B_d^0 \to J/\psi(\mu\mu)K^{*0}$	7.2	82.7	35.1	69.9	1.462	59.0	670.0	0.17 ± 0.03
$B_d^0 \to J/\psi(\mu\mu)K^+$	11.9	89.6	44.8	68.7	3.28	68.0	1740.0	0.37 ± 0.02
$B_s^0 \to J/\psi(\mu\mu)\phi$	7.6	82.5	41.6	64.0	1.672	31.0	100.0	< 0.3
$B_s^0 \to J/\psi(ee)\phi$	6.7	76.5	22.0	28.0	0.315	31.0	20.0	0.7 ± 0.2
$B_s^0 \to J/\psi(\mu\mu)\eta$	10.1	69.6	10.1	64.8	0.461	7.6	7.0	< 5.1
$B_s^0 \to \eta_c\phi$	2.6	69.5	15.8	27.0	0.078	21.0	3.2	< 1.4
$B_s^0 \to \phi\phi$	6.7	79.7	37.9	23.2	0.470	1.3	1.2	< 0.4
$B_d^0 \to \mu^+\mu^-K^{*0}$	7.2	82.4	16.1	73.5	0.704	0.8	4.4	< 2.0
$B_d^0 \to K^{*0}\gamma$	9.5	86.8	5.0	37.8	0.156	29.0	35.0	< 0.7
$B_s^0 \to \phi\gamma$	9.7	86.3	7.6	34.3	0.220	21.2	9.3	< 2.4
$B_c^+ \to J/\psi(\mu\mu)\pi^+$	11.5	89.3	20.7	60.8	1.30	680.0	14.0	< 0.8

Table 8.7: *Summary of the signal efficiencies, untagged annual signal yields and background-over-signal (B/S) ratios from inclusive* $b\bar{b}$ *events. The total efficiency is defined in Equation 8.1. The quoted errors on B/S are from the Monte Carlo (MC) statistics with estimates based on less than 10 MC background events quoted as 90% CL upper limits. Parts of this table first appeared in [70].*

Chapter 9

Conclusion

This thesis has presented work carried out by the author during her time as postgraduate student in the High Energy Physics Group at the University of Cambridge, and as a member of the LHCb collaboration. The work presented is divided into two parts; the characterisation of a pixel Hybrid Photon Detector (HPD) prototype for the RICH detector and studies of the $B_d^0 \to D^+D^-$, $B_s^0 \to D_s^+D_s^-$ and $B_c^+ \to D_s^+\overline{D}^0$ channels.

The photodetector choice for the RICH is the pixel Hybrid Photon Detector (HPD). Studies of the performance of a 10 MHz full-scale prototype HPD are presented and its behaviour is shown to be consistent with that of previous prototypes. The experimental method for determining the pixel HPD detection efficiency to single photoelectrons has been outlined. The prototype studied was found to have efficiency to single photoelectrons of

$$\epsilon_{\text{p.e.}} = 0.827 \pm 0.001\,(\text{stat}) \pm 0.037\,(\text{syst}).$$

Despite a significant bump-bond degradation during manufacture, this particular HPD has an efficiency to single photoelectrons that approaches the target of $\simeq 85\,\%$. This is a necessary requirement for the particle identification of pions and kaons over a wide momentum range by the two Ring Imaging Cherenkov detectors RICH-1 and RICH-2.

Three B $\to$ DD physics simulation studies have been carried out. Studies of these

channels were motivated by methods proposed by Fleischer and Wyler to extract the CKM angle γ [73, 74]. It has been shown that the $B_d^0 \to D^+D^-$ and $B_s^0 \to D_s^+D_s^-$ channels can be detected, reconstructed, selected and triggered with total efficiencies of

$$\epsilon_{\text{total}}(B_d^0 \to D^+D^-) = (0.107 \pm 0.09)\%,$$
$$\epsilon_{\text{total}}(B_s^0 \to D_s^+D_s^-) = (0.091 \pm 0.08)\%.$$

The corresponding event yields are

$$N_{year}(B_d^0 \to D^+D^-) = (2.6 \pm 0.2)\text{ k events/year},$$
$$N_{year}(B_s^0 \to D_s^+D_s^-) = (2.8 \pm 0.3)\text{ k events/year}.$$

The errors on the values of ϵ_{total} and N_{year} are statistical.

Assuming that inclusive $b\overline{b}$ events are the dominant source of combinatorial background then an upper limit to the background-to-signal ratio (B/S) of

$$B/S(B_d^0 \to D^+D^-) < 1.7,$$
$$B/S(B_s^0 \to D_s^+D_s^-) < 2.4,$$

have been set using $\sim \mathcal{O}(10^7)$ inclusive $b\overline{b}$ events, corresponding to approximately 4 minutes of LHCb data-taking. These results are comparable to the performance of other B decays studied using the LHCb detector.

Studies of the $B_c^+ \to D_s^+\overline{D}^0$ channel show that, even after several years of data taking, it is unlikely that it can be studied at LHCb. The values of ϵ_{total}, N_{year} and B/S obtained for this channel are

$$\epsilon_{\text{total}}(B_c^+ \to D_s^+\overline{D}^0) = (0.093 \pm 0.08)\%,$$
$$N_{year}(B_c^+ \to D_s^+\overline{D}^0) = (24.8 \pm 0.2)\times 10^{-3}\text{ events/year},$$
$$B/S(B_c^+ \to D_s^+\overline{D}^0) < 17.3 \times 10^3.$$

Appendix A

Extracting γ from $\mathrm{B}^0_{\mathrm{d(s)}} \to \mathrm{D}^+_{\mathrm{(s)}}\mathrm{D}^-_{\mathrm{(s)}}$

In the case that there are both tree and penguin contributions then the decay amplitude for which the underlying quark process is say $\mathrm{b}\to \mathrm{q}\overline{\mathrm{q}}\mathrm{q}'$, can be written as the sum of three terms with definite CKM coefficients [65] as

$$A\left(\mathrm{q}\overline{\mathrm{q}}\mathrm{q}'\right) = \mathrm{V_{tb}V^*_{tq'}P^t_{q'}} + \mathrm{V_{cb}V^*_{cq'}}\left(\mathrm{T_{c\bar{c}q'}}\delta_{\mathrm{qc}} + \mathrm{P^c_{q'}}\right) + \mathrm{V_{ub}V^*_{uq'}}\left(\mathrm{T_{u\bar{u}q'}}\delta_{\mathrm{qu}} + \mathrm{P^u_{q'}}\right) \qquad \text{(A.1)}$$

where $\mathrm{T_{q'}}$ are the tree diagram contributions to the amplitude, $\mathrm{P}^q_{q'}$ are the penguin diagram contributions to the amplitude and δ_{ij} is the Kronecker delta,

$$\delta_{\mathrm{ij}} = \begin{cases} = 1 & \text{if i} = \text{j} \\ = 0 & \text{if i} \neq \text{j}. \end{cases} \qquad \text{(A.2)}$$

$\mathrm{B^0_d} \to \mathrm{D^+D^-}$ has the underlying quark decay $\mathrm{b}\to \mathrm{c}\overline{\mathrm{c}}\mathrm{d}$ and therefore the contribution to the amplitude has the structure $A\left(\mathrm{q}\overline{\mathrm{q}}\mathrm{d}\right)$ where

$$\begin{aligned} A\left(\mathrm{q}\overline{\mathrm{q}}\mathrm{d}\right) &= \mathrm{V_{tb}V^*_{td}P^t_d} + \mathrm{V_{cb}V^*_{cd}}\left(\mathrm{T_{c\bar{c}d}}\delta_{\mathrm{cc}} + \mathrm{P^c_d}\right) + \mathrm{V_{ub}V^*_{ud}}\left(\mathrm{T_{u\bar{u}d}}\delta_{\mathrm{cu}} + \mathrm{P^u_d}\right) \qquad \text{(A.3)} \\ &= \mathrm{V_{tb}V^*_{td}P^t_d} + \mathrm{V_{cb}V^*_{cd}}\left(\mathrm{T_{c\bar{c}d}} + \mathrm{P^c_d}\right) + \mathrm{V_{ub}V^*_{ud}P^u_d}. \end{aligned}$$

Using the unitarity of the CKM matrix (Equation 2.79),

$$\mathrm{V_{ud}V^*_{ub} + V_{cd}V^*_{cb} + V_{td}V^*_{tb} = 0} \tag{A.4}$$

then by eliminating the $\mathrm{V_{tb}V^*_{td}}$ term, Equation A.3 becomes

$$\begin{aligned} A\left(\mathrm{q\overline{q}d}\right) &= \mathrm{V_{cb}V^*_{cd}}\left(\mathrm{T_{c\overline{c}d} - P^t_d + P^c_d}\right) + \mathrm{V_{ub}V^*_{ud}}\left(\mathrm{P^u_d - P^t_d}\right) \\ &= \mathrm{V_{cb}V^*_{cd}}\left(\mathrm{T_{c\overline{c}d} + P^{ct}_d}\right) + \mathrm{V_{ub}V^*_{ud}P^{ut}_d}, \end{aligned} \tag{A.5}$$

where the notation $\mathrm{P^{qt}_d = P^q_d - P^t_d}$, has been introduced.

$$\begin{aligned} A\left(\mathrm{q\overline{q}d}\right) &= (-\lambda)\, A\lambda^2\left(\mathrm{T_{c\overline{c}d} + P^{ct}_d}\right) + |\mathrm{V_{ub}}| e^{i\gamma}\left(1 - \frac{\lambda^2}{2}\right)\mathrm{P^{ut}_d} \\ &= (-\lambda)\, A\lambda^2\left(\mathrm{T_{c\overline{c}d} + P^{ct}_d}\right) + \left|\frac{\mathrm{V_{ub}}}{\mathrm{V_{cb}}}\right| |\mathrm{V_{cb}}|\, e^{i\gamma}\left(1 - \frac{\lambda^2}{2}\right)\mathrm{P^{ut}_d} \\ &= (-\lambda)\, A\lambda^2\left(\mathrm{T_{c\overline{c}d} + P^{ct}_d}\right) + \left|\frac{\mathrm{V_{ub}}}{\mathrm{V_{cb}}}\right| A\lambda^2\, e^{i\gamma}\left(1 - \frac{\lambda^2}{2}\right)\mathrm{P^{ut}_d}. \end{aligned} \tag{A.6}$$

where

$$\mathrm{V_{ub}} = |\mathrm{V_{ub}}|\, e^{i\gamma}, \quad A \equiv \frac{1}{\lambda^2}|\mathrm{V_{cb}}|, \quad \mathrm{V_{cb}} = |\mathrm{V_{cb}}| = \lambda. \tag{A.7}$$

Therefore

$$\begin{aligned} A\left(\mathrm{q\overline{q}d}\right) &= (-\lambda)\, A\lambda^2\left(\mathrm{T_{c\overline{c}d} + P^{ct}_d}\right)\left\{1 - \frac{1}{\lambda}\left|\frac{\mathrm{V_{ub}}}{\mathrm{V_{cb}}}\right| e^{i\gamma}\left(1 - \frac{\lambda^2}{2}\right)\left(\frac{\mathrm{P^{ut}_d}}{\mathrm{T_{c\overline{c}d} + P^{ct}_d}}\right)\right\} \\ &= (-\lambda)\, A\lambda^2\left(\mathrm{T_{c\overline{c}d} + P^{ct}_d}\right)\left\{1 - \mathrm{R_b}\, e^{i\gamma}\left(1 - \frac{\lambda^2}{2}\right)\left(\frac{\mathrm{P^{ut}_d}}{\mathrm{T_{c\overline{c}d} + P^{ct}_d}}\right)\right\}, \end{aligned} \tag{A.8}$$

where

$$\mathrm{R_b} \equiv \frac{1}{\lambda}\left|\frac{\mathrm{V_{ub}}}{\mathrm{V_{cb}}}\right|. \tag{A.9}$$

Defining

$$ae^{i\theta} \equiv \mathrm{R_b}\left(1 - \frac{\lambda^2}{2}\right)\left(\frac{\mathrm{P^{ut}_d}}{\mathrm{T_{c\overline{c}d} + P^{ct}_d}}\right) \quad \text{and} \quad \mathcal{A} \equiv \lambda^2 A\left(\mathrm{T_{c\overline{c}s} + P^{ct}_d}\right), \tag{A.10}$$

then

$$A\left(q\overline{q}d\right) = -\lambda\mathcal{A}\left\{1 - ae^{i\theta}e^{i\gamma}\right\}. \tag{A.11}$$

$B^0_s \to D^+_s D^-_s$ has the underlying quark decay $b \to c\overline{cs}$ and therefore the contribution to the amplitude has the structure $A\left(q\overline{q}s\right)$ where

$$\begin{aligned} A\left(q\overline{q}s\right) &= V_{tb}V^*_{ts}P^t_s \ + V_{cb}V^*_{cs}\left(T_{c\overline{c}s}\delta_{cc} + P^c_s\right) + V_{ub}V^*_{us}\left(T_{u\overline{u}s}\delta_{cu} + P^u_s\right) \\ &= V_{tb}V^*_{ts}P^t_s \ + V_{cb}V^*_{cs}\left(T_{c\overline{c}s} + P^c_s\right) + V_{ub}V^*_{us}P^u_s. \end{aligned} \tag{A.12}$$

Proceeding in a similar manner to when considering the $B^0_d \to D^+D^-$ decay channel, then using the unitarity of the CKM matrix (Equation 2.80),

$$V_{us}V^*_{ub} + V_{cs}V^*_{cb} + V_{ts}V^*_{tb} = 0 \tag{A.13}$$

and eliminating the $V_{tb}V^*_{ts}$ term, Equation A.12 becomes

$$\begin{aligned} A\left(q\overline{q}s\right) &= V_{cb}V^*_{cs}\left(T_{c\overline{c}s} - P^t_s + P^c_s\right) + V_{ub}V^*_{us}\left(P^u_s - P^t_s\right) \\ &= V_{cb}V^*_{cs}\left(T_{c\overline{c}s} + P^{ct}_s\right) + V_{ub}V^*_{us}P^{ut}_s, \end{aligned} \tag{A.14}$$

where $P^{qt}_s = P^q_s - P^t_s$. Using Equation A.7 then

$$V_{cb}V^*_{cs} = A\lambda^2\left(1 - \frac{\lambda^2}{2}\right) \quad \text{and} \quad V_{ub}V^*_{us} = |V_{ub}|e^{i\gamma}\lambda. \tag{A.15}$$

Therefore

$$\begin{aligned} A\left(q\overline{q}s\right) &= A\lambda^2\left(1 - \frac{\lambda^2}{2}\right)\left(T_{c\overline{c}s} + P^{ct}_s\right) + |V_{ub}|e^{i\gamma}\lambda P^{ut}_s \\ &= A\lambda^2\left(1 - \frac{\lambda^2}{2}\right)\left(T_{c\overline{c}s} + P^{ct}_s\right)\left\{1 + \frac{|V_{ub}|e^{i\gamma}\lambda P^{ut}_s}{A\lambda^2\left(1 - \frac{\lambda^2}{2}\right)\left(T_{c\overline{c}s} + P^{ct}_s\right)}\right\} \\ &= A\lambda^2\left(1 - \frac{\lambda^2}{2}\right)\left(T_{c\overline{c}s} + P^{ct}_s\right)\left\{1 + \frac{1}{\lambda}\left|\frac{V_{ub}}{V_{cb}}\right|\frac{|V_{cb}|e^{i\gamma}}{A\left(1 - \frac{\lambda^2}{2}\right)}\frac{P^{ut}_s}{\left(T_{c\overline{c}s} + P^{ct}_s\right)}\right\} \end{aligned} \tag{A.16}$$

$$= A\lambda^2\left(1-\frac{\lambda^2}{2}\right)\left(T_{c\bar{c}s}+P^{ct}_s\right)\left\{1+R_b\frac{\lambda^2 e^{i\gamma}}{\left(1-\frac{\lambda^2}{2}\right)}\left(\frac{P^{ut}_s}{T_{c\bar{c}s}+P^{ct}_s}\right)\right\}$$

$$= A\lambda^2\left(1-\frac{\lambda^2}{2}\right)\left(T_{c\bar{c}s}+P^{ct}_s\right)\left\{1+R_b\left(1-\frac{\lambda^2}{2}\right)\frac{\lambda^2 e^{i\gamma}}{\left(1-\frac{\lambda^2}{2}\right)^2}\left(\frac{P^{ut}_s}{T_{c\bar{c}s}+P^{ct}_s}\right)\right\}.$$

Using only next-to-leading-order terms in λ then

$$\frac{1}{\left(1-\frac{\lambda^2}{2}\right)^2} = \frac{1}{\left(1+\frac{\lambda^4}{4}-\lambda^2\right)} \approx \frac{1}{(1-\lambda^2)}, \quad \lambda \ll 1. \tag{A.17}$$

Using notation from [73], we define

$$\mathcal{A}^{'} \equiv \lambda^2 A\left(T_{c\bar{c}s}+P^{ct}_s\right) \quad \text{and} \quad a^{'}e^{i\theta^{'}} \equiv R_b\left(1-\frac{\lambda^2}{2}\right)\left(\frac{P^{ut}_s}{T_{c\bar{c}s}+P^{ct}_s}\right) \tag{A.18}$$

so that Equation A.16 becomes

$$A\left(q\bar{q}s\right) = \left(1-\frac{\lambda^2}{2}\right)\mathcal{A}^{'}\left\{1+\left(1-\frac{\lambda^2}{2}\right)a^{'}e^{i\theta^{'}}e^{i\gamma}\right\}. \tag{A.19}$$

Equations A.11 and A.19 are general parametrisations of the decay amplitudes for the channels $B^0_{d(s)} \to D^+_{(s)}D^-_{(s)}$ within the Standard Model. The parametrisation is reliant only upon the unitarity of the CKM matrix (Equations A.4 and A.13). In Equation A.11, the quantity $ae^{i\theta}$ enters the $B^0_d \to D^+D^-$ amplitude in a Cabbibo allowed way. However in Equation A.19 the quantity $a^{'}e^{i\theta^{'}}$ is doubly Cabbibo suppressed in the $B^0_s \to D^+_sD^-_s$ decay amplitude.

Bibliography

[1] K.A. George *et al.*, LHCb 2002-048 RICH (2002).

[2] K.A. George *et al.*, *Nucl. Instr. and Meth. A* **504**, 286 (2003).

[3] K.A. George, LHCb 2003-130 PHYSICS (2003).

[4] K.A. George, LHCb 2004-014 PHYSICS (2004).

[5] G. Lűders, *Annals of Physics* **2**, 1 (1957).

[6] T.D. Lee and C.N. Yang, *Phys. Rev.* **104**, 254 (1956).

[7] C.S. Wu *et al.*, *Phys. Rev.* **105**, 1413 (1957).

[8] N. Cabibbo, *Phys. Rev. Lett.* **10**, 531 (1963).

[9] J.H. Christenson *et al.*, *Phys. Rev. Lett.* **13**, 138 (1964).

[10] A.D. Sakharov, *JETP Lett.* **5**, 24 (1967).

[11] V.A. Kuzmin *et al.*, *Phys. Lett.* **B 155**, 36 (1985).

[12] M. Kobayashi and T. Maskawa, *Prog. Theor. Phys.* **49**, 652 (1973).

[13] DASP Collaboration: W. Braunschweig *et al.*, *Phys. Lett* **B 57**, 407 (1975).

[14] Fermilab E288 Collaboration: S.W. Herb *et al.*, *Phys. Rev. Lett.* **39**, 252 (1977).

[15] W.R Innes *et al.*, *Phys. Rev. Lett.* **39**, 1240 (1977).

[16] CDF Collaboration: F. Abe *et al.*, *Phys. Rev. Lett.* **73**, 225, `hep-ex/9405005` (1994).

[17] D0 Collaboration: S. Abachi *et al.*, *Phys. Rev. Lett.* **74**, 2632, `hep-ex/9503003` (1995).

[18] M.E. Shaposhnikov, *JETP Lett.* **44**, 465 (1986).

[19] NA31 Collaboration: H. Burkhardt *et al.*, *Phys. Lett. B* **206**, 169 (1988).

[20] NA48 Collaboration:,
`http://na48.web.cern.ch/na48`.

[21] CPLEAR Collaboration:,
`http://cplear.web.cern.ch/cplear`.

[22] CPLEAR Collaboration: A. Angelopoulos *et al.*, *Phys. Rep.* **374**, 165 (2003).

[23] BaBar Collaboration:,
`http://slac.stanford.edu/BFROOT/`.

[24] Belle Collaboration:,
`http://belle.kek.jp`.

[25] BaBar Collaboration: B. Aubert *et al.*, *Phys. Rev. Lett.* **87**, 091801, BaBar-PUB-01/18, SLAC-PUB-8904, `hep-ex/0107013` (2001).

[26] Belle Collaboration: K. Abe *et al.*, *Phys. Rev. Lett.* **87**, 091802, KEK preprint 2001-50, Belle preprint 2000-10, `hep-ex/0107061` (2001).

[27] CDF Collaboration: F. Abe *et al.*, *Phys. Rev. Lett.* **81**, 12 (1998).

[28] A. Cerri, *Nucl. Phys. (Proc. Supp.)* **B 99**, 200 (2001).

[29] F. Ohlsson-Malek on behalf of the ATLAS and CMS collaborations, ATL-CONF-2003-006 (2003).

[30] S. Bannerjee on behalf of the CMS collaboration, CMS CR 2001-004 (2001).

[31] BTeV Collaboration: A. Kulyavtsev *et al.*, BTeV Preliminary Technical Design Report, (1999).

[32] BTeV Collaboration:,
`http://www-btev.fnal.gov`.

[33] I. Bigi and A. Sanda, `hep-ph/0401003` (2004).

[34] Super B-factory Workshops:,
`http://www.phys.hawaii.edu/ superb04/links.html`.

[35] V. Weisskopf and E. Wigner, *Z. für Physik* **63**, 54 (1930).

[36] O. Schneider, *Phys. Rev. D* **66** (2002).

[37] Particle Data Group: K. Hagiwara *et al.*, *Phys. Rev. D* **66** (2002).

[38] G. Buchalla, SLAC-PUB-7613, `hep-ph/9707545` (1997).

[39] Y. Nir and H. Quinn, *Ann. Rev. Nucl. Part. Sci.* **42**, 211 (1992).

[40] G. Unal for the NA48 Collaboration, Proceedings of the 31st International Conference on High Energy Physics, `hep-ex/0209064` (2002).

[41] R. Fleischer, DESY-THESIS-2002-022, `hep-ph/0207108` (2002).

[42] Heavy Flavour Averaging Group (HFAG):,
`http://www.slac.stanford.edu/xorg/hfag/`.

[43] G.C. Branco *et al.*, CP Violation, Oxford Science Publications (1999).

[44] L-L. Chau and W.-Y. Keung, *Phys. Rev. Lett.* **53**, 1802 (1984).

[45] L. Wolfenstein, *Phys. Rev. Lett.* **51**, 1945 (1983).

[46] M. Schmidtler and K.R. Schubert, *Z. Phys. C.* **53**, 347 (1992).

[47] A.J. Buras *et al.*, *Phys. Rev. D.* **50**, 3433, `hep-ph/9403384` (1994).

[48] M. Battaglia *et al.*, Proceedings of the First Workshop on the CKM Unitarity Triangle, CERN 13-16 February 2002, CERN-2003-002, `hep-ph/0304132` (2003).

[49] R. Aleksan *et al.*, *Phys. Rev. Lett.* **73**, 18, `hep-ph/9403341` (1994).

[50] P. Ball *et al.*, CERN-TH-2000-101, `hep-ph/0003238` (2000).

[51] T. Nakada, Proceedings of Workshop on Kaon Physics, Orsay, 30 May - 4 June 1996, `hep-ex/9609015` (1996).

[52] H. Hocker *et al.*, *Eur. Phys. J.* **C21**, 225, `hep-ph/0104062` (2001).

[53] Y. Nir *et al.*, *Nucl. Phys.* **B 345**, 301, SLAC-PUB-5209 (1990).

[54] C. Jarlskog, *Phys. Rev. Lett.* **55**, 1039 (1985).

[55] M. Neubert and B. Stech, *Heavy Flavours II* , `hep-ph/9705292` (1997).

[56] CKM Fitter Group:, `http://ckmfitter.in2p3.fr/`.

[57] ALEPH Collaboration: R. Barate *et al.*, *Phys. Lett.* **B492**, 259, CERN-EP/2000-119, `hep-ex/0009058` (2000).

[58] OPAL Collaboration: K Ackerstaff *et al.*, *Eur. Phys. J* **C5**, 379, CERN-EP/98/001, `hep-ex/9801022` (1998).

[59] CDF Collaboration: T. Affolder *et al.*, *Phys. Rev. D* **61**, FERMILAB-PUB-99-225-E, `hep-ex/9909003` (2000).

[60] BaBar Collaboration: B. Aubert *et al.*, *Phys. Rev. Lett.* **86**, 2515, BaBar-PUB-01/01, SLAC-PUB-8777, `hep-ex/0102030` (2001).

[61] Belle Collaboration: A. Abashiau *et al.*, *Phys. Rev. Lett.* **86**, 2509, KEK preprint 2000-142, Belle preprint 2000-01 (2001).

[62] BaBar Collaboration: B. Aubert *et al.*, *Phys. Rev. Lett.* **89**, 201802, BaBar-PUB-02/008, SLAC-PUB-9293, `hep-ex/0207042` (2002).

[63] T.E. Browder for the Belle Collaboration, To appear in the Proceedings of the 2003 Lepton-Photon Conference at Fermilab, `hep-ex/0312024` (2003).

[64] L.K. Gibbons, Talk given at the 28th International Conference on High Energy Physics, Warsaw, Poland, 25-31 July 1996, to appear in the proceedings. `hep-ex/9704017` (1997).

[65] BaBar Collaboration: P.F. Harrison *et al.*, The BaBar Physics Book: Physics at an Asymmetric B Factory, SLAC-R-0504, (1998).

[66] K. Anikeev *et al.*, `http://www-theory.lbl.gov/Brun2/`, `hep-ph/0201071` (2001).

[67] G. Raven for the BaBar Collaboration, Invited talk at the Workshop on the CKM Unitarity Triangle, IPPP Durham, April 2003, `hep-ex/0307067` (2003).

[68] H. Jawahery for the BaBar Collaboration, `http://conferences.fnal.gov/lp2003/program/pages/jawahery.pdf`.

[69] LHCb Collaboration, LHCb Technical Proposal, CERN/LHCC 98-4, LHCC/P4 (1998).

[70] LHCb Collaboration, LHCb Reoptimized LHCb Detector Design and Performance Technical Design Report, LHCb TDR 9, CERN/LHCC 2003-030 (2003).

[71] KOPIO Collaboration:, `http://www.bnl.gov/rsvp/KOPIO.htm`.

[72] KAMI Collaboration:, `http://kpasa.fnal.gov:8080/public/kami/kami.html`.

[73] R. Fleischer, *Eur. Phys. J.* **C 10**, 299, CERN-TH/99-78, `hep-ph/9903455` (1999).

[74] R. Fleischer and D. Wyler, *Phys. Rev. D* **62**, 057503, DESY 00-052, `hep-ph/0004010` (2000).

[75] Belle Collaboration: K. Abe *et al.*, Contributed paper at Lepton Photon 2003, Belle-CONF-0343, `hep-ex/0308043` (2003).

[76] D. Luchessi for the CDF and D0 Collaborations, Invited talk at the Workshop on the CKM Unitarity Triangle, IPPP Durham, April 2003, `hep-ex/0307025` (2003).

[77] R. Aleksan *et al.*, *Z. Phys.* **C54**, 653, CERN-TH-6238-91 (1992).

[78] R. Hierk *et al.*, LHCb 2003-103 (2003).

[79] I. Dunietz., *Phys. Lett.* **B270**, 75, CERN-TH-6161-91 (1991).

[80] K. Akiba *et al.*, LHCb 2003-105 (2003).

[81] R. Fleischer, Invited plenary talk given at the 7th International Symposium on Heavy Flavor Physics, Santa Barbara, California, 7-11 July 1997. CERN-TH/97-241, `hep-ph/9709291` (1997).

[82] R. Fleischer, Invited plenary talk given at the IVth International Workshop on Progress in Heavy Quark Physics, Rostock, Germany, 20-22 September 1997. CERN-TH/97-295, `hep-ph/9710455` (1997).

[83] R. Fleischer, *Eur. Phys. J.* **C 6**, 451, CERN-TH/99-60, `hep-ph/9802433` (1998).

[84] R. Fleischer, *Phys. Lett. B* **459**, 306, CERN-TH/99-79, `hep-ph/9903456` (1999).

[85] R. Fleischer and J. Matias, *Phys. Rev. D* **66**, 054009 DESY/02-040, `hep-ph/0204101` (2002).

[86] U. Marconi *et al.*, LHCb 2003-124 (2003).

[87] T. Hurth and T. Mannel, *Phys. Lett. B* **511**, 196, CERN-TH/2001-090, `hep-ph/0103331` (2001).

[88] ATLAS Collaboration:, `http://atlasinfo.cern.ch/Atlas/Welcome.html`.

[89] CMS Collaboration:,
`http://cmsinfo.cern.ch/Welcome.html`.

[90] ALICE Collaboration:,
`http://alice.web.cern.ch/Alice/AliceNew/`.

[91] TOTEM Collaboration:,
`http://totem.web.cern.ch/Totem.html`.

[92] LHC: The Large Hadron Collider:,
`http://lhc-new-homepage.web.cern.ch/lhc-new-homepage`.

[93] G. Wilkinson *et al.*, LHCb 97-014 TRIG (1997).

[94] P. Nason *et al.*, Report of the 1999 CERN Workshop on SM physics (and more) at the LHC, CERN-2000-004, `hep-ph/0003142` (2000).

[95] T. Sjöstrand *et al.*, *Computer Physics Commum.* **135**, 238 (2001).

[96] B. Epp for the ATLAS Collaboration, Proc. Advanced Studies Institute - Physics at LHC, Prague. (2003).

[97] LHCb Collaboration, LHCb Magnet Technical Design Report, LHCb TDR 1, CERN/LHCC 1999-0037, (1999).

[98] LHCb Collaboration, LHCb Calorimeter Technical Design Report, LHCb TDR 2, CERN/LHCC 2000-0036, (2000).

[99] LHCb Collaboration, LHCb RICH Technical Design Report, LHCb TDR 3, CERN/LHCC 2000-0037, (2000).

[100] LHCb Collaboration, LHCb Muon Technical Design Report, LHCb TDR 4, CERN/LHCC 2001-0010, (2001).

[101] LHCb Collaboration, LHCb VELO Technical Design Report, LHCb TDR 5, CERN/LHCC 2001-0011, (2001).

[102] LHCb Collaboration, LHCb Outer Tracker Technical Design Report, LHCb TDR 6, CERN/LHCC 2001-0024, (2001).

[103] LHCb Collaboration, LHCb Online Sysem Technical Design Report, LHCb TDR 7, CERN/LHCC 2001-0040, (2001).

[104] LHCb Collaboration, LHCb Inner Tracker Technical Design Report, LHCb TDR 8, CERN/LHCC 2002-0029, (2002).

[105] LHCb Collaboration, LHCb Trigger Technical Design Report, LHCb TDR 10, CERN/LHCC 2003-031, (2003).

[106] LHCb Collaboration, Addendum to the LHCb RICH Technical Design Report, LHCb TDR 3 Addendum I, CERN/LHCC 2003-059, (2003).

[107] LHCb Collaboration, LHCb RICH-2 Engineering Design Review Report, LHCb EDR 2002-009, (2002).

[108] P.A. Cherenkov, *C. R. Ac. Sci. U.S.S.R.* **8**, 451 (1934).

[109] P.A. Cherenkov, *Phys. Rev.* **52**, 378 (1937).

[110] I.M. Frank and I.E. Tamm, *C. R. Ac. Sci. U.S.S.R.* **14**, 109 (1937).

[111] G.B. Collins and V.G. Reiling, *Phys. Rev.* **54**, 499 (1938).

[112] H.O. Wyckoff and J.E. Henderson, *Phys. Rev.* **64**, 1 (1943).

[113] J. Seguinot and T. Ypsilantis, *Nucl. Instr. and Meth. A* **142**, 377 (1977).

[114] DELPHI Collaboration: W. Adam *et al.*, *Nucl. Instr. and Meth. A* **343**, 68 (1994).

[115] WA89 Collaboration: U. Műller *et al.*, *Nucl. Instr. and Meth. A* **371**, 27 (1996).

[116] HERA-B Collaboration: I. Arino *et al.*, *Nucl. Instr. and Meth. A* **516**, 445, `hep-ex/0303012` (2003).

[117] J. Seguinot and T. Ypsilantis, *Nucl. Instr. and Meth. A* **343**, 1 (1994).

[118] T. Ypsilantis and J. Seguinot, *Nucl. Instr. and Meth. A* **343**, 30 (1994).

[119] R. Forty, LHCb 96-005 (1996).

[120] M. Adinolfi *et al.*, LHCb 2000-066 RICH (2000).

[121] T. Gys *et al.*, LHCb 2000-064 RICH (2000).

[122] C. Joram *et al.*, LHCb 2000-063 RICH (2000).

[123] F. Muheim *et al.*, LHCb 2000-065 RICH (2000).

[124] SICB: - the LHCb Geant3 based simulation program,
`http://lhcb-comp.web.cern.ch/lhcb-comp/SICB/default.htm`.

[125] GAUDI:,
`http://proj-gaudi.web.cern.ch/proj-gaudi/`.

[126] DIRAC: The LHCb Production Tool,
`http://lhcb-comp.web.cern.ch/lhcb-comp/Production/default.htm`.

[127] GAUSS: The LHCb Simulation Program,
`http://lhcb-comp.web.cern.ch/lhcb-comp/Simulation/default.htm`.

[128] BOOLE: The LHCb Digitization Program,
`http://lhcb-comp.web.cern.ch/lhcb-comp/Digitization/default.htm`.

[129] BRUNEL: The LHCb Reconstruction Program,
`http://lhcb-comp.web.cern.ch/lhcb-comp/Reconstruction/default.htm`.

[130] DAVINCI: The LHCb Analysis Program,
`http://lhcb-comp.web.cern.ch/lhcb-comp/Analysis/default.htm`.

[131] GANGA: Interfacing GAUDI to GRID Services,
`http://lhcb-comp.web.cern.ch/lhcb-comp/Frameworks/Ganga/default.htm`.

[132] M. Alemi *et al.*, *Nucl. Phys. B (Proc. Suppl.)* **78**, 360 (1999).

[133] E. Albrecht *et al.*, *Nucl. Instr. and Meth. A* **442**, 164 (2000).

[134] M. Alemi *et al.*, CERN EP/99-111 (1999).

[135] C. D'Ambrosio *et al.*, *IEEE Trans. Nucl. Sci.* **NS-43(3)**, 2127 (1996).

[136] D. Puertolas *et al.*, *Nucl. Instr. and Meth. A* **387**, 134 (1997).

[137] K. Wyllie, ALICE1LHCb Preliminary Users Manual (unpublished), (2001), `http://kwyllie.home.cern.ch/kwyllie/ALICE1LHCB.htm`.

[138] ALICE Collaboration, ALICE Technical Proposal, CERN/LHCC 95-71, LHCC/P3 (1995).

[139] T. Gys, *Nucl. Instr. and Meth. A* **465**, 240 (2001).

[140] K. Wyllie, LHCb 2000-075 RICH (2000).

[141] IEEE Standard Test Access Port and Boundary-Scan Architecture. IEEE Std 1149.1-1990.

[142] W. Snoeys, *Nucl. Instr. and Meth. A* **465**, 176 (2001).

[143] M. Campbell, Conclusions from the ALICE1LHCb chip, LHCb RICH Electronics Meeting. 07 February 2002 (2002).

[144] T. Gys and D. Piedigrossi, LHCb 97-026 (1997).

[145] Matsusada: HV supply K7-20N,
`http://www.matsusada.com`
`http://www.tilde-gys.home.cern.ch/~gys/LHCb/Testing/1023-01P.K7.72.pdf`.

[146] Bourdon-Haenni instrumentation : PT100 Temperature Sensor,
`http:://www.bourdon-haenni.com/uk/`.

[147] National Instruments : 6035E Data Aquisition Card,
`http://www.ni.com/pdf/products/us/2mhw245-246e.pdf`.

[148] National Instruments : Labview,
`http://www.ni.com/labview`.

[149] ALICE Pixel Chip:,
`http://alice1.web.cern.ch/alice1/Docs/Contents.htm#Test Systems`.

[150] National Instruments:,
`http://www.ni.com`.

[151] P. Chocula *et al.*, ALICE 2000-032 ITS Pixel (2000).

[152] T.T. de Fatis., *Nucl. Instr. and Meth. A* **385**, 366 (1997).

[153] T. Gys *et al.*, *Nucl. Instr. and Meth. A* **449**, 48 (2000).

[154] LHCb RICH Pixel HPD:,
`http://tilde-gys.home.cern.ch/~gys/LHCb/PixelHPDs.htm`.

[155] M. Girone, Tests of the ALICELHCb chip assemblies. Talk given at the LHCb Photon Detector Review. CERN, 31st October 2001.,
`http://agenda.cern.ch/fullAgenda.php?ida=a017682001-10-31`.

[156] M. Girone, Status Report on the ALICELHCb pixel chip. Talk given at LHCb Week, Brazil, 19th September 2001.,
`http://agenda.cern.ch/fullAgenda.php?ida=a015942001-09-19`.

[157] C. Newby and K. Wyllie, LHCb 2003-032 RICH (2003).

[158] T. Gys, The pixel-HPD project, LHCb Photon Detector Review. 08 January 2003,
`http://agenda.cern.ch/fullAgenda.php?ida=a0222562003-01-08`.

[159] Eurorad PR304:,
`http://www.eurio.fr/eurorad/electronics.html`.

[160] Ortec 579:,
`http://www.ortec-online.com/electronics/amp/579.htm`.

[161] MAESTRO-32 MCA Emulator:,
`http://www.ortec-online.com/maest.htm`.

[162] Ortec 926:,
`http://www.ortec-online.com/pdf/926.pdf`.

[163] E.H. Darlington, *J. Phys. D: Appl. Phys.* **8**, 85 (1975).

[164] H. Drescher *et al.*, *Z . Angew. Phys.* **29(6)**, 331 (1970).

[165] C. D'Ambrosio and H. Leutz, CERN-EP/2002-072 (2002).

[166] F. James, MINUIT: Function Minimization and Error Analysis, CERN Program Library Long Writeup D506,
`http://wwwasdoc.web.cern.ch/wwwasdoc/minuit/minmain.html`.

[167] T. Gys, Proc. IEEE Nuclear Science Symposium and Medical Imaging Conference (1999).

[168] T. Gys *et al.*, *Nucl. Instr. and Meth. A* **387**, 131 (1997).

[169] E. Belau *et al.*, *Nucl. Instr. and Meth. A* **214**, 253 (1983).

[170] K. Wyllie, LHCBPIX1 Preliminary Users Manual (unpublished), (2002),
`http://kwyllie.home.cern.ch/kwyllie/LHCBPIX1.htm`.

[171] G.A. Rinella *et al.*, Performance Study of New Pixel Hybrid Photon Detector Prototypes for the LHCb RICH Counters (unpublished).

[172] G.A. Rinella : RICH Group Meeting, 05 September 2003,
`http://agenda.cern.ch/fullAgenda.php?ida=a035217`.

[173] T. Gys : RICH Group Meeting, 05 September 2003,
`http://agenda.cern.ch/fullAgenda.php?ida=a035217`.

[174] M.-L. Delsante *et al.*, Proceedings of the International Conference on Advanced Materials and Processing Technologies, AMPT 2003, Dubline, Ireland, 2003.

[175] CERN Application Software Group. GEANT: Detector Description and Simulation Tool, CERN Program Library Long Write-up W5013, (1993), `http://wwwasdoc.web.cern.ch/wwwasdoc/geant_html3/geantall.html`.

[176] QQ - The CLEO Event Generator:, `http://www.lns.cornell.edu/public/CLEO/soft/QQ`.

[177] V.V. Kiselev, `hep-ph/0308214` (2003).

[178] I.P. Gouz *et al.*, `hep-ph/0211432` (2002).

[179] A. Golutvin *et al.*, LHCb 2003-127 (2003).

[180] R. White. LHCb Week (May) Joint Physics-PID-Tracking Session (2003), `http://agenda.cern.ch/fullAgenda.php?ida=a039972003-05-20`.

[181] 2003 TDR production web page:, `http://lhcb-comp.web.cern.ch/lhcb-comp/ComputingModel/production/prod-tdr.htm`.

[182] M. Calvi *et al.*, LHCb 2003-115 (2003).

[183] O.P. Yushchenko *et al.*, LHCb 2003-113 (2003).

[184] L. Fernandez, LHCb 2003-101 (2003).

[185] LHCb Data Challenge DC04, `http://lhcb-comp.web.cern.ch/lhcb-comp/ComputingModel/datachallenges/CDC04.htm`.